



HAL
open science

Interfacially-controlled soft granular matter: from non-pairwise to elastocapillary interactions in foams and emulsions stabilised by polymeric skins

Gaël Ginot

► **To cite this version:**

Gaël Ginot. Interfacially-controlled soft granular matter: from non-pairwise to elastocapillary interactions in foams and emulsions stabilised by polymeric skins. Physics [physics]. Université de Strasbourg, 2021. English. NNT: 2021STRAE034 . tel-03652081

HAL Id: tel-03652081

<https://theses.hal.science/tel-03652081>

Submitted on 26 Apr 2022

HAL is a multi-disciplinary open access archive for the deposit and dissemination of scientific research documents, whether they are published or not. The documents may come from teaching and research institutions in France or abroad, or from public or private research centers.

L'archive ouverte pluridisciplinaire **HAL**, est destinée au dépôt et à la diffusion de documents scientifiques de niveau recherche, publiés ou non, émanant des établissements d'enseignement et de recherche français ou étrangers, des laboratoires publics ou privés.

ÉCOLE DOCTORALE 182

UPR 22

THÈSE présentée par :

Gaël Ginot

soutenue le : **17 décembre 2021**

pour obtenir le grade de : **Docteur de l'université de Strasbourg**

Discipline/ Spécialité : **Physique**

Interfacially-controlled soft granular matter : from non-pairwise to elastocapillary interactions in foams and emulsions stabilised by polymeric skins

THÈSE dirigée par :

Dr. DRENCKHAN-ANDREATTA Wiebke Directrice de recherche, Université de Strasbourg

RAPPORTEURS :

Dr. HUTZLER Stefan

Professeur, Trinity College, Dublin

Dr. QUILLIET Catherine

Maître de conférences, Université Grenoble I

AUTRES MEMBRES DU JURY :

Dr. CHARITAT Thierry

Professeur, Université de Strasbourg

Dr. GANACHAUD François

Directeur de recherche, INSA Lyon

- *Ook.*
the librarian, *Night Watch*
Terry Pratchett, 2002

Remerciements / acknowledgements

Au moment de procéder aux remerciements en usage lors du rendu d'un manuscrit, il apparaît comme illusoire de vouloir s'y soumettre sans reconnaître au préalable le contexte ayant servi de toile de fond à sa rédaction ainsi qu'aux travaux qui y sont consignés. Le contexte présent, d'abord : une équipe de chercheurs.se.s rejointe il y a trois ans, et dont les traces se retrouveront en différents endroits ; une pandémie avec laquelle il fallut composer, redirigeant sensiblement un projet qui commençait à émerger ; une concentration atmosphérique de CO₂ que mon espèce n'avait jamais connu jusque-là. Le contexte passé, bien évidemment : les travaux sur lesquels nous avons bâti l'histoire que j'ai le plaisir de présenter dans cet ouvrage ; les choix m'ayant amené jusqu'ici aujourd'hui, et ceux les ayant influés ; les expériences passées, partagées et collectives, ayant parfois transformé une observation naïve en constatation perplexes. Le futur également, parfois, la perception des futur.e.s lectrices de cet ouvrage ayant influencé la façon dont il fut construit (bien que la potentialité d'un lectorat ne soit rien de plus qu'une hypothèse heuristique bien pratique pour faire coexister la temporalité longue de la recherche et celle, bien plus courte, de ma présence).

Cette banalité étant réaffirmée, il me tient néanmoins à cœur de remercier ici par désordre d'importance celles et ceux m'ayant accompagné dans ces travaux, dans l'éventualité où un reste de pudeur mal placée s'opposerait à ce que lesdits remerciements ne soient formulés de vive voix.

Je tiens tout d'abord à remercier mon directrice de thèse, Wiebke Drenckhan, pour m'avoir encadré pendant ces trois ans et demi. J'ai eu plusieurs professeur.e.s au cours de mon existence et j'en aurai à n'en pas douter d'autres ; je n'ai eu cependant à ce jour qu'une seule mentor, et je me souviendrai longtemps de tes enseignements. Merci. Je tiens également à remercier Leandro Jacomine, ingénieur aux doigts de fée dont le savoir-faire et l'humeur toujours égale à elle-même ont porté à bout de bras cette thèse jusque dans les derniers instants. Lorsque le monde extérieur nous était interdit en l'attente de jours plus cléments, l'équipe MIM fut pendant des mois le seul réconfort au plus noir de l'hiver : merci à Sébastien, doyen et partenaire de vulgarisation ; merci à Robin, pour ton sel et ton pragmatisme ; merci à Imen, fée des plantes ; merci à Martin, polyglotte renommé ; merci à Emeline, camarade de bureau et trublion ; merci à Friedrich, dont le travail visionnaire a servi de fondation solide à cette thèse ; merci aussi à Manon, Jonathan, Katja, Stéphane, Aurélie. Merci à François, pour la prodigalité avec laquelle il a pu m'éclairer de ses conseils avisés. Merci à Jean, sans qui le découragement aurait ralenti ce projet bien en amont de ce qu'il est aujourd'hui. Merci à Reinhard, sans l'aide duquel ce projet dans son intégralité n'en serait toujours qu'à ses balbutiements. Vielen Dank Matthias, für deine Hilfe um die komplexe Welt zu entdecken. Vielen Dank Jan und Felix für ihre Beteiligung an der Studium den droploons. Merci à Alain pour son aide avec la cryomicroscopie. Merci énormément à Damien et Antoine pour leur aide précieuse dans l'imagerie tomographique, et la patience dont ils ont fait preuve pour m'aider à en sortir le meilleur. Merci à Patrick pour son enthousiasme à étudier mes échantillons au synchrotron. Merci à Thierry pour sa contribution à l'analyse des structures des mousses. Vielen Dank Sascha für mir zu zeigen, dass meine Studium könnte für jemanden von Interesse sein.

Ces trois dernières années à Strasbourg ont été la prolongation d'un séjour entamé neuf ans

plus tôt. Les relations qui s'y sont nouées et les histoires qui s'y sont vécues font de cet endroit une part importante de ce que j'y suis devenu, et, *in fine*, de la façon dont cette thèse a été construite. Y ont donc contribué une zoologie parfaitement foisonnante de caractères, que j'aimerais remercier ici : Aurélien, pour sa capacité toujours neuve à étonner ; Morgane, pour ce qu'elle cache derrière sa nonchalance ; Benji, pour m'avoir montré qu'on n'était jamais trop jeune pour être vieux, ni trop vieux pour être jeune ; Guillaume, pour son poil soyeux ; Thomas, camarade de confession nocturne et de feux de camps ; Cha' et le rhizome qui t'entoure ; Sofian, générateur de chaos et dessoudeur de vilénies (ne le dis pas aux autres, mais tu es mon préféré) ; Lucie, pour la furieuse douceur avec laquelle elle approche la vie Camille, grâce à qui je suis doublement nommé ; Pauline P.-A, pour le cœur avec lequel elle refuse obstinément la méchanceté ; Nico K., pour m'avoir poussé en avant quand j'en avais besoin ; Étienne, pour la démonstration permanente qu'il fait qu'on peut être autonome dans le fun sans être marginal. Merci également, dans le désordre, aux capichefs Erika, Thibault et Ian, Banc, Maiwenn, Paco, Coco, Tom Pouce, Balthazar, Élodie, Nina, Yaya, Vero, Damien E., Babas, Clément, Brice H., Brice P., Schrötti, Foyan, Emeu, Bryan, Ethes, Laurine, Benoît T., Loélia, Maxime V., Nicolas S., Thibaut, Marin, Norbert, Honoré, Ioan, Fati, Chris', Najim, Axel, Thomas F., Alexandra S., Stephen 'Bichette Pinel', Théophile, Léandre, Victor, Laura, Nathan, et Julien, après lequel il n'y a jamais personne. Un merci tout particulier aux vivant.e.s qui se lèvent pour le rester, dont je m'abstiendrai de dresser la liste de peur qu'on se réfère de l'allonger.

Je tiens également à remercier ma famille, pour le soutien qu'elle m'a apporté pendant et avant mes études. Merci à mes parents de n'avoir pas été producteurices de cinéma, sans quoi ces remerciements auraient encombré une cérémonie des Césars et endormi bien trop de monde. Merci à mon frère d'avoir gardé la maison quand je l'ai quittée. Merci à ma tante, mon oncle, mes cousins et ma cousine. Merci à mes grands-parents pour le bouillonnant mélange de lettres, de sciences et de nature dans lequel elles m'ont élevé.

Enfin, merci à ma grand-mère maternelle qui me manque énormément aujourd'hui, sans laquelle il ne ferait aucun doute que ce manuscrit n'existerait pas.

Contents

1	General introduction	7
2	Materials and Methods	16
2.1	Bubble train setup	16
2.1.1	Bubble generation	16
2.1.2	Image acquisition	16
2.1.3	Force calculation	17
2.2	Finite elements method : Surface Evolver simulations	19
2.2.1	Bubbles trapped in a capillary	19
2.2.2	Simulations of elastocapillary bubbles	20
2.3	Polyethylene glycol-in-silicone emulsion	21
2.3.1	Chemical composition	21
2.3.2	Sample preparation procedure	23
2.3.3	Dry PEG preparation	23
2.3.4	Investigation of the role of PEG impurities	24
2.3.5	Dripping setup for PEG drops production	25
2.3.6	Millifluidic drop production	26
2.3.7	PDMS foam generation	28
2.4	Rheological characterisation	28
2.4.1	Bulk shear rheology	28
2.4.2	Interfacial shear rheology	29
2.5	Tomography	30
2.5.1	Image acquisition	30
3	Investigation of bubble deformability, and its impact on bubble-bubble many-body interactions	31
3.1	Introduction	31
3.1.1	Jammed materials	33
3.1.2	Effects of grain deformability on jammed material properties	38
3.2	Interaction at the bubble scale	45
3.2.1	Pairwise interactions	45
3.2.2	N-body interactions	46
3.3	Morse-Witten interaction law	48
3.4	Experimental verification of Morse-Witten interaction law	51
3.4.1	Experimental setup	52
3.4.2	Bubble size acquisition	52
3.4.3	Bubble-bubble deformation	52

3.4.4	Morse-Witten application to cubic geometry	53
3.4.5	Results	56
3.4.6	Discussion and outlook	57
3.5	Beyond low Bond number approximation	58
3.5.1	Gravitational Morse-Witten equations	58
3.5.2	Numerical resolution	60
3.5.3	Results and discussions	61
4	Interfacial elasticity and its role in drop deformability	64
4.1	Introduction	64
4.1.1	Complex fluid-fluid interfaces	64
4.1.2	Foam and emulsions as high specific surface systems	69
4.2	Rheological characterisation of complex interfaces	70
4.2.1	Shear rheology : the double-wall ring experiment	70
4.2.2	Dilatational rheology : the pendant/sessile drop experiment	72
4.3	Constitutive law of drops with elastocapillary interfaces	80
4.3.1	Theoretical framework	80
4.3.2	Perfectly spherical droploons	83
4.3.3	Droploons on capillaries	86
4.4	Numerical modelling	87
4.4.1	Surface Evolver simulations	87
4.4.2	Numerical integration of the shape equations	88
4.5	Results	90
4.5.1	Spherical droploons	90
4.5.2	Droploons on capillaries	92
4.6	Conclusion and outlook	102
5	Rheological properties of the PEG-silicone gel	105
5.1	Introduction	105
5.2	Silicone gel formation	109
5.2.1	Background : physics of gelation	109
5.2.2	Chemistry of the PDMS gel formation	112
5.2.3	Blocking the reaction : addition of a reaction inhibitor	114
5.2.4	Bulk shear rheology	114
5.2.5	Conclusion	119
5.3	PEG-PDMS interfaces	120
5.3.1	Chemistry of the interface	120
5.3.2	Interfacial shear rheology	120
5.4	Experimental model system : PEG-in-PDMS emulsions	122
5.4.1	Millifluidic droploon production	123
5.4.2	Droploons emulsions	123
5.4.3	Skin growth measurement	126
5.5	Conclusion	131
6	Tomographic analysis of the structural properties of the droploon assemblies	132
6.1	Introduction	132
6.1.1	Organisation and force transmission in granular materials	135
6.1.2	Networks in granular science	140

6.1.3	Foams as stress-transmitting particulate materials	144
6.2	X-Ray tomography	148
6.2.1	Principle of X-Ray tomographic imaging	148
6.2.2	X-Ray tomography in the analysis of emulsions	149
6.2.3	Development of an adapted algorithm for interface detection	151
6.3	Image analysis test case : numerically generated foams	161
6.3.1	Generation procedure	161
6.3.2	Results	162
6.3.3	Discussion	166
6.4	Conclusion and outlooks	166
7	General conclusion	169
8	Appendices	179
8.1	Numerical determination of the interfacial deformation	179
8.1.1	Strain represented using convected coordinates	179
8.1.2	Elastic energy	182
8.2	Pressure-deformation relations of droploons on capillaries expressed via radial stretch	184
8.3	C- PDMS foam generation	185

Chapter 1

General introduction

Foams and emulsions are ubiquitous systems, present in a myriad of applications from food to shock-resistant materials and cell culture scaffolds when the continuous phase is solidified. This broad spectrum of experimental realisations with seemingly radically different properties actually hides a shared common structure : the presence of two immiscible fluid phases, either both liquid for emulsions or liquid and gaseous for foams. This immiscibility comes from the differences in polarity between the phases, one being hydrophilic/polar, while the second one is hydrophobic/apolar. The interfacial area between the two phases comes with an extra energy, with an associated intensive thermodynamical quantity called the *interfacial tension* γ_0 . To ensure foam/emulsion stability, their interfaces are covered with surfactant molecules, which have the particularity of having one or more hydrophobic and one or more hydrophilic parts. The surfactant molecules adsorb at the interface, effectively lowering the interfacial tension. The properties of these surfactants, their interactions with the interface and with each others impact the mechanical properties of the interface, putting foams/emulsions in the category of systems with *complex interfaces* [1]. Because of the prevalence of interfacial interactions in foams/emulsions, the physics of foams and emulsions share a lot of common properties despite the difference in the state of matter in the discrete phase. The physical description used for foams can thus often be applied to emulsions, and *vice versa*.

As sketched in Fig. 1.2, the properties of foams/emulsions are the result of a complex interplay of the different lengthscales of the system, ranging from the molecular scale for surfactants adsorbed at the interface (around 10^{-10} m) up to the foam/emulsion scale (around 1 cm). The mechanical properties of a foam can be described using macroscopic observables, such as its response to shear and compression. However, a predictive theory cannot overlook the mechanics at the bubble/drop scale. Other materials composed of inclusions in a continuous bulk phase are often described by averaging the mechanical properties of the two phases as an effective medium approximation, weighted by their relative volume fraction. However, the large fraction of the volume occupied by the bubbles/drops makes this approach unefficient, as they are no longer isolated inclusions in a continuous phase. Rather, they interact through interfacial contacts with their neighbours, and these interactions in turn impact the properties at the foam/emulsion level.

This system composition is similar to that of granular materials, where individual rigid grains interact through interfacial contacts. The nature of this interaction, such as its strength and the presence of static friction, impacts the mechanical properties of the packings. A proper determination of the interaction law between bubbles is therefore naturally sought to understand the foam structure in terms of bubble properties. The first bubble interaction laws proposed by Durian [2]

considered bubbles as rigid overlapping spheres with an interaction strength proportional to the overlapping volume. Inspired by the soft sphere approximation used to describe granular materials, this simple interaction law gives an easy experimental access to the contact forces between deformed bubbles, by relating the drop compression along the axis of a contact to the magnitude of the force exerted. However, Durian’s bubble model does not enforce volume conservation, as the local compression is assumed to have no impact on the rest of the bubble/drop shape. It therefore fails to account effectively for the high deformability of the bubbles, a feature essential to understand the transition from wet to dry foams where the fraction of volume occupied by the continuous liquid phase ϕ_l goes down from 36 % to 0.1 %. Attempts to amend this two-body interaction aimed at explaining the response of bubbles to isotropic compression ended up with complex power-laws [3], with fitting parameters depending on the foam geometry. Since Morse and Witten’s seminal paper [4], the effect of deformability on the bubble-bubble interaction is known to make it non-pairwise, with the compression of a bubble at one point causing a dilation in the rest of the body because of volume conservation. This dilation further exerts extra-forces on other neighbouring bubbles. As a result, the force at one point cannot be determined without considering all the forces applied simultaneously.

The resulting many-body interaction greatly impacts foams, whose macroscopic mechanical behaviour is dominated by the deformations of the bubbles/drops and the mechanical work required to increase their interfacial area. With an increasing number of neighbours, the constrained dilation makes bubbles stiffer, directly linking mechanics and contact topology. Additionally, the deformation of the interfaces causes variations in the surfactant concentration, modifying the interfacial tension and provoking interfacial flows of adsorbed molecules. Similarly, changes in the interfacial interactions change how bubbles/drops organise : static friction reduces the number of contacts at jamming transition, while adhesion stabilises new geometries. These modified structures in turn influence the overall mechanical response of the foam [5, 6]. Typical bubbles/drops join at vertices with a 4-fold connectivity : this underconstrained structure deform primarily by the bending of the Plateau borders joining these vertices, as shown in Fig. 1.1a. By opposition, vertices with a higher than 4-fold connectivity lead to a stretch-dominated mechanical response, represented in the same figure, with a stiffness 10 to 100 times higher than bending-dominated materials with similar material density [7]. This high vertex connectivity is unstable for standard foams/emulsions, but can be stabilised by polymeric skins altering the bubbles/drops interfaces, as shown in Fig. 1.1c-f. The structures, and hence the foam/emulsion mechanics, are thus intrinsically linked to the interfacial interactions between the bubbles/drops. Moreover, because of their millimetric scale, bubbles/drops are insensitive to thermal fluctuations unlike colloidal dispersions. Foams/emulsions are thus good model systems to investigate the relations between interfacial properties, foam/emulsion structure and mechanics.

This thesis is the first contribution to the larger METAFOAM project aiming at the production of metamaterials (i.e. materials with a negative Poisson ratio) in a bottom-up approach, using foams/emulsions as structural scaffolds. The mechanical properties of solidified foams/emulsions are in large part dictated by their structure and the geometrical and topological organisation of the bubbles/drops they are made of. As their structure results from the mechanical equilibrium of bubbles/drops interacting through interfacial contacts, we aim at the controlled modification of this structure by the tuning of their interfacial properties, through the addition of adhesion, friction and interfacial elasticity of controlled magnitudes. The long-term objective is the formulation of rules relating interfacial properties, foam/emulsion structure and mechanics to provide guidelines to the creation of foam/emulsion-based metamaterials with tailored properties.

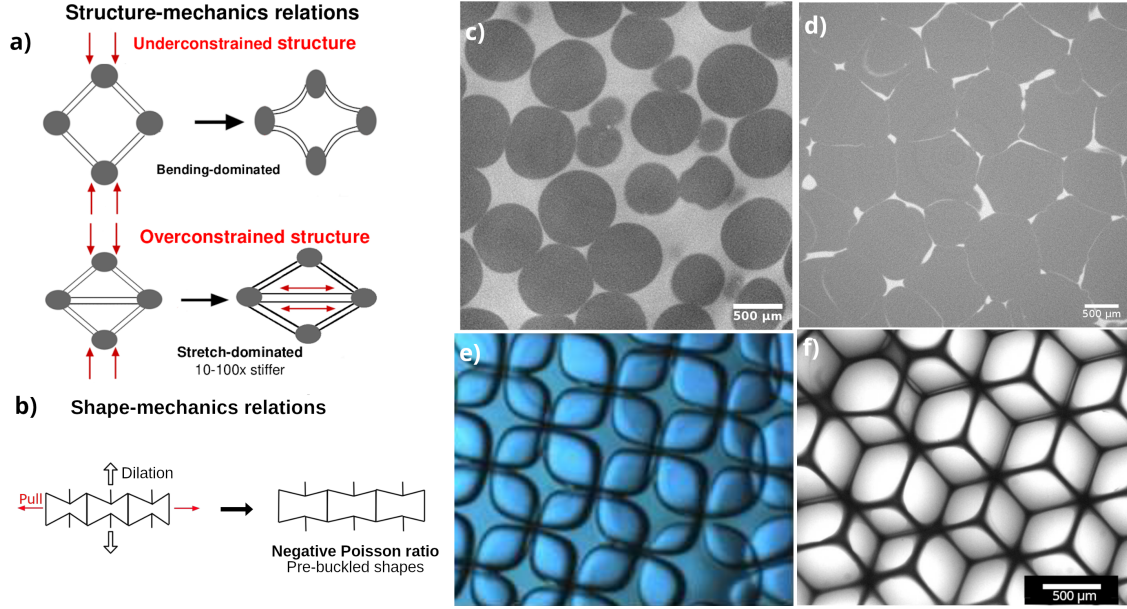


Figure 1.1: a) Examples of the localisation of the deformation for different types of structures. An underconstrained structure deforms by bending. With higher connectivity, the deformation is carried by the stretching of the edges, with a stiffness 10 to 100 times higher for the same material and density. b) Example of a structure with auxetic properties. The uniaxial stretch causes the opening of the pre-buckled shapes, giving an effective negative Poisson ratio to the material [8]. c-f) Differences in the interfacial properties alter the organisation of the foams/emulsions, as well as the shapes of the individual bubbles/drops. c-d) PEG drops in a silicone blend, covered with an interfacial silicone gel described in Chapter 5. The variations in thickness and rigidity modify the interfacial properties. e) Square bubbles [5] and f) rhombic dodecahedra in hydrogel foams [6].

This thesis attempts to lay the groundwork of this project through three approaches. First, it provides an experimental verification of the Morse-Witten interaction law [4] in the context of foams. This description at the bubble/drop level also aims at bridging the gap between foams/emulsions and granular materials, where the relation between inter-grain interactions and packing properties is a long-standing topic of investigation. Second, it provides a description of the foam/emulsion structures, using here again descriptors inspired from granular science. As the interactions are localised in the contacts between deformed interfaces, a rigorous definition of a contact between two bubbles/drops requires to account for this deformation. We therefore provide an algorithm of packing segmentation and analysis from tomographic images, aimed at foams and emulsions. This software proposes a physically relevant definition of the neighbourhood relations and the possibility for future users to control the reconstruction process and parameters, making it a good candidate for future foam/emulsion structure characterisation. Third we investigate the addition of interfacial elasticity on a purely capillary interface through a solid polymeric skin, and its impact on its stress-strain relation. We show that it can be characterised to good approximation as a capillary interface with an additional elastic stress in a new experimental setup, advocating for a modified bubble-bubble interaction in the line of Morse-Witten interaction law. We complete the theoretical model with an experimental model system of emulsion drops with controlled interfacial elastic modulus to probe the transition from purely capillary to purely elastic interfaces in future investigations.

This thesis is structured as follows. In Chapter 2, we describe the materials and methods used in experiments and simulations all throughout the manuscript. In Chapter 3, we propose the first

experimental verification of the Morse-Witten interaction law, using a simple experimental setup of surfactant-stabilised air bubbles in a capillary with a square cross-section. We also confront the results to numerical simulations using the finite elements software Surface Evolver [9], and found that this new force-deformation relation describes the bubble behaviour with a lot more accuracy than previous interaction models. In Chapter 4, we propose a theoretical model to describe the stress-strain relation of a fluid-fluid interface covered with a solid elastic skin. By simplifying the description of the elastic stresses, we show that the elastic shear modulus can be measured using a pendant drop geometry without resorting to complex shape-fitting procedures used beforehand. The comparison with predictions from elastic capsule equations showed that, despite its approximations, our model is in excellent agreement with more complex models, making it more usable for widespread experimental applications. We further use this problem to propose the first benchmark of Surface Evolver to describe elastocapillary interfaces, paving the way for future applications in simulations of elastocapillary foams. In Chapter 5, we propose a refinement of an experimental system consisting previously of PEG inclusions in a commercial silicone matrix [10] to transform it in PEG drops with an interfacial silicone gel of controlled chemical composition, thickness and rigidity. The final experimental system behaves partially as drops/bubbles because of its capillary interface, and partially as elastic balloons because of the interfacial elasticity. For this reason, we refer to them as *droploons* when they are based on drops, and *bubbloons* when they are based on bubbles. We construct a millifluidic setup for the large-scale production of emulsion drops with a controlled skin thickness, and show its impact on the structure of the emulsions. In Chapter 6, we describe our home-made segmentation software aimed at reconstructing and characterising foams/emulsions. We propose a physically relevant definition of neighbourhood relations between bubbles/drops and its numerical implementation using the data obtained from the algorithm. We further apply our algorithm to numerically generated foams of known structures to benchmark its validity, and show the possible analysis that are not accessible with commercially available softwares yet.

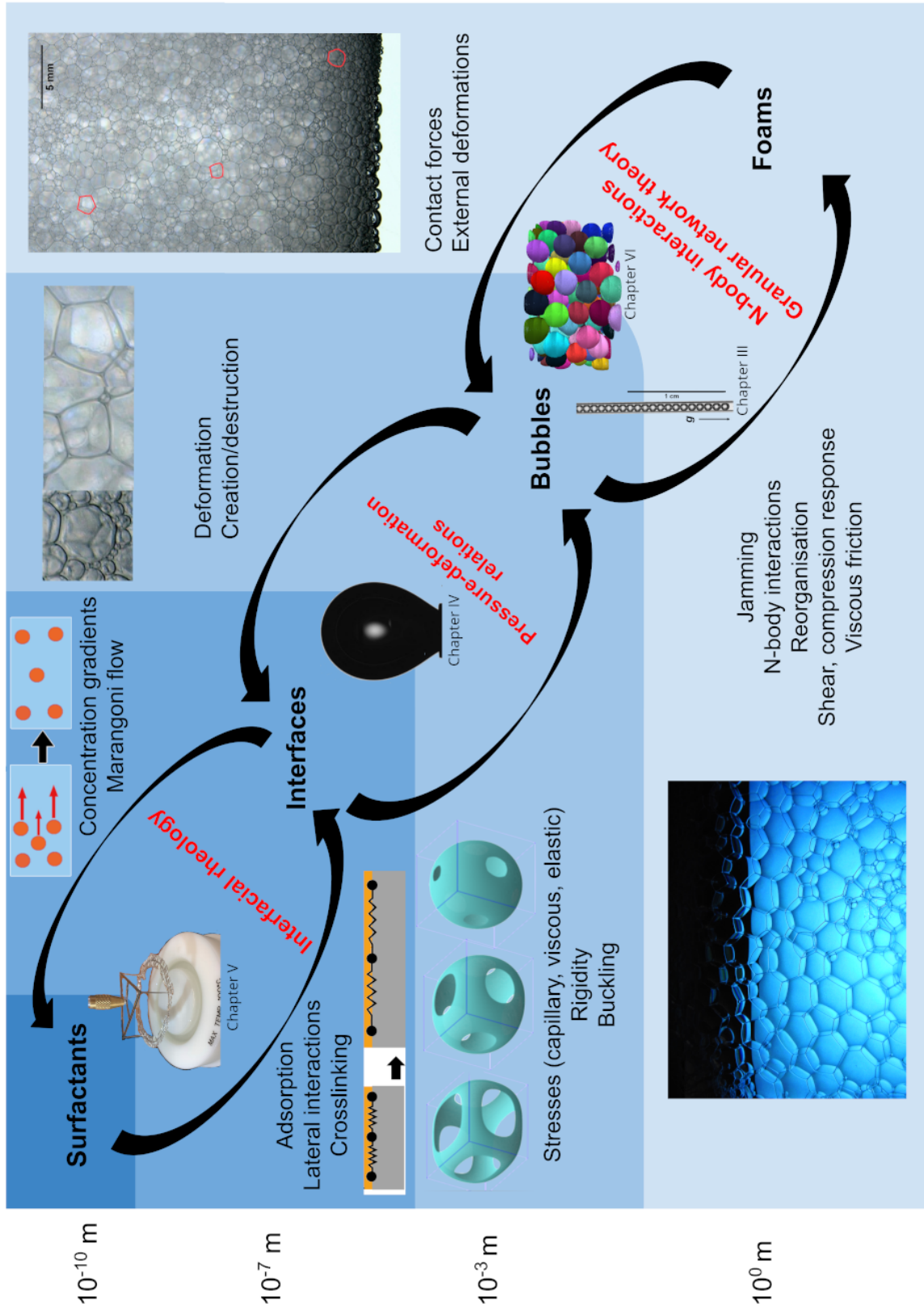


Figure 1.2: Interactions between the different length scales of the foams/emulsions. In this thesis, the relations between the different scales are investigated with adapted experimental methods, represented between the black arrows.

Introduction générale

Les mousses et les émulsions sont des systèmes omniprésents, aux applications variées une fois que la phase continue est solidifiée : de la gastronomie aux matériaux anti-chocs en passant par les substrats pour la culture cellulaire, ces différents usages présentent des points communs malgré leurs propriétés radicalement différentes. Ainsi, elles sont toujours composées de deux phases fluides immiscibles : l'une liquide et l'autre gazeuse dans le cas des mousses, et toutes deux liquides dans le cas des émulsions. L'immiscibilité provient de la différence de polarité entre les deux phases, l'une étant hydrophile (ou polaire) tandis que la seconde est hydrophobe (ou apolaire). Pour compenser cette immiscibilité, la formation d'une interface entre ces deux phases nécessite une énergie dont la quantité intensive associée est appelée la *tension interfaciale* γ_0 . La stabilité des mousses et des émulsions est favorisée par l'ajout des molécules tensioactives, ayant la particularité d'être composées d'une (ou plusieurs) parties hydrophobes, et une (ou plusieurs) parties hydrophiles. Ces molécules s'adsorbent spontanément à l'interface, où elles réduisent la tension interfaciale entre les deux phases. Les propriétés des tensioactifs, leurs interactions avec l'interface et entre eux affecte les propriétés mécaniques de l'interface qu'ils recouvrent, classant les mousses et les émulsions dans la catégorie des systèmes aux *interfaces complexes* [1]. Les interactions interfaciales conditionnent une grande partie des propriétés des mousses et des émulsions. Grâce à ce point commun, ces deux systèmes partagent un grand nombre de propriétés en commun, malgré la différence entre état gazeux et état liquide. De fait, les descriptions physiques des mousses peuvent souvent être appliquées aux émulsions, et *vice versa*.

Les propriétés des mousses et des émulsions résultent de leurs propriétés aux différentes échelles, et de la façon dont ces échelles interagissent l'une sur l'autre, comme représenté Fig. 1.2. Ainsi, une compréhension complète du système étudié nécessite de considérer l'échelle moléculaire pour comprendre le comportement des tensioactifs à l'interface (environ 10^{-10} m) ainsi que l'échelle de la mousse/émulsion dans son ensemble (environ 1 cm). Ainsi, les propriétés mécaniques peuvent être décrites au moyen d'observables macroscopiques, telle que la description d'une déformation de cisaillement ou de compression par un champ continu. Cependant, une description physiquement réaliste de ces déformations ne peut faire l'économie d'une description de la mécanique de déformation à l'échelle de la bulle et de la goutte. Dans d'autres matériaux biphasiques, les parties discontinues du matériau peuvent être décrites comme des inclusions dans une matrice continue, se comportant comme un milieu effectif dont les propriétés d'ensemble sont une moyenne des propriétés des deux phases, pondérée par la fraction volumique qu'elles occupent respectivement. Toutefois, dans le cas des mousses et des émulsions, les bulles et les gouttes qui constituent les inclusions occupent une fraction importante du volume du système, si bien qu'elles ne constituent plus des inclusions isolées dans une phase continue. Au contraire, les bulles et les gouttes interagissent avec leurs voisines au travers de leurs contacts interfaciaux. Ces interactions affectent à leur tour les propriétés des mousses et des émulsions qu'elles constituent.

La structure des mousses et des émulsions est similaire à celle des matériaux granulaires, où

des grains rigides interagissent par contacts interfaciaux. Dans le cas des matériaux granulaires, les propriétés mécaniques de l'ensemble sont affectées par la nature des interactions mises en jeu, telles que la rigidité du contact et la présence ou non de friction statique. De par cette similitude entre mousses, émulsions et matériaux granulaires, une description des mousses et des émulsions au niveau des interactions entre bulles et entre gouttes constitue une piste de réflexion prometteuse pour l'investigation des relations entre structures et propriétés. La première loi d'interaction de bulles, proposée par Durian [2], considérait les bubbles comme des sphères rigides pouvant s'interpénétrer, et dont la force d'interaction était proportionnelle au volume d'interpénétration des deux sphères. Cette interpénétration tenait alors lieu de déformation. Cette loi d'interaction est inspirée de l'approximation de sphères molles utilisée pour les matériaux granulaires : elle confère une façon simple d'associer la compression d'une sphère dans l'axe d'application d'une force à l'amplitude de cette force. Cependant, la compression dans le modèle de Durian n'est pas assortie d'une contrainte sur la conservation de volume, la compression en un point de la bulle ne provoquant pas de déformation du reste de la surface. Le modèle de Durian échoue ainsi à considérer la déformabilité des bulles, pourtant essentielle à la compréhension de la transition d'une mousse humide à une mousse sèche, quand la fraction du volume occupée par le liquide décroît de 36 % à 0.1 %. Des tentatives de raffinement de cette loi à deux corps, focalisée sur la réponse mécanique à une compression isotrope, transforment cette loi simple en une loi de puissance à la forme extrêmement complexe [3], reposant sur des paramètres numériques fonction de la géométrie de la mousse. *A contrario*, la déformabilité est identifiée comme faisant de l'interaction bulle-bulle une interaction à N -corps depuis l'article séminal de Morse et Witten [4] : la compression en un point de la bulle cause sa dilatation dans le reste du corps de la bulle, du fait de la conservation du volume. Cette dilatation cause à son tour une augmentation de la force exercée par la bulle compressée sur ses voisines. La détermination d'une force de contact exercée en un point de la bulle ne peut donc se faire sans considérer simultanément toutes les forces appliquées à la surface.

L'interaction à N -corps qui en découle influence les mousses, dont le comportement macroscopique est dominé par les déformations des bulles et le travail mécanique nécessaire à l'augmentation de leur aire interfaciale. Avec un nombre croissant de voisins, la contrainte sur la dilatation rend les bulles plus rigides, établissant un lien direct entre la mécanique et la topologie des contacts. De plus, la déformation des interfaces provoque des variations dans la concentration de surface des tensioactifs, modifiant la tension interfaciale et provoquant des écoulements interfaciaux des molécules adsorbées. De même, des changements dans ces interactions interfaciales modifient la façon dont les bulles et gouttes s'organisent : la friction statique réduit le nombre de voisins par bulle nécessaire pour obtenir une mousse mécaniquement stable à la transition d'encombrement, tandis que l'adhésion entre bulles stabilise des géométries qui seraient instables pour des mousses classiques. Ces structures modifiées vont à leur tour affecter la réponse mécanique des mousses [5, 6]. Ainsi, des bulles et gouttes classiques se rejoignent sur des sommets à 4, formant des structures sous-contraintes dont le mode de déformation principal est la flexion des bords de Plateau joignant ces sommets, comme représenté Fig. 1.1a. À l'inverse, des sommets joignant plus de 4 bulles se déforment principalement par étirement de Plateau (Fig. 1.1a), avec une rigidité finale 10 à 100 fois plus importante, à densité de matériau identique, que les structures se déformant par pliage [7]. Cette haute connectivité des sommets est instable pour les mousses et émulsions standards, mais peut être stabilisée par l'addition de peaux de polymères à l'interface des bulles et gouttes, comme représenté Fig. 1.1. La structure, et donc les propriétés mécaniques des mousses et des émulsions, sont donc intrinsèquement liées entre bulles et entre gouttes. De plus, les bulles et les gouttes sont insensibles aux fluctuations thermiques du fait de leur taille millimétrique, contrairement aux dispersions colloïdales. Les mousses et les émulsions sont donc des systèmes modèles

idéaux pour étudier les relations entre propriétés interfaciales, structurales et mécaniques.

Cette thèse constitue la première contribution du projet METAFOAM visant à la production de métamatériaux auto-assemblés, en se servant des mousses et des émulsions comme échaffaudages structuraux. Les propriétés mécaniques des mousses et émulsions solidifiées sont en grande partie dictées par leur structure et l'organisation des bulles et des gouttes qui les composent. Ces structures résultant de l'équilibre mécanique entre bulles et gouttes interagissant par contacts interfaciaux, ce projet vise à la modification contrôlée de la structure par la modification de l'interface, grâce à l'addition d'adhésion, de friction et d'élasticité interfaciale de magnitudes contrôlées. À long terme, ce projet vise à formuler un ensemble de règles reliant les propriétés interfaciales, la structure les propriétés mécaniques, de façon à guider la création de métamatériaux aux propriétés contrôlées, basés sur ces mousses et émulsions.

Ce manuscrit tâche de poser les bases de ce projet par trois approches. Premièrement, par une vérification expérimentale de la loi d'interaction de Morse et Witten [4] appliquée aux mousses. Cette description à l'échelle de la bulle vise également au renforcement de la similitude entre les mousses et les matériaux granulaires, de façon à tirer profit de l'expérience de la science des matériaux granulaires dans l'établissement des relations entre interactions entre grains et propriétés d'ensembles. Deuxièmement, en proposant une description quantitative des structures de mousses et d'émulsions, en utilisant là aussi des quantités importées de la science des matériaux granulaires. L'interaction entre particules étant localisée au niveau des contacts entre bulles et gouttes déformées, une définition rigoureuse de ces contacts nécessite de prendre en compte cette déformation. Nous proposons donc un algorithme de segmentation et d'analyse de mousses et d'émulsions à base d'images tomographiques. Ce logiciel propose une définition physiquement pertinente des relations de contact. De plus, la possibilité pour de futurs utilisateurs et futures utilisatrices de contrôler le processus de reconstruction ainsi que ses paramètres en fait un bon candidat pour des investigations futures sur les structures des mousses et des émulsions. Troisièmement, nous étudions l'ajout d'une élasticité interfaciale sur une interface purement capillaire au travers d'une peau solide de polymères, ainsi que sa conséquence sur sa relation stress-déformation. Nous montrons que cette relation peut être décrite comme une interface capillaire dotée d'un stress élastique additionnel dans une nouvelle configuration expérimentale. Cette relation simplifiée peut ainsi être intégrée directement dans la loi d'interaction de Morse et Witten, de façon à obtenir une loi d'interaction modifiée prenant en compte cette élasticité. Nous complétons ce modèle théorique avec un système expérimental modèle, constituée de gouttes ayant un module d'élasticité interfaciale contrôlée. Ce modèle servira à l'avenir à étudier la transition d'une interface purement capillaire à une interface purement élastique.

Ce manuscrit est structuré comme suit. Dans le Chapitre 2, nous décrivons les matériaux et méthodes employés dans les expériences et les simulations à travers le manuscrit. Dans le Chapitre 3, nous proposons une première vérification expérimentale de la loi d'interaction de Morse et Witten au moyen d'un montage expérimental simple de bulles d'air stabilisées par des tensioactifs, confinées dans un tube capillaire de section carrée. Nous confrontons ces résultats à des simulations numériques au moyen du logiciel d'éléments finis Surface Evolver [9], et trouvons que cette nouvelle relation force-déformation décrit le comportement des bulles avec bien davantage de précision que les modèles d'interaction précédents. Dans le Chapitre 4, nous proposons un modèle théorique pour décrire la relation stress-déformation d'une interface fluide-fluide couverte d'une peau élastique solide. En simplifiant cette description des stress élastiques, nous montrons que le module de cisaillement élastique peut être mesuré au moyen d'une expérience de goutte pendante sans recourir

aux procédures complexes d'ajustement de forme utilisées dans la littérature. La comparaison de ces résultats avec ceux de l'équation de forme des capsules élastiques montre que, malgré ses approximations, notre modèle est en accord avec des modèles plus complexes, le rendant de fait plus accessible dans une gamme plus grande de configurations expérimentales. Nous proposons également la première utilisation de Surface Evolver pour décrire des interfaces élastocapillaires, et montrons que ces simulations sont physiquement réalistes. Ainsi, nous ouvrons la possibilité à de futures simulations de mousses élastocapillaires. Dans le Chapitre 5, nous proposons l'amélioration d'un système expérimental consistant en des inclusions de PEG dans une matrice de silicone gélifié [10], pour transformer les transformer en goutte de PEG couvertes d'un gel interfacial de silicone à la composition chimique, rigidité et épaisseur contrôlées. Nous y détaillons un dispositif millifluidique pour la production à grande échelle de gouttes à peau d'épaisseur contrôlée, et montrons l'impact de ces peaux sur la structure des émulsions. Dans le Chapitre 6, nous décrivons notre programme de segmentation développé spécifiquement pour la reconstruction et la caractérisation de mousses et d'émulsions. Nous proposons une définition physiquement pertinente des relations de contact entre les bulles et entre les gouttes, ainsi que son implémentation computationnellement efficient en utilisant les données obtenues par notre algorithme de segmentation. Nous appliquons ensuite cet algorithme à des mousses tests générées numériquement de structure connue pour vérifier la validité des résultats obtenues, et montrons les analyses rendues possibles qui restaient jusque là inaccessibles avec les logiciels commerciaux actuels.

Chapter 2

Materials and Methods

2.1 Bubble train setup

2.1.1 Bubble generation

Bubbles are produced by blowing ambient air at constant pressure (Elveflow pressure controller PG1113, $P = 11$ mbar) through needles (Nordson EFD) with circular cross-sections of different inner radii R_C ($R_C = 150 - 330\mu\text{m}$) into an aqueous solution containing sodium dodecyl sulfate (SDS, Sigma Aldrich, L3771). The solutions are freshly prepared in Millipore water every two days by stirring for 30 min. The SDS is used at a concentration of 7 g/L, corresponding to 2.9 times the critical micellar concentration. This concentration is high enough to ensure bubble stability. It is also low enough to neglect attractive depletion forces created between the bubbles by the SDS micelles [11].

The interfacial tension of the solution is measured to be $\gamma = 0.034 \pm 0.001$ N/m at room temperature (20 °C) using a pendant drop device (TRACKER from TECLIS). For sufficiently small gas flow rates, the generated bubble radius R_0 is proportional to $R_C^{\frac{1}{3}}$, which therefore serves to control the bubble size. The generated bubbles are trapped in glass capillaries with square cross-section of different internal widths $0.6 \text{ mm} \leq W_C \leq 1 \text{ mm}$ (VITROCOM), whose dimensions are systematically verified using a Keyence numerical microscope (KEYENCE VHX5000). The bubbles are trapped manually by holding the end of the capillary above the point of bubble generation. Once the capillaries are filled with about 20 bubbles, they are sealed at either end using Blu-Tack adhesive paste. Each capillary can be used for about 3 h before gas exchange between the bubbles leads to measurable bubble-size variations.

2.1.2 Image acquisition

A sketch of the overall experimental setup is shown in Fig. 2.1. The square capillary is attached to a metal frame which also holds the digital camera (IDS UI-3580LE and TAMRON M118FM50 camera lens). It fixes the relative positions of the camera and the capillary. The entire frame can be rotated with respect to gravity. The capillary is imaged in front of a diffusive white screen with homogeneous lighting. The latter is placed 40 cm behind the capillary in order to benefit from optical effects which make the bubble boundaries appear dark black [12]. A thin wire with an attached weight suspended in the field of view of the camera is used to detect the vertical direction in the images. The angle β between the normal of the capillary and the direction of gravity is then obtained from image analysis. Every time the angle is varied, we wait until there is no more

measurable change in the bubble train between two consecutive images taken at an interval of 5 min. This equilibration takes 15-30 minutes, depending on the inclination angle β and the drainage speed. To obtain the length L_B of each bubble along the bubble train, we use the image analysis program ImageJ to measure the profile of gray values along the centre line of the capillary. Due to optical effects, the contact zones between neighbouring bubbles appear as three bright spots, surrounded by dark areas. The actual border between two bubbles is the central bright spot [12]. A home-made Python algorithm detects the central spot, indicated by red crossed in Fig. 2.1c. A

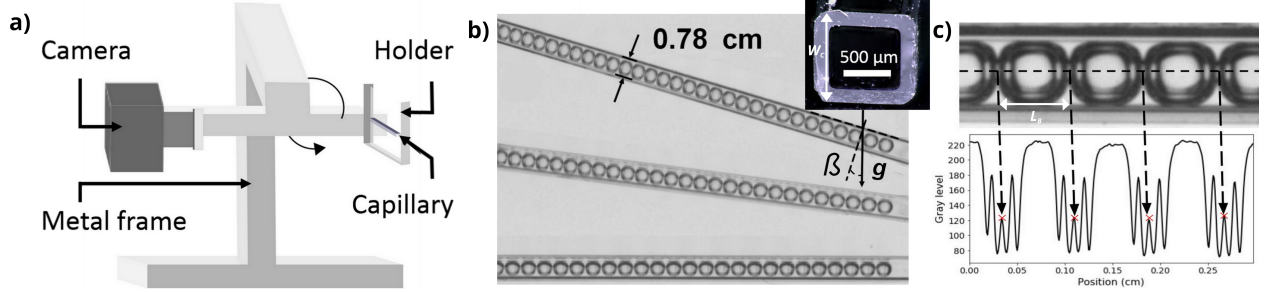


Figure 2.1: a) Experimental set-up used to test the Morse-Witten interaction law. Camera and capillary are held by the same metal arm which can rotate to tilt the capillary with respect to gravity. The camera takes photographs of the capillary to measure the deformation of the bubbles. b) Examples of photographs of bubble trains in capillaries ($W_C = 0.78$ mm) at three different tilting angles β . Inset : microscope image of the cross-section of the capillary. c) Illustration of image treatment used to obtain the bubble length L_B . Top: profile view of bubbles trapped in capillary. Bottom: gray value profile with detection of bubble boundary (red cross).

The volume of the bubbles in the capillaries is determined by measuring their length L_B at $\beta = 0$. This length is then converted into the undeformed bubble radius R_0 using the following equation obtained from fitting Surface Evolver simulations and theory of isolated bubbles in capillaries [13], as shown in Fig. 2.2 :

$$\frac{L_B}{W_C} \approx -19.6 \left(\frac{W_C}{2R_0} \right)^3 + 60 \left(\frac{W_C}{2R_0} \right)^2 - 62.6 \left(\frac{W_C}{2R_0} \right) + 23.2 \quad (2.1)$$

where R_0 is the radius of the undeformed bubble, and W_C is the capillary width.

2.1.3 Force calculation

The contact force $F_B(n)$ exerted by the bubble train at the bottom of each bubble n (counted from the bottom bubble with the first bubble being $n = 1$) is obtained by calculation of the buoyancy force exerted by the $n - 1$ bubbles underneath as shown in Fig. 2.3, i.e.

$$F_B(n) = \sin(\beta)g\rho(n-1)\frac{4}{3}\pi R_0^3, \quad (2.2)$$

where g is the gravitational acceleration and ρ is the density of water. We calculate the overall force $F(n)$ exerted on the n^{th} bubble as the average of the force exerted on its bottom and top contact

$$F(n) = \frac{1}{2} (F_B(n) + F_B(n+1)). \quad (2.3)$$

If the hydrostatic pressure variations across one bubble are negligible, $F_B(n) = F(n)$. We present the normalised force per bubble, given as

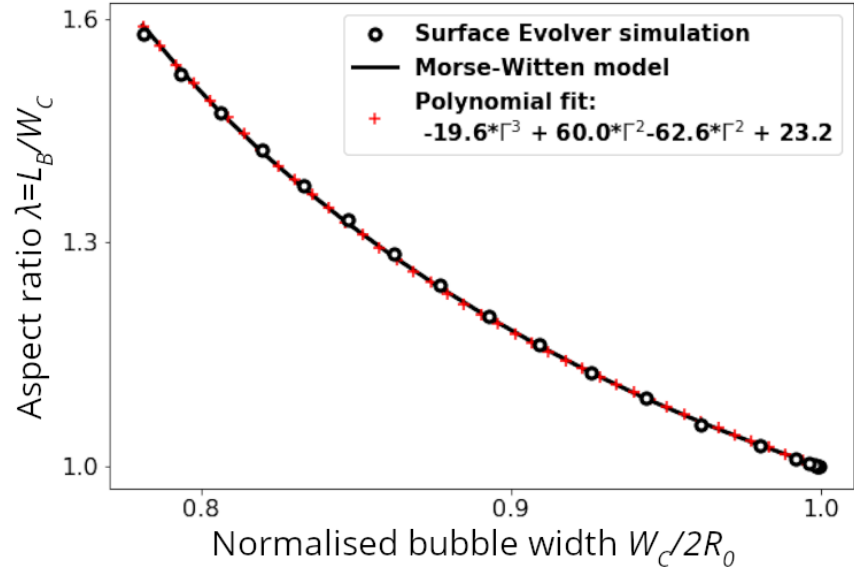


Figure 2.2: Longitudinal to lateral aspect ratio for a single bubble trapped inside a square capillary. The Surface Evolver prediction is interpolated with an empirical polynomial fit of third order. This fit is used to deduce the undeformed radius of the bubble from its aspect in the capillary.

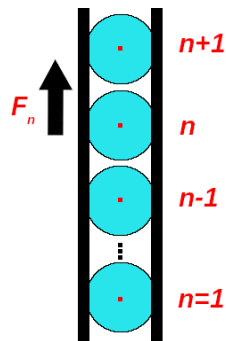


Figure 2.3: Illustration of the forces exerted on bubble $n + 1$ by its neighbours.

$$f(n) = \frac{F(n)}{\gamma R_0}. \quad (2.4)$$

In the experiments we have access only to the bubble-bubble forces, but not to the bubble-wall forces. Nevertheless, bubble-wall forces are consistently provided through the simulations and the modeling. They are normalised in the same manner.

2.2 Finite elements method : Surface Evolver simulations

We use the 2.70 version of Surface Evolver [9], with a PC with an Intel Xeon E-2176M CPU @ 2.70 GHz x 12 (Intel Corporation, Santa Clara, CA, USA), 32 GiB of RAM on GNU/Ubuntu 20.04.3 LTS x86-64 OS. The program is compiled from the source code provided on the Surface Evolver website [14] following the standard *makefile* procedure.

2.2.1 Bubbles trapped in a capillary

In static equilibrium the interfacial energy of a bubble is minimal with respect to small variations of its shape, for a fixed bubble volume and a given confinement by walls or neighbours. This principle is the basis of our simulations, performed using the Surface Evolver software, where the gas-liquid interface is represented as an assembly of finite elements whose energy is proportional to their surface area.

As shown in Fig. 2.4a, we represent initially the bubble as a truncated octahedron. Facets in contact with capillary walls and neighbouring bubbles are highlighted in red. The surface energy is minimised by moving the mesh vertices using a conjugate gradient algorithm respecting volume conservation and geometrical constraints. Minimisation steps are iterated until the system reaches a convergence threshold fixed by a convergence criterion ϵ set at 10^{-8} . When the energy difference after 100 iterations is smaller than ϵ , the meshing as a whole is refined by subdividing each facet into smaller triangles. This allows a better representation of curved surfaces, leading to a progressive decrease of the energy. This convergence procedure must be preserved from energy pitfalls, such as facets and edges becoming exceedingly small compared to average and that may stall the convergence procedure. To prevent this from happening, sequences of energy minimisation steps are alternated with the removal of anomalous facets, using mesh optimisation tools provided in the Surface Evolver software. The mesh near the bubble-bubble and bubble-wall contacts is particularly critical. These contacts are rectangular in the initial coarse mesh and must become approximately circular in the fully refined and converged structure. This implies stretching and compression of the mesh near the contact line which generate the anomalous facets mentioned above.

Surface Evolver is not suited to simulate surfaces joining at null contact angle θ [15]. At $\theta = 0^\circ$, the tangent to the gas-liquid interface must become parallel to the wall as the contact line is approached. The progressive separation of the two interfaces is intrinsically hard to represent with the plane elements used by Surface Evolver, especially in the absence of a finite contact angle delimiting clearly surfaces in contact from those not in contact. To approach the $\theta = 0$ case, the interfacial tension γ_0 of the interfaces in contact with walls and neighbours are decreased by 10% in the first steps of the simulation to a reduced value γ_0^* . The resulting contact angle is then non-zero, and given by $\theta = \arccos(\gamma_0^*/\gamma_0)$. In the last steps of the simulation, γ_0^* is increased again. The force at zero contact angle is then extrapolated from its changes with contact angle, in the $\gamma_0^* \rightarrow \gamma_0$ limit.

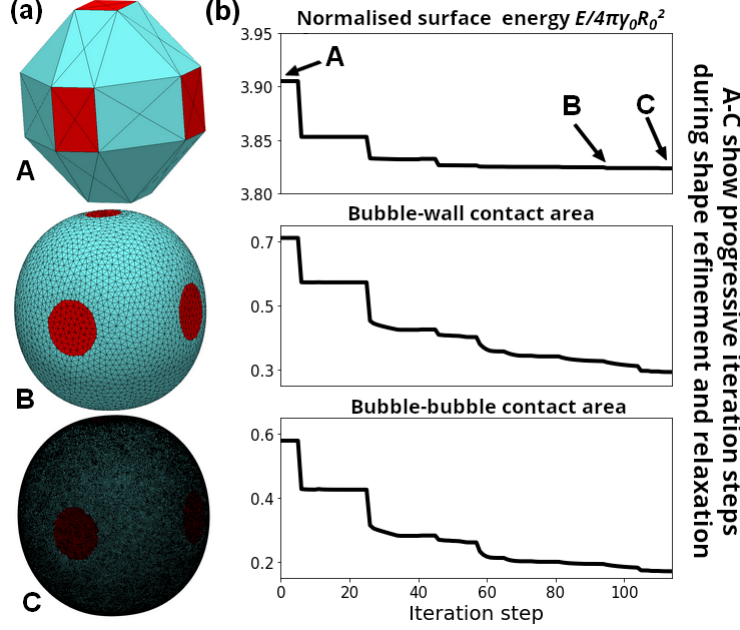


Figure 2.4: a) Simulation of a bubble trapped in the capillary with Surface Evolver. The initial shape (top) is minimised with respect to interfacial energy, and refined by adding new vertices to the meshing of the interface. Red facets simulate the flat interfaces in contact with the capillary walls and the neighbouring bubbles. b) Surface energy and contact forces of the bubbles in the three steps of minimisation A, B and C. The surface energy is deduced from the total area of the facets, while the contact force is deduced from the area of the red facets. Even at equivalent interfacial energy, the contact forces deduced from the simulations continue to decrease through further relaxation steps.

The convergence criterion must be chosen carefully : as shown in Fig.2.4b, a quick convergence of the interfacial energy can be reached, followed by a step of no significant decrease. In the meantime, the contact areas continue to slowly evolve and decrease in a significant manner which is not visible in the surface energy. This is due to the difficult convergence of the mesh along the contact lines. An effective convergence criterion has thus to consider both energy and contact area convergence. In our simulations, we consider that convergence is reached when the relative energy variation $|E^{n-1} - E^n|/E^{n+1}$ and relative contact area variation $|A^{n-1} - A^n|/A^{n+1}$ over 100 minimisation steps is smaller than 10^{-8} .

2.2.2 Simulations of elastocapillary bubbles

The neo-Hookean elasticity is implemented using the *neo_hookean* method [16]. The reference configuration is obtained by letting the shape relax to its configuration of minimal energy when interfacial tension is the only energy term. The reference configuration is then defined for every facet by giving to every vertex $\{s_1, s_2, s_3\}$, reference coordinates attributed as a 1x3 real array. The vectors between these reference positions are used to compute the form factors of the facets in their reference shape, as described in Appendix 8.1. We give to every facet the following elastic coefficients: Lamé first parameter $\lambda = 10^{12}$, Lamé second parameter $\mu = 1$, Poisson ratio $\nu = 0.5$. The deformation is then imposed by changing the volume constraint inside the drop and letting the shape relax with iteration steps. As in Section 2.2.1, successive iteration steps are performed until the relative energy variation $|E^{n-1} - E^n|/E^{n+1}$ over 100 minimisation steps is smaller than 10^{-8} . We provide the code freely accessible online for interested users¹.

¹<https://www.rsc.org/suppdata/d1/sm/d1sm01109j/d1sm01109j1.zip>

2.3 Polyethylene glycol-in-silicone emulsion

2.3.1 Chemical composition

The silicone blend is composed of three different silicone polymers, represented in Fisher projection in Fig. 2.5a-c :

1. Plain PDMS, where all substitutive groups are methyl groups (Bluestar Silicone FLD 47v100)
2. PDMS where 25% to 35% of the Si-CH₃ groups are replaced with Si-H, also referred to in this manuscript as MHDS (Gelest Inc. HMS-301)
3. PDMS where methyl end groups at the end of the chain are replaced with a vinyl group (DMS-V21)
4. Polyethylene glycol (PEG-400) is bought from Sigma Aldrich (SA 8074859025), Acros Organics (10634892) and Merck (25322-68-3) which we compare using TGA characterisation in Section 2.3.4

The platinum catalyst (represented in Fig 2.5e) is bought from Sigma-Aldrich (479527-5g) with the catalyst molecule complexed at 0.1 M in a solution of vinyl-terminated PDMS. The dimethyl maleate inhibitor (Fig. 2.5f) is also bought from Sigma Aldrich (238198-100G). The densities of the three silicone oils and PEG are measured using Metler Toledo Excellence D4 density meter, at 20 °C and 25 °C. The values for the viscosities and molar weight are taken as described by the providers. Their characteristics are summarised in Table 2.5. All chemicals are used as provided without further purification.

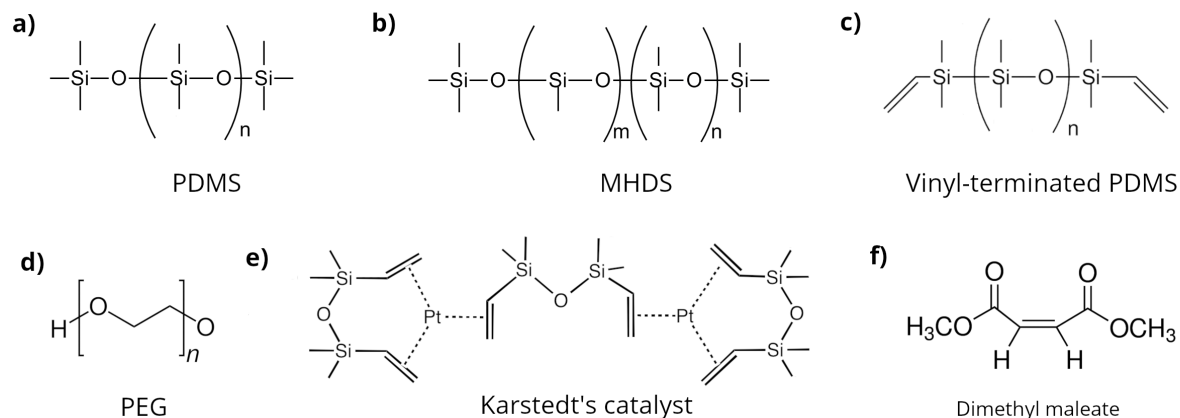


Figure 2.5: a) Plain PDMS. b) MHDS, with n unfunctionalised monomers and m functionalised ones. c) Vinyl-terminated PDMS. d) Polyethylene glycol. e) Platinum(0)-1,3- divinyl-1,1,3,3-tetramethyldisiloxane . f) Dimethyl maleate.

Number	Full name	Short name	Reference	Relative density (g/mL) (20 °C/25 °C)	Viscosity (cSt)	Molecular weight M_w (g/mol)	Functionalisation degree f
(1)	Plain PDMS	PDMS	BLUESIL FLD 47v100 (Bluestar Silicone)	0.9674/0.9629	100	25000	0
(2)	(25-35% methylhydrosiloxane)- dimethylsiloxane copolymer, trimethylsiloxane terminated	MHDS	HMS-301 (Gelest Inc.)	0.9721/0.9674	25-35	1900-2000	≈ 9
(3)	Vinyl terminated polydimethylsiloxane	vin.-term. PDMS	DMS-V21 (Gelest Inc.)	0.9682/0.9637	100	6000	2
(4)	Poethyleneglycol 400	PEG-400	8.07485.1000 (Merck) 8.07485 (Sigma Aldrich) 10634892 (Acros Organics)	1.126/1.122 1.124 / NA (provider) 1.1275 (provider)	97-110 97-110 110-125	NA 380-420 NA	NA
	Platinum(0)-1,3-divinyl- 1,1,3,3-tetramethyldisiloxane complex solution	Pt-cat.	479527 (Sigma Aldrich)	0.98 (provider)	NA	381.48	NA
	Dimethyl maleate		238198 (Sigma Aldrich)	1.152 (provider)	NA	144.13	NA

Figure 2.6: Chemicals used in the PEG-silicone emulsion system.

2.3.2 Sample preparation procedure

The reactive silicone blend is prepared by mixing (1) PDMS, (2) MHDS and (3) vinyl-terminated PDMS. The mass ratio between (2) and (3) is fixed at stoichiometric ratio of the functional groups, with $R = \frac{m_{vin.-term.}}{m_{MHDS}} = \frac{M_{wvin.-term.}f_{MHDS}}{M_{MHDS}f_{vin.-term.}} \approx \frac{6000 \cdot 9}{2000 \cdot 2} \approx 13$. The mass fraction of reactive silicone ϕ_r is defined as

$$\phi_r = \frac{m_{MHDS} + m_{vin.-term.}}{m_{PDMS} + m_{MHDS} + m_{vin.-term.}}. \quad (2.5)$$

Along with R , it is used to determine the relative mass proportions of the three silicone polymers. The choice of a mass ratio is dictated by the sake of simplicity in the sample preparation, as weighing silicone oils is easier than taking precise volumes of viscous liquids with the quantities involved. Before the production of the drops, the silicone blend is mixed with a magnetic stirrer for at least two days to ensure a homogeneous blend of the different silicone oils.

The second phase is prepared by drying the PEG-400 at 40°C at 100 mbar for 16 h. The determination of the optimal drying procedure is described in Sections 2.3.3 and 2.3.4. The catalyst is then added and mixed using an ULTRA-TURRAX disperser of 15 mm diameter at 6000 rpm for 2 minutes, before covering the solution under argon to avoid ambient water absorption. The quantity of catalyst added to the PEG phase is fixed by the volume fraction

$$\phi_p = \frac{V_{Pt-cat.}}{V_{PEG} + V_{Pt-cat.}}, \quad (2.6)$$

where the choice of volume fraction was used because of the simplicity of taking precise catalyst volumes with micropipettes.

Similarly, the P3 phase composed of unreactive silicone and the dimethyl maleate inhibitor is prepared with a mass fraction of inhibitor $\phi_m = \frac{m_{inhibitor}}{m_{PDMS}} = 5.5 \text{ wt.}\%$ (where the ratio between dimethyl maleate and Karstedt’s catalyst is 6:1, as recommended in literature [17]), and mixed with an ULTRA-TURRAX disperser of 15 mm diameter at 6000 rpm for 2 minutes shortly before use.

2.3.3 Dry PEG preparation

The two main reactions in the PEG-silicone system come with side reactions involving water (Section 5.2.2).

Among them, the reaction between water and hydrogens carried by the MHDS molecules produce gaseous H₂ byproducts (Fig. 5.8C in Section 5.2.2), with gas bubbles appearing in the final solution and altering the emulsion packing mechanism. PEG is hydrophilic and hygroscopic, meaning that it absorbs water from the ambient atmosphere. It is therefore crucial to dry the PEG prior to producing the drops, which we decided to do before each experiment.

Drying is achieved using the variation of PEG humidity absorption with temperature and ambient humidity [18, 19]. In order to establish the appropriate drying protocol, we compared PEG-400 dried for 16h at 40°C at 100 mbar with PEG-400 for 3h at 120°C at room pressure. At 120°C, the water completely evaporates from the PEG, but the high temperature degrades the PEG molecules [20, 21, 22]. The degraded solution is nonetheless a benchmark to compare the water content in the PEG solution dried at low temperature. The two dried solutions are compared using thermogravimetric analysis (TGA), which measures the fraction of mass of the solution evaporated when

increasing the temperature step-wise. The temperature was increased between 25°C and 200°C, with a temperature ramp of 10 °C per minute. The results of the TGA analysis on the two dried solutions and an undried PEG solution are shown in Fig. 2.7. The mass fraction of wet PEG decreases with temperature, indicating the progressive evaporation of water. While the weight of the undried PEG decreases significantly, indicating a water content of $\approx 1.5\%$, the dried PEG maintains constant weight up to 120 °C within the experimental accuracy. This indicates that the water content is negligible. Beyond this point, the weight decreases slightly, which can be associated with the progressive degradation of the PEG.

The difference of mass fraction between the two dried solutions is small within the experimental accuracy ($< 0.1\%$), suggesting that water evaporates efficiently with both drying procedures. The PEG solutions used to produce the emulsion samples are thus dried using 40 °C for 16 h at 100 mbar.

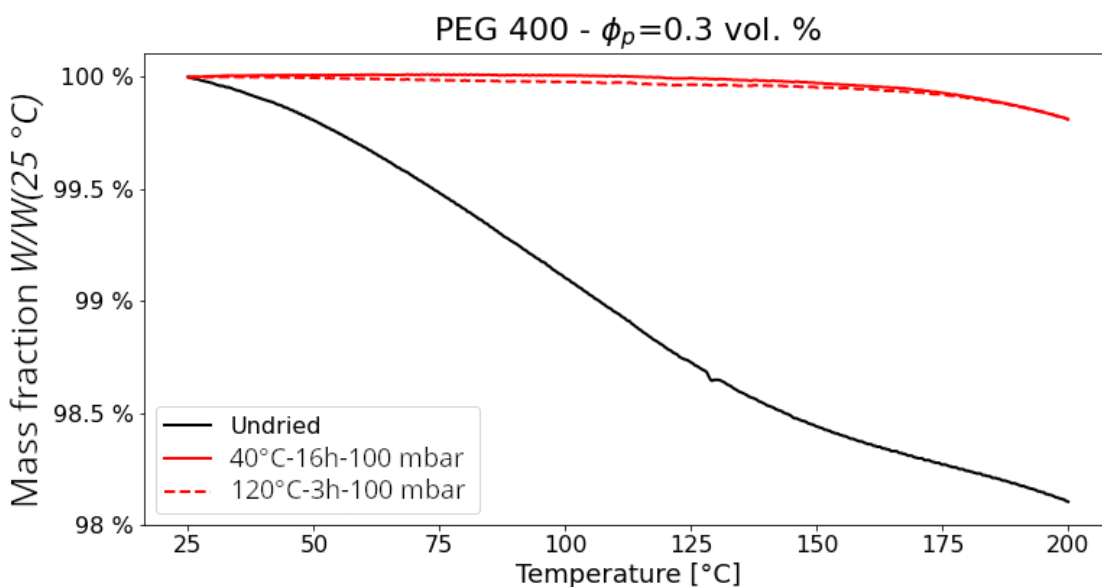


Figure 2.7: Results of thermogravimetric analysis for undried PEG 400, PEG 400 dried at 40°C for 16h at 100 mbar and PEG 400 dried at 120°C and room pressure for 3h. A fraction of the PEG mass evaporates during the heating procedure, depending on its purity and the presence of other chemical species (e.g. water). The overlap of the two dried PEG indicated that the slow drying procedure (40°C, 16h, 100 mbar) evaporates water as efficiently as the fast drying procedure above water evaporation temperature (120°C, 3h, room pressure).

2.3.4 Investigation of the role of PEG impurities

In the preliminary experiments, different PEG were tested. For some solutions, the skin formation did not happen as expected, resulting in wrinkled drops and unstable emulsions. We therefore tested and compared three commercially available PEG-400 solutions, to detect potential impurities and their impact on the skin formation.

Three PEG-400 solutions from three different providers were characterised using TGA after the drying procedure detailed in Section 2.3.3 : Sigma Aldrich (SA-8074855000), Acros Organics (A0-10389123) and Merck (S5807285 944). The liquids were exposed to an increasing temperature, with a temperature ramp of 10 °C per minute between room temperature and 800 °C. The evolution of the remaining mass fraction is shown in Fig. 2.8. The fraction of mass left in the container

diminishes as its components evaporate. Higher mass fraction at high temperatures indicates the presence of impurities with a higher evaporation temperature.

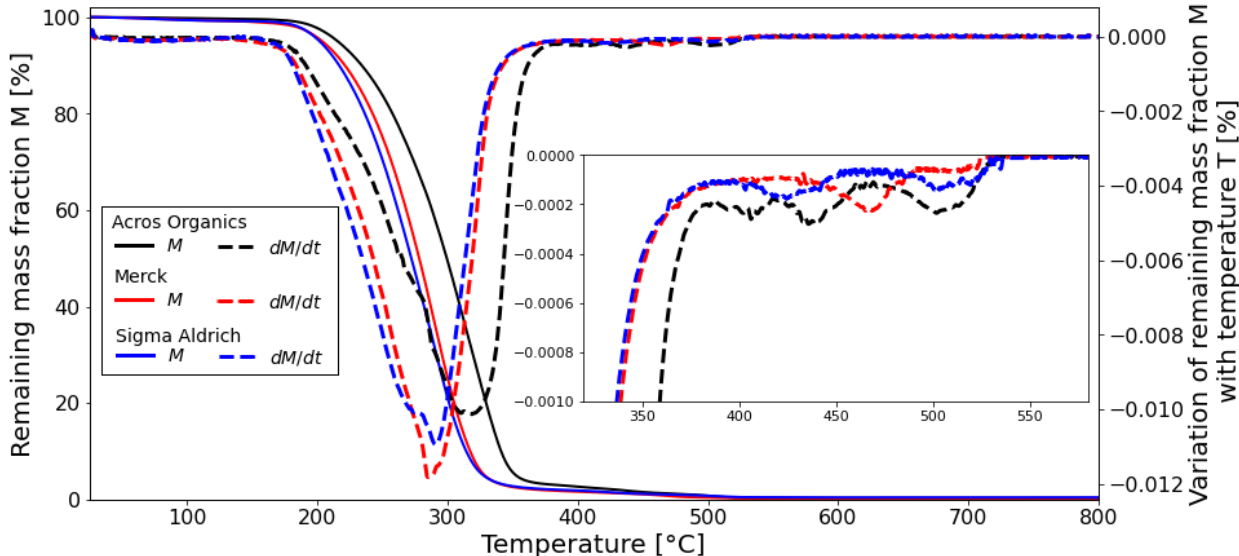


Figure 2.8: Thermogravimetric analysis of PEG from Acros Organics, Merck and Sigma Aldrich, for a temperature increasing by 10°C every minute. The relative remaining mass fraction M is shown along its variation with temperature change dM/dT . The difference in remaining mass fraction indicates the presence of impurities in the Acros Organics PEG. We thus discard the PEG from this provider in further experiments.

The TGA results show that PEG provided by Acros Organics evaporates at higher temperature than its counterparts provided by Merck and Sigma Aldrich. This could indicate the presence of impurities in the product, corroborated by the changes in skin formation we observe when Acros Organics product is used in the drops. In the remaining of our experiments, we therefore switch to Merck and Sigma Aldrich products exclusively.

2.3.5 Dripping setup for PEG drops production

Millimetric drops are produced from a syringe containing the PEG-400/catalyst mixture expelling its content at constant flow rate driven by a syringe pump (Harvard Apparatus Standard PHD Ultra). The PEG flow exits the tube through a needle of inner diameter d , forms a drop attached to the needle, and then falls in the silicone solution in a container placed under the needle when gravitational forces pulling the drop downwards become more important than the interfacial tension forces pulling it upwards, as shown in Fig. 2.9b. The setup is represented in Fig. 2.9a. In the quasi-static regime (that is, at low flow rates), the relation between the drop radius R and the needle radius d is given by the Tate's formula

$$R = \left(\frac{3}{2f} \frac{\gamma}{\Delta\rho g} d \right)^{\frac{1}{3}} \quad (2.7)$$

where γ is the interfacial tension between the PEG solution and the needle material, $\Delta\rho$ the density difference between inner and outer fluids, g the gravitational acceleration, and f a geometrical parameter of order 1 accounting for the part of the drop volume that stays on the needle when the drop detaches [23, 24].

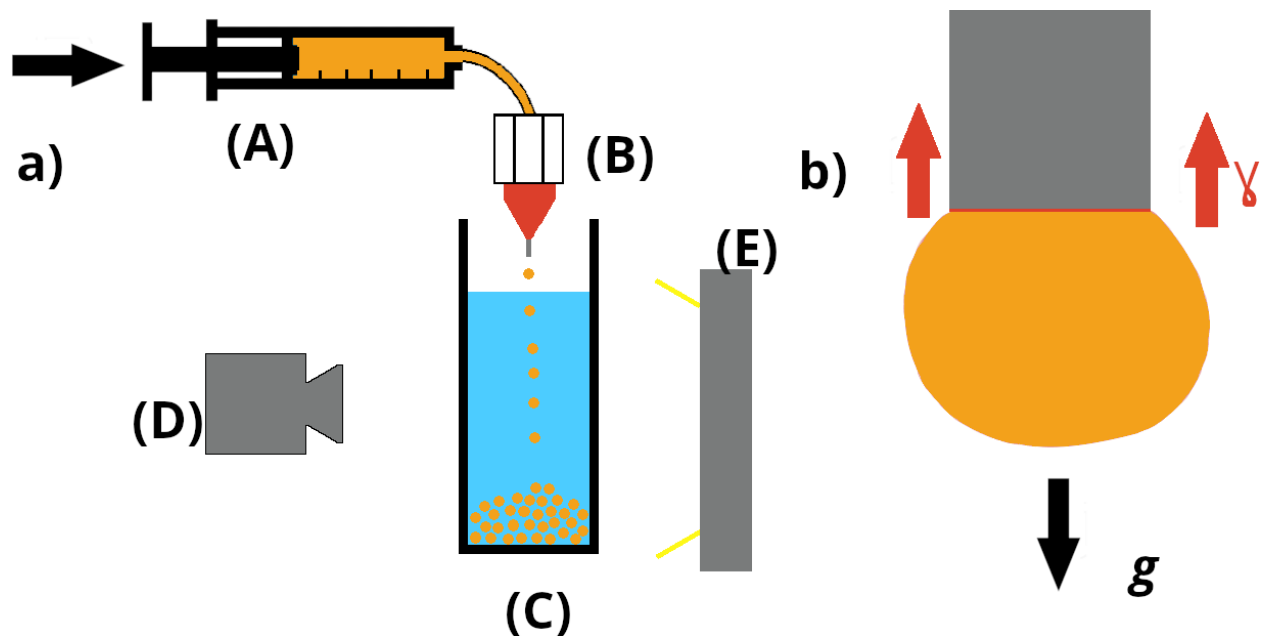


Figure 2.9: Experimental setup to test the production and the stability of millimetric drops. a) Dripping setup. (A) PEG filled syringe, pushed by a syringe pump. (B) Needle with a controlled diameter allowing to tune the drop radius. (C) Sample collector. (D) Camera. (E) Backlight with homogeneous lighting. b) Schematic of the formation of the drop at the needle. The drop formed at the bottom of the needle detaches when it reaches a critical size, where the gravitational force overcomes the interfacial tension force between PEG and the metal composing the needle.

2.3.6 Millifluidic drop production

PEG-in-silicone emulsions are prepared using a millifluidic setup, represented in Fig. 2.10. The reactive silicone fraction ϕ_r typically ranges between 50 wt.% and 100 wt.%, a catalyst fraction ϕ_p between 0.1 vol.% and 1.0 vol.%, and a maleate mass fraction ϕ_m of 5.5 wt.%. All the liquids are prepared following the procedure described in Section 2.3.2.

The reactive silicone phase is placed in two syringes (A) (60 mL PLASTIPAK), connected to a Y-junction with plastic tubes (TYGON E-3603) with an inner diameter of 1.59 mm. The two syringes are put in a double syringe pump (Harvard Apparatus Standard PHD Ultra) to impose the same flow rate on both of them. The PEG phase is put in a single syringe (B) (60 mL PLASTIPAK), placed in a syringe pump (Harvard Apparatus Pump 11 Elite). The two inlets are connected to a T-junction (C) of inner diameter 1 mm with plastic tubes (TYGON E-3603) of inner diameter 1.59 mm, with the PEG phase inlet plugged on the perpendicular pipe of the T-junction. The outlet of the junction is plugged to a plastic tube (D) (TYGON E-3603) of inner diameter 2.38 mm. This tube, where the main reaction happens, is typically 40-240 cm long. It is coiled and kept flat using a cross-shaped tube holder with drilled grooves of size matching the tube outer diameter. The end of the tube is connected to the parallel inlet of a second T-junction. The silicone/maleate solution is put in a syringe (E) (60 mL PLASTIPAK) placed in a syringe pump (Harvard Apparatus Pump 11 Elite), connected to the perpendicular inlet of the second T-junction with a plastic tube TYGON E-3603) of inner diameter 2.38 mm. The outlet of the second T-junction is plugged to a 2.38 mm plastic tube of short length, hanging directly in the container (F) where the emulsion is collected.

The size of the drops is controlled by the flow rates of the reactive silicone phase (Q_1) and the PEG phase (Q_2), while the flow rate of the silicone/maleate phase (Q_3) is tuned to ensure excess in-

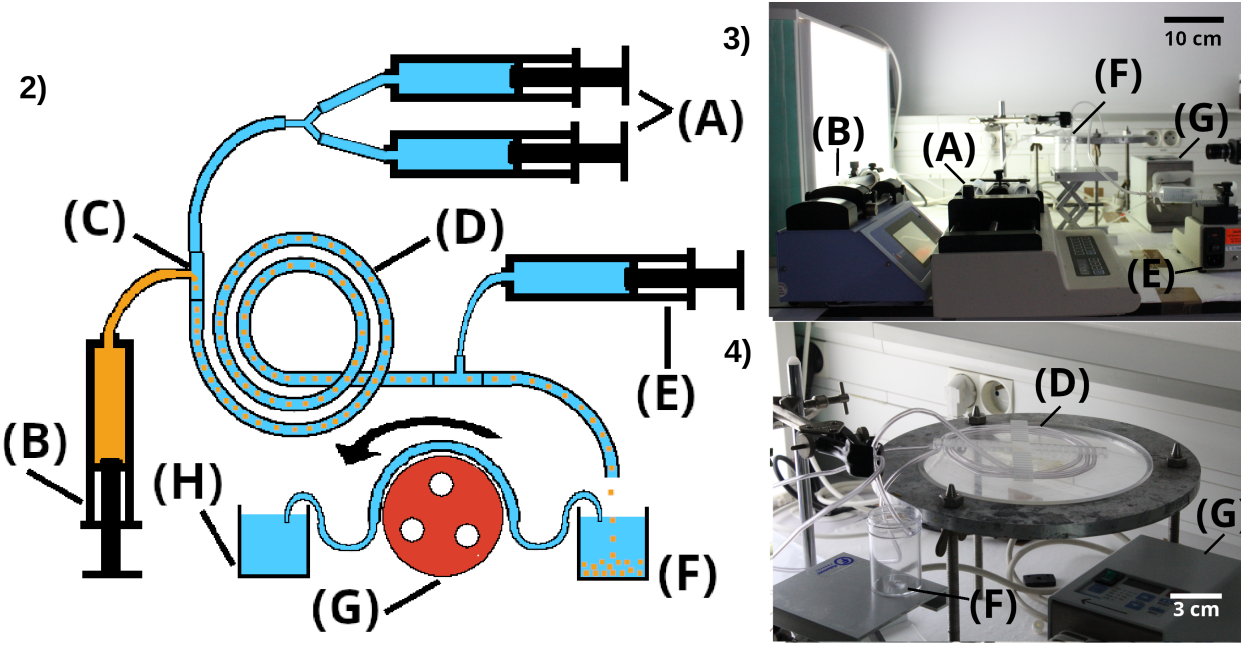
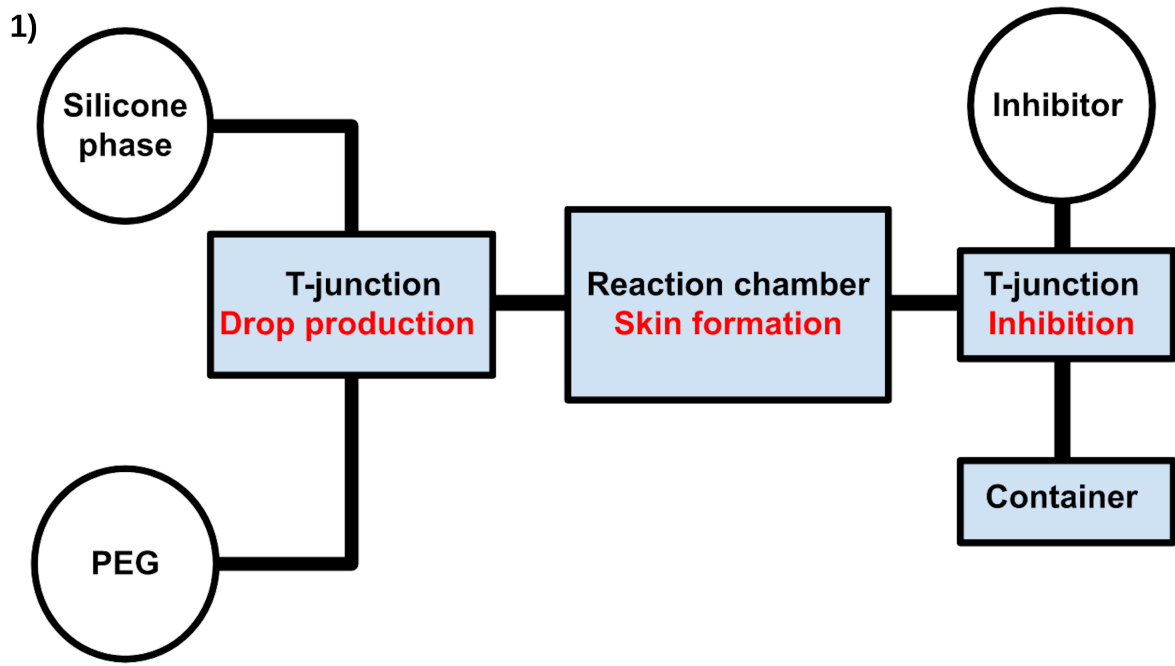


Figure 2.10: 1) Diagram of the millifluidic production setup. 2) Photograph of the setup. 3) Spiral tube close-up. A : two syringes containing the reactive silicone phase. B : Syringe filled with the PEG+catalyst phase. C : T-junction, where the drops are formed. D : spiral tube where the skin of the drop grows while being kept in motion by the laminar flow. E : syringe filled with PDMS and dimethyl maleate. F : sample container where the drops are collected. G : peristaltic pump removing the excess of silicone. H : silicone waste container. 4) Flow-chart of the millifluidic drop production.

hibitor to catalyst concentration ratio. Typical flow rates for stable drop sizes are $Q_1 = 10$ mL/hr (with the actual silicone flow rate being double because of the double syringe setup), $Q_2 = 1.5$ mL/hr and $Q_3 = 5$ mL/hr. Stabilisation of drop production rate usually happens around 5 to 10 min after the beginning of drop formation.

Because of the large difference of silicone/PEG flowrate, the sample is mainly composed of silicone made unreactive by the addition of inhibitor. A peristaltic pump (G) (ISMATEC ISM832C), with an inlet hanging at the top of the sample container, transfers the silicone in a waste container (H) when its volume reaches the top of the container.

2.3.7 PDMS foam generation

For the PDMS foam generation, the reactive silicone blend was split in two parts prepared in two different syringes : a first blend of 184 μ L containing (1) plain PDMS and (2) MHDS at ϕ_r mass ratio, and a second solution containing 2.4 mL (1) plain PDMS, (3) vinyl-terminated PDMS at ϕ_r mass ratio and platinum catalyst, with the volume of catalyst determined as a fraction ϕ_p of the total volume. The platinum catalyst is placed in the second part, as it is dispersed in vinyl-terminated PDMS : adding it to the first part would thus trigger crosslinking reaction before the foam generation. The two phases are prepared such that the intended r , ϕ_r and ϕ_p are obtained in the final blend. A volume V_g of dry air is then added to the second syringe, depending on the desired volume fraction. The two syringes (PLASTIPAK 30 mL) are joined with a Luer Lock connector. The foam is produced by push-and-pull motions imposed by hand on the pistons of the syringes. The procedure is repeated until an experimental reaction time, defined with the help of the scaling law for gelation kinetics investigated in Section 5.2.4. At the end of this step, the solidifying foam is pushed in one of the two syringes. The syringe is closed at the end and its piston is pulled at 1/3 of the total blend volume to produce a gas depression and inflate the bubbles inside the foam. The piston is maintained in place for 2 minutes until the foam is fully gelified.

2.4 Rheological characterisation

2.4.1 Bulk shear rheology

The reacting silicone mixture was prepared in two different vials : one containing plain, unreactive PDMS and MHDS, the second one containing plain PDMS, vinyl-terminated PDMS and platinum catalyst (see Section 2.3.1 for the description of the chemicals). The two parts were mixed using a magnetic stirrer for two days to ensure homogeneity of the solutions. Before the experiment, each part is put in a separate syringe (Plastipak 10 mL). The two syringes are connected by their luer locks with a plastic connector, as depicted in Fig. 2.11c, making sure that no air enters the system. The two parts are then mixed by pushing back and forth on the plungers 30 times, before releasing the mixed solution on the Peltier plate of the rheometer. The plane plate geometry is then brought at gap distance of the Peltier plate, before launching the predefined oscillation procedure.

Shear bulk rheology measurements are performed with a TA Discovery HR-3 hybrid rheometer, with a stainless steel, sandblasted, parallel plate geometry, shown in Fig. 2.11a-b. The gelifying solution is poured on a Peltier plate kept at 25°C. The gap between the plate and the support is set at 1000 ± 1 μ m. In case of shrinking/dilation of the blend during the gelation, the plates must be moved to avoid external constraints on the gel. This option is available only for the plane plate geometry with our experimental device, hence fixing the geometry choice. The plate-support is thus allowed to vary during the gelation. It is determined by forcing the rheometer to impose a compressive force on the gel, of amplitude 0.1 N. This amplitude is the smallest possible force within

the experimental accuracy, so that the plate remains in contact with the blend while applying as little force as possible. The device is operated using the TRIOS 5.1.1.46572 software, provided by the rheometer manufacturer. During the experiment, the rheometer imposes an oscillating strain at 1% of angular deformation. The oscillation is constructed using the multi-wave frequency mode, allowing to probe the stress response at three frequencies simultaneously : a first oscillation mode at 1 Hz and 100% of the amplitude, a second oscillation mode at 2 Hz and 70% of the amplitude, and a third oscillation mode at 4 Hz and 50% of the amplitude. The comparison of the shear modulus at different frequencies is used to detect the gel point, as described by Winter [25]. The acquisitions records one data point every 10 seconds, containing time, oscillation torque and displacement, storage and loss moduli, phase angle and temperature.

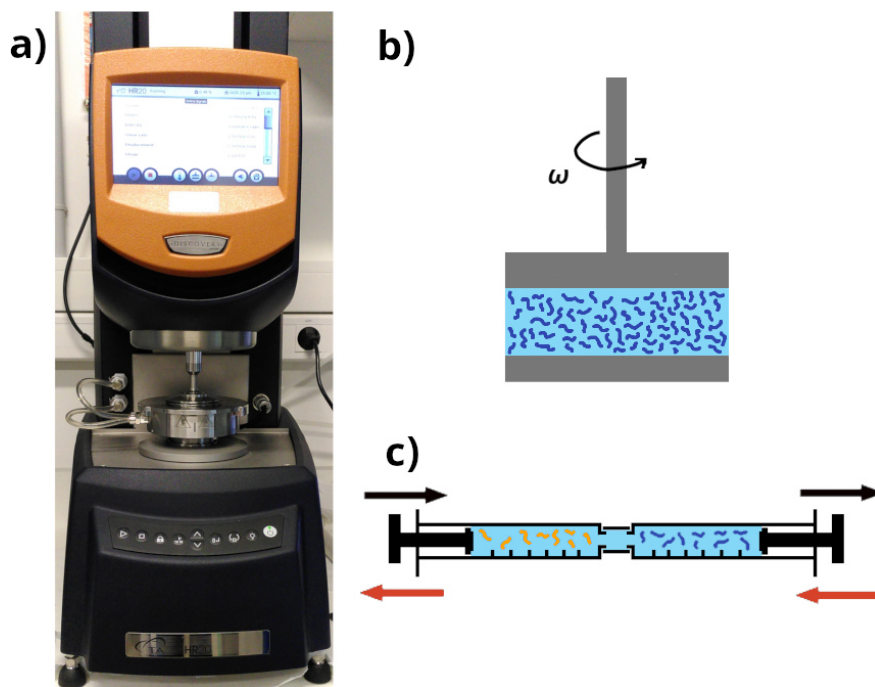


Figure 2.11: a) TA Rheometer used for bulk and interfacial shear rheology experiments. b) Scheme of parallel plates in a shear rheometer. c) Scheme of the double syringe setup used to mix the two silicone phases.

2.4.2 Interfacial shear rheology

Similarly to shear bulk rheology, shear interfacial rheology measurements [26, 27] are performed with a TA Discovery HR-3 hybrid rheometer. We use a double-wall ring geometry (DWR), with an inner/outer diameter of 69.0/71.0 mm, respectively, schematised in Fig. 2.12a. The bottom PEG solution is poured in a cup with a groove of inner/outer diameter of 62.0/79.0 mm, respectively, as shown in Fig. 2.12b. The system is kept at 25°C with the Peltier plate all throughout the experiment. During the experiment, the rheometer imposes a 1% oscillating angular deformation at a 1 Hz frequency.

The two phases of the system are prepared separately. Silicone phase, containing plain PDMS, MHDS and vinyl-terminated PDMS, is prepared at the desired reactive fraction, and left mixing for two days using a magnetic stirrer. For the PEG phase, pure PEG is dried for 10h at 40°C and 100 mbar. The platinum catalyst is then added to the PEG, and mixed using an ULTRA-TURRAX disperser of 15 mm diameter at 6000 rpm for 2 minutes, before covering the solution under argon.

The PEG phase is poured inside the cup up to the top of the groove. The DWR is brought at the interface and the shear oscillation starts. The silicone phase is then poured in the cup along its walls for a slow, homogeneous deposition at the interface, as represented in Fig.2.12. The acquisition records one data point every 10 seconds, containing time, oscillation torque and displacement, storage and loss moduli, phase angle and temperature. The interfacial rheology was performed by Leandro Jacomine.

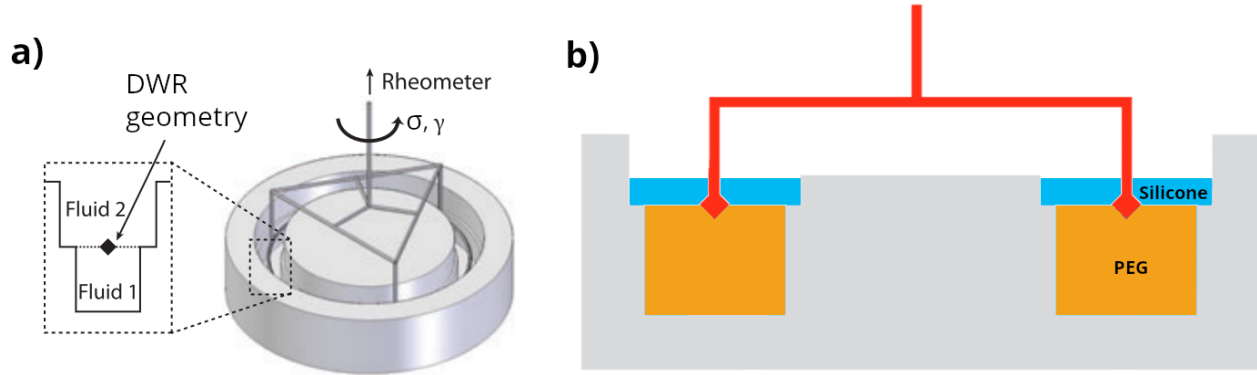


Figure 2.12: a) Double-wall ring geometry used in interfacial rheology [28]. The rotation of the ring shears the interface and imposes the desired deformation rate and amplitude. b) Schematic of experimental configuration of the PEG/silicone interfacial rheology [29].

2.5 Tomography

2.5.1 Image acquisition

Tomographic projections are produced using RXSolutions EasyTom setup, and reconstructed in horizontal slices using the in-built software. The X-Ray source is a LaB6 filament in a Opentype Microfocus X-Ray Source L10711 tube from Hamamatsu. It is calibrated using a black calibration (no X-Ray emission) followed by a white calibration (no object between the detector and the source). The filament is powered with a DC current (90 kV, 60 μ A) and follows the automatised warm-up procedure until it reaches a stable emission level. The filament is then set in large focal spot mode, limiting the generator power to 90 kV. The detector is a PaxScan 2520 amorphous silicon digital X-Ray detector from Varian, with a 1920x1536 pixels matrix, each pixel with a 127 μ m width. The projections are reconstructed into vertical slices using XCAT filtered backprojection algorithm. Images are filtered using a noise reduction Butterworth appodization filter with 75% frequency. Borders are filtered to reduce projection overlap, using a vertical Tukey filter with 80% of the image area left unfiltered. Ring filter is applied on every slice with a 20 voxels kernel. Beam hardening correction is applied with parameters automatically detected by XCAT.

Chapter 3

Investigation of bubble deformability, and its impact on bubble-bubble many-body interactions

3.1 Introduction

Foams are composed of discrete gas bubbles in a continuous liquid phase, their interface being covered with surfactant molecules that lowers the interfacial tension γ_0 (Fig. 3.1a-b). When the fraction of volume occupied by gas ϕ_g exceeds a threshold called the critical jamming fraction ϕ_g^* , contacts appear between the bubbles as shown in Fig. 3.1 that rigidify the packing, as shown in Fig. 3.1c. Increasing ϕ_g above this critical value further rigidifies foams, changing significantly their viscoelastic response to external shear.

For that reason, foams have for long been considered as a good example of jammed systems [30], a class of materials encompassing sands, powders, emulsions, particle dispersions and traffic jam [31, 32]. In their large variety, all these systems share the common property of being composed of discrete, unbound particles that form a rigid packing when brought in close contact with each others. This transition in behaviour is typically reached when the volume fraction occupied by particles reaches a critical value, hence its name of jamming transition. In this family of granular materials, foams fall in the sub-category of athermal systems, where grain are large enough for thermal agitation to be negligible compared to the other interactions involved.

Foams have features that distinguish them from other jammed systems. Their interstitial space is filled with a liquid phase, obeying the laws of hydrodynamics. Their soft, deformable interfaces are loaded with surfactants, which can flow when subjected to shear caused by the liquid phase. Resulting changes in surface concentration translates in interfacial tension gradients, with net restoring flows from high-concentration areas to low-concentration areas known as Marangoni flows, a feature absent from systems with solid interfaces. Most importantly, bubbles deform easily when subjected to compression, changing their shape to minimise their total interfacial energy. This particularity, albeit not exclusive to foams, is identified as an important part of foam behavioural change when increasing packing fraction. For this reason, foam behaviour is often studied separately close to jamming transition (*wet foam* limit) and far away from it (*dry foam* limit).

Despite their particularities, part of the collective behaviour of foams can be explained following the same approaches developed as for other jammed materials. The current jammed material point of view on foams focuses on interactions at the droplet scale [33, 34, 35], modeled in most cases as an elastic force represented by harmonic-like interaction of spring constant k , and a viscous force

scaling like a power-law with velocity difference between neighbouring bubbles.

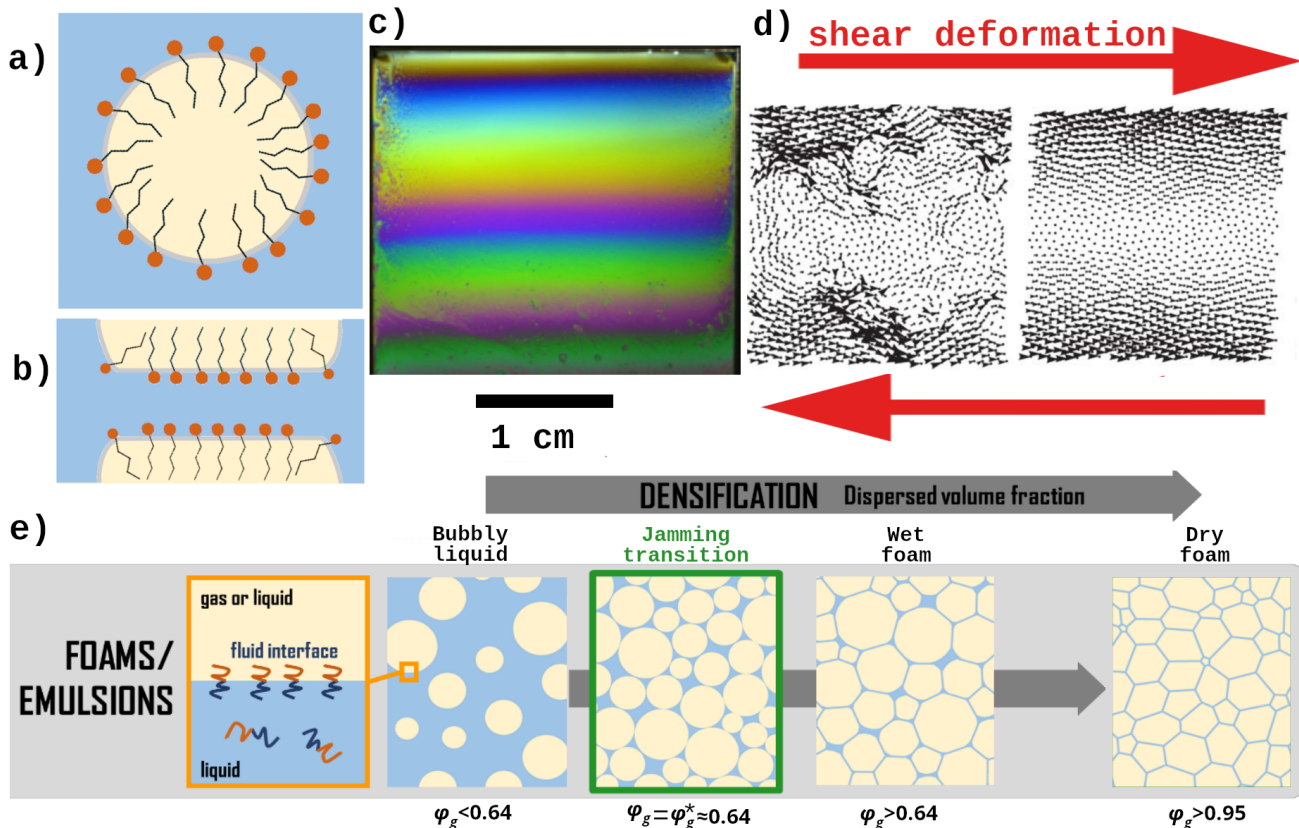


Figure 3.1: a) Bubbles are gas pockets in a liquid solution. Their surface is covered with amphiphilic molecules, called surfactants. b) Liquid film between two gas bubbles. Surfactant molecules repel each other through electrostatic and/or steric interactions, giving films a finite thickness. c) Liquid DBP-732 film (Gelest Inc.) held vertically. Colors come from interferences between the multiple reflected light rays (from [36]). d) Displacement field of simulated bubble packings close to jamming (left) and at high density (right) [34]. Weakly compressed bubbles exhibit non-affine motions and swirling deformation patterns. e) Compression of 2D gas bubbles. Interfaces are covered with surfactant molecules. Spherical, undeformed bubbles are brought in contact during the jamming transition. Electrostatic repulsions between surfactant molecules ensure a finite thickness of the liquid films between bubbles, even for very dry foams.

Foam jamming is canonically captured through what is called the 'unjamming transition' [34][37]. In the dry limit, bubbles are tightly packed against each others. Deformation of the foam causes a stretch of the liquid interfaces, with an increase in interfacial area and a resulting restoring force. When the foam becomes wetter, gas bubbles get back to their spherical shapes and are increasingly free to move around and break contact with their neighbours. Before rigidity loss at the unjamming transition, bubbles displacements can thus deviate from affine, continuous deformation field [38]. These deviations become increasingly important when approaching the critical jamming fraction ϕ_g^* , and effectively changes the resistance of foam systems to shear and compression. This non-affinity onset is a general mechanism for soft jammed materials, and can also be found in non-foams systems [39, 40, 41, 42].

On the other hand, bubbles differ significantly from classical representation of grains as soft, interpenetrating spheres, a canonical model of granular matter summarised in Section 3.1.1. Firstly, their interactions are controlled by the contact of their interfaces. Bulk composition of the discrete phase can only marginally affect overall foam behaviour through interface-subphase interactions.

Secondly, because of volume conservation, any compression by two neighbours would lead to an expansion normal to the compression axis. This expansion would in turn exert an extra-force to the other neighbours, making the bubble-bubble contact interaction intrinsically non-pairwise. This simple property significantly impacts the overall behaviour of foams, with consequences that are summarised in Section 3.1.2. Pairwise bubble-bubble interactions describe foams with good accuracy in some limit cases. Some commonly used interactions are described in Section 3.2. In Section 3.3, I focus on a first-principle interaction law first proposed by Morse and Witten [4], which advantageously predicts the force-deformation relation in the small deformation limit in any arbitrary geometry. I propose a first experimental verification of this interaction law in a simple configuration in Section 3.4, showing excellent agreement between theoretical predictions, experimental results and numerical simulations with no free fitting parameters. Finally, in Section 3.5, I investigate the impact of the bubble-scale buoyancy force on Morse-Witten law, and show that it can in fact be neglected for a wide range of Bond number Bo .

3.1.1 Jammed materials

Jammed materials are most often modeled as spherical particles interacting through solid contacts at their interfaces. These contacts often involve solid friction resulting from roughness of surfaces, making a system of individually simple particles extremely complex[31][32]. Nonetheless, much physical insight has been gained by simplifying those interactions, before treating the particles particularities as perturbations to an idealised system.

A commonly used model for jamming consist of soft spheres interacting through a soft-core repulsive potential, neglecting friction and adhesion. Within this model sketched in Fig. 3.2a, particles (denoted with indices i and j) can overlap with an extra-energy cost V_{ij} , related to their normalised overlap $\delta_{ij} = 1 + \frac{r_{ij}}{R_i + R_j}$, where r_{ij} is the center-to-center distance of the particles, while R_i and R_j are their individual radii. One then commonly define the interaction potential as

$$V_{ij} = \begin{cases} \delta_{ij}^\alpha & \text{if } \delta_{ij} > 0 \\ 0 & \text{if } \delta_{ij} \leq 0 \end{cases} \quad (3.1)$$

The exponent α depends on the strength of the interaction, and is typically of three sorts : harmonic ($\alpha = 2$), hertzian ($\alpha = 5/2$) or hernian ($\alpha = 3/2$). Harmonic interactions are simple spring interactions, and are one intuitive way to approximate physical repulsion between two bodies. Hertzian interaction is the standard framework for representing two rigid bodies in contact mechanics, derived from the deformation of the grain around the contact. Hernian interaction, less standard than the two others, has been found to be a good predictor of packing properties of foams and emulsions in numerical simulations [42].

As the force f between two bubbles is just $f = \frac{dV_{ij}}{d\delta_{ij}} \sim \delta_{ij}^{\alpha-1}$ and the interaction spring constant k is $k = \frac{d^2V_{ij}}{d^2\delta_{ij}} \sim \delta_{ij}^{\alpha-2}$, hertzian and hernian interactions represent springs becoming stiffer and weaker upon compression, respectively, whilst harmonic spring stiffness remains constant. These interaction laws advantageously simplify the complexity of contacts between two solid bodies by representing it as an interpenetration of soft materials. Durian [2] successfully applied this approximation to bubbles in foams, showing that the mechanical and topological properties of foams could be described as spring interactions between soft spheres.

Such a description is, of course, a crude approximation in general, as it decreases artificially the total volume of particles when they deform against each other, without any consideration of material compressibility. At characteristic contact forces close to jamming, most grains can be considered as incompressible. Because of total volume conservation, a local volume reduction in some parts

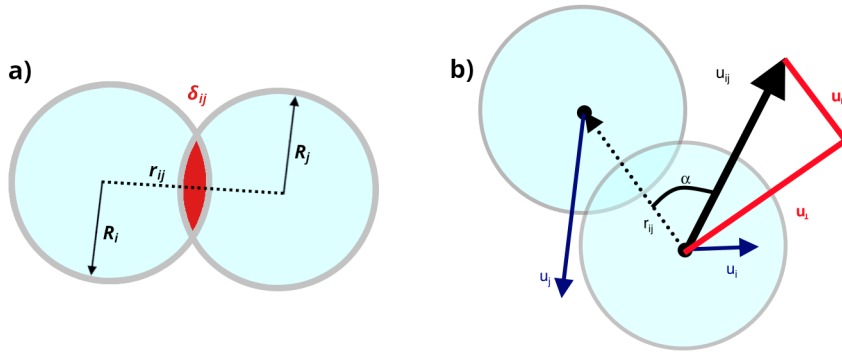


Figure 3.2: a) Spheres approaching at a distance r_{ij} smaller than the sum of their radii. The associated interaction energy is expressed as a function of this overlap. b) Decomposition of the relative motion u_{ij} between two particles in a longitudinal component $u_{\parallel ij}$ and a transverse component $u_{\perp ij}$ (figure from [37]).

of the grains should be compensated by a local volume increase of equal amount somewhere else in that same body. Furthermore, soft-core repulsion is an idealised interaction law that does not require any *a priori* knowledge about the bulk and interfacial properties of the grains. It may then lead to erroneous conclusions about the packing properties when the actual interaction law deviates strongly from its idealised form. To state an example, a vast amount of literature discussing the impact of solid friction on soft-core repulsion [43] shows the importance of modifications of idealised interactions laws with physical considerations on grains non-ideal features.

We shall nonetheless review how these simplified interaction laws can be used to predict collective properties of soft grains, before giving examples of how accounting for grain deformations in the interaction laws modify these predictions. From now on, we will refer to grains as bubbles, as our investigations focused on foam properties. Similarly, we will refer to the continuous phase as liquid phase, associated to liquid fraction ϕ_l , and the discrete phase as gas phase with its associated gas fraction ϕ_g . This notation choice should not hide the fact that any knowledge on foams can be transferred to emulsions and vice-versa, providing the physico-chemical details allow it.

Mechanical properties of grain assemblies

At jamming fraction ϕ_g^* , grains are in contact with each other without overlapping with their neighbours. They are thus at zero potential energy in terms of soft-core repulsion. Any further compression beyond the jamming point requires bubbles to be pressed against neighbours and overlap. A simplifying and fruitful approach is the effective medium theory (EMT) that assumes that (1) averaged and macroscopic quantities can be obtained by averaging over individual contacts and (2) a global deformation of the packing manifests as a similar, uniform deformation at the bubble scale, the latter hypothesis being known as the affine deformation hypothesis [44]. Under EMT assumptions, any increase $\Delta\phi_g = \phi_g - \phi_g^*$ of gas fraction is directly proportional to total system overlap (i.e. $\Delta\phi_g \sim \delta$) and its associated potential energy depending on the interaction law chosen. In foams, the amount of mechanical work dW required to extract an infinitesimal amount of liquid dV_l is related to the *osmotic pressure* Π [45, 46] defined as $\Pi = -\frac{dW}{dV_l}$. Pressure being related to contact force, Π is thus scaling as $\Pi \sim f \sim \frac{dV}{d\delta} \sim \delta^{\alpha-1} \sim \Delta\phi_g^{\alpha-1}$ [41] as shown in Fig. 3.3a. This consideration based on physical arguments is corroborated by numerical simulations of 3D monodisperse and bidisperse spheres, and of 2D bidisperse discs [42]. Osmotic pressure is

thus a first-hand example of the impact of individual interactions on collective properties of grain assemblies.

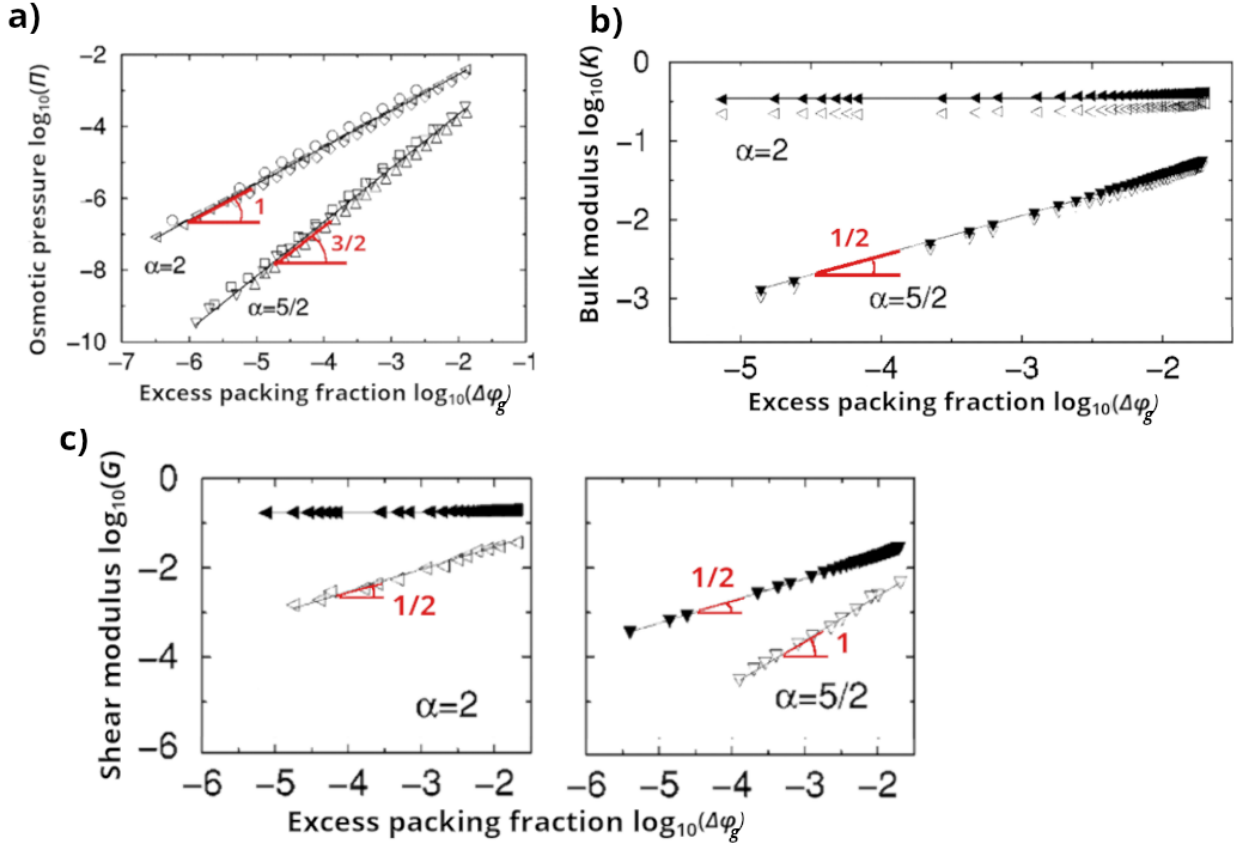


Figure 3.3: a) Osmotic pressure Π evolution with excess packing fraction $\Delta\phi_g$ for harmonic ($\alpha = 2$) and hertzian ($\alpha = 5/2$) interactions of frictionless spheres. b) Bulk modulus K for the same interactions. Filled symbols are computed directly after deformation. Open symbols are the same computation obtained after letting the grains relax. c) Shear modulus G in the same conditions. Change in power-law after relaxation is linked to non-affine deformation field. Non-affinity decreases as foams become drier. Figure adapted from [42].

Osmotic pressure is not the only mechanical property depending on gas fraction and interaction law. In particular, the resistance of granular materials to shear and compression is often taken as a relevant material description, as arbitrary deformation can always be decomposed in a combination of a pure shear and a pure compression. Similarly, relative particle displacement can be decomposed in transverse and longitudinal displacement u_{\perp} and u_{\parallel} , respectively, represented in Fig. 3.2b. Affine deformation hypothesis allows to express compression modulus K and shear modulus G as proportional to interaction spring constant k , such that $K \sim G \sim k \sim \frac{d^2V}{d\delta^2} \sim \delta^{\alpha-2} \sim \Delta\phi_g^{\alpha-2}$ [41] (Fig. 3.3). In this prediction, however, EMT failure is two-fold.

At jamming transition, the compression modulus K jumps discontinuously from zero to a non-zero value[41, 42] as shown in Fig. 3.3b. This discontinuity, referred to as anomalous compression modulus in the literature, was at one point seen as rigidity percolation as contacts appear between particles. Further simulations by Ellenbroek *et al.*[47] showed that random networks of grains connected by springs do not exhibit anomalous bulk modulus at percolation, but rather a function decreasing smoothly with average number of springs per particle. It is now believed that the anomalous bulk modulus at jamming is of geometrical origin, emerging from its peculiar organisation of

particles.

Many simulations have shown that the shear modulus G actually scales with excess gas fraction as $G \sim \Delta\phi_g^{\alpha-3/2}$ [41, 44, 42, 39, 47]. Authors hypothesized that shear modulus anomalous scaling is caused by the break of the affine deformation hypothesis due to the relative motion of grains. Non-affine deformation of a bond \vec{r}_{ij} is quantified by the displacement angle $\tan(\alpha_{ij}) = \frac{u_{\perp ij}}{u_{\parallel ij}}$ following the convention introduced by Ellenbroek *et al.*, and is found to be of great importance close to jamming [47].

Longitudinal and transverse displacement translates differently in terms of relative motion and change in overlap, as shown in Fig. 3.2b. Their relative contribution to energy change also differs, following the relation found in [39]

$$\Delta E = \frac{1}{2} \sum_{i,j} k_{ij} \left(u_{\parallel ij}^2 - \frac{\delta_{ij}}{\alpha - 1} u_{\perp ij}^2 \right) \quad (3.2)$$

Non-affine deformations are thus found to affect shear and bulk moduli. Their impact can be evidenced by simulating jammed packings of grains subjected to an external strain [42]. In a first step, grains are moved with respect to each other, following an affine deformation field. Elastic moduli are then extracted from the resulting energy change. The resulting moduli are shown with the filled symbol in Fig. 3.3b-c. In a second step, the grains are let to relax to their new equilibrium position. The resulting moduli are shown with the open symbols in Fig. 3.3b-c. From these results, it appears that relaxation introduces non-affinity in the displacement field, and effectively decreases both bulk and shear moduli when they are computed after relaxation.

Geometrical properties of grain assemblies

Changes in the macroscopic mechanical properties of spheres assemblies interacting through short-range potentials are intuitively expected to be tightly linked to structural changes in their local organisation. Such structural changes are known to be the signature of phase transition in e.g. amorphous systems and glass transition [30]. Among them, the pair correlation function $g_2(r)$ has been studied in the jamming transition of hard frictional spheres [48], soft frictionless spheres [41] and emulsions [49, 50]. Increasing excess packing fractions triggers structural changes in all of these systems, whilst keeping their distinctive features depending on their physico-chemical details.

The pair-correlation function $g_2(r)$, also referred to as radial distribution function, is defined as the probability, knowing that a position \vec{r}_i in space is occupied by a first body, that a second point \vec{r}_j is occupied with another particle

$$g_2(r) = \frac{V}{N^2} \sum_i \sum_{i \neq j} \delta(r - r_{ij}) \quad (3.3)$$

where V is the volume considered, N the number of particles within this volume, used as normalisation factor, and δ is the Dirac delta function where $\delta(r - r_{ij}) = 1$ if $r = r_{ij}$, and 0 otherwise.

For perfectly ordered crystalline lattices, $g_2(r)$ shows strong peaks at the position of grain's neighbours. The heights and positions of the peaks typically depend on the underlying crystalline structure as shown in Fig. 3.4 for the example of a body-centered cubic lattice. For hard monodisperse spheres, the first shell of neighbours exist at a distance corresponding to particle diameter D . The second peak location depends on the crystalline geometry : expressed in units of D , typical values are $\sqrt{2}D$ for a face-centered cubic lattice, and $2/\sqrt{3}D$ for a body-centered cubic lattice. For

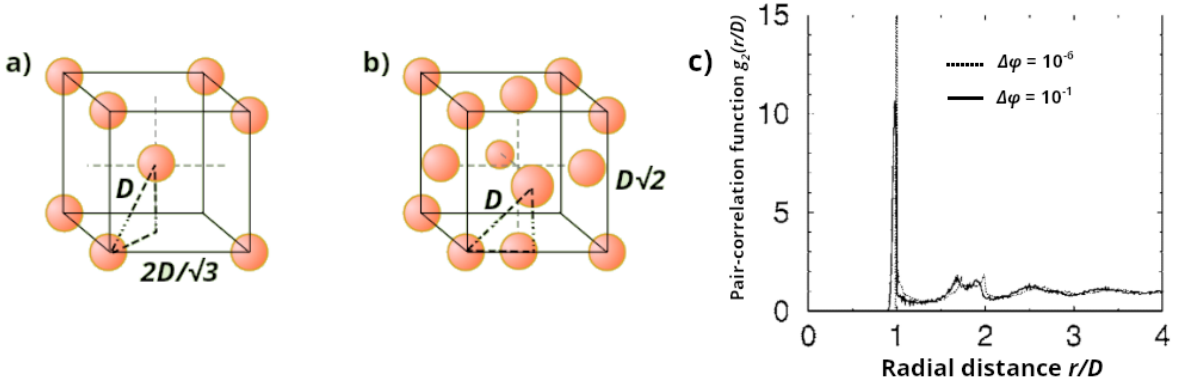


Figure 3.4: a) Body centered cubic lattice, with 1st neighbours at a distance D , and 2nd neighbours at $2D/\sqrt{3}$. b) Face centered cubic lattice, with 1st neighbours at a distance D , and 2nd neighbours at a distance $D\sqrt{2}$. Figures from [51]. c) Pair-correlation function for jammed harmonic spheres at two different packing fractions [52].

that reason, $g_2(r)$ is often scaled with D and expressed as $g_2(r/D)$. At jamming transition, $g_2(r)$ at first peak $r = D$ diverges according to the power law $g_2(r/D) \sim \frac{1}{\sqrt{r/D-1}}$. [42].

Thermal fluctuations, defects and deviations from hard-core repulsion impact grains organisation, modifying the positions and widths of the peaks. Additionally, increasing packing fraction reduces centroid-centroid distances as particles interpenetrate. First-shell neighbours become closer than the undeformed particle diameter D (see Fig. 3.2.a), which makes $g_2(r/D < 1)$ non-zero. The width of the $g_2(r)$ distribution in this $r/D < 1$ regime is called its left-hand width w_L , and increases with excess packing fraction. As the interparticle distance distribution broadens, the height of the $g_2(r)$ peaks decreases as well, depending also on excess packing fraction.

For soft, interpenetrating particles, radial distribution function becomes non-zero at small distances ($r < D$) when particles start to overlap. the progressive change of $g_2(r < D)$ with packing fraction is intrinsically linked to interparticle interactions. Silbert *et al.* [52] studied the evolution of the first peak with excess packing fraction in simulations of frictionless spheres interacting through harmonic and hertzian potentials They showed that the peak distribution broadens as particles are compressed, evolving from a δ function to a wider and lower distribution as spheres interpenetrate. The height of the first peak $g_2(r/D = 1)$ is found to scale as $g_2(r/D = 1) \sim \Delta\phi_g^{-1}$, while its value in the region closer than particle diameter $g_2(r/D < 1)$ is found to scale as $g_2(r/D < 1) \sim (r/D - 1)^{-1/2}$ slightly above jamming ($\Delta\phi_g \sim 10^{-8}$). This scaling law was found to hold for hertzian and harmonic interactions, being counterintuitively independent from the interaction law. In the evolution of the first peak, the width of the distribution on the left-hand side of the first peak ($r < D$) w_L is expected to be directly impacted by the mechanisms at play in the overlap. Interestingly, Silbert *et al.* [52] found again no difference between harmonic and hertzian soft spheres when looking at w_L , which was shown to scale as $w_L \sim \Delta\phi_g$ in both cases.

Whether or not this scaling depends on the interaction strength is an unsettled matter. In their own simulations, Donev *et al.* [53] found different scaling laws depending on the interaction. Their method of computation voluntarily excluded freely moving particles (*rattlers*), and found different scaling laws depending on interaction. On the other hand, Silbert and coworkers did not perform such selection, arguing that rattlers cannot be neglected with respect to packing stability in shear deformation [54]. They found no difference between hertzian and harmonic repulsion, a conclusion that must be hold in regard of their assumptions on rattlers.

Topological properties

In addition to their mechanical properties and their local geometrical order, foams can be characterised at the bubble scale by their number of neighbours Z , also sometimes referred to as contact number. As argued in the literature [37], changes in mechanical properties can be explained in terms of changes in average contact number, as individual contact forces add up : elastic moduli can be understood as the average number of ‘springs’ per grain [2]. This contact number jumps discontinuously from zero to a finite value called the isostatic contact number Z_c at the jamming transition, then increases as a power-law of excess packing fraction [42, 52, 38, 55]:

$$\Delta Z = Z - Z_c \sim \Delta\phi_g^{1/2} \quad (3.4)$$

Values of Z_c differ depending on interactions. For frictionless bubbles interacting in d dimensions, $Z_c = 2d$, corresponding to the number of degrees of freedom of a single particle, considering the rotations. For frictional particles, static friction at the interface hinders the rotations, decreasing progressively the isostatic contact number Z_c as Coulomb friction coefficient μ increases, down to $Z_c = 2d - 2$ for large friction coefficients. The exponent of the power-law also changes with static friction, going from a square-root power law to a linear dependency [56] as the static friction coefficient increases.

Excess contact number ΔZ can also be derived from geometrical considerations. It can be integrated from $g_2(r)$ through [41]

$$\Delta Z = \int_1^{1+\delta} g_2(\xi) d\xi \sim \int_1^{1+\delta} d\xi \frac{1}{\sqrt{\xi-1}} \sim \delta^{1/2} \quad (3.5)$$

where δ is the overlap between neighbouring bubbles, and $\xi = \frac{r}{D}$ the reduced distance between their centroids. From this definition, excess contact number ΔZ can be defined for every grain individually. Similarly, gas fraction can be locally defined $\phi_g(r)$ using the Set Voronoi diagram to segment space [57]. This tessellation is an adaptation of Voronoi diagrams to aspherical particles : every particle is enclosed in a Voronoi cell, defined as the ensemble of points closer to the surface of this particle than to any other particle. In the case of deformable grains, this is much more appropriate than classical Voronoi diagram usage of centroid position : as grains do not remain spherical under deformation, centroid-centroid distance can not predict grain contact. Numerical tools to compute the Set Voronoi diagram of arbitrarily shaped particles are also readily available online in open-source programs, such as Pomelo developed by Weis *et al.* [58, 59].

These locally defined quantities play a key role in packing mechanics close to jamming. In fact, failures of effective medium theory are arguably due to its lack of proper consideration of contact numbers and local liquid fraction [15, 60, 61, 38, 62, 63]. These two factors show strong fluctuations close to the jamming point because of non-affinite displacements.

3.1.2 Effects of grain deformability on jammed material properties

The currently available physical description of the jamming properties of soft bulk grains, despite its efficiency to explain some parts of their properties, remain fundamentally flawed by its assumptions when applied to foams and emulsions. For example, the absence of viscous force modelling immediately forbids from considering dynamical aspects of foam rheology, in disregard of the rich frequency-dependent behaviour of foams [65]. The high deformability immediately changes the distances between neighbouring particles interfaces, which in turn affects their contact number [15]. Overlapping volumes change the effective gas fraction significantly, a worsening issue for large excess packing fraction [66].

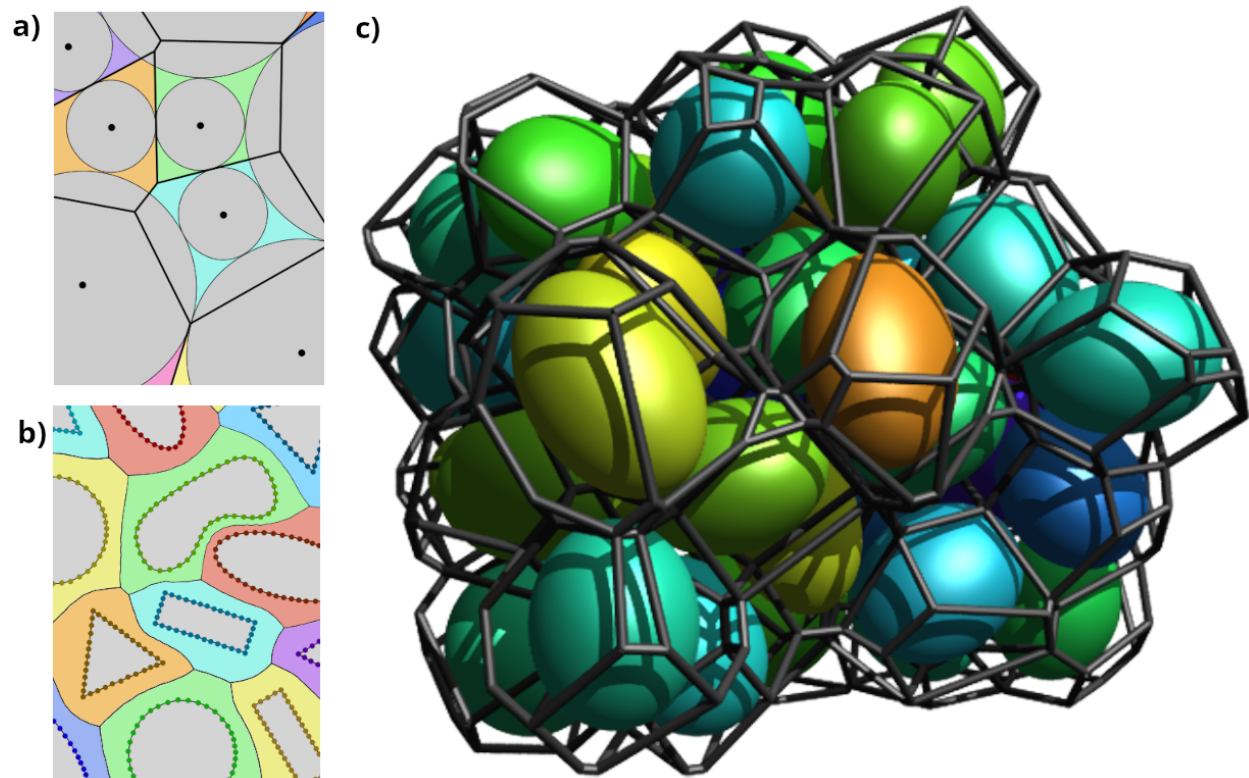


Figure 3.5: a) Voronoi diagram for circles with different radii. Space segmentation fails to consider differences in shape, and large circles exceed the borders of their cell. b) With Set Voronoi diagram, the cell is computed using the location of the interface. Any arbitrary shape can thus be considered. Figure from [64]. c) Ellipsoidal shapes represented inside their set Voronoi cells. These cells (black edges) of a bubble consists of all the points closer from its surface than to the surface of any other bubble. Figure from [59].

Foams are a good example of systems where grain deformations play a key role in structural and mechanical properties of the packing. Under atmospheric conditions, capillary forces are too small to compress gases significantly. When at rest, bubbles in perfectly dry foams fill space with energy minimisation constraints [33]. In most cases, this energy is simply proportional to the surface area, with the proportionality factor being the surface tension γ . The resulting, surface-minimising space-tiling is a well known mathematical problem, with a few examples of solutions shown in Fig. 3.6a. In 2D, a simple solution is the honeycomb lattice, where hexagonal bubbles fill up the plane. In 3D, the problem is more complex and has no definitive answer yet. The Kelvin cell (Fig. 3.6b) was long believed to be the lowest energy configuration for a regular space-filling bubble [67], with 6 square faces and 8 hexagonal faces. Assisted with numerical simulations, Weaire and Phelan recently managed to find a more energetically favorable configuration called Weaire-Phelan structure [68] (Fig. 3.6c), composed of two subcells : one with 12 pentagonal faces, and one with 12 pentagonal faces and 2 hexagonal faces. The Weaire-Phelan structure tops Kelvin cell with 0.3% energy gain.

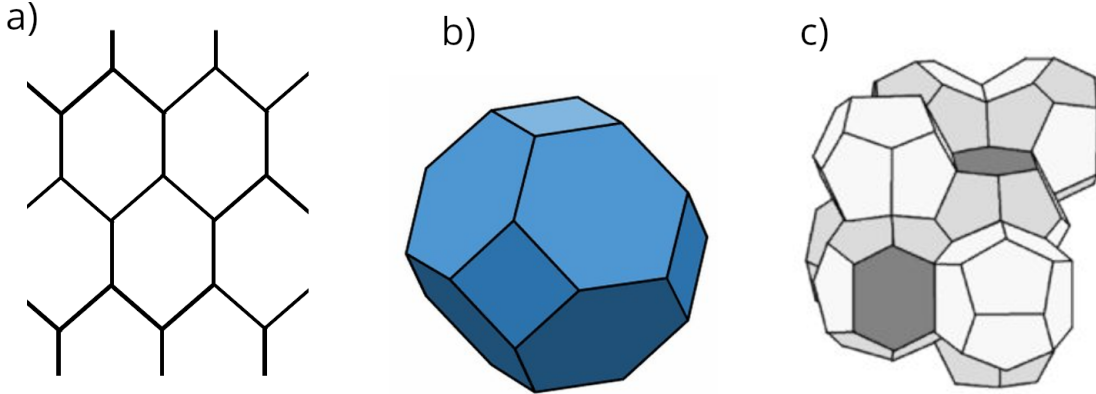


Figure 3.6: a) The honeycomb lattice is the optimal space tiling lattice in two dimensions. b) The Kelvin cell is the optimal space filling known to date in 3D with a single type of cell. Figure from [69]. c) The Weaire-Phelan structure beats Kelvin cell by 0.3% energy gain, with a subunit of two cells. Figure from [70].

These extreme cases of deformations concern foams with very low liquid fraction ($\phi_l = 1 - \phi_g < 0.1\%$) known as the dry limit. In real foams, the difference $\Delta\rho$ in the density of the two phases causes naturally liquid to drain down, while capillary forces maintain some liquid in the Plateau borders. The Princen length $l_c = \sqrt{\frac{\Delta\rho g}{\gamma_0}}$ is the characteristic lengthscale beyond which gravity wins over capillary forces. Foams higher than l_c thus exhibit a variation of the liquid fraction. If in contact with a liquid bath, it ranges from critical fraction $\phi_l^* = 1 - \phi_g^*$ (also called the wet limit) to lower values [46]. Nonetheless, bubbles deformation happens as soon as jamming transition happens.

Mechanical properties of foams

In foams, the shapes and organisation of bubbles are driven by interfacial tension γ alone, assuming incompressibility of the gas. It therefore simplifies the expression of a non-entropic osmotic pressure Π : the work required to extract an infinitesimal volume of liquid dV_l is proportional to the variation of interfacial area dS [71, 45] :

$$-\Pi dV_l = \gamma_0 dS, \quad (3.6)$$

$$\Pi(\phi_l) = -\gamma_0(1 - \phi_l)^2 \frac{\gamma_0}{R_{32}} \frac{d}{d\phi_l} \left(\frac{S(\phi_l)}{S_0} \right), \quad (3.7)$$

where R_{32} is the Sauter mean bubble radius, S the foam surface at liquid fraction ϕ_l , and S_0 the surface of the undeformed bubbles at jamming. A more explicit expression of osmotic pressure would require assumptions about the geometrical arrangement of bubbles. Experimental and numerical studies [45] of different foam structures revealed that their interfacial energy density variation with liquid fraction differs, as shown in Fig. 3.7b: face-centered cubic (fcc) organisation is energetically more favorable than the Kelvin structure (bcc) close to jamming. This tendency inverts at a critical fraction ($\phi_l < 6.3\%$), causing an irreversible transition from fcc to Kelvin cell geometry.

Because of this plasticity in geometry, osmotic pressure is often expressed differently in the wet [3, 73] and in the dry [71, 74] limit, with very different assumptions: interactions in very wet foams are often approximated as pairwise and local. On the other hand, dry foams can be treated as a space-tiling problem with increasing amount of liquid localised in the Plateau borders – a wet foam construction technique known as the decoration theorem [75]. Nonetheless, osmotic pressure can be fitted with a reasonable accuracy through liquid fraction changes with the empirical formula [71, 46]

$$\Pi = 7.3 \frac{\gamma_0}{R_0} \frac{(\phi_l - \phi_l^*)^2}{\sqrt{\phi_l}}. \quad (3.8)$$

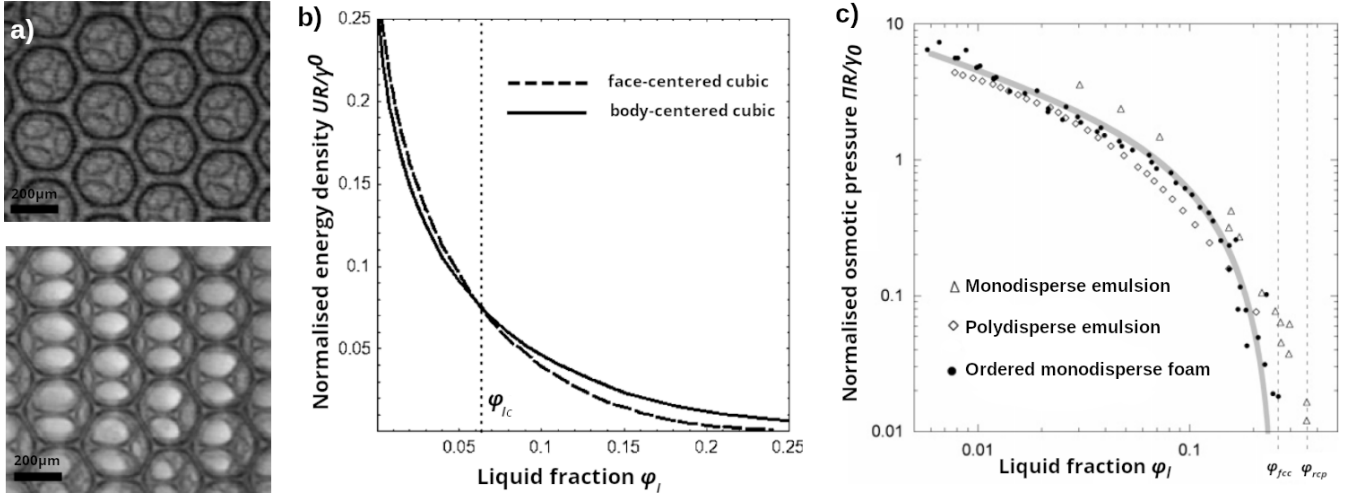


Figure 3.7: a) Change in geometrical organisation from fcc to bcc with decreasing liquid fraction. b) Excess energy per unit area for fcc and bcc structure. ϕ_{lc} is the critical liquid fraction under which bcc structure is more energetically favorable than fcc. c) Normalised osmotic pressure variation with liquid fraction for monodisperse emulsion, polydisperse emulsion and monodisperse emulsion. Full gray line is the theoretical prediction $\Pi\gamma_0/R_0 = 7.3 \frac{(\phi_l - \phi_l^*)^2}{\sqrt{\phi_l}}$, where ϕ_l^* depends on the packing geometry. Figure from [71].

Rheological properties of foams result from a complex interplay of the different scales involved, from the foam scale down to the molecular structure of surfactant-loaded interfaces. They are generally measured through shear rheology experiments [76], where the foam is subjected to an oscillating shear strain ϵ and the corresponding shear stress σ is measured. In the static limit (constant shear strain i.e. null oscillation frequency), the viscosity of the liquid phase plays no role in the elastic response. The shear modulus G_0 therefore depends only on interfacial tension γ_0 and on the Sauter mean bubble radius R_{32} [45, 77, 78], with results shown in Fig. 3.8c. Furthermore,

dry foams exhibit higher rigidity, while unjamming transition ($\Delta\phi_l \rightarrow 0$) comes with total loss of rigidity. Elastic shear modulus in the static regime can therefore be expressed as

$$G_0 = \alpha\phi_l(\phi_l - \phi_l^*)\frac{\gamma_0}{R_{32}}, \quad (3.9)$$

where α is a numerical prefactor, experimentally found to be $\alpha \approx 1.4$ [79, 80]. Interestingly, this law remains valid for polydisperse bubbles as well, as shown in Fig. 3.7c.

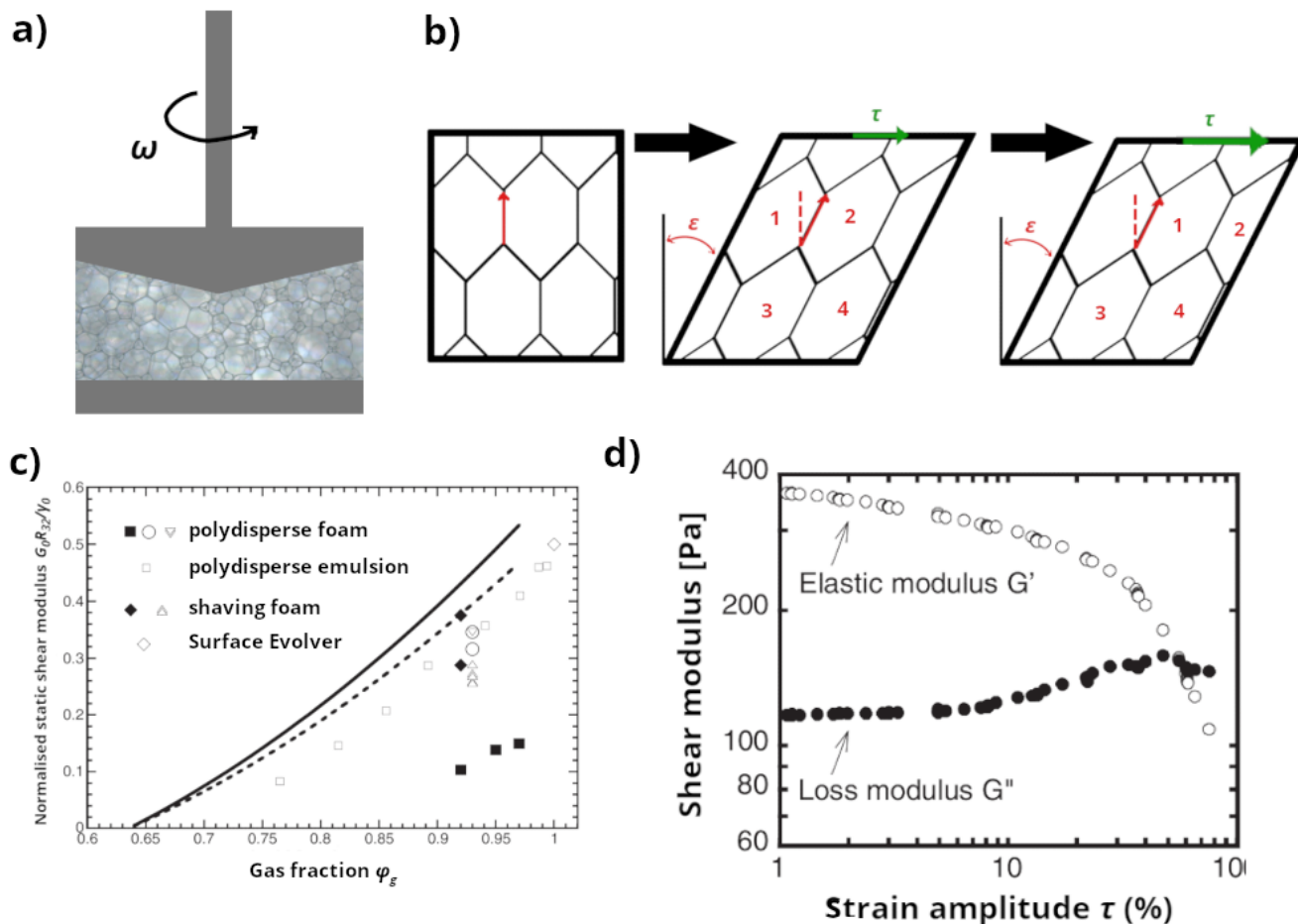


Figure 3.8: a) Shear rheology of a foam imposes a shear deformation at angular frequency ω . b) Scheme of a shear deformation of a honeycomb lattice in 2D. c) Variation of static shear modulus with liquid fraction ϕ_l for polydisperse foams and emulsions. d) Variation of elastic and loss moduli with strain amplitude. Loss modulus crossover determines the transition from solid-like to liquid-like behaviour. Figures c and d from [65].

The linear elastic response of a foam only holds up to a critical yield strain ϵ_y . Above this critical deformation, bubbles locally rearrange and foam flows. This process translates locally to the deformation of bubbles following Plateau laws, shrinking Plateau borders. When their length reaches zero, the foam is in a locally unstable configuration and neighbouring bubbles switch their positions [68, 81]. This transformation is called a T1 transition, a 2D representation of which can be found in Fig. 3.8b. The foam is then plastically deformed to a new rest configuration. This reorganisation events can happen locally at the bubble scale, or occur as avalanche events, triggering large-scale reorganisations [75].

Through local rearrangements, foams minimise their total energy under a given shear strain.

This effectively reduces their shear modulus. For large enough strain amplitude as shown in Fig. 3.8d, rearrangements in the foam happen so frequently that the foam starts to behave like a liquid rather than a solid, with a viscous loss modulus G'' greater than its elastic storage modulus G' . A description of these moduli is given in Chapter 5.

As foams imply liquid flows with finite viscosity, their mechanical response is always dependent on the shear oscillation frequency ω and the ageing processes (drainage, coarsening and coalescence) happening inside of it. A detailed explanation of their contributions to foam rheology is beyond the scope of this thesis. Interested readers are referred to the dedicated literature [65, 82, 83, 75].

Geometrical properties of foams

Regardless the spatial organisation of foams, bubbles in dry foams always follow geometrical rules known as Plateau's laws shown in Fig. 3.9, provided they reached mechanical equilibrium and have constant interfacial tension. These simple laws were first experimentally evidenced by Joseph Antoine Ferdinand Plateau [84], and are the following :

1. Each liquid film has a constant mean curvature
2. Three liquid films meet in a Plateau border at angles of 120° , illustrated in Fig. 3.9b
3. Four Plateau borders meet in a vertex with tetrahedral symmetry (see Fig. 3.9c)

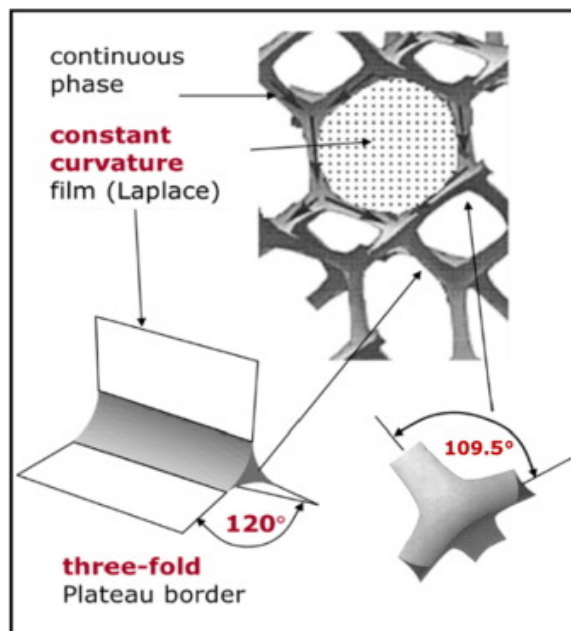


Figure 3.9: Two bubbles join at a film of constant curvature, shaped by the pressure difference between the bubbles. Three films meet at a Plateau border, with 120° angles between the films. Four organise in a Plateau junction, with Plateau borders meeting at $\sim 109.5^\circ$. Figure from [85].

These strong local geometrical constraints do not, however, determine the lattice geometry of the underlying foam structure. As such, the Kelvin structure, the Weaire-Phelan structure and disordered foams all obey Plateau's laws while differing significantly from one another.

Because of bubble deformability, interfaces originally far from each other are brought into close proximity, altering the $g_2(r)$ radial distribution function (see Section 3.1.1) found in undeformable

granular materials. Zhang and Makse [49] simulated packings of drops interacting through an approximated interaction law valid for weakly deformed drops, where the interaction force is computed as $f \sim A\gamma R_1 R_2 / (R_1 + R_2)$, where A is the contact area between the two drops. This interaction law and its underlying assumptions are discussed in Section 3.2.1. With large ensembles of individual particles, using methods from molecular dynamics simulations, they showed, as represented in Fig. 3.10a, that the first peak of $g_2(r)$ is less affected by the variation of the excess packing fraction $\Delta\phi_g$ for deformable particles compared to soft, rigid particles (see Section 3.1.1). Moreover, the introduction of deformability through the interaction law induces a change in the behaviour of the second peak of the pair correlation function. This second peak splits in two subpeaks close to each other, around the distance r at which the second shell of neighbours is expected [50, 86, 49]. The reasons for this splitting are still debated today [87], but it is now believed to emerge naturally in liquid to glass transition with the emergence of a local order inherited from the inherent structure of liquids [88]. In their simulations, Zhang and Makse [49] found that this splitting disappears when particles interact through the interaction law mentioned above, with a large, very broad second peak that is represented in Fig. 3.10a. Comparison with adhesive and elastic emulsions further modify this second peak, shown in Fig. 3.10b, highlighting once again the importance of interfacial interactions on foam structure.

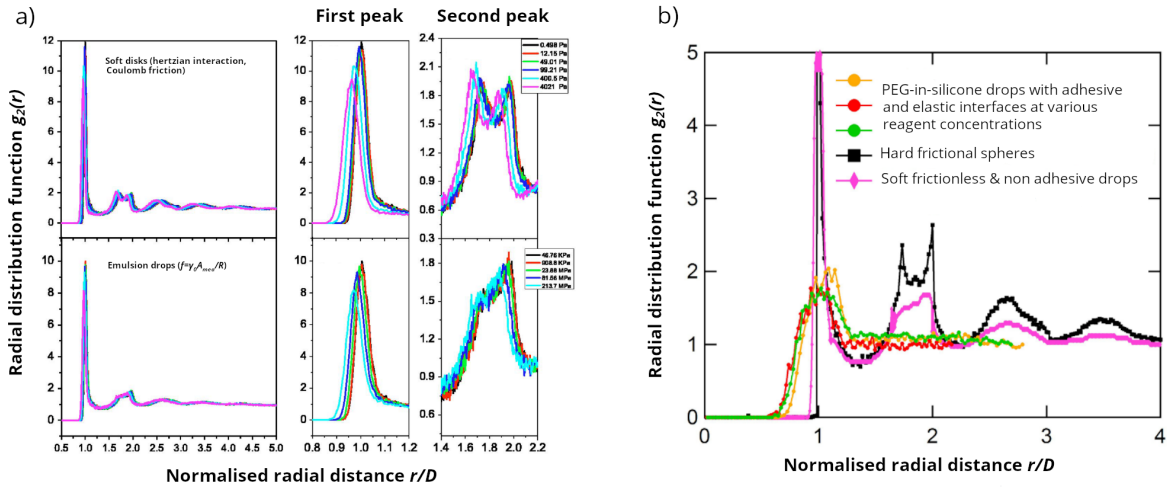


Figure 3.10: a) Radial distribution function for soft frictional spheres and emulsions. First peak height and second peak splitting varies with the considered interaction law. Figure from [49]. The different line colors from black to pink represent the radial distribution functions of the same packings for increasing osmotic pressure. b) Pair correlation function comparison for hard frictional spheres, soft, frictionless, non-adhesive drops, and emulsion drops with adhesive and elastic skin. Further modification of the contact interaction continues to alter the pair-correlation function. Figure from [50].

Topological properties of foams

In terms of granular matter, bubbles behave as soft frictionless grains. As there is no deformation at jamming transition, the isostatic contact number does not depend on the interaction law. Foams therefore have an isostatic contact number $Z_c = 2d$ [89, 37] where d is the dimension of the packing. As excess packing fraction increases, more bubbles deform and are brought in contact, increasing the average contact number. The excess contact number $\Delta Z = Z - Z_c$ has been shown to scale as [38, 62, 90, 2]

$$\Delta Z \sim \Delta\phi_g^{1/2} \quad (3.10)$$

This scaling is believed to hold regardless of the bubble size distribution.

Recently, Winkelmann *et al.* [15] proposed compelling evidence that such scaling behaviour may not hold in certain cases. Using numerical simulations with PLAT software [91, 92], they simulated realistic 2D foams under the geometrical constraint of Plateau laws, and found a linear scaling $\Delta Z \sim \Delta\phi_g$. Rather than simulating foams by focusing on bubble interfaces, PLAT works by adjusting the positions of Plateau vertices so as to satisfy curvature at the interface between two bubbles of different pressures and liquid film curvature at Plateau borders. PLAT can simulate with good accuracy wet foams with zero contact angles between liquid interfaces. Surface Evolver, on the other hand, can not simulate zero contact angles because of its finite element framework, and requires finite contact angles, an issue with consequences that still need to be examined. Likewise, the experimental evidence of the square-root scaling [38] is challenged by noting that gas fraction is accessed experimentally by measuring the fraction of area occupied by gas bubbles, with all associated projection problems, as shown in Fig. 3.12a-b. While this radical change in point of view may have consequences in 3D foams, it is still an area to be investigated in the future. Some authors [4, 3, 93] suggested that the observed deviation can be explained by the non-pairwise interactions between bubbles. This is discussed in detail in Section 3.2.

3.2 Interaction at the bubble scale

3.2.1 Pairwise interactions

As shown in Section 3.1.2, physical insights from granular matter can be brought to foams by considering the interactions at the bubble scale in the same way granular matter treats grain-scale interactions [34, 30, 42, 37]. A decent amount of literature tries to describe bubble-scale interactions as combinations of elastic, viscous and random external forces, with good predicting power. Among them, let us recall Durian interaction law [2] sketched in Fig. 3.11a, in which the equation of motion is resolved at bubble scale as

$$\vec{v}_i = \langle \vec{v}_j \rangle + \frac{F_0}{b} \sum_j \left(\frac{1}{|\vec{r}_i - \vec{r}_j|} - \frac{1}{R_i + R_j} \right) (\vec{r}_i - \vec{r}_j) + \frac{\vec{F}_i^a}{b} \quad (3.11)$$

where \vec{v}_j is the average velocity of all bubbles in contact with i , F_0 is set by surface tension, b the viscous drag force, and \vec{F}_i^a a random external force. This law predicts accurately the scaling of contact number $\Delta Z = \Delta\phi_g^{1/2}$, but fails to predict correctly the scaling of the shear modulus by giving a linear square-root scaling $G \sim \Delta\phi_g^{1/2} \sim \Delta Z$.

Another interaction model proposed by Katgert *et al.* [34] models interdrop interactions as pairwise forces with a combination of a spring and a dashpot (Fig. 3.11b), accounting for both elastic and viscous contributions. Despite its pairwise aspect, this model can probe the frequency-dependence of the elastic response to shear of foams and predicts a solid-to-liquid like transition, an important feature of foam rheology (see Section 3.1.2).

Finally, an important interaction law first derived by Princen [94] sketched in Fig. 3.11c is currently considered as the cornerstone interaction law in emulsion science. This interaction law considers the case of two drops of radii R_1 and R_2 . In the limit of small deformations (i.e. small variation in interfacial area), the pressure inside the drop is approximated to be constant while the applied stress translates in surface deformation only. The normal force between the drops is then given by the product of the average pressure difference $\langle \Delta P \rangle = \frac{P_1 + P_2}{2}$ and the overlap area

between the drops A

$$f = \langle \Delta P \rangle \cdot A = A\gamma \frac{R_1 + R_2}{R_1 R_2} \quad (3.12)$$

where pressure and curvature are related through Young-Laplace equation. Because of its simplicity and its involvement of surface tension – the main driving force for shape and rheology in foams and emulsions – this interaction is widely used to determine interparticle forces and reconstruct force chain networks [35, 95, 96].

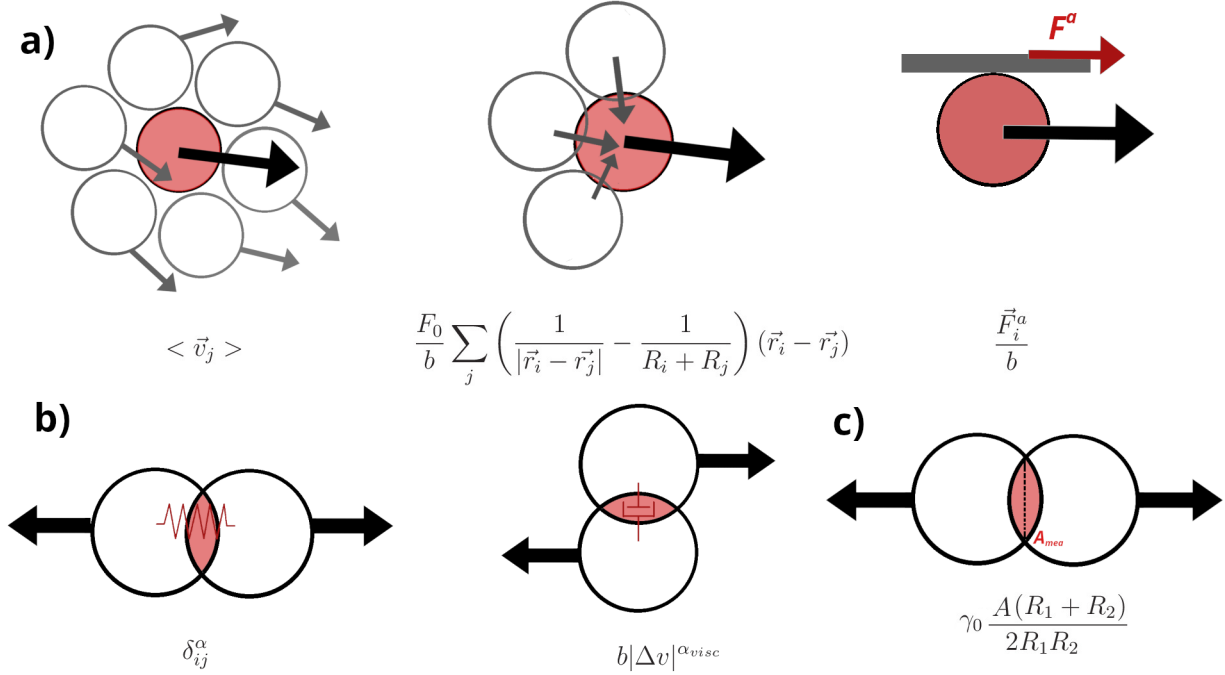


Figure 3.11: Illustrations of the force decomposition in different bubble interaction models. a) Contributions to drop velocity in the Bubble Model by Durian [2]. From left to right : average neighbour velocity, soft sphere repulsive potential damped by viscous friction, external shear force. b) Elastic and viscous forces by Katgert [34]. From left to right : elastic soft sphere potential, and viscous dissipation due to velocity gradients between neighbours. c) Empirical interaction force between two droplets described by Brujic [35]. Interaction amplitude comes from an ‘overlap’ parameter and the area of the flat contact zone.

3.2.2 N-body interactions

Despite their respective success, these pairwise interactions fail to consider non-pairwise effects coming from bubble deformations. Even for simple interactions such as connected springs [97], deformability renders interparticle interactions non pairwise-additive. The presence of neighbours can hinder deformation and make the particle appear stiffer : thus, energy associated to deformation is a function of both deformation amplitude and number of neighbours. Numerous models for particle deformation have been proposed [98, 99, 100, 101, 102, 103, 73, 3, 4], and can be classified in two categories : (1) modified two-body interaction laws and (2) intrinsically non-pairwise interactions.

Modified two-body interaction laws compute the force-deformation relation pairwise, using free parameters obtained from fitting numerical simulations [73, 3]. These free parameters will depend on coordination number Z and lattice geometry. They are generally extracted from simulations of

isotropic compression, and will fail when looking at anisotropic compression or shear deformation [72]. An example of such an interaction law given in [3, 73] reads as

$$\frac{f(\delta_{12})}{\gamma_0 R_0} = \begin{cases} \kappa(z)\alpha(z)\frac{((1+\delta_{12})^{-3}-1)^{\alpha(z)-1}}{(1+\delta_{12})^4} & \text{for } \delta_{12} < 0 \\ 0 & \text{for } \delta_{12} \geq 0. \end{cases} \quad (3.13)$$

where $\kappa(Z)$ and $\alpha(Z)$ are fitting parameters depending on the coordination number Z , δ_{12} is defined as the overlap parameter $\delta_{12} = \frac{|\vec{r}_1 - \vec{r}_2|}{(R_1 + R_2)} - 1$ between two spherical particles of radii and centre positions (R_1, \vec{r}_1) and (R_2, \vec{r}_2) , respectively. This simplified interaction still considers bubbles as soft spheres, but its modified interaction law allows for a more accurate description of foam mechanics.

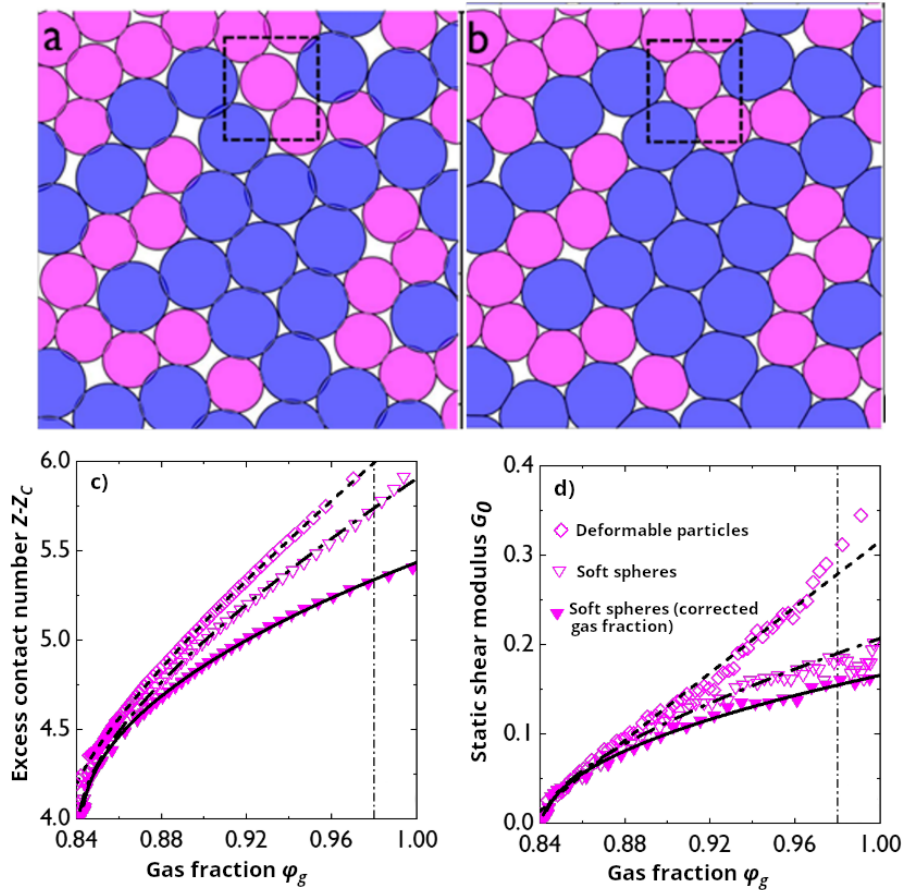


Figure 3.12: a) Soft frictionless jammed particles with overlapping areas, misrepresenting total gas fraction. b) Same jammed particles interacting through Boromand deformable particle model [98]. c)-d) Variation of excess contact number and static shear ratio with gas fraction. Diamonds represent deformable particles, while open triangles represent rigid particles interacting through a soft-sphere potential. Full triangles represent the same soft particles, but where gas fraction has been corrected to account for the overlap between the particles in a true packing fraction point of view. Figures from [66].

Intrinsically non-pairwise interaction laws, on the other hand, explicitly affect an energy term to the deformation. The effect of deformability is accounted in the interaction itself, rather than extrapolated from an approximated rigid body interaction. Deformable particle model by Boromand *et al.* [98, 66] is a good illustration of the issues raised by not accounting for bubble deformability, as

shown in Fig. 3.12)a-b : the overlap of soft particles modify the packing fraction ϕ_g upon compression, introducing an error in its measure. Additionally, deformation creates new contacts between bubbles distant from more than one diameter, a feature absent with soft particles. Similarly, with particles overlap forbidden, contact number and shear modulus scaling with excess packing fraction changes significantly, with different regimes depending on the excess packing fraction. As shown in Fig. 3.12c-d, Boromand *et al.* [98, 66] found that a better scaling law is obtained as

$$\Delta Z \sim A_Z \Delta \phi_g^{1/2} + B_Z \Delta \phi_g \quad (3.14)$$

$$G \sim A_G \Delta \phi_g^{1/2} + B_G \Delta \phi_g \quad (3.15)$$

where A_Z, B_Z, A_G and B_G are fitting coefficients. This behaviour is obtained by representing bubbles as polygonal shapes, deformability coming from the degree of freedom on the angle between two successive edges.

The non-pairwise interaction laws presented above either rely on empirical laws with free parameters needing to be fitted with experimental results, or on *ad hoc* models that simplify the deformation of the shape without any connexion to the physical properties of the bubbles. Despite their predictive power, they must be used cautiously for they overlook physical details of bubbles interfaces. Among them, a first-principle interaction law proposed by Morse and Witten [4] stands out by its complete derivation of a many-body interaction starting from the well established Young-Laplace law with no free parameter. Having for long being overlooked for its mathematical complexity, it recently gained attention by being applied successfully to simple geometries encountered in foams [72]. I propose here a description of this model and its assumptions, as well as the first experimental verification of its validity for bubble-bubble interactions in a controlled geometry.

3.3 Morse-Witten interaction law

In their seminal paper of 1993, Morse and Witten [4] treated the case of emulsion drops slightly above the jamming transition. Their deformability is the source of emulsions behaviour in the wet limit ($\Delta \phi_g \rightarrow 0^+$). Furthermore, the interactions between bubbles and drops, are driven by the interfacial tension between their two phases. Morse and Witten's work on drop deformation can be readily transferred to bubbles and wet foams.

In the limit of small deformations and small pressure gradient between the top and the bottom of the drop, the shape of drops remains spherical. The radius of the undeformed drop is R_0 . Moreover, interfaces are taken to be at mechanical and thermodynamical equilibrium, where interfacial tension γ_0 is taken as constant and isotropic at every point of the interface. At equilibrium, drop shape is dictated by the well-established Young-Laplace law, relating the two principal curvature radii R_1 and R_2 of the interface to the pressure jump across it (see Fig. 3.13) :

$$\Delta P = P_{int} - P_{ext} = \gamma_0 \left(\frac{1}{R_1} + \frac{1}{R_2} \right) \quad (3.16)$$

Eq.(3.16) gives $\Delta P = 2 \frac{\gamma_0}{R}$ for a spherical interface $R_1 = R_2 = R$. This local equation holds at any point of the interface, localised by a solid angle coordinate Ω . Therefore, it can account for a local variation in pressure and radius $\delta P(\Omega)$ and $\delta R(\Omega)$, respectively. One may then write their local expression as

$$\begin{aligned} R(\Omega) &= R_0 + \delta R(\Omega) \\ P_i(\Omega) &= P_{i0} + \delta P_i(\Omega) \\ P_e(\Omega) &= P_{e0} + \delta P_e(\Omega) \end{aligned} \quad (3.17)$$

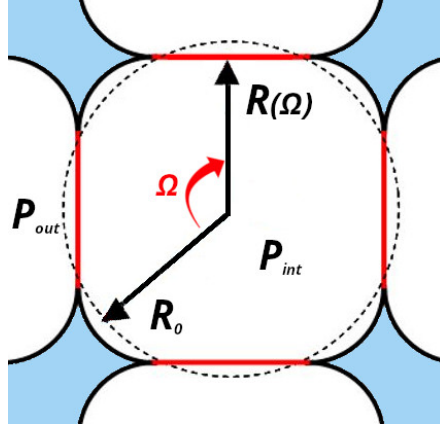


Figure 3.13: Scheme of a bubble of inner pressure P_{int} immersed in a liquid of pressure P_{ext} . In its undeformed shape, the bubble has a radius R_0 at any point of the surface. Under deformation, this radius changes at every point of the surface : radius at a specific point of the surface is localised by its solid angle coordinate Ω .

Inner pressure P_i is equivalent in the whole body, and is therefore uniform over the whole surface $\delta P_i(\Omega) = \delta P_{i0}$. The sum of local principal curvature C of the drop surface obeys the Young-Laplace equation

$$\gamma C(\Omega) = P_i - P_e(\Omega) \quad (3.18)$$

Expanding Eq.(3.18) to first order of radius variation $\delta R(\Omega)$ gives the equilibrium relation

$$-(\nabla^2 + 2)\delta R(\Omega) = \delta P_i - \delta P_e(\Omega) \quad (3.19)$$

where ∇^2 is the Laplacian operator on a unit sphere. Eq.(3.19) can be solved as follows : δP_i , $\delta P_e(\Omega)$ and $\delta R(\Omega)$ can be expressed using spherical harmonic functions Y_{lm} , which represent the different modes of deformation of the interface allowed by the spherical symmetry of the drop (see Fig. 3.14). As inner pressure is isotropic, δP_i only contributes to the isotropic $l = 0$ channel of deformation. Moreover, since the $l = 1$ channel corresponds to an unbalanced force associated to a net translational motion, the $l = 1$ component of $\delta P_e(\Omega)$ must vanish for mechanical equilibrium to be preserved.

The deformation of the droplet interface can be expressed through a Green function $G(\Omega, \Omega')$ that represents the deformation at a point Ω caused by a force applied at point Ω' . This function satisfies the equation

$$-(\nabla^2 + 2)G(\Omega, \Omega') = \sum_{l \geq 2, m} Y_{lm}^*(\Omega) Y_{lm}(\Omega') \quad (3.20)$$

where the summation is truncated to $l \geq 2$ because of the isotropic inner pressure and incompressibility conditions discussed above. A summation over spherical harmonic expansion gives a closed form of G [104]

$$G(\theta) = \frac{-1}{4\pi} \left\{ \frac{1}{2} + \frac{4}{3} \cos \theta + \cos \theta \ln [\sin^2(\theta/2)] \right\} \quad (3.21)$$

where θ is the angle between the point where deformation is considered and the point of force application.

Point-like forces are not usual contact interactions between neighbouring drops. For a more physical representation of contact zones, point-localised deformation is replaced by a flat circular contact section of radius r with an associated force $f = \pi r^2 \Pi_i$ centered at point Ω . This approximation holds for small deformations and forces, assuming $r \ll R_0$ and $f \ll \gamma_0 R_0$. In 2D,

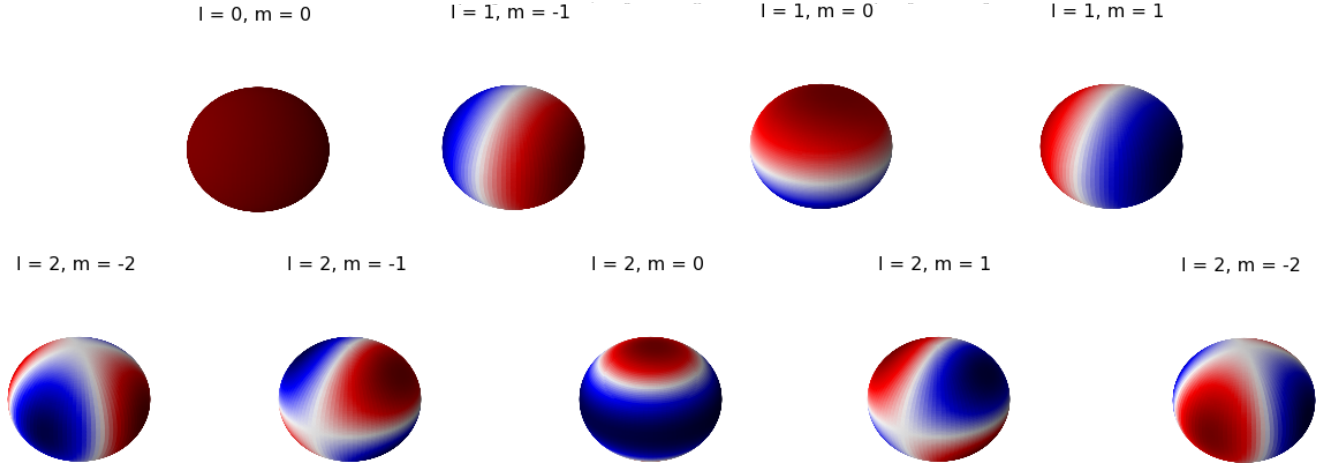


Figure 3.14: Visualisation of spherical harmonics as modes of deformation of the surface of a sphere. Blue areas represent zones of compression, while red are zones of dilation. The $l = 0$ channel corresponds to an isotropic dilation of the volume, forbidden by the volume conservation hypothesis. Higher harmonics are deformation modes of spatial frequency. Figures obtained using code found in scipython online user’s guide <https://scipython.com/book/chapter-8-scipy/examples/visualizing-the-spherical-harmonics>.

approximating contact areas with flat surfaces as sketched in Fig. 3.15b overestimate the contact surface, with a relative error that can be shown to be of order $\mathcal{O}\left(\frac{f}{\gamma_0 R_0}\right)^3$, so as to be negligible in the small force limit [105]. With these approximations, one is finally able to express the complete set force-deformation relations

$$\delta R_i = \frac{1}{24\pi} \left[5 + 6 \ln \left(\frac{f_i}{8\pi} \right) \right] f_i - \sum_{i \neq j} G(\theta_{ij}) f_j \quad (3.22)$$

where i denotes the force and deformation at the point of interest on the surface, and j lists all the forces applied at point different from i . Eq. (3.22) decomposes the radius variation at point i in two parts : one local contribution, coming from the force applied at point i , and a non-local contribution coming from the forces applied at other points j of the interface and whose deformation field propagates to i along the interface. The complete analytical derivation from variational principles for a drop compressed between two parallel plates found equivalent results in the small deformation limit [3].

Surface Evolver simulations in geometries with more neighbours ($n \geq 2$) indicate that relative excess energy per facet increases with the number of facets n , as shown in Fig. 3.15c. Non-pairwise effects thus increases with contact number Z [3] : the force required to achieve the same deformation increases with the number of neighbours, because of the deformation hindering.

Despite its complex mathematical background, the application of the Morse-Witten force-deformation relation is straightforward in any arbitrary geometry. When tested in situations with different coordination numbers, it has been shown to predict more accurately macroscopic stress response to shear and uniaxial strains than two-body interaction law, and without any free fitting parameter [72]. Its predictions also agree with Surface Evolver simulations on stress prediction and on the increasing effect of many-body interactions with increasing contact number Z [3, 72]. While its predictions have been confronted successfully to numerical simulations, the Morse-Witten law remains yet to be tested experimentally for multi-body interactions. We propose here its first experimental verification in a simple, controlled geometry and confront it with Surface Evolver simulations.

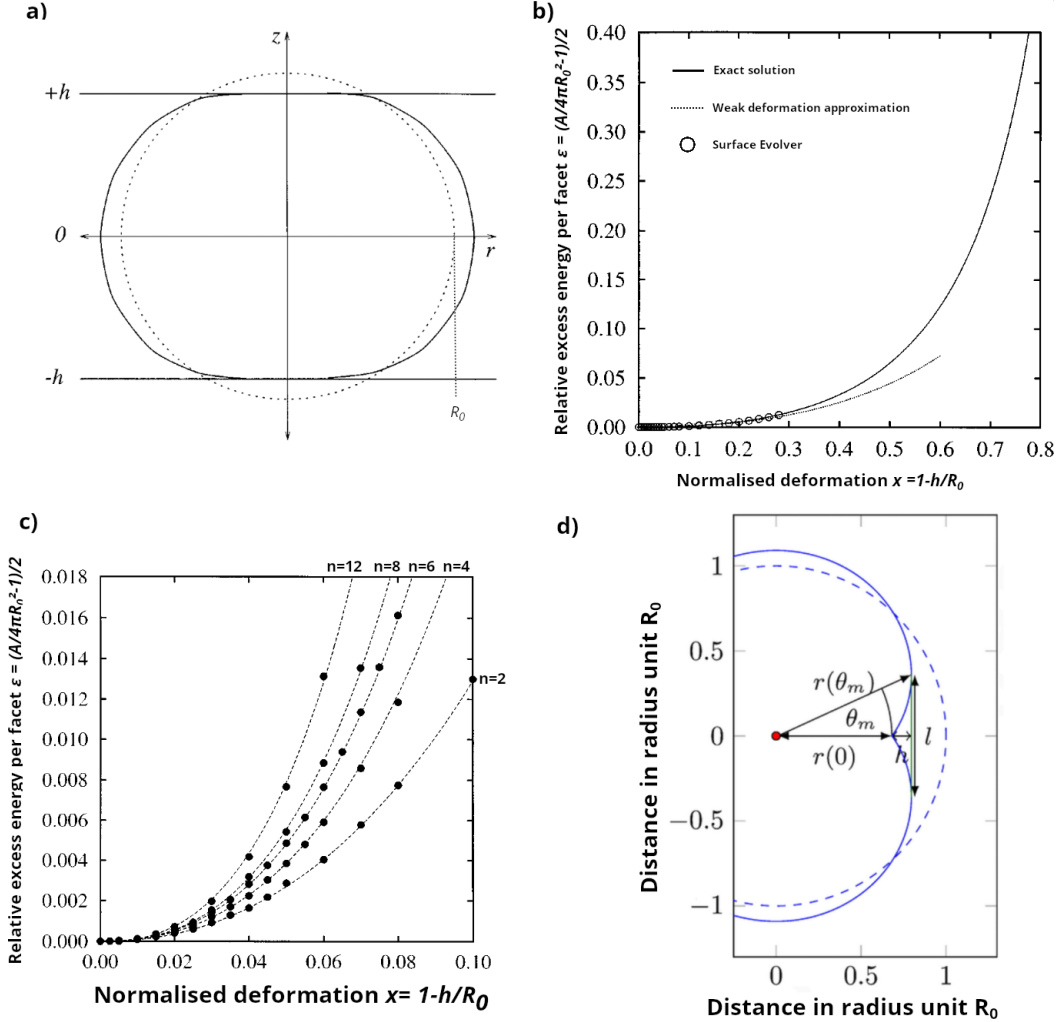


Figure 3.15: a) Scheme representation of the compressed 2D drop and the relevant quantities. The drop, of undeformed radius R_0 , is compressed between two parallel plates distant from $2h$. Figure adapted from [3]. b) Variation of relative excess energy per facet ϵ with normalised compression $x = 1 - h/R_0$ for the compressed drop in a. c) Excess energy per facet with isotropic compression. Energy per facet increases with the number of facets n . d) Point-like compression is approximated with a flat cap centered at the point of force application. The volume error is of order $\mathcal{O}(l^3)$ for 3D drops [105].

3.4 Experimental verification of Morse-Witten interaction law

Morse and Witten [4] proposed a description of the deformation of a simple drop subjected to a point-like force, taking effectively in account the deformation of a single drop in their interaction law. As far as we know, the validity of this interaction has been tested experimentally for single drops [106, 107, 108], but remains to be investigated for interactions between drops. We thus propose in this Section an experimental verification of the Morse-Witten interaction law, and delimit its range of validity. Experimental setup, acquisition methods and assumptions are described in Sections 3.4.1, 3.4.2 and 3.4.3, respectively. In Section 3.4.4, we describe how Morse-Witten theory is applied to our experimental system in its particular system, and how experimental results are compared with its predictions. In Section 2.2.1, we describe how our system is simulated in Surface Evolver and how we ensure that numerical results converge to physically sound solutions. We finally present our experimental, numerical and theoretical results in Section 3.4.5, and draw conclusions

about Morse-Witten law validity and its potential applications in Section 3.4.6.

3.4.1 Experimental setup

A complete description of the experimental setup can be found in Chapter 2. We recall here briefly its main aspects. We focus this study on a model system consisting of equal-volume bubbles organised in a capillary. We produce air bubbles in an aqueous SDS solution at 7 g/L by blowing air at constant pressure through a needle. In the quasi-static bubbling regime, the bubble radius is controlled by balance between interfacial tension and buoyancy, which gives a low bubble polydispersity. Bubbles are then trapped inside a square capillary of width W_C (Fig. 3.17c) where they form a bubble train. In this situation, each bubble is compressed in six directions, four being the capillary walls and two the upper and lower neighbours. The interactions between two bubbles, and between a bubble and a fully wetted wall are treated as equivalent regarding the deformation response to an applied force.

3.4.2 Bubble size acquisition

In the first step of the experiment, the capillary is put in horizontal position so that bubbles apply no force on their neighbours. Neglecting the impact of gravity on its position, the bubble center is assumed to stay at the center of the capillary, so that deformation coming from wall contact is the same in every direction. A complete determination of bubble deformation requires to determine its length L_B in the capillary direction. The length of every bubble is acquired with an optical camera, the capillary being illuminated from the back by a white screen with homogeneous lighting. We place the light source at a distant large enough so that bubble boundaries appear black from front. In this configuration, bubbles appear as bright ellipses surrounded by black borders (see Fig. 3.17). Due to optical effects, the contact zones between neighbouring bubbles appear as three bright spots, surrounded by dark areas. The actual border between two bubbles is the central bright spot [12].

To ensure monodispersity, we need to measure the volumes of the bubbles trapped inside the capillary. At the beginning of the experiment, we measure bubble lengths L_B and deduce their radii R_0 for a fully horizontal capillary ($\beta = 0^\circ$), using an interpolated polynomial relation obtained from Surface Evolver simulations and Morse-Witten theory (see Eq.(3.36)) for a drop constrained between four walls. A bubble of radius R_0 trapped inside a capillary of width W_C exhibits an aspect ratio λ that can be fitted by the third order polynomial

$$\lambda = \frac{L_B}{W_C} \approx -19.6 \left(\frac{W_C}{2R_0} \right)^3 + 60 \left(\frac{W_C}{2R_0} \right)^2 - 62.6 \left(\frac{W_C}{2R_0} \right) + 23.2 \quad (3.23)$$

Eq.(3.23) is numerically inverted to yield undeformed bubble radius R_0 . We resume experiments if polydispersity index $PI = \left(\frac{\langle R_0^2 \rangle}{\langle R_0 \rangle^2} - 1 \right)^{1/2} < 5\%$.

3.4.3 Bubble-bubble deformation

We tilt incrementally the capillary, which causes the bubbles at the bottom to exert a force on their upper neighbour because of buoyancy. Bubbles are increasingly compressed along the capillary, because of the accumulated buoyancy force (see Fig. 3.17a). The net force along the axis of the capillary exerted by one bubble is computed as $f = \Delta\rho g \frac{4\pi}{3} R_0^3 \sin(\beta)$ where β is the tilting angle

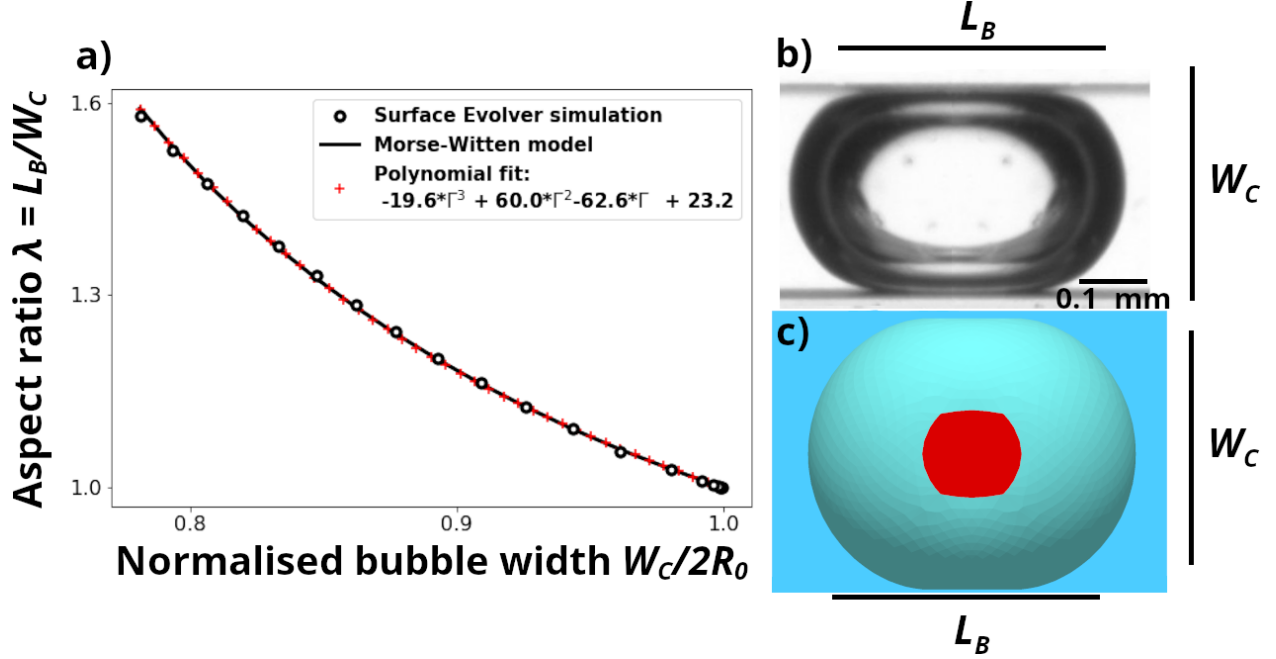


Figure 3.16: a) Aspect ratio for a single bubble trapped inside a square capillary. The polynomial fit is used to deduce the undeformed radius of the bubble from its aspect in the capillary. b) Side view of a single bubble trapped inside a capillary and c) its numerical counterpart.

between the capillary and the vertical axis (Fig. 3.17a). The total force exerted on the n -th bubble in the bubble train by all its lower neighbours is

$$f_B(n) = (n - 1)\Delta\rho g \frac{4\pi}{3} R_0^3 \sin(\beta) \quad (3.24)$$

counting from the lowest bubble. We calculate the overall force $f(n)$ exerted on the n -th bubble as the average of the force exerted on its bottom and top contact

$$f(n) = \frac{1}{2} (f_B(n) + f_B(n + 1)) \quad (3.25)$$

If $f_B(n) - f_B(n+1) \ll f_B(n)$, Eq.(3.25) can be approximated by $f(n) = f_B(n)$. This approximation is valid in the low Bond number limit $Bo = \frac{\Delta\rho g R_0^2}{\gamma_0} < 1$, comparing the energy coming from gravitation and interfacial tension. In this limit, the deformation of the bubble under the influence of gravity can be neglected with comparison with interfacial tension, and the interface can be approximated as being driven by interfacial tension only. We give a more comprehensive derivation accounting for large Bond numbers in Section 3.5. Bubble-wall forces f_w , on the other hand, are not directly accessible.

3.4.4 Morse-Witten application to cubic geometry

In the limit of low Bond number, all bubbles and capillary walls exert equal forces F_B and F_C , respectively. For simplicity, we use normalised quantities $f_B = F_B/\gamma_0 R_0$ and $f_C = F_C/\gamma_0 R_0$. The small force hypothesis made by Morse and Witten [4] and detailed in Section 3.3 then becomes $f_B < 1$ and $f_C < 1$. We define the associated normalised deformations x_B and x_C of the bubble its confined geometry shown in Fig. 3.17c

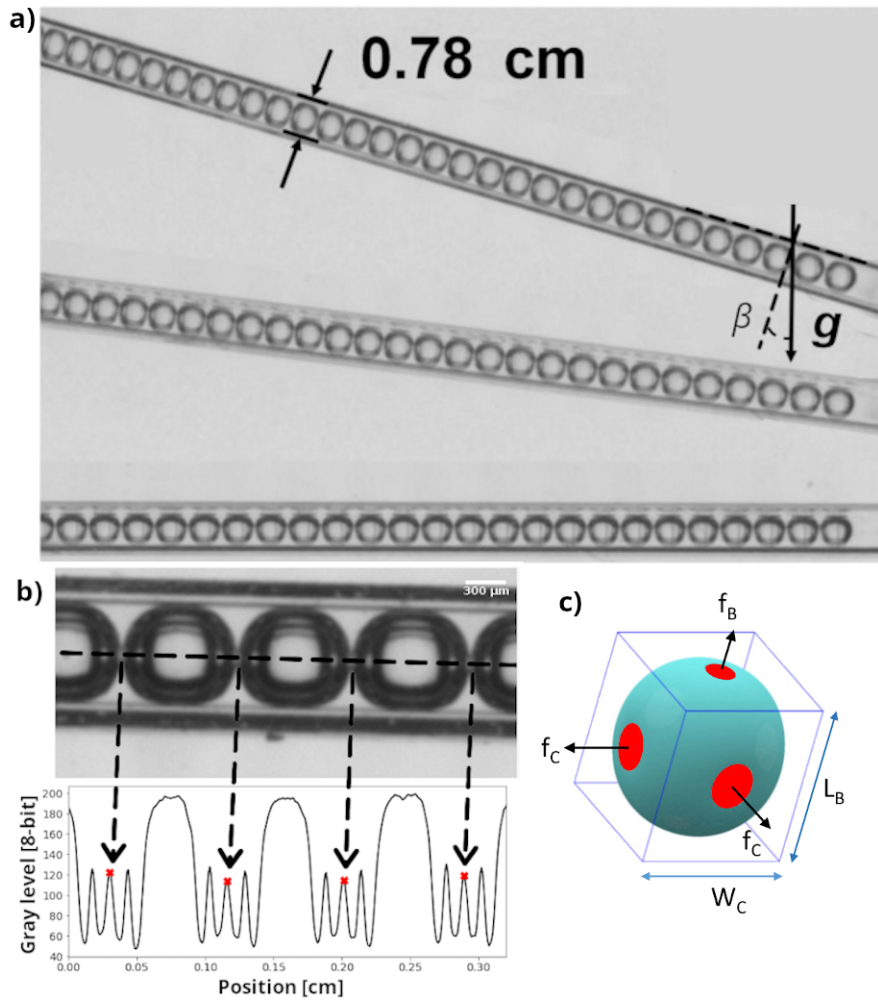


Figure 3.17: a) Square capillary filled with a train of monodisperse air bubbles. The increase of the tilting angle β progressively increases the buoyancy force exerted on upper bubbles, causing their compression. b) Bubble boundary detection using gray level peaks detection at the interface. c) Scheme representation of the bubble width W_C and length L_B , with bubble-bubble force f_B and bubble-wall force f_C .

$$x_B = \frac{L_B}{2R_0} - 1 \quad (3.26)$$

$$x_C = \frac{W_C}{2R_0} - 1. \quad (3.27)$$

Considering the geometry of the compressed bubbles (see Fig. 3.17.c), Eq. (3.22) simplifies to

$$x_B = \frac{1}{24\pi} \left[5 + 6 \ln \left(\frac{f_B}{8\pi} \right) \right] f_B - 4G(\pi/2)f_C - G(\pi)f_B \quad (3.28)$$

$$= \frac{1}{4\pi} \ln \left(\frac{f_B}{8\pi} \right) f_B + \frac{1}{2\pi} f_C \quad (3.29)$$

$$x_C = \frac{1}{24\pi} \left[5 + 6 \ln \left(\frac{f_C}{8\pi} \right) \right] f_C - 2G(\pi/2)f_C - G(\pi)f_C - 2G(\pi/2)f_B \quad (3.30)$$

$$= \frac{1}{4\pi} \ln \left(\frac{f_C}{8\pi} e \right) f_C + \frac{1}{4\pi} f_B \quad (3.31)$$

where we used the fact that Eq. (3.21) for $\theta = \pi/2$ and $\theta = \pi$ simplifies to

$$G(\pi/2) = -\frac{1}{8\pi}, \quad (3.32)$$

$$G(\pi) = \frac{5}{24\pi}.$$

As the force f_C exerted by capillary walls is inaccessible experimentally, it is convenient to express it as a function of physically accessible quantities. We achieve this through the special Lambert function W , defined as branches of the inverse relation of the function of xe^x , such that $W_k(xe^x) = x$ for any integer k . This function is available in most mathematical software. In our implementation, W is computed using the Python library *scipy.special*. We restrict the investigation to the $k = -1$ branch, which has the physically correct asymptotic behaviour $x \sim f \ln(f)$ [105] for the Morse-Witten problem. We therefore obtain

$$f_C = \frac{4\pi x_C - f_B}{W_{-1} \left(\frac{(4\pi x_C - f_B)e}{8\pi} \right)} \quad (3.33)$$

Inserting Eq.(3.33) in (3.29) yields an expression for x_B

$$x_B = \frac{1}{4\pi} \ln \left(\frac{f_B}{8\pi} \right) f_B + \frac{1}{2\pi} \frac{4\pi x_C - f_B}{W_{-1} \left(\frac{(4\pi x_C - f_B)e}{8\pi} \right)} \quad (3.34)$$

where x_B is expressed as a function of the bubble-bubble interaction force and the capillary confinement x_C is taken as a fixed parameter. We further develop Eq. (3.34) to express the length of a bubble only compressed by the capillary as a function of capillary width W_C , used to determine R_0 at zero tilting angle (see Section 3.4.2) :

$$\frac{L_B}{2R_0} = 1 + \frac{1}{4\pi} \ln \left(\frac{f_B}{8\pi} \right) f_B + \frac{1}{2\pi} \frac{4\pi \frac{W_C}{2R_0} - 4\pi - f_B}{W_{-1} \left(\frac{e}{2} \left(\frac{W_C}{2R_0} - 1 \right) - \frac{e}{8\pi} f_B \right)} \quad (3.35)$$

$$\frac{L_B}{2R_0} (f_b \rightarrow 0) = 1 + 2 \frac{\frac{W_C}{2R_0} - 1}{W_{-1} \left(\frac{e}{2} \left(\frac{W_C}{2R_0} - 1 \right) \right)} \quad (3.36)$$

3.4.5 Results

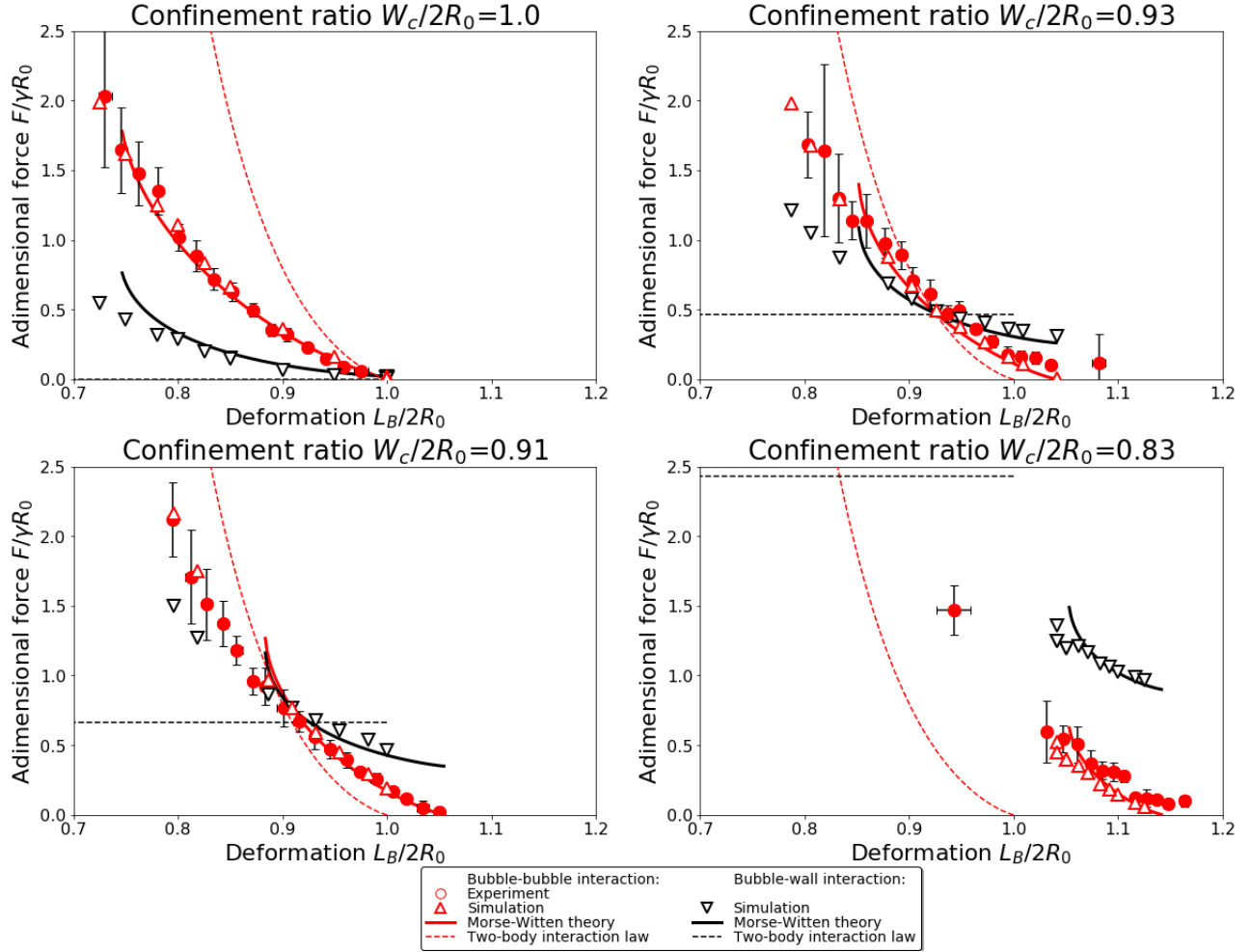


Figure 3.18: Experimental results, simulations and model predictions for four different confinement ratios $W_C/2R_0$. The normalised bubble-bubble and bubble-wall contact forces are plotted versus the normalised bubble length along the capillary axis. The experimental data are averaged of data obtained for different inclination angles of the capillary β ranging from 0° to 30° and for different Bond numbers in the range of $0.044 < Bo < 0.087$. Bottom-right graph ($W_C/2R_0 = 0.83$) is the limit case for the small force hypothesis $f < 1$ to remain valid. Experimental and numerical results corroborate the Morse-Witten theory in the regime where its approximations are valid, strongly differing from the two-body approximation from Lacasse *et al.* [3].

We first discuss the predictions of the effective two-body interaction model (Eq.(3.13)), of the model based on Morse-Witten theory (Section 3.3) and of the Surface Evolver simulations (Section 2.2.1). We assume in each case that gravity-induced pressure gradients in the continuous phase are negligible on the scale of a bubble ($Bo \rightarrow 0$) - which will be shown later to be a reasonable approximation within the range of investigated experimental parameters. Since the Surface Evolver simulations rely on the numerical solution of the Laplace equation without additional approximations, we use them as a reference to check the analytical models.

Figure 3.18 shows how the normalised bubble-bubble (red) and bubble-wall forces (black) $F/\gamma_0 R_0$ depend on the normalised bubble length $L_B/2R_0$ for confinement ratios in the range $0.83 \leq W_C/2R_0 \leq 1$. Morse-Witten theory is in good agreement with the Surface Evolver simula-

tions all over the predicted range of validity ($F/\gamma_0 R_0 < 1$). For a confinement ratio of 1, for which the undeformed bubble fits exactly into the capillary, all contact forces go to zero when the bubbles stop touching their neighbours at $L_B/2R_0 = 1$, as expected. As the bubble train is compressed along the axis of the capillary, bubble-bubble forces build up and, at the same time, bubble-wall forces appear since the bubbles expand laterally and push on the wall. This latter effect is ignored by the two-body interaction model which also over-predicts the bubble-bubble forces. For confinement ratios smaller than 1, the undeformed bubble radius R_0 is too large for spherical bubbles to fit into the capillary. They therefore exert wall forces even if the bubble-bubble deformation x_B is zero. This effect is shown clearly by the Surface Evolver simulations and predicted quantitatively by the Morse-Witten theory - in contrast to the two-body interaction model.

For the confinement ratios 0.91 and 0.93, there is a specific value of the normalised bubble length $L_B/2R_0$ where the bubble-bubble and the bubble-wall forces coincide. This is the only case where the two-body interaction model provides the correct prediction. This is indeed expected, since the free parameters of the two-body model were fitted to Surface Evolver simulations of bubbles subjected to *isotropic* compression [3]. For the smallest investigated confinement ratio of 0.83, even the smallest bubble-wall contact forces are already close to 1. Since this is the strongest confinement that can be handled by the Morse-Witten theory, one sees a rapid divergence between simulation and theory. Smaller confinement ratios are therefore not investigated in the following in order to focus on experiments which satisfy the approximations made in the theory.

3.4.6 Discussion and outlook

Experimental results, numerical simulations and Morse-Witten show excellent agreement for the different confinement ratios in the limit of small force $F/\gamma_0 R_0 \ll 1$, as expected by the starting hypothesis detailed in Section 3.3. Effective two-body interaction, on the other hand, strongly differs our experimental findings. As forces are independent in the pairwise models, compression of the bubble along the capillary axis does not change the force exerted by the walls when only pairwise interactions are considered. Effective two-body interaction law still predicts correctly the deformation when F_B and F_C are equal : this is because the fitting parameters are extracted from numerical simulations of bubbles isotropically compressed, hence their correct prediction.

Our experiments, analytical theory and Surface Evolver simulations therefore consistently show that the interactions of bubbles are non-pairwise : the mechanical response of a bubble to a contact force must be expressed as a function of the deformation at all of its other contacts, and cannot be captured by independent forces alone. This has a direct consequence on bubble stiffness, i.e. its resistance to an applied force, which increases with its number of contact. This is illustrated in Fig. 3.19, which shows that the force required for an isotropic compression of a bubble increases non-linearly with the number of contact facets n . A new contact facet makes the bubble stiffer and more resistant to deformation, but also increases its rigidity at the other contact points. This property, coming solely from the deformability of the bubble, has consequences that remain to be investigated, particularly in the deeply jammed state where the average contact number increases with excess packing fraction (see Section 3.1.2).

The simplicity of our experimental setup makes it a good candidate for testing interaction laws in other situations, such as elastic beads or bubbles with more complex interfaces. A natural extension of our 1D experiment would focus on quasi-2D foams constrained between two parallel plates such as Hele-Shaw cells, provided the distance between the two plates is large enough for the MW theory to be valid. Application of MW interaction to simulated 2D foams already allowed

to implement realistic interparticle forces, paving the way to a physically relevant force network reconstruction [109] and its extension to 3D foams. An experimental verification of MW validity in 2D and 3D systems would still be required before yielding any conclusive results.

As Morse-Witten interaction is valid in the small deformation limit, it is the most accurate close to the unjamming transition, where non-affine displacements become more important [34]. Further analysis of non-affine displacements could yield insightful informations about shear behaviour close to jamming, particularly shear and bulk moduli scaling [42].

Analysis could use previously existing data from experiments on weakly compressed emulsions, and compare quantitatively discrepancies between different interactions laws. The substantial gain of computational power required compared to classical Surface Evolver simulations would come with the benefit of an explicit impact of non-pairwise interactions on foams jamming, flowing and yielding. Using force network tools would also bridge the gap with more classical granular matter, where contact and force chain networks have for long been used to predict mechanical properties of grain packings subjected to external stresses [110, 111, 112, 113]. Furthermore, the reconstructed force networks would have to be compared to networks reconstructed using pairwise interactions [114, 35, 61].

Our capillary setup could be used aiming in another direction : knowing bubble volumes and their interaction laws, a progressive tilt of the capillary allows for a measure of their interfacial tension by comparing their deformation to the applied force, but requires sufficient foam stability. This measuring device would be complementary to tensiometry techniques such as pendant and oscillating drop. Finally, simulations based on the Morse-Witten interaction model could also be used for bubbles and drops confined in parallelepipedic geometries, a scenario relevant in microfluidic applications.

3.5 Beyond low Bond number approximation

In Section 3.4.4, we simplified our equations using the hypothesis that pressure variation at bubble scale would not affect significantly their shape. A direct consequence is its requirement of equal upper and lower neighbour forces, a constraint incompatible with the incrementally increasing buoyancy force. A more rigorous approach thus needs to consider hydrostatic pressure variation. We now generalise our study to account for this pressure gradient, and check the conditions under which our previous approximation remains valid.

3.5.1 Gravitational Morse-Witten equations

As shown in Fig. 3.20, in the same geometry as in Section 3.4.4, tilted by an angle β to the direction of gravity, the bubble is compressed in six directions. As two side walls of the capillary remain vertical all throughout the tilting, their forces are equal by symmetry. This reduces the number of independent forces, that we groupe in bubble-bubble forces (f_{Bb}, f_{Bt}) and bubble-wall forces (f_{Cb}, f_{Ct}, f_{Cv}), where b, t and v stand for top, bottom and vertical, respectively. The associated deformations are written (x_{Bb}, x_{Bt}) and (x_{Cb}, x_{Ct}, x_{Cv}), respectively. In this framework, normalised bubble length and confinement ratios are given by

$$\frac{L_B}{2R_0} = 1 + \frac{x_{Bt} + x_{Bb}}{2} \quad (3.37)$$

$$\frac{W_C}{2R_0} = 1 + x_{Cv} = 1 + \frac{(x_{Ct} + x_{Cb})}{2} \quad (3.38)$$

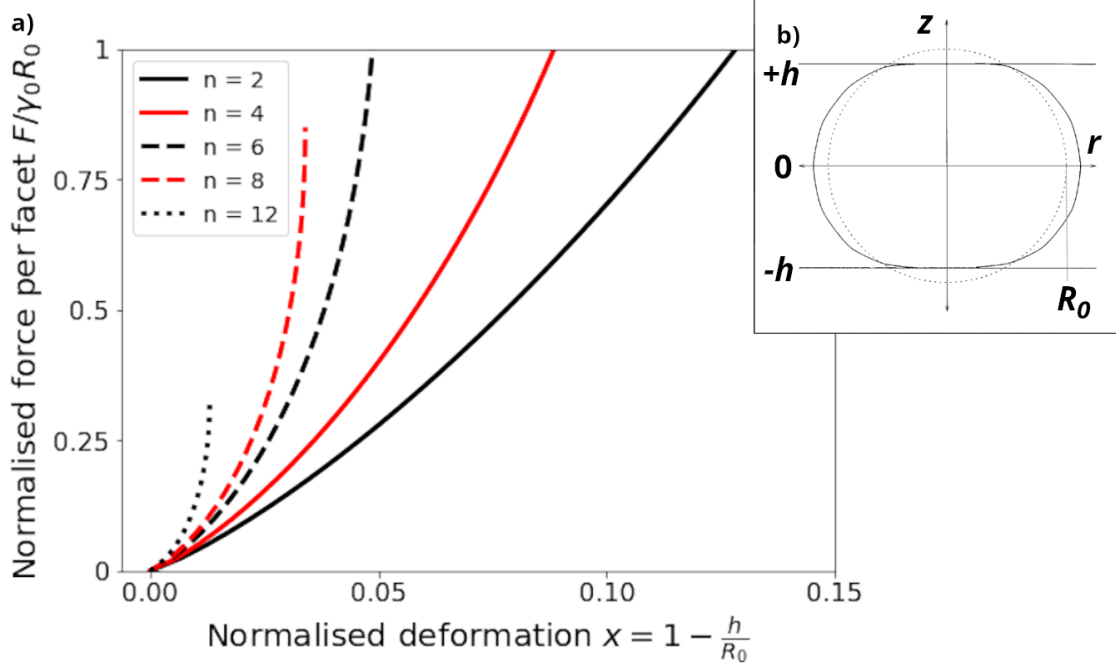


Figure 3.19: a) Force-deformation relation for different number of facets n , as predicted by Morse-Witten equation (Eq. (3.22)). Compared to Fig. 3.15c, this prediction does not rely on the Lacasse deformation model, but on the Morse-Witten model and its underlying assumptions. Geometries are parallel planes ($n = 2$), tetrahedron ($n = 4$), simple cubic ($n = 6$), body-centered cubic ($n = 8$) and face-centered cubic ($n = 12$). b) Scheme of a drop deformation between two parallel planes ($n = 2$). The normalised deformation is computed using the distance between bubble center and contact point h . Figure from [3].

Mechanical equilibrium requires these six forces to compensate the buoyancy force acting on the bubble. The latter is due to the bubble volume $V_0 = \frac{4\pi}{3}R_0^3$, and therefore reads as $f_{buoy} = \frac{4\pi}{3}\Delta\rho g R_0^3$. A normalisation by the unit interfacial force $\gamma_0 R_0$ allows to rewrite it as $f_{buoy}/\gamma_0 R_0 = \frac{4\pi\Delta\rho g R_0^2}{3\gamma_0} = \frac{4\pi}{3}Bo$ where $Bo = \frac{\Delta\rho g R_0^2}{\gamma_0}$ is the Bond number of the bubble, evaluating the competition between capillary and gravitational energies. From geometrical considerations, we can relate the upper and lower bubble-bubble and bubble-wall forces through

$$f_{Ct} - f_{Cb} = \frac{4\pi}{3}Bo \cos \beta \quad (3.39)$$

$$f_{Bt} - f_{Bb} = \frac{4\pi}{3}Bo \sin \beta \quad (3.40)$$

Eq. (3.22) finally relates deformations through the applied forces. Considering the geometry of

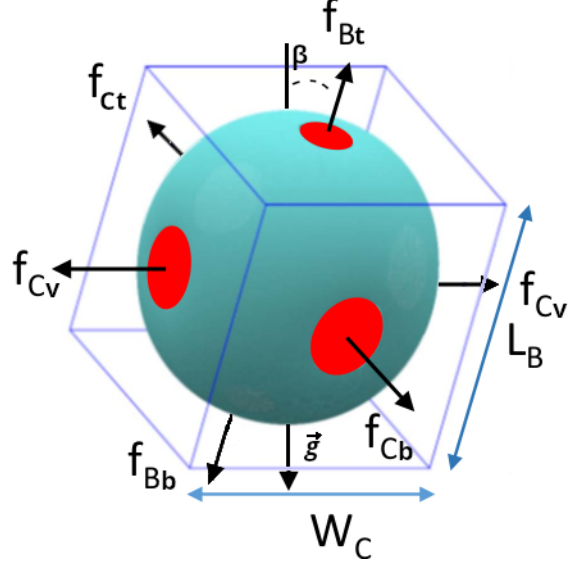


Figure 3.20: Scheme of a bubble trapped inside a capillary, considering asymmetries induced by gravity. The capillary axis is tilted by an angle β from gravity direction \vec{g} .

the problem, this gives rise to the following system of equations

$$x_{Bt} = \frac{1}{4\pi} \ln \left(\frac{f_{Bt}}{\Lambda} \right) f_{Bt} - G \left(\frac{\pi}{2} \right) (2f_{Cv} + f_{Ct} + f_{Cb}) - G(\pi) f_{Bb} \quad (3.41)$$

$$x_{Bb} = \frac{1}{4\pi} \ln \left(\frac{f_{Bb}}{\Lambda} \right) f_{Bb} - G \left(\frac{\pi}{2} \right) (2f_{Cv} + f_{Ct} + f_{Cb}) - G(\pi) f_{Bt} \quad (3.42)$$

$$x_{Cv} = \frac{1}{4\pi} \ln \left(\frac{f_{Cv}}{\Lambda} \right) f_{Cv} - G \left(\frac{\pi}{2} \right) (f_{Ct} + f_{Cb} + f_{Bt} + f_{Bb}) - G(\pi) f_{Cv} \quad (3.43)$$

$$x_{Ct} = \frac{1}{4\pi} \ln \left(\frac{f_{Ct}}{\Lambda} \right) f_{Ct} - G \left(\frac{\pi}{2} \right) (2f_{Cv} + f_{Bt} + f_{Bb}) - G(\pi) f_{Cb} \quad (3.44)$$

$$x_{Cb} = \frac{1}{4\pi} \ln \left(\frac{f_{Cb}}{\Lambda} \right) f_{Cb} - G \left(\frac{\pi}{2} \right) (2f_{Cv} + f_{Bt} + f_{Bb}) - G(\pi) f_{Ct} \quad (3.45)$$

where the constant $\Lambda = 8\pi e^{-5/6}$ was introduced for the sake of readability. In this framework, the reduced bubble length $L_B/2R_0$ can be deduced by combining Eqs.(3.37), (3.41) and (3.42).

$$x_{Bt} + x_{Bb} = 2 \left(\frac{L_B}{2R_0} - 1 \right) = \frac{1}{4\pi} \ln \left(\frac{f_{Bt}}{\Lambda} \right) f_{Bt} + \frac{1}{4\pi} \ln \left(\frac{f_{Bb}}{\Lambda} \right) f_{Bb} + \frac{1}{4\pi} (2f_{Cv} + f_{Ct} + f_{Cb}) - \frac{5}{24\pi} (f_{Bb} + f_{Bt}) \quad (3.46)$$

$$\frac{L_B}{2R_0} = 1 + \frac{1}{8\pi} \ln \left(\frac{f_{Bt}}{\Lambda} \right) f_{Bt} + \frac{1}{8\pi} \ln \left(\frac{f_{Bb}}{\Lambda} \right) f_{Bb} + \frac{1}{8\pi} (2f_{Cv} + f_{Ct} + f_{Cb}) - \frac{5}{48\pi} (f_{Bb} + f_{Bt}) \quad (3.47)$$

3.5.2 Numerical resolution

The system of equations in Section 3.5.1 cannot be solved analytically. Nonetheless, we solve it by first simplifying it, using cautious considerations. First, as f_{Bb} and f_{Bt} can be accessed experimentally, we can simplify the system by defining the mean bubble-bubble force $f_{Bm} = \frac{f_{Bb} + f_{Bt}}{2}$.

Furthermore, realising that capillary width W_C is the same in every direction, one can write $x_{Ct} + x_{Cb} = 2x_{Cv}$, which yields

$$2x_{Cv} = x_{Ct} + x_{Cb} = f_{Cb} \left(\frac{1}{4\pi} \ln \left(\frac{f_{Cb}}{\Lambda} \right) - \frac{5}{24\pi} \right) + \frac{f_{Cv} + f_{Bm}}{2\pi} + \left(f_{Cb} + \frac{4\pi}{3} Bo \cos(\beta) \right) \left(\frac{1}{4\pi} \ln \left(\frac{f_{Cb} + \frac{4\pi}{3} Bo \cos(\beta)}{\Lambda} \right) - \frac{5}{24\pi} \right) \quad (3.48)$$

Combined with Eq. (3.44), one can write a new system of equations

$$x_{Cv} = \frac{f_{Cv}}{4\pi} \ln \left(\frac{f_{Cv}}{\Lambda} \right) + \frac{Bo \cos \beta}{6} + \frac{f_{Cb} + f_{Bm}}{4\pi} - \frac{5}{24\pi} f_{Cv} \quad (3.49)$$

$$x_{Ct} = \ln \left(\frac{f_{Cb} + \frac{4\pi}{3} Bo \cos \beta}{\Lambda} \right) \left(\frac{Bo \cos \beta}{3} + \frac{f_{Cb}}{4\pi} \right) + \frac{f_{Cv} + f_{Bm}}{4\pi} - \frac{5}{24\pi} f_{Cb} \quad (3.50)$$

$$2x_{Cv} - x_{Ct} = \frac{f_{Cb}}{4\pi} \ln \left(\frac{f_{Cb}}{\Lambda} \right) + \frac{f_{Cv} + f_{Bm}}{4\pi} - \frac{5}{24\pi} f_{Cb} - \frac{5}{18} Bo \cos(\beta) \quad (3.51)$$

This non-linear set of equations is solved numerically, using autocohrent loop as schematised in Fig. 3.21. At first, it is rewritten as a matrix product $\mathbf{A}\mathbf{F} = \mathbf{B}$ by splitting unknown quantities f_{Cv} , f_{Cb} and x_{Ct} in linear and logarithmic terms, with explicit expression as

$$\begin{pmatrix} \frac{1}{4\pi} \ln \left(\frac{f_{Cv}^{n-1}}{4} \right) - \frac{5}{24\pi} & \frac{1}{4\pi} & 0 \\ \frac{1}{4\pi} & \frac{1}{4\pi} \ln \left(\frac{f_{Cb}^{n-1} + \frac{4\pi}{3} Bo \cos(\beta)}{\Lambda} \right) - \frac{5}{24\pi} & -1 \\ \frac{1}{4\pi} & \frac{1}{4\pi} \ln \left(\frac{f_{Cb}^{n-1}}{\Lambda} \right) - \frac{5}{24\pi} & 1 \end{pmatrix} \begin{pmatrix} f_{Cv}^n \\ f_{Cb}^n \\ x_{Ct}^n \end{pmatrix} = \begin{pmatrix} x_{Cv} - \frac{Bo \cos(\beta)}{6} - \frac{f_{Bm}}{4\pi} \\ -\frac{f_{Bm}}{4\pi} - \frac{Bo \cos(\beta)}{3} \ln \left(\frac{3f_{Cb}^{n-1} + 4\pi Bo \cos(\beta)}{3\Lambda} \right) \\ 2x_{Cv} + \frac{5Bo \cos(\beta)}{18} - \frac{f_{Bm}}{4\pi} \end{pmatrix} \quad (3.52)$$

Inversion of the matrix product $\mathbf{F} = \mathbf{A}^{-1}\mathbf{B}$ yield values for the linear terms, superscripted with the indices n contained in \mathbf{F} . For any values different from the solution, the values computed differ from the logarithmic terms, superscripted with the indices $n - 1$. The terms of the n^{th} iteration can then be plugged back into matrices \mathbf{A} and \mathbf{B} before repeating matrix inversion. Successive results of this iterative operation should yield converging results with a decreasing relative difference $|f^n - f^{n-1}|/f^{n-1}$, provided that initial values f^0 are not too distant from final results. For this purpose, initial terms at the input are solutions of Eq. (3.34), valid of the low Bond number limit solved in previous section. This procedure is repeated until relative variation between two iterations becomes lower than an arbitrary threshold criterion ϵ . Final values are then checked by plugging them into Morse-Witten full equations.

3.5.3 Results and discussions

Fig. 3.22 shows the variation of average bubble-bubble force $f_{Bm} = (f_{Bb} + f_{Bt})/2$ with bubble deformation, for a fixed confinement ratio $W_C/2R_0$. The zero Bond number approximation is shown, along with its equivalent for $Bo = 0.08$ (the highest Bond number encountered in experiments Section 3.4), $Bo = 0.25$ and $Bo = 0.5$. The three graphs represent three different tilting angles, with $\beta = 0$ (corresponding to a fully horizontal capillary), $\beta = \pi/2$ (fully vertical) and $\beta = \pi/4$. To keep the physical meaning of the quantities computed, we show the average bubble-bubble force f_{Bm}

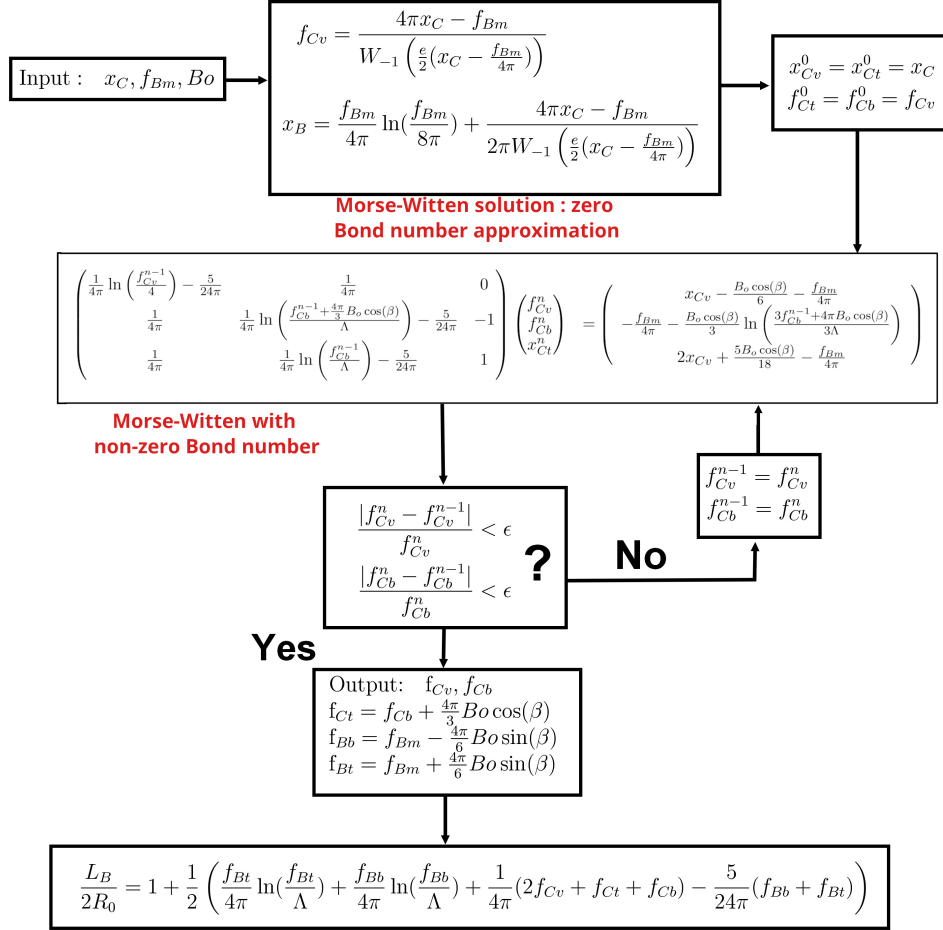


Figure 3.21: Scheme of the auto coherent algorithm used to solve Eqs.(3.51). The input values of the contact forces f_B and f_C are taken as the results of the exact solution of the Morse-Witten equations in the limit of zero Bond number. The convergence criterion ϵ is an arbitrary threshold, tuned according to the desired precision.

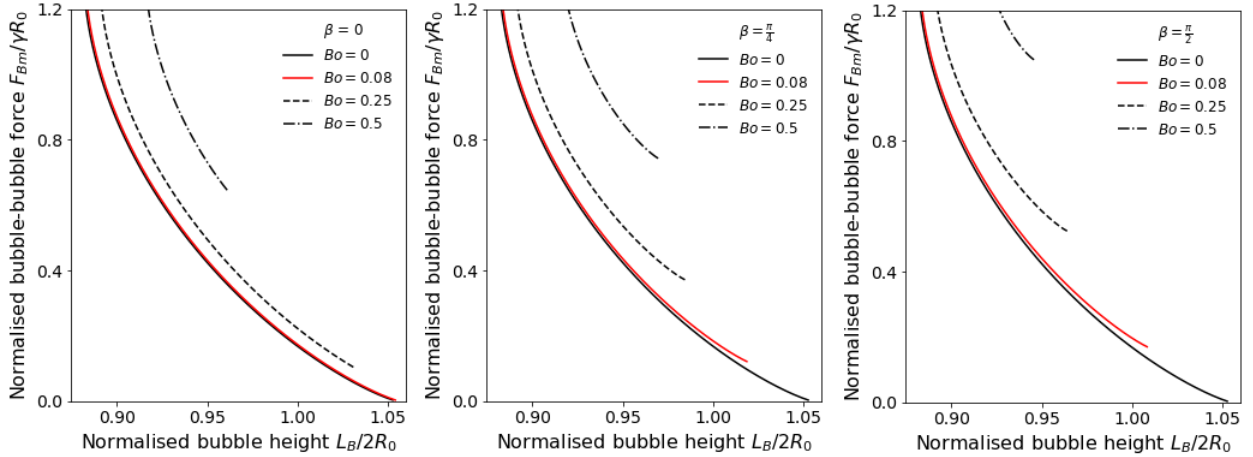


Figure 3.22: Inter-bubble contact forces (f_{Bm} in the equations) versus dimensionless bubble length along the axis of the tube predicted by Morse-Witten theory. The confinement ratio $W_C/2R_0$ is 0.91. The behavior in the absence of pressure gradients, analyzed in Section 3.4.4 is given by the black line which is identical on the three plots. The effect of a gravity induced pressure gradient in the liquid depends on the Bond number Bo and on the inclination of the bubble train with respect to gravity β , as indicated on the figures and discussed in Section 3.4.4.

only in the case where bottom force f_{Bb} is greater than zero. The inter-bubble force, defined here as the average of the top and the bottom contact force, cannot be arbitrarily small for $\beta > 0$. Even if the force at the bottom $f_{Bb} = 0$ because we consider the lower end of a bubble train, force at the top contact f_{Bt} is always required to maintain static equilibrium with pressure gradient, such that $f_{Bt} = \frac{4\pi}{3}Bo \cos(\beta)$.

As expected, for zero Bond number, the force-deformation relation is independent from the tilting angle. In the presence of gravity ($Bo \neq 0$), the bubbles are squeezed all over their gas-liquid interfaces by buoyancy forces acting in addition to the contact forces exerted by the neighbouring bubbles. If the capillary is held horizontally ($\beta = 0$), the bubbles are squeezed against the top capillary wall, inducing an extension on its length axis L_B . Hence, bubbles with larger Bond numbers require bigger forces for the same deformations. With increasing tilting angle, the force magnitude shift $\Delta f_B = \frac{4\pi}{3}Bo \sin(\beta)$ increases and so does the difference with zero Bond number. This is due to the increase of the local component of the deformation, as predicted by Eq. (3.22).

Finally, our calculations derived from Morse-Witten theory show that the effects of pressure gradients do not modify the relation between inter-bubble forces and bubble length L_B in the range of Bond numbers relevant for our experiments, for all inclination angles β . We therefore conclude that the impact of gravity on the pressure gradient can be neglected for Bond number $B_0 < 0.1$.

Chapter 4

Interfacial elasticity and its role in drop deformability

Rheology of bubble interfaces manifests simultaneously at the film, bubble and foam scale. Control of these properties offer a promising way of producing structures with new properties by tuning interfaces and letting drops self-assemble following their modified contact interactions [115]. Relation between individual and collective properties is far from straightforward, especially considering the complexity of contact interactions between viscoelastic interfaces. Briding this gap requires robust characterisation techniques of elastocapillary interfaces, in a framework transferable to more ordinary foams and emulsions. In Section 4.1, we introduce interfacial rheology and its applications to foams and emulsions. In Section 4.2, we review characterisation methods in pendant drop experiments. In Section 4.3, we propose a constitutive law for a spherical elastocapillary interface, giving a simplified access to area dilatational modulus. We complete it with finite element simulations, using Surface Evolver [9] software in Section 4.4. To our knowledge, it is the first time Surface Evolver is used for elastocapillary interfaces : we confront it to theoretical predictions of pendant capsule elastometry, and show its reliability in the tested configurations. In Section 4.5, we quantify the error introduced by our simplifying hypothesis. We propose experimental restrictions on drop and needle sizes under which deviation from ideal case remains small within the range of measurement errors.

4.1 Introduction

4.1.1 Complex fluid-fluid interfaces

Ordinary foams and emulsions consist of two immiscible phases, one hydrophilic and one hydrophobic. Interface between the two phases has an associated energy term F . At thermodynamical equilibrium, a variation dA in interfacial area modifies the surface energy by an amount dF

$$dF = \gamma dA, \quad (4.1)$$

where γ is the interfacial tension, the intensive thermodynamical quantity conjugated to change in area. γ thus has the dimension of a stress ($\text{N}\cdot\text{m}^{-1}$) or energy per area ($\text{J}\cdot\text{m}^{-2}$). Typical values range around $1 - 100 \text{ mN}\cdot\text{m}^{-1}$. A classic example is the water-air interfacial tension $\gamma_{w/a} = 72.8 \text{ mN}\cdot\text{m}^{-1}$ at 20°C . It varies with temperature and presence of chemicals. The interfacial tension of gas/liquid interfaces is commonly called surface tension.

Foams and emulsions are stabilised by adding amphiphilic molecules to one bulk phase. These compounds are made of hydrophobic parts and hydrophilic parts. For this reason, they anchor to the interface, where its antagonistic components float in their corresponding phases. The energy cost of a hydrophobic/surfactant/hydrophilic interface is lower than that of a simple hydrophobic/hydrophilic interface. By their intercession, they effectively lower the interfacial tension between the two phases. Because of their role as surface active agents, they are often referred to as surfactants. Chemical compounds falling in the category of surfactants range from low molecular weight amphiphilic molecules, as shown in Fig. 4.1a, to large block-copolymers with blocks of different hydrophobicities represented in Fig. 4.1b. The physico-chemical details of the surfactants have a large impact on the mechanical behaviour of the interfaces, as we will explain in this chapter.

Interfacial tension γ can vary along the interface because of temperature gradient or inhomogeneous coverage of the interface by surfactants. Such variations can create local gradients of interfacial tension, adding the so-called Marangoni stress to the interface [116]. This stress can only be balanced by viscous stresses coming from the interface of two fluids in motion relatively to each other. Applied to bubbles and foams, Marangoni flow manifests as soon as interfaces are deformed or sheared by external flow. Historical example comes from the settling velocity of a rising bubble, behaving like a rigid sphere instead of a fluid body obeying Navier-Stokes equations [117]. Shear flow of the interface creates interfacial tension gradient, with surfactants accumulating at the drop's rear as shown in Fig. 4.4a. Resulting Marangoni stress increases bubble friction [118], making the deformable drops (see Chapter 3) behave more akin to a rigid sphere. For foams, deformation of thin films creates concentration gradients that are compensated by Marangoni flows, favoring foam stability [119, 120].

When added to a bulk solution, surfactant molecules reduce its interfacial tension. An increase in surfactant bulk concentration c results in a decrease in interfacial tension γ , until a plateau value for γ is reached for a critical concentration c^* . At this critical micellar concentration (CMC), it is thermodynamically more favorable for surfactant molecules to stay in bulk phase and hide their hydrophobic components in fluid aggregates called micelles (see Fig. 4.1c). The CMC and the plateau interfacial tension are of course dependent on the two phases and surfactant chemistry. Coverage of the interface with surfactant molecules cannot be deduced from bulk concentration in a straightforward manner. Surface coverage Γ_s describes the number of surfactant molecules per unit area. Its invert, the area per molecule $a = \Gamma_s^{-1}$, describes the average area occupied by each surfactant molecule at equilibrium. It is dictated by the molecule size, but also by its interactions (attractive or repulsive) between neighbouring surfactant molecules. At thermodynamic equilibrium, the relation between surface coverage and bulk concentration is given by an adsorption isotherm. For a species i in solution in one phase at dilute concentration c_i and insoluble in the second phase, adsorption is described by Gibbs isotherm

$$\Gamma_{si} = -\frac{1}{RTx} \frac{d\gamma}{d\ln(c_i)}, \quad (4.2)$$

where R is the ideal gas constant, T the temperature in Kelvin, and x a factor depending on the type of surfactants used. A typical value for ionic surfactants (such as sodium dodecyl sulfate, see Chapter 2) in salt solutions gives $x = 2$. Isotherms of course vary greatly depending on the chemical species considered, but such considerations are outside the scope of this thesis. Interested readers are referred to the dedicated literature [121]

Surfactant compounds at the interface are not inert molecules stuck between two phases. They dynamically switch between bulk phase and interface, relaxing towards equilibrium over character-

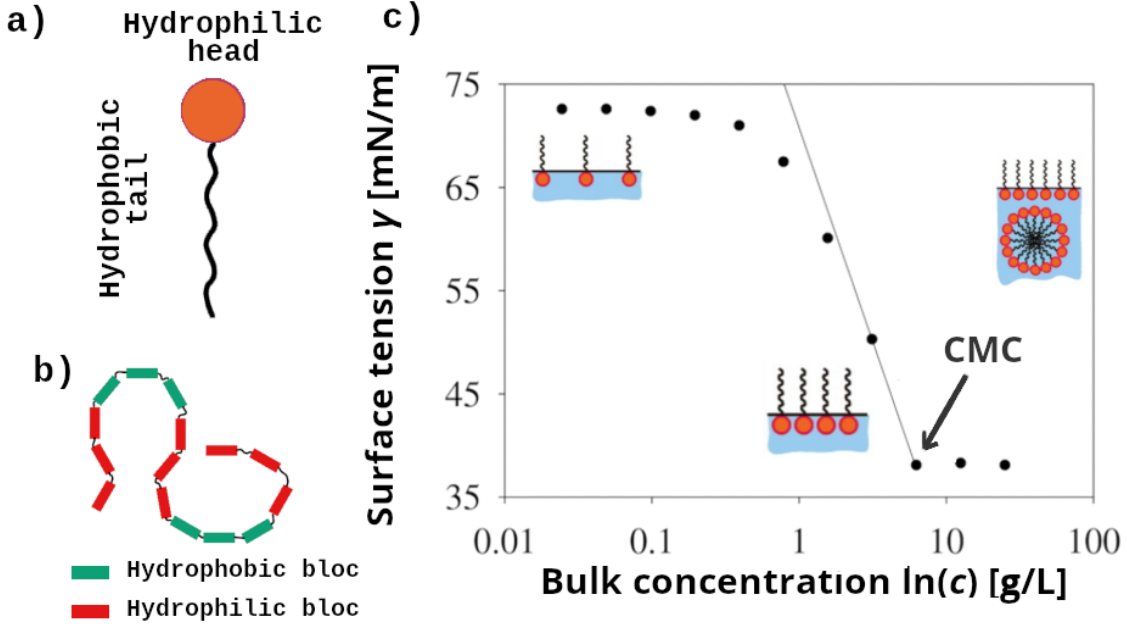


Figure 4.1: a) Typical low molecular weight amphiphilic molecule. Hydrophobic tail consists of carbon chains. b) Amphiphilic polymer with alternance of hydrophilic and hydrophobic blocs. c) Variation of interfacial tension γ with concentration of surfactant mixture (linear alkyl benzene sulfonate-sodium dodecyl sulfate-isoridecyl alcohol at 1:1:2.94 weight ratios). Ionic concentrations affect electrostatic interactions between surfactants and the subsequent interfacial tension. Surfactants migrate to the interface until maximal equilibrium concentration is reached at CMC. Excess surfactants molecules then form micelles in the bulk phase and interfacial tension no longer changes. Adapted from [122].

istic time which depends on the surfactant, its concentration and the bulk phases. The constraint of confinement to a 2D interface forces a lateral order, with interactions between molecules with a particular forced orientation (Fig. 4.2.a). Adsorbed surfactants interact with their neighbours through what Vermant and coworkers describe as *lateral interactions* [123, 28, 1, 124]. The resulting mechanical response thus depends on the physico-chemical details of the surfactant moieties (bound molecules through crosslinking reaction[125], rafts of connected solid particles [126, 127]). Unbound, surfactant molecules react to dilation by balancing their surface concentration through Marangoni flow, and adsorption/desorption mechanism, represented in Fig. 4.2b. Molecules crosslinked with their neighbours form solid layers, deforming elastically under surface dilation, as sketched in Fig. 4.2c. The resulting deformation differs from the previous case, e.g. by its possible anisotropic shear state after deformation.

Just as molecules in bulk phase, surfactants thus react to deformations of the interfaces they are adsorbed to and adapt to new equilibrium conditions. Understanding stress response to deformation requires to consider how lateral interactions are affected by deformations.

Definition of interface deformation is borrowed from solid elasticity [128], assuming continuous variation of deformation. The position \vec{X} of every point in the initial body configuration Ω_0 is associated to a final position \vec{x} in the deformed configuration Ω , a transformation shown in Fig. 4.3a. A displacement vector \vec{u} is defined for every point \vec{X} as $\vec{u} = \vec{x} - \vec{X}$. In the limit of small displacements, deformation is described at first order with the infinitesimal strain tensor ε_{ij}

$$\varepsilon_{ij} = \frac{1}{2} \left(\frac{\partial u_i}{\partial X_j} + \frac{\partial u_j}{\partial X_i} \right) \quad (4.3)$$

used in the Shuttleworth stress-strain equation (4.4). It contains information about the deforma-

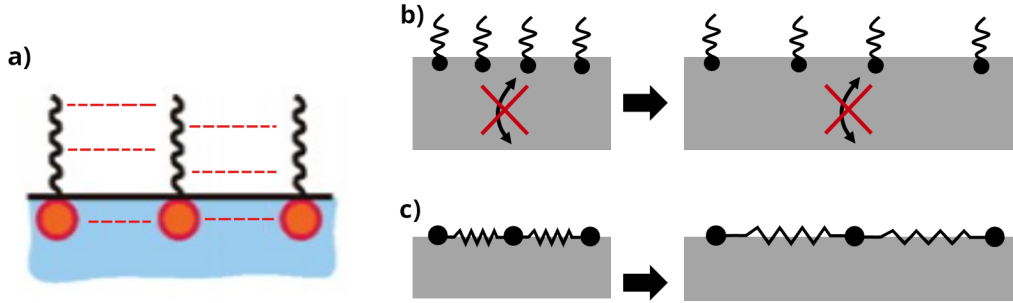


Figure 4.2: a) Adsorbed molecules organise within the planar organisation. For interacting molecules, description of the interface requires to account for the intermolecular interactions in this particular configuration, referred to as lateral interactions [28]. b) At fluid-fluid interfaces, dilation of the interface reduces the surface coverage, increasing the interfacial tension. For irreversibly adsorbed molecules, molecular rearrangements at the interface cancel gradients of surface concentrations ; hence, stresses in fluid-fluid interfaces are always isotropic. c) Crosslinked polymers on a deformed interface stretch elastically, storing energy in their intermolecular bonds. Irreversible bonds forbid molecular reorganisation, and anisotropic deformations impose anisotropic stresses.

tion which is invariant to rotation and translation, neglecting nonlinear and dynamical effects [128]. Larger deformations require the formalism of gradient deformation tensor \mathbf{F} , which we describe in Section 4.3.

Shuttleworth [129] studied the tangential stress τ_{ij} acting on an interface of interfacial energy f subjected to a strain ε_{ij} . The general stress-strain relation reads as

$$\tau_{ij} = f\delta_{ij} + \frac{\partial f}{\partial \varepsilon_{ij}} \underset{\text{isotropic}}{\Rightarrow} f + \frac{\partial f}{\partial \varepsilon} = \gamma. \quad (4.4)$$

where the last part of Eq. (4.4) is valid for interfaces unable to sustain anisotropic stress. Examples are restricted to pure liquids [130] with no microstructure effects (Fig. 4.2b) : in that situation, tangential stresses are isotropic and can be expressed as a interfacial tension γ . For more complex interfaces, scalar quantities are unable to describe tangential stresses, and tensorial description must be used.

Arbitrary deformations are often a mix of shear and dilation. Any deformation field ε_{ij} can always be decomposed in a pure dilation with no shear $\frac{1}{3}\varepsilon_{ll}\delta_{ij}$ and a pure shear with no dilation $\varepsilon_{ij} - \frac{1}{3}\delta_{ij}\varepsilon_{ll}$ [128], as shown in Fig. 4.3a. Rheological characterisation is a measure of resistance of the probed interface to both modes of deformation, with interfacial dilatational modulus K and interfacial shear modulus G , respectively. Associated experimental methods are described in Section 4.2.

For fluid interfaces, gradients of surface concentration are quickly equilibrated by Marangoni flow (Fig. 4.3b) . Interfaces in their final state are thus uniformly covered, and hence cannot sustain anisotropic stress caused by shear deformation. In that case, interfacial rheology is characterised by Gibbs area dilatational modulus K_G

$$K_G = \frac{d\gamma}{d\ln(A)} \quad (4.5)$$

The interfacial tension is independent of deformation amplitude, and thus has a zero K_G . Complex interfaces, however, may exhibit non-zero dilatational modulus because of bulk/interface

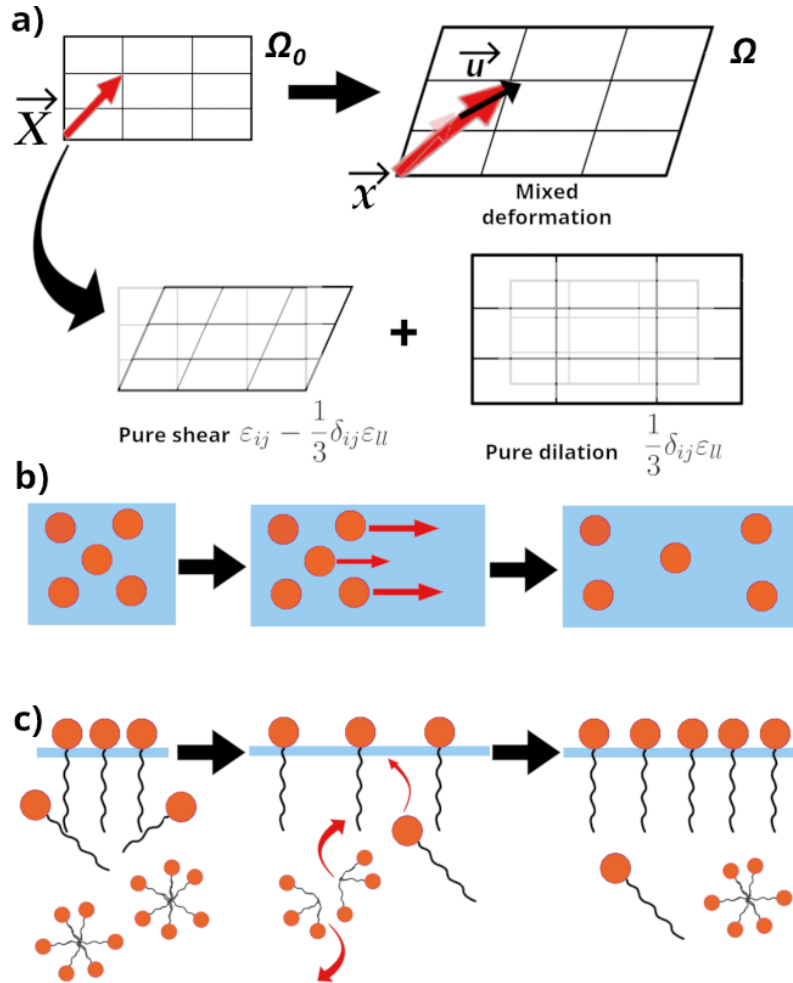


Figure 4.3: a) Top : arbitrary deformation of an initial reference state Ω_0 with coordinates \vec{X} to a new state Ω with coordinates \vec{x} . Bottom : decomposition the deformation in a pure shear (left) and a pure dilation (right). b) Anisotropic area dilation causes surfactant transport because of gradient of interfacial tension and Marangoni flow. Interface in its final state has an isotropic tangential stress τ_{ij} similar to a interfacial tension γ . c) Dilation reduces surface coverage, compensated by adsorption of bulk and micellar molecules.

transport phenomena and interfacial microstructures. The first happens when surfactant molecules adsorb/desorb from the strained interface to approach equilibrium concentration as sketched in Fig. 4.3c, following their adsorption isotherm (Eq.(4.2)). In that case, interfacial tension follows a relaxation process involving diffusional surface/bulk exchange and micellar breakdown [131].

Because of its intrinsic dynamic nature, the temporal evolution of $K_G(t)$ is often measured and brings important informations about surface rheology. Adsorption/desorption being quicker for smaller molecules, small amphiphilic molecules quickly equilibrate the interfacial concentration when the interface is deformed. On the other hand, the adsorption timescale of block-copolymers can be orders of magnitude larger, introducing a delay between the deformation and the interface reaching equilibrium. These timescales depend also strongly on the surfactant concentration. Transient elastic modulus $K_G(t) = \frac{d\gamma(t)}{\Delta A/A_0}$ is used to describe interfacial response to step strain and oscillatory experiments (see Section 4.2.2). While it is originally used as a description of fluid-fluid interfaces, it can also describe solid microstructured interfaces deformed isotropically [132, 28]. Time-dependent $K_G(t)$ gives then access to frequency-dependent dilatational modulus $K_G^*(\omega) = K_G'(\omega) + iK_G''(\omega)$ by a standard Fourier transform, where $K_G'(\omega)$ is the dilatational storage modulus and $K_G''(\omega)$ is the dilatational loss modulus. While the dilatational modulus is deformation independent at small deformations, this hypothesis does not hold in general at large deformations, where structural properties of the interface and lateral interactions between adsorbed molecules play a role in its mechanical response [133, 28].

The rheological response of the interface is also affected by the shape of the surfactant molecules and their local arrangement at the molecular scale. The most energetically favorable organisation gives rise to microstructures with their own mechanical behaviour, depending on the intermolecular interactions. A deformation of the interface stretches the molecules and adds extra-stresses to the interface. This external perturbation can, under some conditions, trigger modifications of the microstructure such as phase transitions [134, 24, 135], which are known to affect the rheological properties of foams and emulsions [136]. A proper description of the interface thus requires an appropriate constitutive model, depending on the composition of the interface. So far, this approach has been used to describe polymer solutions, polymer melts, liquid crystalline phases, soft glasses and gels [137, 132, 138, 139]. The contributions of phase transitions are again more present for large polymeric surfactants, as low molecular-weight surfactants do not form complex microstructures [26].

4.1.2 Foam and emulsions as high specific surface systems

The structure of interfaces affect how bubbles interact together and with their medium. Rigid interfaces increase the resistance of bubbles to deformations, modifying their force-deformation behaviour solely driven by interfacial tension we detailed in Chapter 3. Interfacial strain caused by the flow of outer medium around the drops brings interfacial rheology into play in bubble rising behaviour [117], as shown in Fig. 4.4a, and wet foam rheology [65, 140]. In drainage, the flow along the interfaces generated by gravity interacts with the adsorbed molecules. The rigidity of the interface impacts the velocity profile of the drainage flow ; rigid interfaces (i.e. large amphiphilic molecules) impose a null interfacial velocity [141, 142], while mobile interfaces (i.e. small amphiphilic molecules) shear under flow, resulting in gradients in interfacial tension and Marangoni flows [143, 144, 145, 140], as represented in Fig. 4.4b. These differences in interfacial boundary conditions modify the drainage regime at the foam scale [146].

Foams are systems with high specific surface, and high associated interfacial energy. Over

time, this energy is dissipated through bubble coarsening and coalescence [147]. A bubble has a higher pressure than its surrounding medium, as predicted by the Young-Laplace law $\Delta P = 2\gamma/R_0$. It therefore expels gas in the outer medium. For bubbles in contact, small bubbles have higher pressure than their larger counterparts, and end up transferring gas to their large neighbours, with an evolution over time of the structure of the foam to large, polydisperse bubbles. A similar process happens in emulsions, where it is called Ostwald ripening.

Halting foam coarsening is deeply looked after to favour foam stability and preservation of its structure over long timescales [148, 149]. One particularly efficient way to stop coarsening is *via* the addition of interfacial elasticity [150, 151, 152, 153, 154, 155, 156]. Following the pioneering work of Gibbs, the impact of an interfacial elasticity on bubble coarsening is often tackled using Gibbs elasticity, where resistance to deformation is characterised by the dilatational elastic modulus K_G (Eq.(4.5) in Section 4.1.1). Bubble shrinkage is naturally stopped when a radius reduction does not decrease the bubble pressure ($\partial\Delta P/\partial R > 0$). Expressed within Gibbs elasticity, this condition becomes

$$\frac{\partial\Delta P}{\partial R} = 2\frac{\partial}{\partial R}\left(\frac{\gamma}{R}\right) = \frac{2}{R}\frac{\partial\gamma}{\partial R} - \frac{2\gamma}{R^2} = \frac{2}{R}(2K_G - \gamma) > 0 \rightarrow \frac{K_G}{\gamma} \geq \frac{1}{2} \quad (4.6)$$

Eq. (4.6) is known as *Gibbs criterion*, which determines the stability of a bubble with respect to coarsening. Irreversibly adsorbed molecules and particles have been used successfully to stabilise foams against coarsening [157, 158, 159, 155, 160], while the change of dynamics of bubble growth significantly alters the evolution of radius distribution at the foam scale [161]. This effect can also be achieved by soluble surfactants, as long as surface variation changes are fast enough compared to the adsorption/desorption dynamics described in Section 4.1.1.

4.2 Rheological characterisation of complex interfaces

The development of dedicated interfacial shear rheometers has enabled reliable measurements of the interfacial shear modulus G [163, 164]. Interfacial rheology, like its bulk counterpart, is concerned about the viscoelastic properties of interfaces separating bulk phases. Usually, these properties are measured by imposing a strain on the interface and measuring how this transformation translates in interfacial stress, although the deformation response to an imposed stress can also be used to measure the mechanical properties of the interface. Pure fluid-fluid interfaces cannot sustain tangential surface stress : the rheological response comes from the covering of the interface by surface active species interacting with each others, and the effect of those interactions on the stress-strain response of the interface [165]. As solid deformation, an interface's strain can always be decomposed as a combination of pure shear and pure dilation (Fig. 4.3a). Rheological characterisation proceeds by applying one or the other deformation mode, and measuring viscous and elastic response. In many techniques, both deformation modes are actually intrinsically coupled.

In this part, we present double-wall ring (DWR) rheometry (Section 4.2.1), a shear rheology method used to characterise the polymer skin of the PEG-silicone model system described in Chapter 5. We then proceed to describe pendant drop experiments in Section 4.2.2, used originally to characterise interfacial tension at simple fluid-fluid interfaces, and present how it has been extended to measure dilatational properties of complex interfaces.

4.2.1 Shear rheology : the double-wall ring experiment

Double-wall ring rheometer [166] consists in a fluid chamber with two levels, represented in Fig. 4.5a. At first, the heaviest fluid is put at the bottom, up to the delimitation line between the two

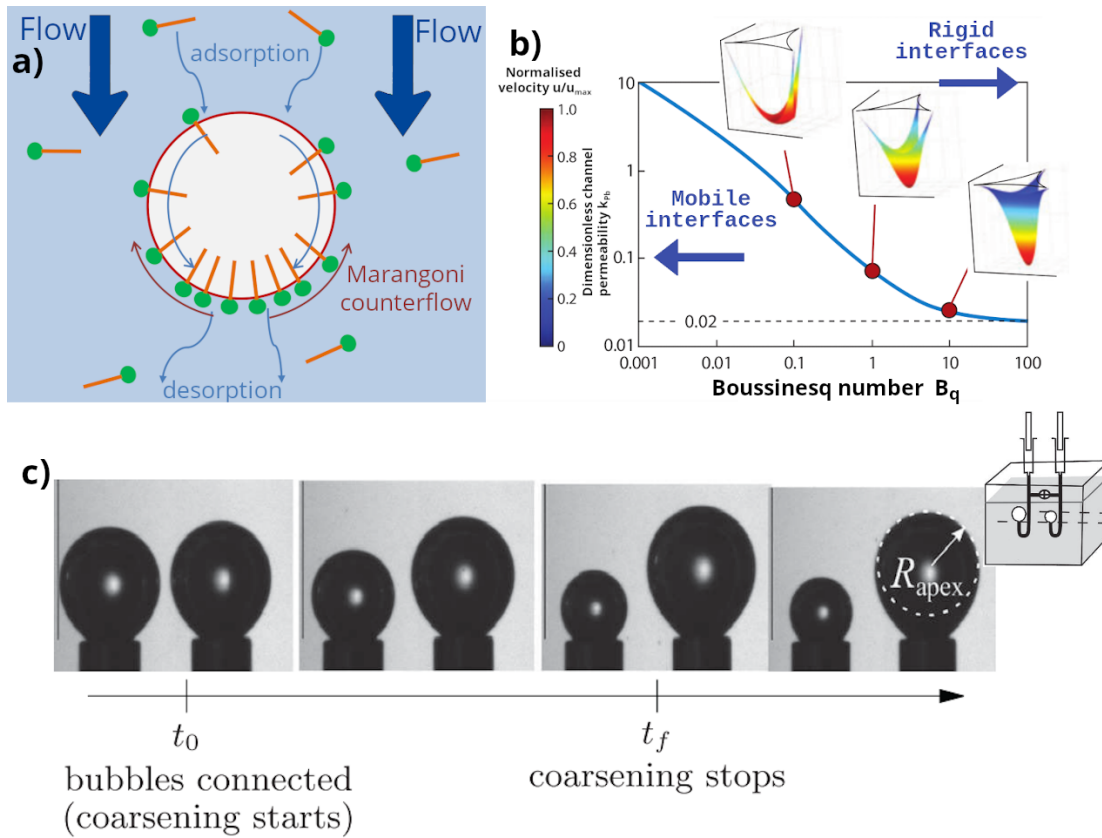


Figure 4.4: a) Flow around a drop covered with surfactants shears the interface and accumulates adsorbed surfactants at the back of the drop. Gradient of interfacial tension creates a backwards Marangoni counterflow. From Heitkam's lecture [162] b) Evolution of velocity profile with surface mobility. For rigid interfaces ($B_q \ll 1$), the no-slip boundary condition focuses the flow in the middle of the Plateau border. For more mobile interfaces, the flow is close to a bulk flow. c) Experimental setup by Salonen *et al.* [161] to measure the impact of interfacial elasticity on bubble coarsening. Two bubbles of different radii are connected through a closed tube (represented in the inset). At $t = 0$, the valve is opened and bubbles can equilibrate in pressure through liquid flow through their shared tube. Contrary to purely capillary interfaces, drops with interfacial elasticity stop exchanging gases before the smaller bubble is absorbed by its larger counterpart.

subvolumes. A probe, composed of a ring of perimeter L and area A , is put at the interface before adding the second liquid. Application of a torque on ring axis causes a shear deformation of the interface, in a step-by-step deformation method or with oscillating shear deformation at frequency ω . A measure of the rotation of the axis gives access to the strain of the interface, while in-phase and out of phase responses characterise elastic and viscous shear responses, respectively. Fourier transform of the Fourier shear modulus $G(t)$ gives access to the complex frequency-dependent shear modulus $G^*(\omega) = G'(\omega) + iG''(\omega)$, where $G'(\omega)$ is the elastic shear modulus and $G''(\omega)$ is the viscous shear modulus.

Experimental errors in interfacial measurements come from the coupling of interfacial flow to flow in the bulk subphase. Experimental setup should thus ensure that bulkflow contribution is negligible in front of interfacial flow. The competition between these two contributions is estimated with the Boussinesq number $B_q = \frac{\text{surface drag}}{\text{subphase drag}} = \frac{\mu_s}{\mu[A/L]}$ where μ_s is the interfacial shear viscosity and μ the bulk viscosity. Ring geometry should therefore be of maximal diameter at given surface for optimal sensitivity [166, 167]. Proper measurements can be conducted for large Boussinesq number $B_q \gg 1$.

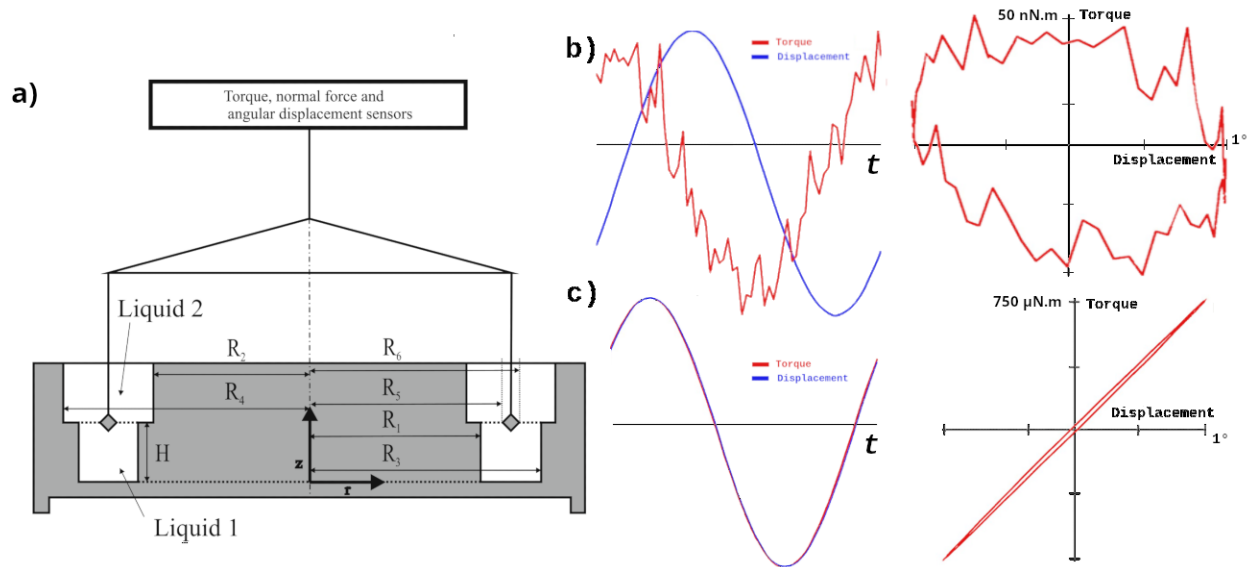


Figure 4.5: a) Double-wall ring geometry [166] used for shear interfacial rheology. The ring is put at the interface between the two phases and oscillated with a pulsation ω . The formation of a gel at the interface modifies its mechanical properties. b) In-phase deformation caused by oscillatory strain, corresponding to an elastic response. c) Out of phase deformation, associated with a viscous response.

4.2.2 Dilatational rheology : the pendant/sessile drop experiment

The characterisation of the dilatational modulus K remains challenging, due to the experimental difficulty of applying an accurately controlled homogeneous dilation to an interface and of assessing the accuracy of the modulus measurement if the deformation is only approximately a homogeneous dilation. Since the volume change of a sphere leads to a perfect dilation of its surface, measuring the pressure-radius relation of a small, spherical elasto-capillary droplets should be the preferred method to determine the dilatational modulus. This has been implemented for capsules using osmotic pressure variations [168] or acoustic pressure fields [169]. However, these approaches introduce

physico-chemical or technical complexity. It is much more convenient to study the pressure/shape relation of drops held by a needle with circular cross section (see Fig. 4.6a-b), a technique called capillary tensiometry or pressure tensiometry when shape or pressure analysis is used, respectively. Furthermore, fluid circulation inside suspended drops favors homogeneous concentration of surface active species within the bulk phase and at the interface [133]. The interfaces, having uniform properties, are more reliably characterised in that case. In the next two sections, we first summarise experimental methods commonly used to determine interfacial tension and stresses in a pendant drop configuration. In the third one, we present a generalisation of these techniques adapted to elastic capsules, developed by Kierfeld and coworkers [126, 170] which serve as a benchmark to test the accuracy of our model.

Drop shape analysis (DSA)

Drop shape analysis (DSA) - also sometimes called profile analysis tensiometry- is a long-standing method for measuring interfacial tension [171, 172]. It is based on the fitting of the profile of deformed drops or bubbles attached to a capillary with the numerical solution of Young-Laplace equation in the configuration depicted in Fig. 4.6.a-b. The density difference between the two phases produces a hydrostatic pressure gradient $\Delta\rho gz$ in the vertical direction, parallel to the drop's symmetry axis. The pressure difference across the interface increases with height accordingly. In this configuration, the Young-Laplace equation becomes

$$\Delta P(z) = \Delta P_0 + \chi \Delta \rho g z = \gamma(\kappa_\phi + \kappa_s), \quad (4.7)$$

where $\Delta\rho = \rho_{in} - \rho_{out}$ is the density difference between the two phases, g gravity acceleration, χ a factor with $\chi = 1$ for a pendant drop and $\chi = -1$ for a rising bubble, and z the height along the symmetry axis taken from the needle. κ_ϕ and κ_s are the circumferential and meridional curvatures. Representation of this parametrisation is shown in Fig. 4.6c. Drop profiles are described taking advantage of the axisymmetry of the pendant drop, using arc length from the origin s at the apex of the drop and the parametrisation $(R_2 \sin(\psi), z)$ where ψ is the angle tangent to the surface [173]. In this parametrisation, Young-Laplace equation becomes

$$\frac{d\psi}{ds} = \frac{2}{R_0} - \chi \frac{\Delta\rho g}{\gamma} z - \frac{1}{R_2}. \quad (4.8)$$

Eq.(4.8) is numerically integrated with a test pair of input parameters $(\Delta P_0, \gamma)$. The profile obtained experimentally is then compared to numerically integrated shapes, with an error estimation function measuring the distance between points of the experimental shape and points coming from the pair test. This process is iterated while trying to minimise the error function, and stopped within the desired accuracy.

Although shape analysis is a time-consuming procedure, drop profile can be recorded and treated afterwards. Pendant drop is an appropriate setup to probe fast processes [175, 176, 177], because the volume control device can reach oscillation frequencies down to 1 Hz. Measure of interfacial viscoelasticity is obtained by imposing periodic surface oscillations to the bubble. Russev *et al.* [171] treated the case of an interface submitted to sinusoidal area oscillations $A(t)$ at a single frequency ω and its interfacial tension response $\gamma(t)$

$$A(t) = A_m(1 + \alpha_a e^{i\omega t}), \quad (4.9)$$

$$\gamma(t) = \gamma_m + K_G^*(\omega, \alpha_a) \alpha_a e^{i\omega t}, \quad (4.10)$$

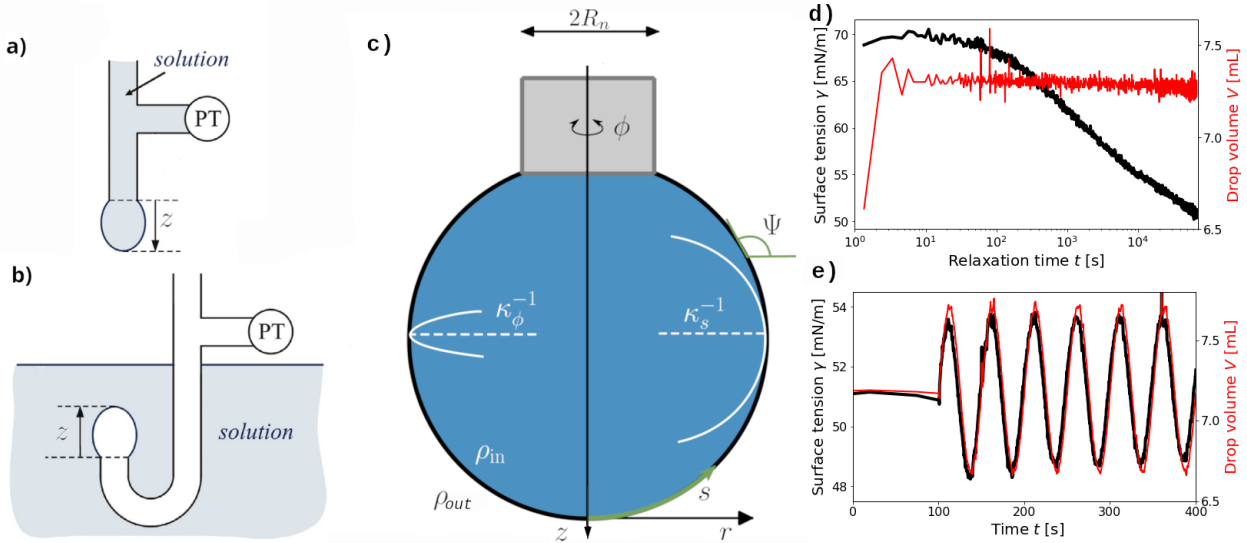


Figure 4.6: a) Pendant drop and b) rising bubble setup from [172]. Pressure transducer (PT) is used in capillary pressure tensiometry (Section 4.2.2), with a pressure shift between detector and bubble interface due to gradient in hydrostatic pressure. c) Surface parametrisation of pendant drop shape. Figure from [174]. d) Relaxation of an air-water interface in a solution of sodium polystyrene sulfonate at 1 g/L. At initial time $t = 0$, the volume is increased by 10% then kept constant. Interfacial tension decreases slowly as the NaPSS adsorbs at the interface e) Oscillating bubble for the same NaPSS setup. A sinusoidal cycle of volume variation of 5% is imposed on the bubble while the interfacial tension is deduced. As oscillation period is order of magnitude smaller than relaxation timescale, no relaxation happens and interface response is in-phase with volume oscillation. Results courtesy to Stéphane Pivard.

where α_a is the amplitude of surface deformation, $K_G^*(\omega, \alpha_a)$ is the complex area dilatational modulus, and A_m and γ_m are the mean area and interfacial tension, respectively. A typical volume variation with forced oscillation is shown in Fig. 4.6e. In the limit of small amplitude strain, the elastic modulus remains linear and depends on oscillation frequency ω only, so that K_G^* can be decomposed in a elastic part $K_G'(\omega)$ and a viscous part $K_G''(\omega)$ [178], as described in Section 4.1.1.

DSA has major drawbacks. Relying on shape analysis, it is highly sensitive to image noise, especially since it relies on the definition of a contour and (x, z) variation. The iterative integration scheme is computationally costly : each test pair has to be fully integrated before being evaluated. For this reason, analysis can often not be performed *in situ*, especially for large drop deformations, but rather performed after the experiments, so that interfacial tension measurement cannot be used to monitor drop deformations. The density difference $\Delta\rho$ is the driving factor for the drop deformation under gravity : therefore, fluids with small density variations (e.g. emulsions) are not suited for DSA experiments and drops should have a minimal deformation before DSA results can be trusted [133]. More importantly, DSA assumes the isotropy of surfaces stresses, and is therefore not appropriate for surfaces where stress isotropy is not ensured.

Capillary meniscus dynamometry (CMD)

Fluid-fluid interfaces cannot sustain anisotropic stresses : a gradient of surface coverage by surfactants is balanced by Marangoni flow until the stress is uniform and isotropic again, as described in Section 4.1.1. On the other hand, solid interfaces, e.g. polymeric skins, remain in a state of anisotropic stresses.

For a two-dimensional layer, the tangential stress can always be decomposed in two orthogonal

components. The surface is defined as a locus of points \vec{r} as functions of two independent parameters α and β $\vec{r} = \vec{r}(\alpha, \beta)$. For α -lines and β -lines of the surface perpendicular to each other, as in Fig.4.7, α and β are called the orthogonal curvilinear coordinates of the surface, with the orthogonality relation $\frac{\partial \vec{r}}{\partial \alpha} \cdot \frac{\partial \vec{r}}{\partial \beta} = 0$.

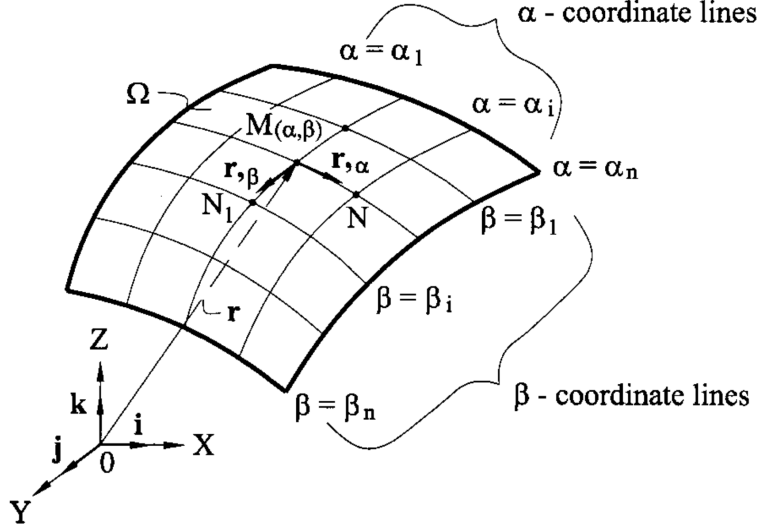


Figure 4.7: Surface parameterisation with curvilinear coordinates. The point \vec{r} of the surface Ω is a function of the curvilinear coordinates α and β . The α -lines ($\alpha_1, \dots, \alpha_n$) and β -lines (β_1, \dots, β_n) are orthogonal at any point of the surface. Figure from [179].

For the geometry of the pendant drops, a natural decomposition of the stress includes one component along the profile of the drop, called the meridional direction of index s , and one component normal to the first one, called the longitudinal direction, of index ϕ . This decomposition is represented in Fig. 4.6c. The pendant drop geometry naturally induces a stress anisotropy, by imposing the longitudinal curvature κ_ϕ with the needle radius $R_n = 1/\kappa_\phi$. On the other hand, at the apex radius ($z = z_{max}$), the symmetry of the system imposes the isotropy of the stresses associated to the principal directions $\sigma_s = \sigma_\phi$. The determination of the two distinct stresses therefore requires extra considerations on the shape equations, as does CMD.

With the rise of high-frequency and precision pressure detectors, DSA setup has been improved by adding a pressure transducer to measure the pressure of the inner phase, as shown in Fig. 4.6a-b. Compared to DSA, capillary meniscus dynamometry (CPMD) is well suited for systems of low density difference and small deformations [180, 133]. The shape of the drop is recorded at any stage of the deformation, as well as its inner pressure, as shown in Fig. 4.8a. By fitting the shape of the drop and using the inner pressure in the stress balance equation, CMD can deduce the tangential stresses at any point of the surface of the drop, as shown in Fig. 4.8b-c.

Using again axisymmetry of the pendant drop/rising bubble, shape is described using cylindrical coordinates (r, ϕ, z) with coordinate origin at the drop apex, where z is the coordinate on the symmetry axis, $z = 0$ corresponding to the apex of the drop/bubble. Profile can then be parametrised

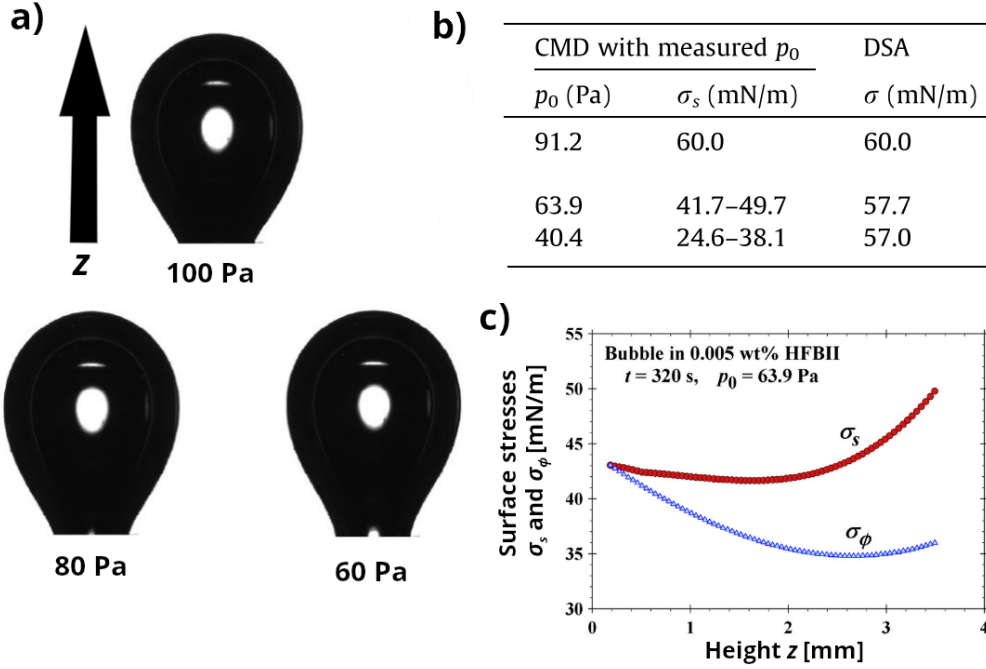


Figure 4.8: a) Evolution of buoyant bubble profile in a 0.005 wt% HFBII hydrophobin solution. Pressure is measured through the capillary at the bottom of the needle. [172] b) Surface meridional stress deduced from capillary meniscus dynamometry and drop shape analysis. DSA assuming isotropic stress state, circumferential σ_ϕ is assumed to be equal to σ_s . [172] c) Distribution of surface stresses along the drop profile deduced from CMD. [172]

as depicted in Fig. 4.6.c, with the arc length s such that

$$\begin{aligned} \frac{dr}{ds} &= \cos(\psi) \\ \frac{dz}{ds} &= \sin(\psi) \end{aligned} \quad (4.11)$$

where ψ is the slope angle.

This new system of orthogonal coordinates (s, ϕ) defines the stresses in the two principal directions σ_s and σ_ϕ , tangential to the s and ϕ coordinates, respectively. Force balance requires the following equilibrium relations [181, 182, 183]

$$\sigma_\phi = \frac{d}{dr}(\sigma_s r) \text{ (tangential),} \quad (4.12)$$

$$\Delta P(z) = \kappa_s \sigma_s + \kappa_\phi \sigma_\phi \text{ (normal).} \quad (4.13)$$

Eq.(4.12) is the tangential stress balance in the meridional direction [133], and Eq.(4.13) is the anisotropic generalisation of the Young-Laplace law. κ_s and κ_ϕ are the two principal curvatures. They are defined as

$$\begin{aligned} \kappa_s &= \frac{d\psi}{ds} \\ \kappa_\phi &= \frac{\sin(\psi)}{r} \end{aligned} \quad (4.14)$$

Eqs. (4.11), (4.13) and (4.14) are then combined to get the differential equation relating meridional stress σ_s to pressure difference

$$\frac{d}{dr}(\sigma_s r \sin(\psi)) = \Delta P r \quad (4.15)$$

Integrating this equation gives access to the meridional stress σ_s . Writing the pressure difference $\Delta P(z) = \Delta P(0) + \chi \Delta \rho g z$, the meridional tension reads as

$$\sigma_s(z) = \frac{\pi r^2 p_0 + \pi \chi g \Delta \rho (\int_0^z r^2(\tilde{z}) d\tilde{z} - r^2 z)}{2\pi r(z) \sin(\psi(z))} \quad (4.16)$$

where \tilde{z} is an integration variable. The circumferential stress is then deduced by inverting the anisotropic Young-Laplace equation (4.13)

$$\sigma_\phi(z) = \frac{p_0 - \varepsilon g z \Delta \rho - \kappa_s(z) \sigma_s(z)}{\kappa_\phi(z)}. \quad (4.17)$$

Using only surface force balance equation, $\sigma_s(z)$ and $\sigma_\phi(z)$ can be determined on the whole interface without any assumption about the material law describing the interface. Robust determination of slope angle $\psi(z)$, derivative in the meridional curvature expression (Eq.(4.14)) and the integral in Eq. (4.16) form the sensitive part of the CMD technique. The shape of the pendant drop is fitted using Chebyshev polynomials [1] whose analytical expressions are used to compute derivatives and integrals. This numerical fitting, however, is very sensitive to noise, and yield unphysical longitudinal stress in the regime of small deformations. Moreover, the stresses at the apex sometimes fail to converge to isotropic values, which should be guaranteed by the symmetry of the system. The results of CMD should thus be taken critically, as products of a complex numerical procedure. Interested readers are referred to the dedicated literature [172].

CMD thus works by shape integrations, allowing faster measurement of interfacial tension, and even on the spot control during experiments. With this procedure and the additional measure of the inner pressure, CMD can measure anisotropic surface stresses with its meridional and longitudinal components σ_s and σ_ϕ , respectively. Comparison of DSA and CMD results in Fig. 4.8b highlights the limits of isotropic hypothesis. Danov *et al.* [172] studied the effect of hydrophobin HFBII coating on air bubbles at different imposed inner pressures. Stresses σ_s and σ_ϕ are computed at each step with CMD equations, and compared to DSA result. DSA error increases with pressure variation. At the apex of the bubble $z = z_{max}$ however, $\sigma_s = \sigma_\phi$ for any pressure difference: because of the symmetry of the drop, longitudinal and meridional direction are equivalent at this point. Although subjected to the same optical errors than DSA and requiring non-trivial numerical integration, CMD is more reliable than DSA : access to the inner pressure is thus highly appreciated, though not being always available in experimental conditions.

Pendant capsule elastometry (PCE)

CMD measures the stresses at the interface of the drop, without any assumption about its constitutive law. Detection of anisotropy can be linked to elasticity, but stress measurements are unable to predict the shape changes of an interface under an arbitrary deformation. Any knowledge about the interface is thus not easily transferable to other configurations. The field of elastic capsules and microcapsules is more interested in the behaviour of solid interfaces under non-linear deformations, such as large strains, buckling and fracking [184, 185, 186, 187, 188, 189, 190, 191, 183]. Most often, capsules are produced by interfacial reactions such as polymerisation or adsorption of

surfactants [192]. The pendant drop geometry, where the shape of the interface is close to that of a drop, and where the elastic skin is formed in the same conditions as for capsules, is thus a relevant configuration for the characterisation of thin elastic shells. As for DSA and CMD, the interface is deformed by inflating and deflating the drop and recording its deformed profile. This configuration has already been applied successfully to elastocapillary interfaces [193, 194].

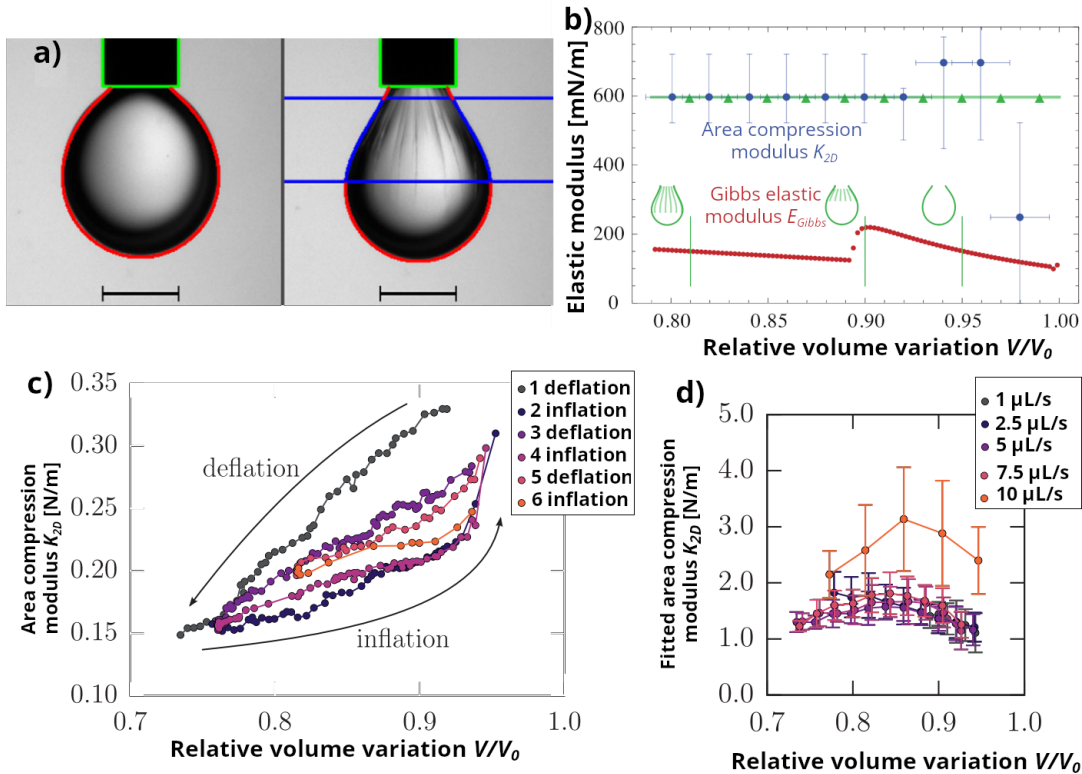


Figure 4.9: a) Deflated drop on the needle. Area between the blue lines exhibit wrinkles corresponding to compressive circumferential stress $\sigma_{phi} < 0$ from which bending modulus E_B can be fitted. [126] b) Fit of elastic moduli using the same theoretical (red circles) drop shape obeying Hookean elasticity (green triangles), with Gibbs elasticity $K_G = A \frac{d\gamma}{dA}$ and area compression modulus K_{2D} (blue circles) from [126]. Fitted K_G varies with deformation, because Gibbs elasticity is not suited for solid elastic interfaces. Difference between simulation and fitted coefficient comes from the noise introduced on the numerically generated contour. Because of shape-fitting sensitivity to noise, weakly deformed profiles are hard to fit and large errors on modulus fit follow. c) Variation of fitted area compression modulus K_{2D} with number of deformation cycles [170] and d) deformation rate [170]. Change in fitted moduli are a sign of aging and viscoelasticity, respectively.

Another approach of pendant drop experiments aims at overcoming the limitations of CMD : pendant capsule elastometry (PCE) [126, 170] provides a measure of the elastic coefficients of thin elastic membranes at fluid-fluid interfaces. Usual PCE experiments are conducted as follows : in a first step, a drop is produced at the bottom of the capillary. If surfactants are present in the solution, they adsorb at the interface, lowering interfacial tension. The shape is driven by the balance of interfacial tension γ_0 and the gravitational force $\Delta\rho g$, as for usual DSA experiments. In a second step, an elastic skin forms at the interface, shaped like the pendant drop. In this configuration and before any deformation is applied, the membrane is supposed to be in its state of zero elastic stress. An example is shown in Fig. 4.9a (left).

This is taken as reference shape of the interface, corresponding to the profile of a laplacian drop of interfacial tension γ attached to a needle of radius R_n . Once the skin has finished to form, the capsule is deflated by suction of the inner subphase through the needle. An example of such a

deflated shape is shown in Fig. 4.9a (right). Comparative theoretical contours are produced with the shape equations described in Section 4.4.2 (Eqs. (4.54-4.56)). These equations rely on the stress balance equations, and can be implemented for any constitutive law of known stress-strain relation. The shapes are computed with a set of input parameters (whose elements depend on the chosen constitutive law) and compared to the contour of the pendant drop, detected with automatical segmentation, as shown in Fig. 4.9a. The accuracy of the input parameters is then estimated with a measure of the mean-square deviation between the theoretical and experimental contours. The shape regression is here driven by the minimisation of this mean-square deviation.

For instance, Neo-Hooke material law is well suited to describe the mechanical response of polymer melts [195, 196]. For Neo-Hookean membranes, this set of parameters consists of normalised pressure difference $\Delta\tilde{P}_0 = \frac{R_n\Delta P_0}{\gamma}$ and normalised surface Young modulus $\tilde{Y}_{2D} = 2K_{2D}(1 - \nu_{2D})/\gamma$ where K_{2D} is the area compression modulus and ν_{2D} is the 2D Poisson ratio.

Current implementation of the shape-analysis software takes pressure difference ΔP as an additional fitting parameter. Optionally, an external measure of the pressure can be provided to the linear regression software to enhance the precision of the elastic moduli estimation, such as proposed by Hegemann *et al.* [170, 126] with their OpenCapsule software.¹

In addition to Y_{2D} and ν_{2D} , deflation also allows to fit the bending modulus of the membrane. Bending deformation is often overlooked in shape analysis for thin layers of elastic materials ($h_0 \ll R_0$, where h_0 is the undeformed skin thickness and R_0 its reference shape curvature radius). In the thin skin limit, bending moments can be neglected, and capsules are well described by elastic membrane theory. For thicker membranes however, bending cannot be neglected anymore and a better description is obtained with the elastic shell theory. Deflated capsules with thick membranes wrinkle in the meridional direction when the meridional stress becomes compressive $\sigma_\phi < 0$ [172], a phenomenon shown in Fig. 4.9a. The wrinkled region therefore extends on all the interface where this condition is met. Analysis of the wrinkle wavelength allows to fit the membrane bending modulus E_B , related to 3D Young's modulus Y_{3D} and 3D Poisson ratio by $E_B = Y_{3D}h_0/1(1 - \nu_{3D}^2)$. For thin layers of materials, the rheological properties are best described with interfacial moduli. As such, the surface Young modulus is related to its 3D counterpart through $Y_{2D} = Y_{3D}h_0$: difference of scaling between bending modulus ($E_B \propto h_0^3$) and surface Young modulus ($Y_{2D} \propto h_0$) further highlights the diminishing importance of bending deformation in the thin skin limit.

Although capsule elastometry assumes a perfectly elastic skin, non-elastic properties of the interface (e.g. viscosity and plasticity) can alter the deformation dynamics and final state. These effects cannot be measured quantitatively within the current capsule elastometry framework: however, some of these effects can still be detected by looking at the deviation from the perfectly elastic response during the course of the deformation. Changes of obtained fitted values with volume variation rate as in Fig. 4.9c indicates viscous or creep effects. A rapid change in elastic response indicates a phase change at the interface. Modification of the elastic moduli with cycle repetition is linked to fatigue and aging effects. A proper description of these effects would then require to consider the microstructure of the particular interface considered.

Despite its assumption of pure elasticity, capsule elastometry is a powerful analysis tool for thin elastic interfaces. We further turn towards its framework in Section 4.3.1 to describe drops and bubbles with elastocapillary interfaces, in the limit of small deformations. This limit corresponds to weakly compressed foams and emulsions, a scenario of great scientific interest as we have seen

¹github.com/jhegemann/opencapsule

in Chapter 3.

4.3 Constitutive law of drops with elastocapillary interfaces

Since the recent literature has seen many debates about the physically correct description of the deformation of complex interfaces, we consider it necessary to start here with a fairly general introduction to clarify our point of view and the approximations we stand on before introducing the specific concepts used later in this Chapter.

We treat here a simple model interface, as sketched in the left of Fig. 4.10. We assume it to be composed of a liquid/liquid interface of interfacial tension γ_0 , on which a permanently crosslinked, polymeric gel of thickness h_0 is grown. The liquid phase containing the gel is supposed to be a good solvent for the gel, such that the interfacial tension between the gel and the solvent is negligibly small. We furthermore assume that this gel layer is thick enough to be considered a bulk isotropic material with bulk shear modulus G_{3D} and that its mechanical response can be described by a Neo-Hookean model described in Section 4.3.2. For this purpose, we make the simplifying assumption that the gel can be considered as incompressible, in the sense that its bulk modulus is much larger than its shear modulus. Last but not least, we make the assumption that the gel is dilute enough such that neither its presence nor its deformation modifies the liquid/liquid interfacial tension, thus equal to that of a pure solvent γ_0 .

In this Section, we describe the mathematical framework using elasticity theory (Section 4.3.1) and its applications to an uniform sphere, corresponding to an idealised droplet (Section 4.3.2). In Section 4.3.3, we propose a term of geometrical correction to adapt the sphere approximation to the case of a pendant drop. Analytical equations of pressure-deformation are proposed for Gibbs, Hookean and Neo-Hookean elasticity.

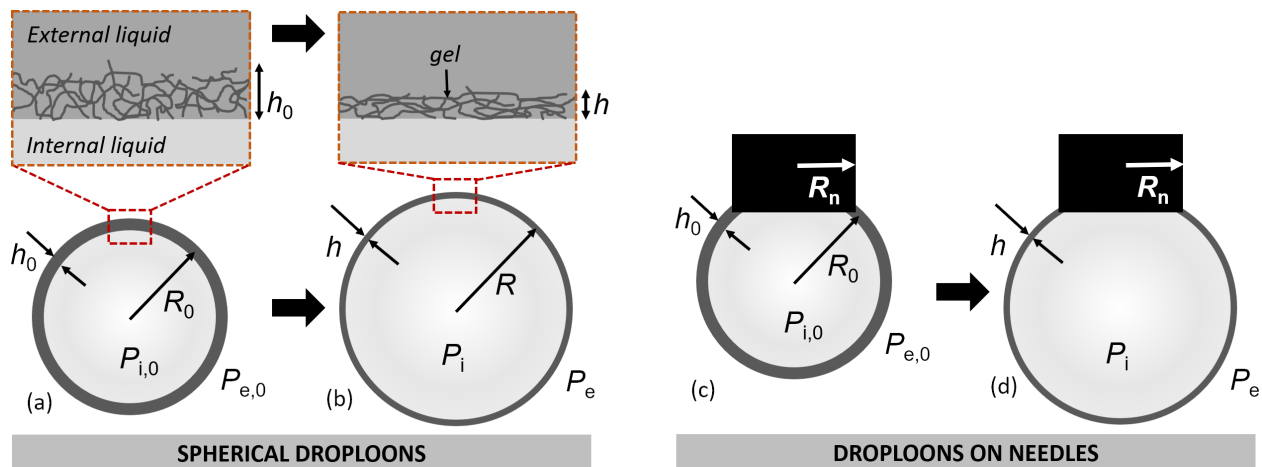


Figure 4.10: Schematics of the deformation of drops with an elastic interface, for spherical and pendant drops. The interfacial gel, of thickness h_0 , is stretched by the deformation. Its deformed thickness h can be deduced from the area dilation $\lambda_A = A/A_0$, assuming gel incompressibility. The deformation of the drops is modeled as the in- and deflation of spherical drops around a reference state of radius R_0 . These drops are either isolated or attached to a needle with a circular cross-section of radius R_n .

4.3.1 Theoretical framework

Interfaces are characterised by the amount of *interfacial free energy per surface area*, that we will denote f . If the *interfacial stress* is independent of area changes, the work needed to increase the

area by dA is $\gamma dA = f dA$; f and γ are in this case equivalent quantities. However, this is no longer true if the stress and energy density are modified by interfacial area changes. This can be due to interacting surfactant molecules in a fluid-like interface (top of Fig. 4.2), or due to a solid, elastic (polymer) skin adsorbed to the interface (bottom of Fig. 4.2), or due to a mixture of both.

In this general case, the interfacial stress is no longer necessarily isotropic and its description requires a second rank tensor σ_{ij} , where $i, j = 1, 2$ specify components in a 2D cartesian coordinate system locally tangent to the interface. Assuming that the stresses due to the liquid interfacial tension $\gamma\delta_{ij}$ and those due to the adsorbed elastic skin τ_{ij} are simply additive one may write [27]

$$\sigma_{ij} = \gamma\delta_{ij} + \tau_{ij}, \quad (4.18)$$

where δ_{ij} is the Kronecker symbol with $\delta_{ij} = 1$ if $i = j$ and $\delta_{ij} = 0$ otherwise. τ_{ij} may contain both isotropic and anisotropic contributions, in contrast to $\gamma\delta_{ij}$ which is purely isotropic. The additive decomposition in Eq. (4.18) should not be taken for granted: if surfactants are cross-linked or co-adsorbed with a polymeric skin, the different contributions to the interfacial stress may be hard to tell apart, not only experimentally but also conceptually. In the present paper, we will not consider this issue further.

Any measure of interfacial strain is based on the coordinates of a given interfacial point: X_i in the reference state and x_i after the deformation ($i = 1, 2, 3$). From these, one may derive the displacement field $U_i(X_i) = x_i - X_i$, where U_1 and U_2 are the tangential displacements and U_3 the displacement normal to the interface. For an interface with the two principal radii of curvature in the reference shape R_{01} and R_{02} , displacements give rise to an *infinitesimal* strain tensor [128] defined in Section 4.1.1

$$\varepsilon_{ij} = \frac{1}{2} \left(\frac{\partial U_i}{\partial X_j} + \frac{\partial U_j}{\partial X_i} + \frac{\partial U_3}{\partial X_i} \frac{\partial U_3}{\partial X_j} \right) + \delta_{ij} \frac{U_3}{2} \left(\frac{1}{R_{01}} + \frac{1}{R_{02}} \right) \quad (4.19)$$

describing the interfacial 2D strains ($i, j = 1, 2$). For a spherical surface, the two principal curvature radii are equal ($R_{01} = R_{02} = R_0$) and $\frac{1}{2}(\frac{1}{R_{01}} + \frac{1}{R_{02}}) = \frac{1}{R_0}$. It contains information about the deformation which is invariant to rotation and translation [128]. Following Kirchhoff's hypothesis [179], we apply classical thin shell approximations, and neglect all strains in the plane normal to the interface, $\varepsilon_{i3} = \varepsilon_{3i} = 0$ ($i = 1, 2, 3$). Both in the Surface Evolver simulations and in the shape equation calculus we will employ alternative *finite strain* measures, which are introduced below. Their relation to the infinitesimal strain tensor is provided in Appendix 8.1.

For fluid-like interfaces, stress and strain are isotropic, and in this case scalar quantities of the stress σ and the strain ε are useful. They are defined as

$$\sigma = \frac{1}{2}(\sigma_{11} + \sigma_{22}) \quad (4.20)$$

$$\varepsilon = \varepsilon_{11} + \varepsilon_{22}. \quad (4.21)$$

ε is equal to the relative variation of surface area dA/A .

A rigorous description of *finite strains* can be derived either by considering nonlinear corrections to the kinematics based on the infinitesimal strain tensor [128, 197] or using the displacement gradient tensor [195, 198]

$$F_{ij} = \frac{\partial x_i}{\partial X_j}, \quad (4.22)$$

and finally the left Cauchy-Green strain tensor

$$B_{ij} = F_{ik}F_{jk}, \quad (4.23)$$

or the right Cauchy-Green tensor

$$C_{ij} = F_{ki}F_{kj}, \quad (4.24)$$

which extract from F_{ik} information about the strain which is independent of rotation and translation. Please note that in this Chapter, we consider right Cauchy Green tensors in 2 and 3 dimensions. To avoid confusions, we denote them respectively as \mathbf{C} and \mathcal{C} .

In this Chapter, Surface Evolver computes numerically the strain of the surface using the right Cauchy-Green-Tensor, whose explicit expression in the finite element method is derived in the Appendix 8.1. For theoretical expressions, however, we will use the left Cauchy-Green tensor, to conform to the commonly used stress-strain expression derived using the Cayley-Hamilton theorem [196]. As stressed by Beatty [195], both tensors have identical principal values ($\text{Tr}(B_{ij})=\text{Tr}(C_{ij})$, $\text{Tr}(B_{ij}^2)=\text{Tr}(C_{ij}^2)$, $\det(B_{ij})=\det(C_{ij})$), and are hence equivalent regarding the computation of strain energy. In Eqs. (4.22) and (4.23), we use Einstein's summation convention: indices occurring twice should be summed over, with $i, j = 1, 2$ for 2D tensors and $i, j = 1, 2, 3$ for 3D tensors.

In some models, the Hencky strain is found to be convenient. In the case of an extension that transforms a length L measured in the reference state into a length L' , the infinitesimal strain definition in this scalar case would yield $(L - L')/L$ while the Hencky strain is defined as $\ln(L'/L)$. Extensions of the Hencky strain to the tensorial case have been discussed in the literature [199].

To build constitutive laws, the strain must be connected to energy density and stress. Shuttleworth has demonstrated the following general relation between surface stress σ_{ij} and surface energy density, assuming constant temperature [129]

$$\sigma_{ij} = f\delta_{ij} + \frac{\partial f}{\partial \varepsilon_{ij}}, \quad (4.25)$$

where $i, j=1, 2$. f combines potential energy contributions due to the excess energy of solvent molecules at the interface, adsorbed molecules or elastic potential energy of the skin.

In the case of fluid interfaces without skins where the stress is isotropic, a scalar model is sufficient. By taking half of the trace of Eq. (4.25) and using Eq.s (4.21) we obtain the average surface stress, which is equal to the surface tension

$$\sigma(\varepsilon) = \gamma(\varepsilon) = f + \frac{\partial f}{\partial \varepsilon}. \quad (4.26)$$

For the more general case, we can consider a first order expansion of $\sigma(\varepsilon)$ around the reference state yielding

$$\sigma(\varepsilon) = \sigma(0) + K\varepsilon, \quad (4.27)$$

where we have introduced the elastic dilational modulus

$$K = \left. \frac{\partial f}{\partial \varepsilon} \right|_{\varepsilon=0}. \quad (4.28)$$

In the spirit of the Hencky strain, the following alternative definition of a dilational modulus, commonly called "Gibbs modulus" (Section 4.1.1), is often used [200, 201]

$$K_G = \frac{\partial f}{\partial \ln A}. \quad (4.29)$$

For infinitesimal strains, $d \ln A = dA/A = \varepsilon$ and both definitions (Eqs. (4.28) and 4.29) coincide so that $K = K_G$. For finite strains, there is a distinction between dA/A where the area A evolves

along the deformation and $dA/A_0 = \varepsilon$ where A_0 is the area in the reference state. However, since the Gibbs modulus and the dilational modulus can vary independently as a function of strain, there is no contradiction between the two definitions. Using the Gibbs modulus and assuming its independence of strain amounts to choosing a particular type of constitutive law which appears to describe well some experimental systems [161, 199].

Let us now turn to interfaces with an adsorbed solid skin. Eq. (4.18) illustrates our simple hypothesis that the total surface stress is the sum of an interfacial tension and the elastic stress from the skin. To model this latter contribution, we focus on the case where plastic or viscous response is negligible so that the stress can be derived from a mechanical potential energy. Such materials are called hyperelastic. We focus further on incompressible materials and recall that in this case, the most general constitutive law relating the three-dimensional elastic stress to deformation can be cast in the form [195, 198]

$$\sigma_{ij}^{3D} = -p\delta_{ij} + \beta_1\mathcal{B}_{ij} - \beta_{-1}\mathcal{B}_{ij}^{-1}, \quad (4.30)$$

where $i,j=1,2,3$ and where p is the 3D pressure. The so-called response functions β_1 and β_{-1} depend on the properties of the material and must be expressed as functions of the invariants of the strain tensor to ensure frame invariance. In the simplest case, they are constants leading to what is commonly called the "Mooney-Rivlin" model. It has proven successful in describing many polymeric systems [196, 202]. Within this class of models, the case $\beta_{-1} = 0$ is of particular interest. It leads to the so called Neo-Hookean model where β_1 is equal to bulk the shear modulus G [195] so that

$$\sigma_{ij}^{3D} = -p\delta_{ij} + G\mathcal{B}_{ij}. \quad (4.31)$$

This Neo-Hookean model has been derived from a simplified microscopic description of polymer dynamics using statistical mechanics [203, 202], and it successfully describes the stress response under finite strains. Since for moderate deformations, the Neo-Hooke model remains very close to the Mooney-Rivlin model, it is the method of choice for our simulations. In the limit of small deformations, the Neo-Hookean model reduces to the well known Hookean model of linear elastic response. The 3D mechanical elastic energy density of a Neo-Hookean solid can be expressed as

$$W = \frac{G}{2}(I_B - 3), \quad (4.32)$$

where I_B is the first invariant of the left Cauchy Green tensor [195, 196] defined in Eq. (4.23), defined as its trace. This will be useful for the simulations presented in Section 4.4.

4.3.2 Perfectly spherical droploons

As given in Eq. (4.18) and sketched in Figs. 4.2 and 4.10, we assume that the total interfacial stress can be modeled as the sum of surface tension and elastic contribution. In the case of fluid-like interfaces, this elastic contribution is given by a Gibbs elasticity. In the case of a solid-like interface, the extra elastic stresses arise from a Neo-Hookean skin.

If the interface is fluid, i.e. only Gibbs elasticity is present, one can integrate Eq. (4.29) assuming a constant Gibbs dilational modulus K_G . In the limit of negligible gravity (i.e. low density mismatch between the phases or $\Delta\rho g R_0^2/\gamma_0 \ll 1$), the reference shape of the drop is spherical and the principal radii of curvature can be assumed to be equal ($R_{01} = R_{02} \equiv R_0$). This gives for a spherical droploon of radius R

$$\sigma(A) = \gamma(A) = \gamma_0 + K_G \ln\left(\frac{A}{A_0}\right) = \gamma_0 + 2K_G \ln\left(\frac{R}{R_0}\right). \quad (4.33)$$

From this, the pressure drop ΔP across the interface is obtained via the Young-Laplace law

$$\Delta P = \frac{2\gamma}{R}. \quad (4.34)$$

In the reference state $R = R_0$ and $\gamma = \gamma_0$ so that $\Delta P_0 = 2\gamma_0/R_0$.

To prepare our analysis of solid-like and fluid-like contributions, we introduce the following normalised quantities. We define an "elastocapillary number"

$$\alpha = \frac{K_{2D}}{\gamma_0}, \quad (4.35)$$

which compares the surface dilational modulus K_{2D} to the interfacial tension γ_0 of the reference state. K_{2D} is either due to Gibbs elasticity (denoted K_G in this case) or to a solid-like elasticity, as given later.

For spheres, the stretch λ is given by

$$\lambda = \frac{R}{R_0}. \quad (4.36)$$

Moreover, we introduce the normalised interfacial stress

$$\hat{\sigma} = \frac{\sigma}{\gamma_0}. \quad (4.37)$$

In the case where only Gibbs elasticity is present, the total interfacial stress is therefore given by

$$\hat{\sigma} = \hat{\gamma} = 1 + 2\alpha \ln \lambda. \quad (4.38)$$

In the small-deformation limit this reduces to

$$\hat{\sigma} = \hat{\gamma} = 1 + 2\alpha(\lambda - 1). \quad (4.39)$$

Whatever the origin of the tension and elastic response may be, the normalised pressure is obtained using

$$\Delta \hat{P} = \frac{\Delta P}{\Delta P_0} = \frac{\hat{\sigma}}{\lambda}. \quad (4.40)$$

Let us now consider solid-like interfaces. For the case of a spherical balloon with initial skin thickness $h_0 \ll R_0$, starting from Eq. (4.30), Beatty [195] derived a pressure-deformation relation valid for any hyperelastic material

$$\Delta P(\lambda) = \frac{2\sigma}{R} = \frac{2h_0}{\lambda R_0} \left[1 - \frac{1}{\lambda^6} \right] (\beta_1 - \lambda^2 \beta_{-1}). \quad (4.41)$$

In the Neo-Hookean case this yields the following expression for the elastic stress in the skin

$$\sigma_{Balloon} = Gh_0 [1 - \lambda^{-6}]. \quad (4.42)$$

In several more recent models of non-linear mechanical behavior, nonlinear variations of the response functions with the strain invariants are considered, as reviewed in [204, 205]. However, for the remainder of this Chapter, we restrict ourselves to the use of the Neo-Hookean model.

Sphere model	Normalised surface stress $\hat{\sigma}$	Critical stretch $\lambda_{A,c}$	Stretch at maximum pressure $\lambda_{A,m}$
Gibbs (liquid)	$1 + \alpha \ln \lambda_A$	$\exp\left(-\frac{1}{\alpha}\right)$	$\exp\left(2 - \frac{1}{\alpha}\right) = e^2 \lambda_{A,c}$
Neo-Hooke (solid)	$1 + \frac{\alpha}{3}(1 - \lambda_A^{-3})$	$\left(\frac{\alpha}{\alpha+3}\right)^{1/3}$	$\left(\frac{7\alpha}{\alpha+3}\right)^{1/3} = 7^{1/3} \lambda_{A,c}$
Hooke	$1 + \alpha(\lambda_A - 1)$	$\left(1 - \frac{1}{2\alpha}\right)^2$ (for $\alpha > 0.5$)	no maximum

Table 4.1: Summary of the normalised expressions for the normalised surface stress $\hat{\sigma} = \sigma/\gamma_0$; the critical stretch $\lambda_{A,c}$ at which the pressure changes sign; and the stretch at maximum pressure $\lambda_{A,m}$ for the Gibbs, Neo-Hooke and Hooke model.

We characterised the elastic skin, assumed to be isotropic and incompressible, by its 3D shear modulus G . To link it to the 2D dilational modulus, we note that the skin is in a state of plane stress, and that in this case

$$\varepsilon = \varepsilon_{11} + \varepsilon_{22} = \frac{\sigma_{11} + \sigma_{22}}{2E} = \frac{\sigma}{h_0 E} \quad (4.43)$$

where E is Young's modulus. Here, the biaxial stress in the solid induced by stretching is expressed as a skin tension divided by the skin thickness. In view of Eq. (4.27), this means that $K = Eh_0$ in the present case. For incompressible materials $E = 3G$, so that for isotropic, small deformations

$$K = 3Gh_0. \quad (4.44)$$

In the case of an elastic skin attached to an interface with tension γ_0 we therefore obtain for the elastocapillary number

$$\alpha = \frac{3Gh_0}{\gamma_0}. \quad (4.45)$$

The total interfacial stress of a spherical Neo-Hookean droplet is therefore given by

$$\hat{\sigma} = 1 + \frac{Gh_0}{\gamma_0}(1 - \lambda^{-6}) = 1 + \frac{\alpha}{3}(1 - \lambda^{-6}). \quad (4.46)$$

In the small deformation limit one obtains the prediction of the linear elastic Hooke model

$$\hat{\sigma} = 1 + 2\alpha(\lambda - 1), \quad (4.47)$$

which is identical to Eq. (4.39). This result shows that in the limit of isotropic and small deformations both Gibbs elasticity and Neo-Hookean elasticity lead to a linear elastic response captured by Hooke's law in two dimensions with a compression modulus $K_G = 3Gh_0$.

Eq. (4.47) shows that for $\alpha > 1/2$, an extensional stretch induces a positive total surface stress, acting as a restoring force while for $\alpha < 1/2$ an extensional stretch yields a negative total stress which favors further deformation. Analogous tendencies are predicted for compression. The condition $\alpha = 1/2$ has therefore received particular attention and is often called the "Gibbs criterion" since the physical response of a system may change fundamentally around this value (Section 4.3.2). This is known, for example, for the case of bubble dissolution and foam coarsening [159, 161].

In the case of spheres, it is natural to express interfacial stresses and curvatures via the radial stretch λ . However, for more general surfaces, the relationship between both depends on the geometry of the surface. In this case it is more appropriate to express the dilational stresses via the area stretch $\lambda_A = A/A_0$. For spheres, the relationship between area and radial stretch is simply

$$\lambda = \frac{R}{R_0} = \left(\frac{A}{A_0}\right)^{1/2} = \lambda_A^{1/2}. \quad (4.48)$$

In Table 4.1 we summarise the interfacial stresses for the Gibbs, Neo-Hookean and Hookean model expressed via their area stretches, together with some critical stretches which are discussed in Section 4.5.1. In the following we will use those relations.

4.3.3 Droploons on capillaries

Let us now consider droploons attached to capillaries with circular cross-section of radius R_n (Fig. 4.10). In this case one geometrically removes a cap of radius R_n from the droploon and fixes the perimeter of the resulting circular hole to the end of the capillary. For fluid interfaces with Gibbs elasticity, the interfacial stresses are isotropic and constant everywhere in the interface, even if the droploon is inflated or deflated. Hence, the droploon shapes remain spherical sectors and, as we show below, all pressure-deformation relations can be calculated analytically, giving useful insight into the impact of the geometry change. In the case of interfaces with a solid skin, this is much less straightforward. Fixing the interface points on the capillary boundary induces shear deformation in the vicinity of the capillary upon inflation or deflation and hence deviations from the shape of a perfect sphere. The presence of the capillary in the case of a solid-like skin therefore combines a geometrical impact (as for the Gibbs elasticity) with one of a non-isotropic deformation. Both contributions are coupled and their relative importance depends on the capillary number α , on the deformation A/A_0 and on the capillary-to-drop size ratio R_n/R_0 .

Let us assume in the following that shear stresses remain negligible and that we can estimate the droploon shape by spherical sectors derived from perfect spheres of radius R from which a cap of radius R_n is removed, as depicted in Fig. 4.10. The interfacial area A is then given by

$$A(R) = 2\pi R^2 \left(1 \mp \sqrt{1 - \left(\frac{R_n}{R}\right)^2} \right), \quad (4.49)$$

where the two signs correspond to droploons larger than a hemisphere ("+") or smaller than a hemisphere ("-"). The latter geometry introduces a major difference between drops with and without capillaries: the radius of the drop *increases* upon further deflation from the hemisphere. This changes dramatically the pressure-deformation relation, which is why we will exclude this case in the remaining discussion.

Eq. (4.49) can be used to relate the area stretch λ_A and the radial stretch λ via

$$\begin{aligned} \lambda &= \lambda_A^{1/2} \frac{1 + \sqrt{1 - \left(\frac{R_n}{R_0}\right)^2}}{\sqrt{2 \left[1 + \sqrt{1 - \left(\frac{R_n}{R_0}\right)^2} \right] - \left(\frac{R_n}{R_0}\right)^2 \frac{1}{\lambda_A}}} \\ &= \lambda_A^{1/2} f \left(\frac{R_n}{R_0}, \lambda_A \right). \end{aligned} \quad (4.50)$$

i.e. when comparing with the full sphere expression of Eq. (4.36), the presence of the capillary introduces a correction factor $f \left(\frac{R_n}{R_0}, \lambda_A \right)$ to the relationship between the radial and the area stretch.

For a given area stretch λ_A - which is experimentally and computationally more easily accessible than the radial stretch λ - we can then rewrite the pressure-deformation relation as

$$\Delta \hat{P} = \frac{\hat{\sigma}(\lambda_A)}{\lambda} = \frac{\hat{\sigma}(\lambda_A)}{\lambda_A^{1/2}} f^{-1} = \Delta \hat{P}_S f^{-1}, \quad (4.51)$$

where $\Delta \hat{P}_S$ is the pressure of the sphere with the same area stretch and the interfacial stress $\hat{\sigma}$ is given in Table 4.1 for the different models. Hence, in the approximation of negligible shear

contributions, the capillary may be considered to impose a simple geometrical correction on the pressure-deformation relation which depends only on the capillary size $\frac{R_n}{R_0}$ and the area stretch λ_A . In the case of fluid-like interfaces (Gibbs elasticity), Eq. (4.51) is accurate, while in the case of solid-like interfaces (Neo-Hooke & Hooke), this is an approximation. We shall see in Section 4.5.2 that this remains nevertheless an excellent approximation over a wide range of parameters.

Here we have chosen to express the pressure-deformation relations in terms of area stretch λ_A since it simplifies comparison with simulations and experiments. One may also choose to express them in terms of radial stretch λ . In this case it is the expression of the interfacial stress $\hat{\sigma}$ which needs to be modified, leading to more complex expressions. We provide these relations for the interested reader in Appendix 8.2.

4.4 Numerical modelling

4.4.1 Surface Evolver simulations

Surface Evolver [9] is a widely used software that determines the equilibrium structure of systems containing several fluid phases separated by interfaces. It uses the principle that in equilibrium, the interfacial energy must be minimal under the constraints imposed by boundary conditions. Examples of this are foams where the volume of each bubble is fixed [206, 105, 72, 13]. Surface Evolver can also be used to model elastic membranes [16, 184].

In Surface Evolver simulations, interfaces are represented as meshes of triangular facets whose energy is evaluated. Most previous studies on bubble or drop shapes focus on systems where this energy is proportional to the interfacial area, the proportionality factor being the surface tension γ . Additionally to this contribution, Surface Evolver simulations can also take into account an elastic energy induced by the deformation of each facet, simulating an elastic skin. Several constitutive laws are implemented in the Evolver Software and can be used: Hooke's law describing linear elastic response, as well as the non-linear Saint-Venant or Neo-Hooke's law [16]. In the work reported here, we use Neo-Hooke's law introduced in Section 4.3.1. We implement, for the first time to our knowledge, an interface with both surface tension and Neo-Hooke interfacial elasticity. As a first implementation, we thoroughly compare Surface Evolver results to the numerical solution of the shape equations (Section 4.4.2), and ensure that it provides physically sound results in the investigated range of parameters.

In contrast to fluid interfaces where the interfacial area uniquely determines the energy, the energy of elastic skins depends on their deformation with respect to a reference state Ω . The reference state of an interface element is given by a shape with zero interfacial elastic stress. This state is encoded in the reference positions of the facet vertices. The implementation of elastic stress in the framework of the Surface Evolver requires an expression of the facet deformation energy for arbitrary large strains, given as a function of the vertex positions. A detailed presentation of this feature and the implementation of elastic energy in the Surface Evolver has not been published so far to our knowledge. We therefore provide this information in the Appendix 8.1 to clarify for the interested reader how exactly the software operates. Here we shall concentrate on a very general description of the approach.

Our Surface Evolver calculations simulate an experiment where a bubble or drop is inflated at the tip of a cylindrical hollow capillary inserted into a liquid, as illustrated in Fig. 4.10. In the first step, we need to obtain a physically correct reference shape for a drop without interfacial elasticity. For this purpose, an initially very coarse mesh is attached to a cylindrical boundary representing the capillary. The interfacial area is then minimised for the given drop target volume assuming that

interfacial energy is due only to a uniform and constant surface tension². Successive refinements and energy minimisations of the mesh are then performed to simulate the drop shape and the pressure in the reference bubble accurately. When the relative variation of total interfacial energy $|E^{n+1} - E^n|/E^n$ remains smaller than 10^{-8} over 100 iteration steps we consider that convergence has been achieved.

In the second step of the simulation, an elastic skin is added to the drop surface of the obtained reference state, so that initially there is no elastic stress. Numerically, it consists in saving the current positions $\{\vec{X}_i\}$ of the vertices as their reference positions, and setting a non-zero elastic modulus value for the interfacial energy computation for further minimisation iterations. How reference and current positions are used for deformation computation is detailed in Appendix 8.1. The third step consists in inflating or deflating this droploon up to a new volume where mechanical equilibrium is again established via progressive mesh relaxation. Frequent merging of facets significantly smaller than average and refinement of facets larger than average hastens convergence whilst avoiding to trap the system in local energy minima. These operations are all performed by Surface Evolver in-built routines as part of a standard energy minimisation procedure. When the mesh management and energy minimisation have converged ($|E^{n+1} - E^n|/E^n < 10^{-8}$), the elastic stress in the skin, the pressure in the bubble and the bubble shapes are recorded.

4.4.2 Numerical integration of the shape equations

We solve for the shape and stress/strain profile of an axi-symmetric capsule by numerically integrating the *shape equations* [170, 126]. Because we impose axial symmetry, the droploon can be parametrised as a single arc with arc length s and arc angle Ψ as sketched in Fig. 4.6c. The transformation from arc length parametrisation to cylindrical coordinates $\{r, \phi, z\}$ gives the first two shape equations

$$\frac{dr}{ds} = \cos \Psi \quad \text{and} \quad \frac{dz}{ds} = \sin \Psi. \quad (4.52)$$

The remaining shape equations, needed to close the set of partial differential equations, take into account the constitutive material law and reflect the force balance at every point along the arc s . They are derived by searching for the stationary solutions of the appropriate energy functional.

In the experimentally relevant setting we control either the droploon volume or the mechanical pressure at the capillary inlet. Thus, the appropriate energy functional is the enthalpy

$$H = \int dA_0 W_{2D} + \int dA \gamma_0 - \int dV \Delta P, \quad (4.53)$$

with a contribution from the elastic surface energy W_{2D} , measured with respect to the undeformed area A_0 , from the surface tension γ_0 and from the volumetric work against a pressure difference ΔP . We find the stationary states of the enthalpy H of Eq. (4.53) via the first variation, $\delta H = 0$ (see [126, 170] for details), leading to the shape equations

$$\frac{d\Psi}{ds} = \kappa_s = \frac{1}{\sigma_s} (\Delta P - \kappa_\phi \sigma_\phi), \quad (4.54)$$

$$\frac{d\sigma_s}{ds} = \frac{\cos \Psi}{r} (\sigma_\phi - \sigma_s), \quad (4.55)$$

where (κ_s, κ_ϕ) and (σ_s, σ_ϕ) are the meridional and circumferential curvatures and surface stresses, respectively. The curvatures are given by $\kappa_\phi = \sin \Psi / r$ and $\kappa_s = d\Psi / ds$. Note that the shape

²This could represent a physical system where the elastic skin forms progressively at an initially "naked" interface

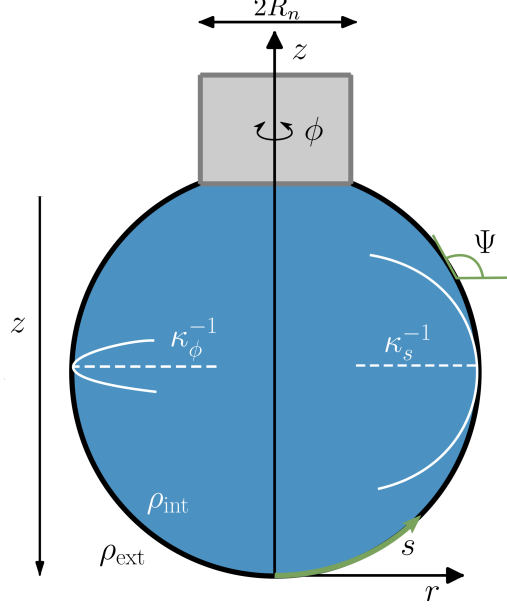


Figure 4.11: Schematic of a pendant droplet parametrised in arc-length s and arc-angle Ψ . Figure adapted from [174].

equations (4.52), (4.54) and (4.55) still require a constitutive material law for closure. At this point, no detailed knowledge about the 2D surface energy functional W_{2D} is required, as we define

$$\sigma_{s,\phi} = \frac{1}{\lambda_{\phi,s}} \left(\frac{\partial W_{2D}}{\partial \lambda_{s,\phi}} + \frac{\partial(\gamma_0 \lambda_s \lambda_\phi)}{\partial \lambda_{s,\phi}} \right), \quad (4.56)$$

where λ_s and λ_ϕ are the meridional and circumferential stretch ratios of the droplet. The shape equations (4.52), (4.54) and (4.55) are written in terms of the arc length s of the deformed shape. For the numerical solution we reparametrise in terms of the *undeformed* arc length coordinate s_0 of the original undeformed shape by using the relation $ds/ds_0 = \lambda_s$, which is necessary in order to gain access to the meridional stretches λ_s . The circumferential stress $\lambda_\phi = r/r_0$ is given by the ratio of undeformed and deformed radial coordinate.

The surface energy W_{2D} accounts for the material specific model and can incorporate various effects, such as film thinning. To express the constitutive equation in terms of our parametrisation we write the right 2D Cauchy-Green tensor, discussed in Section 4.4 and in Appendix 8.1, as

$$\mathbf{C} = \text{diag}(\lambda_s^2, \lambda_\phi^2). \quad (4.57)$$

For a two-dimensional Neo-Hookean elastic material the surface energy is given by Eq. (8.26) from the Appendix 8.1.2

$$W_{2D} = \frac{Gh_0}{2} \left(\text{Tr} \mathbf{C} + \mathcal{C}_{33} + \frac{G}{\Lambda} \mathcal{C}_{33}^2 \right). \quad (4.58)$$

with 3D Lamé parameters G and Λ . Here, \mathbf{C} is the 2D Cauchy-Green tensor describing deformations within the surface, while \mathcal{C}_{33} is the component of the 3D Cauchy-Green tensor describing normal (thickness) deformations of the elastic skin. Requiring the absence of normal stresses, \mathcal{C}_{33} becomes a function of G/Λ and $\det \mathbf{C}$ as derived in Appendix 8.1.2.

From this surface energy, we extract the constitutive law needed to close the shape equations using Eq. (4.56),

$$\sigma_{s,\phi} = Gh_0 \left(\frac{\lambda_{s,\phi}}{\lambda_{\phi,s}} - \frac{\mathcal{C}_{33}}{\lambda_s \lambda_\phi} \right) + \gamma_0. \quad (4.59)$$

In the following, we focus on the incompressible limit $G/\Lambda \ll 1$, where $\mathcal{C}_{33} \approx 1/\det\mathbf{C} = 1/\lambda_s^2\lambda_\phi^2$.

For a given undeformed shape (described by a function $r_0(s_0)$), the shape equations, along with the constitutive equations, are numerically integrated from the apex ($s = 0$) to the attachment point at the capillary ($s = L$) using a Runge-Kutta scheme, paired with a shooting algorithm to satisfy the boundary conditions

$$r(s = 0) = z(s = 0) = \Psi(s = 0) = 0 \quad \text{and} \quad r(s = L) = R_n. \quad (4.60)$$

In the fitting procedure, we prescribe an apex stress $\sigma_s(s = 0)$ and iteratively search for a pressure drop ΔP satisfying the attachment boundary condition at the capillary. Moreover, we restrict the prescribed apex stresses to the physically relevant ones for our context giving $\sigma_s(s = 0) > 0$ (no compressive stresses), and do not exceed the maximal possible apex stress allowed by the constitutive equations, $\sigma_{s,\phi}(s = 0)^{\max} = Gh_0 + \gamma_0$.

4.5 Results

In Section 4.5.1 we compare the theoretical predictions of the different elastic laws in Eqs. (4.38), (4.45) and (4.46), and the results obtained from Surface Evolver simulations. In Section 4.5.2, we compare the numerical simulations to the analytical predictions where the needle is treated as a geometrical perturbation truncating an isotropic droploon (Section 4.3.3). These two results are compared to the direct numerical predictions (Section 4.4.2), which account both for the geometrical perturbation and the anisotropy imposed by the needle. Finally, we quantify the perturbation of the pressure induced by the needle, and show that it can be in large part explained by the geometrical perturbation. In the last step, we use the direct numerical predictions to quantify the importance of anisotropic stretches, and provide experimentalists with guidelines to predict the parameter ranges over which the influence of the capillary (shape change and/or stress anisotropy) can be neglected.

4.5.1 Spherical droploons

We run Neo-Hookean Surface Evolver simulations (Section 4.4.1) for spheres with four different elastocapillary numbers ($\alpha = 0.1, 0.5, 1, 10$, as defined in Eq. (4.45)) imposing inflation and deflation while recording the normalised pressure difference $\Delta\hat{P}$. The results are shown in Fig. 4.12 as a function of area stretch λ_A along with the theoretical predictions for the Gibbs, Hooke and Neo-Hooke models provided in Section 4.3.2.

The simulations show excellent agreement with the Neo-Hookean theory over the full range of investigated deformations. As expected and discussed in Section 4.3.2, all three models coincide in the small deformation limit $\lambda_A \approx 1$. However, for deformations of a few percent, the three models already show very pronounced differences, indicating the importance of choosing the physically most realistic model for the interpretation of pressure-deformation relations.

For non-zero α , in the case of the Gibbs and Neo-Hookean elasticity, the initially monotonously decreasing Young-Laplace-like behaviour is replaced by a pressure-deformation relation with a well-pronounced pressure maximum $\Delta\hat{P}(\lambda_{A,m})$ at a characteristic stretch $\lambda_{A,m}$. Upon deflation ($\lambda_A < 1$), this leads to the apparition of a critical stretch $\lambda_{A,c}$ at which the pressure difference is zero, and beyond which it becomes negative. This point corresponds to elastic instabilities of compressed interfaces, which manifest themselves in buckling phenomena [128, 188, 207]. A proper handling of this range requires to take into account the bending energies of the interfaces. Since this is neither of interest here, nor implemented in our simulations, we stay away from the buckling range in our analysis.

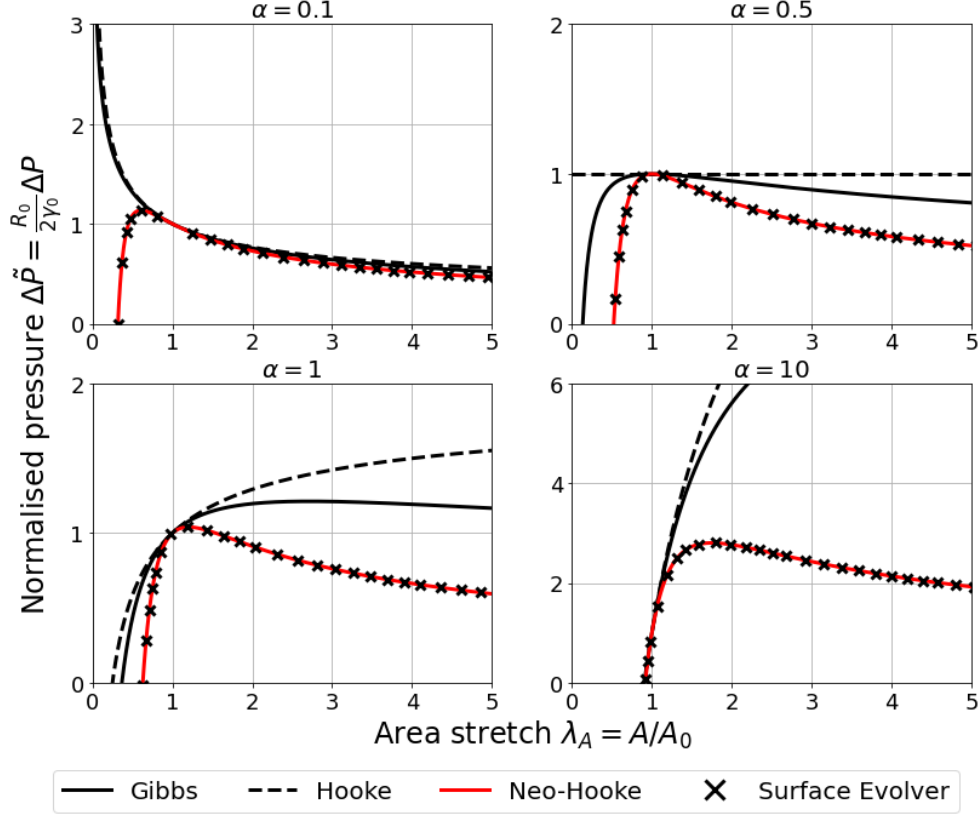


Figure 4.12: Normalised pressure as a function of area stretch λ_A for spherical droplets whose skin elasticity is described by Gibbs', Neo-Hooke's or Hooke's law. Four characteristic elastocapillary number values ($\alpha = 0.1, 0.5, 1, 10$) are investigated. The data obtained by Surface Evolver simulations are obtained assuming Neo-Hookean elasticity.

The variation of $\lambda_{A,c}$, $\lambda_{A,m}$ and of the pressure difference $\Delta\tilde{P}$ at $\lambda_{A,m}$ with elastocapillary number α for the different models are shown in Fig. 4.13. The corresponding analytical expressions are given in Table 4.1. They put in evidence clear differences between Gibbs, Hookean and Neo-Hookean models. In comparison to Gibbs elasticity, the Neo-Hookean critical and maximal stretches vary only mildly with α . The Surface Evolver results again agree very well with theory. The critical stretch for Hooke's model appears when the elastocapillary number crosses the Gibbs criterion $\alpha = 0.5$. The Gibbs critical stretch tends exponentially towards 0, as $\lambda_{A,c} = \exp(-1/\alpha)$. In the limit of large α , the critical stretches all converge towards $\lambda_{A,c} = 1$, that is, a shell so rigid that it buckles as soon as compressed. Hooke elasticity does not predict a local pressure maximum at any elastocapillary number. But it predicts an interesting deformation-independent pressure for $\alpha = 0.5$, i.e. at the "Gibbs criterion". Gibbs and Neo-Hooke, on the other hand, have a maximal pressure stretch increasing with α . In particular, at the Gibbs criterion $\alpha = 0.5$, the maximal pressure is reached at null deformation ($\lambda = 1$). Lower elastocapillary numbers move $\lambda_{A,m}$ to the compression regime ($\lambda_{A,m} < 1$), while $\alpha > 0.5$ shift $\lambda_{A,m}$ to the dilation regime ($\lambda_{A,m} > 1$). The most remarkable features of the elastocapillary transition (onset of significant critical stretch, variation of the maximal pressure stretch) occur for elastocapillary numbers between 0.1 and 10. For this reason, we expose in this article results for $\alpha = 0.1, 1$ and 10, so as to span two decades of elastocapillary numbers. Because of its history as the Gibbs criterion and its pivot point between capillarity and elasticity, $\alpha = 0.5$ will also be represented.

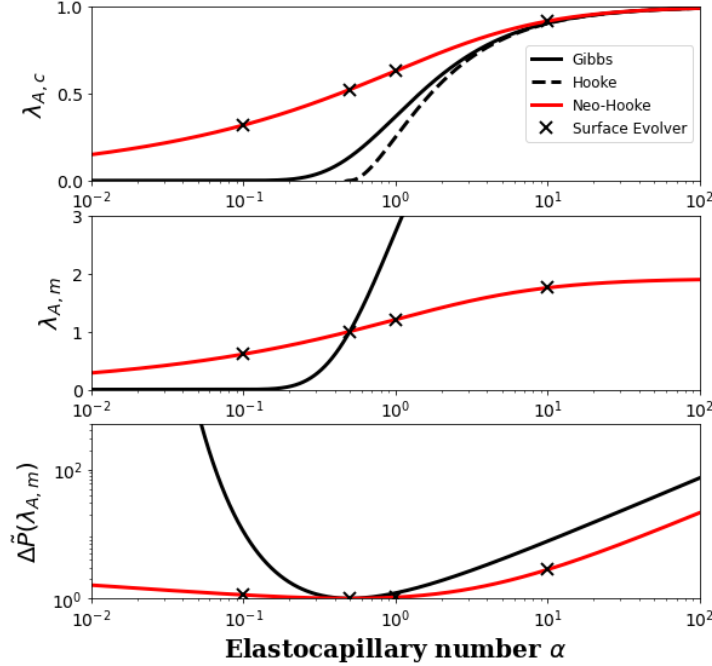


Figure 4.13: Variation of characteristic features (critical area stretch $\lambda_{A,c}$, stretch $\lambda_{A,m}$ at maximum pressure and maximum pressure $\Delta\hat{P}(\lambda_{A,m})$) with the elastocapillary number α predicted for droploons with skins presenting Gibbs, Neo-Hookean and Hookean elasticity. Surface Evolver simulations are performed for the Neo-Hooke case.

4.5.2 Droploons on capillaries

In a second step, we run Surface Evolver simulations of pendant droploons attached to a capillary with circular cross-section of radius R_n (Fig. 4.10c-d). The droploons are inflated and deflated while their interfacial area and inner pressure are recorded (Section 4.4.1). Three ratios between the capillary radius R_n and the radius R_0 of the droploon in the reference configuration are used: $R_n/R_0 = 0.1, 0.5$ and 0.9 . Representative examples of obtained droploon shapes are shown in Fig. 4.14 for three characteristic area stretches ($\lambda_A = 0.8, 1, 2$) for the case of $\alpha = 0.5$.

In Fig. 4.15 we show the obtained pressure-deformation relations for the elastocapillary numbers $\alpha = 0.1, 0.5, 1, 10$. Along with the Surface Evolver results (crosses) we plot results obtained by direct numerical predictions (empty circles) using the Neo-Hookean shape equations for the same set of parameters (Section 4.4.2). The excellent agreement between both for all elastocapillary numbers, capillary radii and deformations demonstrates the reliability of Surface Evolver simulations for such systems.

The solid lines shown in Fig. 4.15 correspond to the analytical approximation given in Eq. (4.51) which models droplets as spherical sectors covered with a Neo-Hookean skin. The agreement is excellent in the whole deformation range for all capillary sizes and elastocapillary numbers. This means that in this parameter range the deviation from the predictions for spherical droploons without any capillary (gray line in Fig. 4.15) are essentially a result of the associated change of the geometry induced by the capillary, rather than due to the shear deformation in the vicinity of the capillary. Deviations from the simple model set in only for large capillary sizes ($R_n/R_0 = 0.9$) and large elastocapillary numbers ($\alpha = 10$).

To investigate why the spherical sector approximations fit the results so well, Fig. 4.16 plots different measures of the anisotropy of the stretch distributions on the droploon surface obtained

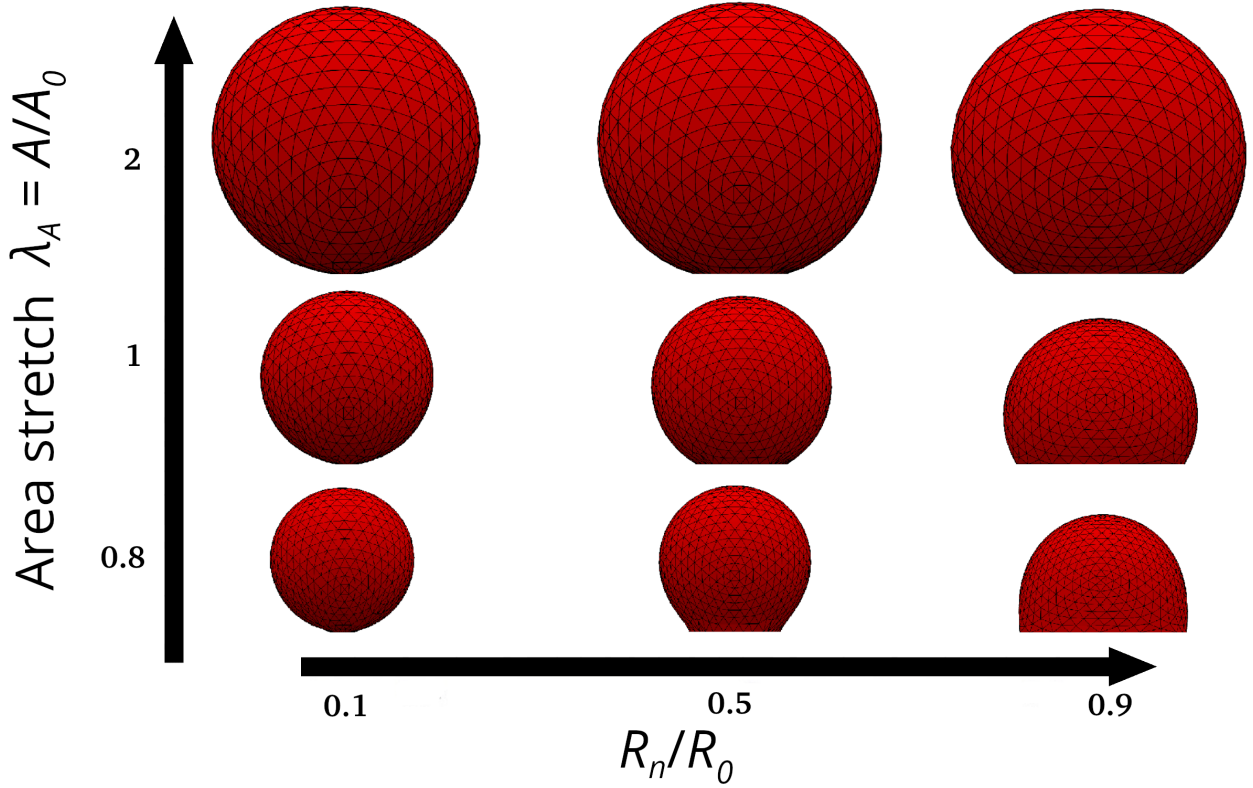


Figure 4.14: Examples of Neo-Hookean droploons at different area stretches and capillary ratios R_n/R_0 obtained for $\alpha = 0.5$ using Surface Evolver.

from the Neo-Hookean shape equations for the same parameter ranges as in Fig. 4.15. In the case of fully isotropic deformation, corresponding to a spherical sector shape, the deviation of the mean stretch ratio along the contour $\langle \frac{\lambda_s}{\lambda_\phi} \rangle - 1$ (Fig. 4.16a,b) and the standard deviation of the meridional and circumferential stretches $\text{std}_s(\lambda_{s,\phi})$ (Fig. 4.16c,d) are both zero. Since we neglect gravitational effects, it is clear that the unstressed shape of the capsule at $\lambda_A = 1$ *must* be a spherical sector. The stretched shape will be anisotropically stressed, in general, because of the boundary condition imposed by the attachment at the capillary. We can find, however, another particular stretch, where the *stressed* shape is a spherical sector. This is reached at the critical stretch $\lambda_{A,c}$ (see also Section 4.5.1) at which $\Delta \hat{P} = 0$. The force balance for every point on the capsule requires that the pressure force cancels the tension force. For $\Delta \hat{P} = 0$, we therefore have $\sigma_s = \sigma_\phi = 0$ all over the surface, i.e. the surface is stress-free everywhere at this critical stretch. Since $\sigma_s = \sigma_\phi = 0$ implies isotropic stretching, the shape at this point is again correctly described by the spherical sector equation (4.51). If the stretch is further decreased to $\lambda_A < \lambda_{A,c}$ both $\sigma_s < 0$ and $\sigma_\phi < 0$ will become compressive and buckling or wrinkling instabilities of the droploon interface will occur [128, 126].

For stretch values other than $\lambda_A = 1$ or $\lambda_{A,c}$, the droploon shape is non-spherical, because of the anisotropy ($\lambda_s \neq \lambda_\phi$) introduced by the boundary condition at the capillary. This can clearly be seen in Figs. 4.16a,b. For inflated shapes $\lambda_A > 1$, we find $\langle \frac{\lambda_s}{\lambda_\phi} \rangle - 1 > 0$ indicating that stretching is biased towards meridional deformations resulting in slightly prolate shapes, whereas for deflated

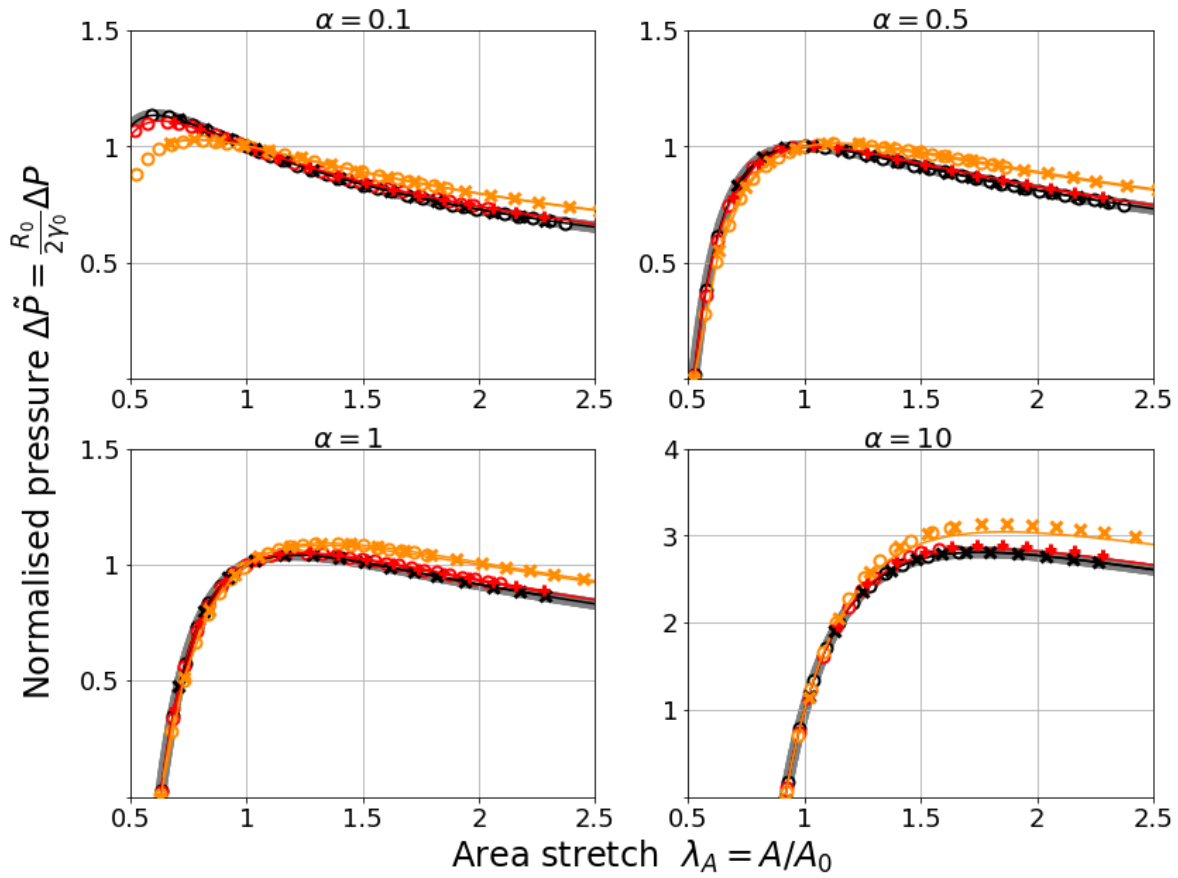


Figure 4.15: Normalised pressure as a function of area stretch λ_A of Neo-Hookean droplets on capillaries for three ratios of capillary and initial droplet radius ($R_n/R_0 = 0.1, 0.5, 0.9$), and four characteristic elastocapillary numbers ($\alpha = 0.1, 0.5, 1, 10$). Surface Evolver simulations are compared with direct numerical predictions (Section 4.4) and with the analytical expression of Eq. (4.46) using a simple geometrical correction to the perfect sphere theory.

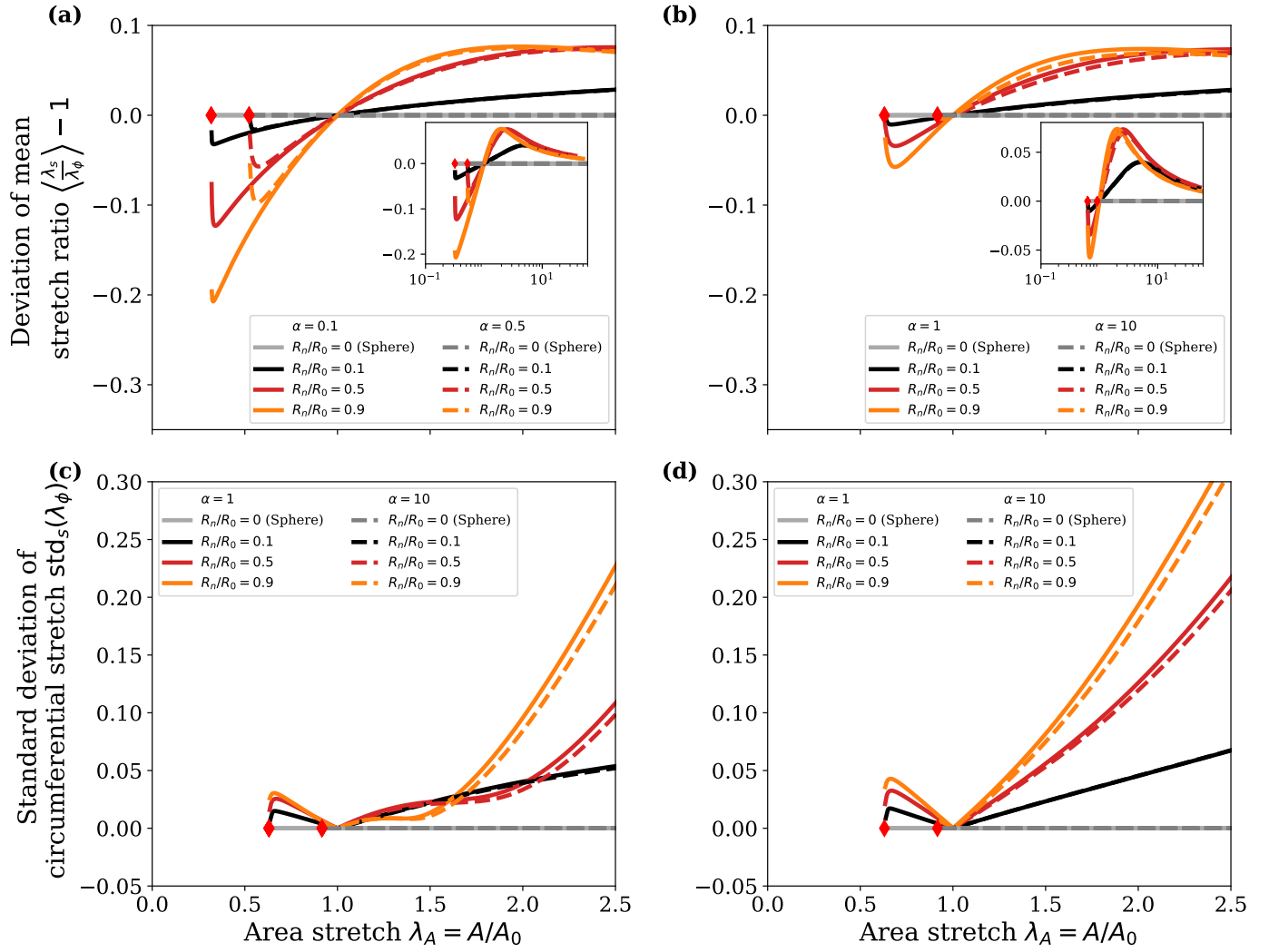


Figure 4.16: Characterization of the stretch anisotropy and the stretch inhomogeneity. (a,b) The mean ratio of meridional and circumferential stretches $\langle \frac{\lambda_s}{\lambda_\phi} \rangle - 1$ along the contour characterizes stretch anisotropy and is shown for (a) $\alpha \leq 0.5$ and (b) $\alpha > 0.5$. The standard deviations of (c) meridional stretches λ_s and (d) circumferential stretches λ_ϕ along the contour characterize the inhomogeneity of stretches. We show the critical stretches $\lambda_{A,c}$ as red diamonds in (a-d).

shapes $\lambda_A < 1$, $\left\langle \frac{\lambda_s}{\lambda_\phi} \right\rangle - 1 < 0$ and circumferential deformations are preferred, resulting in slightly oblate shapes. The mean anisotropy increases upon inflation before decreasing again at much higher stretches (see the insets in Fig. 4.16a,b for a wider deformation range), when the influence of the capillary becomes again negligible.

Furthermore, the standard deviation of the stretches along the contour $\text{std}_s(\lambda_s)$ and $\text{std}_s(\lambda_\phi)$ shown in Figs. 4.16c,d characterizes the inhomogeneity of the stretches along a contour. A standard deviation of $\text{std}_s(\lambda_s) = \text{std}_s(\lambda_\phi) = 0$ corresponds to a spherical sector. The meridional and circumferential stretches of an inflated droploon are isotropic at the apex with $\lambda_s(s=0) = \lambda_\phi(s=0)$. At the capillary, the attachment condition mandates $\lambda_\phi^{\text{cap}} = 1$ while λ_s^{cap} increases with λ_A , which introduces anisotropy and inhomogeneity into the problem with meridional stresses accumulating at the capillary. The spherical approximation will hold well for shapes where the stretches are approximately *homogeneous* over a large arc length, corresponding to a small standard deviation of the stretches, and *isotropic*, corresponding to a mean stretch along the contour $\left\langle \frac{\lambda_s}{\lambda_\phi} \right\rangle$ close to unity. This is fulfilled at the two spherical configurations $\lambda_A = 1$ and $\lambda_{A,c}$. The spherical configuration with $\lambda_{A,c}$ appears to be highly sensitive, and small changes in λ_A lead to large deviations in the anisotropy (and inhomogeneity). It is interesting to note that at small deformations around $\lambda_A = 1$, the anisotropy evolution depends only on the ratio R_n/R_0 and not on α .

We argue that the evolution of the anisotropy and inhomogeneity can be grasped by considering that the capillary acts similarly to a rigid inclusion in a stretched elastic membrane as both enforce the absence of circumferential stretching ($\lambda_\phi = 1$) at their boundary. A rigid inclusion in a stretched elastic membrane is known to concentrate the meridional stresses creating anisotropy and inhomogeneity, similar to the stress concentration around a crack tip. For flat membranes, a rigid inclusion is a classic problem that was studied for Neo-Hookean membranes by Wong and Shield [208]. For the droploon we have a curved geometry, which gives rise to an even more pronounced increase of anisotropy around the capillary.

We see clear evidence of the increased anisotropy around the capillary in numerical solutions to the full anisotropic shape equations from Section 4.4.2 as shown in Fig. 4.17. In Fig. 4.17a,b,c, we show the stretch ratios λ_s and λ_ϕ and the redistribution of arc length along the contour of inflated droploons. These results show the rise of meridional stretch close to the capillary. Fig. 4.17d reveals that the resulting stretch anisotropy $\lambda_s/\lambda_\phi - 1$ is localised at the capillary and that it decays exponentially over a characteristic arc length s_0^* away from the capillary. Here, s_0 is the arc length of the undeformed reference shape (the spherical droplet), which is related to the arc length s of the deformed shape by the meridional stretch ratio, $ds/ds_0 = \lambda_s$ (see section 4.4.2). We use the logarithmic derivative of $\lambda_s/\lambda_\phi - 1$ to numerically determine the size s_0^* of the zone of increased anisotropy around the capillary.

We propose that the relative meridional extent of the anisotropy zone along the *deformed* droploon contour provides a non-dimensional number Q , which is suitable to characterize the importance of elastic anisotropy effects in the regime $\alpha > 1$, where elastic energies dominate. We thus define $Q \equiv s^*/L$, where s^* is the meridional length of the anisotropy region measured in terms of the *deformed* arc length, while L is the total arc length of the deformed droploon contour. For $\alpha < 1$, elastic energies are small compared to droplet surface tension such that also elastic anisotropy becomes less important.

In order to evaluate the anisotropy parameter Q , we use the general relation $ds/ds_0 = \lambda_s$ between deformed and undeformed arc length at the capillary and $L \sim \pi R_0 \lambda_A^{1/2}$ for the total arc length L in the limit $R_n \ll R_0$ to obtain

$$Q \equiv \frac{s^*}{L} \sim \frac{s_0^* \lambda_s^{\text{cap}}}{L} \sim \frac{s_0^* \lambda_s^{\text{cap}}}{\pi R_0} \lambda_A^{-1/2} \quad (4.61)$$

where λ_s^{cap} is the meridional stretch at the capillary. To make further progress, we derive relations for the size s_0^* of the anisotropy zone and the stretch ratio λ_s^{cap} at the capillary from numerical results shown in Fig. 4.18.

Because the maximal stretch anisotropy is found at the capillary and $\lambda_\phi = 1$ at the capillary, the meridional stretch at the capillary actually equals the maximal stretch anisotropy, $\max\left(\frac{\lambda_s}{\lambda_\phi}\right) = \lambda_s^{\text{cap}}$. While in the case of flat membranes the maximal anisotropy $\lambda_s^{\text{cap}} \propto \lambda_s(s = \infty)$ is proportional to the radial stretch at infinity [208], our numerical results for curved droploons indicate that λ_s^{cap} first increases upon inflation $\lambda_A > 1$ but saturates for highly inflated droploons with area stretches λ_A exceeding a fairly well-defined value λ_A^\dagger , as shown in Fig. 4.18c for the case of $\alpha = 10$. Further numerical analysis of the saturation value as performed in Fig. 4.18b allows us to quantify the saturation value as

$$\max\left(\frac{\lambda_s}{\lambda_\phi}\right) \approx \lambda_s^{\text{cap}} \equiv \text{const} \left(\frac{R_n}{R_0}\right)^{-1/3} \quad (4.62)$$

with $\text{const} \approx 1.47$ in the regime $\alpha > 1$. This saturation value is solely determined by the geometrical parameter R_n/R_0 of the undeformed droploon, which demonstrates that saturation is induced by droplet curvature. We also find $\lambda_A^\dagger \sim (\lambda_s^{\text{cap}})^{3/2}$ for the area stretch, where saturation of the maximal anisotropy sets in. The maximal anisotropy given in Eq. (4.62) diverges in the limit $R_n/R_0 \approx 0$, which seems counter-intuitive at first, because the spherical approximation works best for exactly this limit. This issue will be resolved below.

Let us quantify the size s_0^* of the anisotropy zone around the capillary. From Fig. 4.18a, we find a conservative bound

$$s_0^* \leq \frac{R_n}{2}. \quad (4.63)$$

This relation reveals that the size of the stretch anisotropy zone is set by the geometry parameter R_n/R_0 of the reference state rather than the elastocapillary number α .

Using Eq. eq4.63 for s_0^* and the saturation value given in Eq. (4.62) for λ_s^{cap} in (4.61), we obtain

$$Q = \frac{\text{const}}{2\pi} \left(\frac{R_n}{R_0}\right)^{2/3} \frac{1}{\lambda_A^{1/2}} \quad (4.64)$$

for the anisotropy parameter Q for highly inflated droploons $\lambda_A > \lambda_A^\dagger$. This parameter remains small for $R_n \ll R_0$ indicating that we can neglect anisotropy effects in this limit.

At smaller deformations $1 < \lambda_A < \lambda_A^\dagger$, where saturation of the capillary anisotropy has not yet set in, we numerically find that the maximal stretch anisotropy scales with $\log(\lambda_A)$ (see Fig. 4.18c), giving

$$Q = \frac{R_n}{R_0} \frac{\lambda_s^{\text{cap}} - 1}{3\pi \log(\lambda_s^{\text{cap}})} \frac{\log(\lambda_A)}{\lambda_A^{1/2}}, \quad (4.65)$$

where we again use the saturation value λ_s^{cap} from Eq. (4.62).

We obtain a full contour plot of the anisotropy parameter Q in Fig. 4.18d by joining the results in the two regimes ($\lambda_A > \lambda_A^\dagger$ and $\lambda_A < \lambda_A^\dagger$) with a smooth interpolating function. This plot confirms that Q is small ($Q \ll 1$) for shapes where the spherical approximation works best. In particular, we find that we can neglect anisotropy effects ($Q \ll 1$) in the limit $R_n/R_0 \approx 0$, resolving the counter-intuitive behaviour of the maximal anisotropy. We emphasize the fact that Eq. (4.65) only depends on R_n/R_0 and λ_A and *not* on α , as long as $\alpha > 1$. This indicates that stretch anisotropy is mainly governed by geometry rather than by elastic energy contributions. As already pointed out above, elastic contributions and, thus, also elastic anisotropy effects become increasingly irrelevant

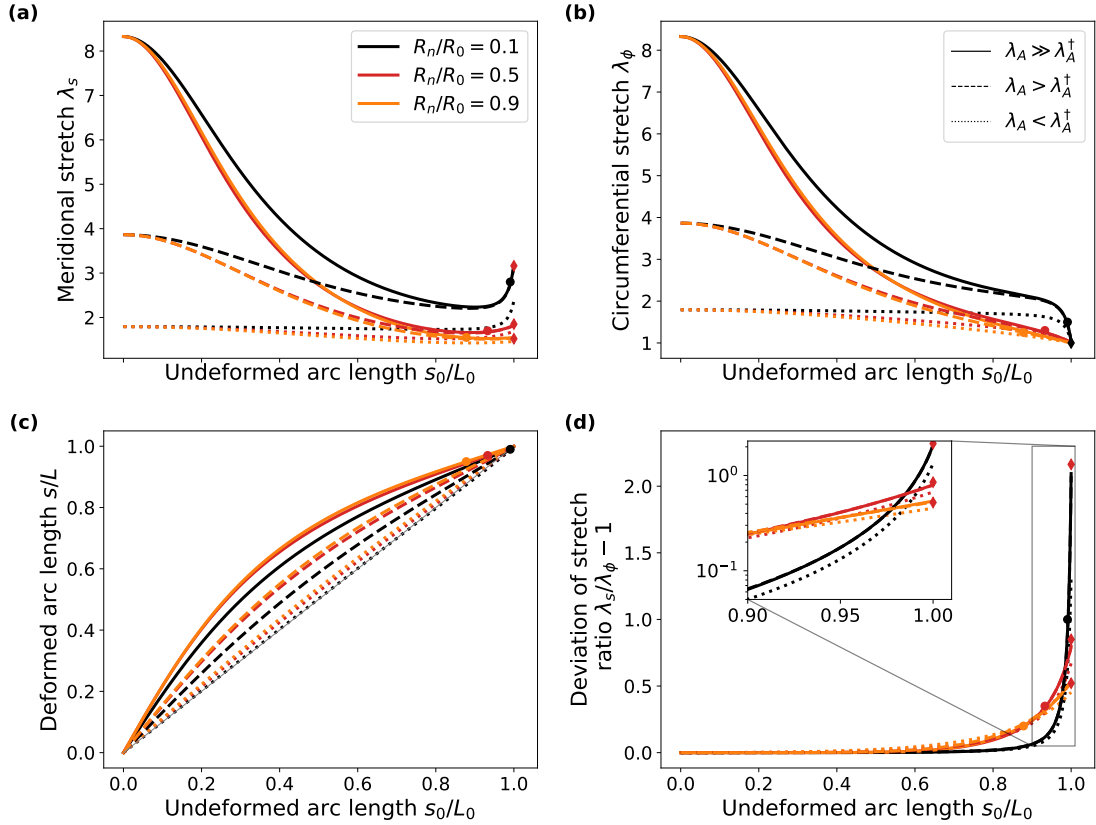


Figure 4.17: Stretch anisotropy of droplon shapes with $\alpha = 10$ for three values of R_n/R_0 for each of three area stretches $\lambda_A \gg \lambda_A^\dagger$, $\lambda_A > \lambda_A^\dagger$, and $\lambda_A < \lambda_A^\dagger$ (see also Fig. 4.18 for a definition of the characteristic area stretch λ_A^\dagger). (a,b) Stretch ratios λ_s and λ_ϕ as a function of the undeformed arc length s_0/L_0 along the contour. While λ_ϕ is approaching the undeformed value of 1 at the capillary ($s_0/L_0 = 1$), λ_s rises at the capillary. (c) shows that the deformed arc length s considerably deviates from the undeformed arc length s_0 along the contour. (d) The resulting stretch anisotropy $\lambda_s/\lambda_\phi - 1$ is localized at the capillary. The size of the anisotropy zone around the capillary can be characterized by an exponential decay arc length s_0^* , which is calculated from the logarithmic derivative of $\lambda_s/\lambda_\phi - 1$ at the capillary for the solid lines and shown as colored dots in all plots (a-d). We also show the maximal stretch at the capillary from Eq. (4.62) as red diamonds in (a) and (d).

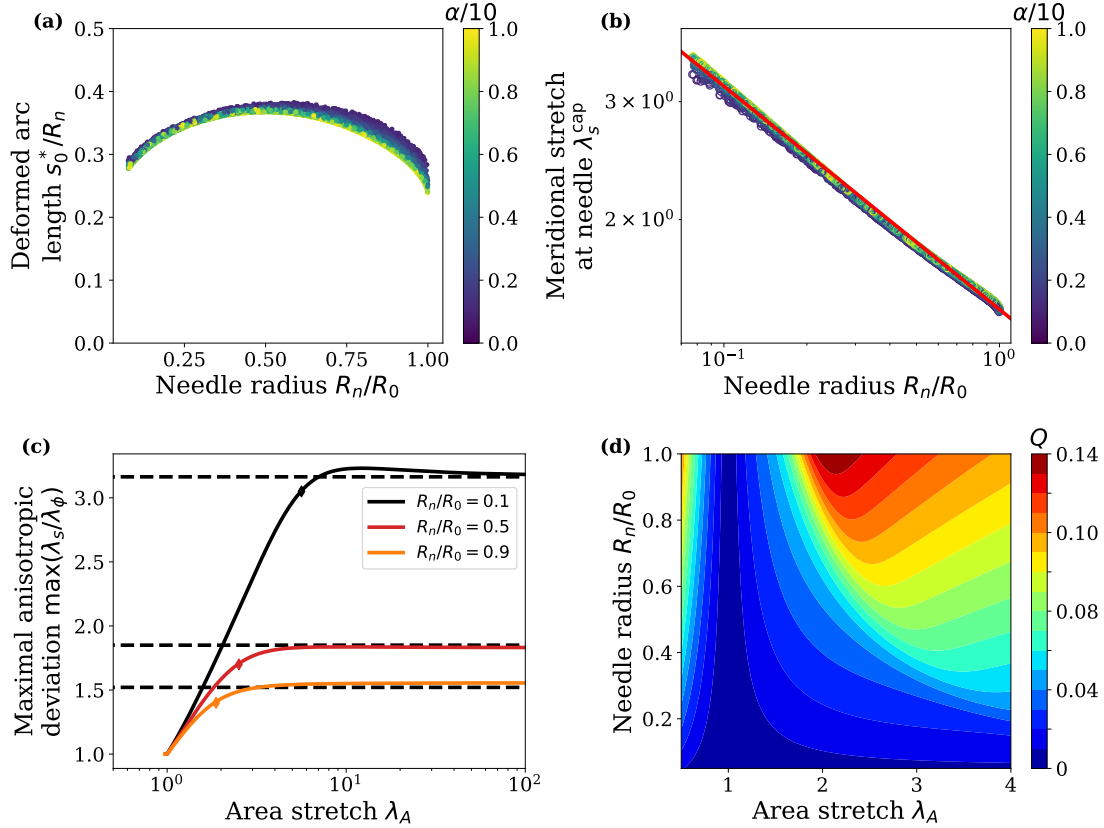


Figure 4.18: Analysis of the anisotropy zone and the anisotropy parameter Q from numerical solutions of the anisotropic shape equations. (a) The size of the anisotropy zone s_0^* is roughly constant giving rise to the bound (4.63). (b) The saturation value is mainly determined by the parameter (R_n/R_0) , see Eq. (4.62). (c) As a function of the area stretch λ_A , the maximum anisotropy saturates at large deformations beyond a value λ_A^\dagger (results for $\alpha = 10$ shown as colored diamonds). (d) Contour plot of the non-dimensional anisotropy parameter Q according to Eq. (4.61). Stretch anisotropy effects are negligible for $Q \ll 1$.

for $\alpha < 1$, where surface tension dominates and the shape resembles a spherical liquid droplet. The regions $\lambda_A > \lambda_A^\dagger$ and $\lambda_A < \lambda_A^\dagger$ differ markedly in their functional dependence on λ_A . This results in a maximum of the parameter Q for area stretches $\lambda_A \sim \lambda_A^\dagger \propto (R_n/R_0)^{-1/2}$ at a fixed value of R_n/R_0 . This, in turn, indicates that stretch anisotropy is most relevant for these intermediate area stretches.

The possibility of approximating the droploon shape by a spherical sector over a wide range of parameters is an important piece of information for experimentalists since it means that the analytical expression of Eq. (4.51) can be used to quantify reliably the elastocapillary properties of the droploon interfaces over a reasonably wide range of elastocapillary numbers. We also remind the reader that from the expressions it is evident that within our geometrical approximations, the critical area stretch at which the pressure changes sign is independent of the size of the capillary. The combined numerical analysis provides another important piece of information: for reasonably small capillary sizes ($R_n/R_0 < 0.5$), the pressure-deformation relation is actually well described by the simple sphere equations without capillary (Section 4.3.2), making the quantitative interpretation of experimental data fairly straightforward. In order to quantify the deviation from the simple sphere theory, we plot in Fig. 4.19 the heatmap of the normalised deviation of the numerically predicted pressure $\Delta\hat{P}$ with capillary (using Surface Evolver) from that predicted by the sphere theory $\Delta\hat{P}_S$

for a given area stretch, i.e. we plot

$$\left| \frac{\Delta \hat{P}_S - \Delta \hat{P}}{\Delta \hat{P}} \right| = \left| 1 - \frac{\Delta \hat{P}_S}{\Delta \hat{P}} \right|. \quad (4.66)$$

Making the spherical sector hypothesis of Eq. (4.51), this expression becomes simply

$$\left| 1 - \frac{\Delta \hat{P}_S}{\Delta \hat{P}} \right| = |1 - f|, \quad (4.67)$$

which is plotted as lines of equal relative error. These isolines are identical in all four graphs of Fig. 4.19 since they are independent of α (see Eq.(4.50)).

Deviations of the heatmaps in Fig. 4.19 from the geometrical prediction have two origins: imperfect relaxation in the simulations and the influence of shear contributions of the solid skin which are neglected in the geometrical approximations. The first is at the origin of most of the deviations for $\alpha < 10$, while the latter starts to be clearly visible for $\alpha = 10$. Nevertheless, this latter difference remains small ($< 0.5\%$), confirming again that shear contributions play a minor role in most of the investigated parameter range in accordance with the non-dimensional Q -parameter plotted in Fig. 4.18d. Our geometrically-corrected pressure-deformation relation of Eq. (4.51), although not accounting for stretch anisotropy, is therefore a very good approximation for pendant drops with Neo-Hookean elastic interfaces within the parameter range investigated here.

Let us now turn to the analysis of the heatmaps themselves. They indicate that in the small deformation limit ($\lambda_A \approx 1$), the error made in using the sphere approximation remains smaller than 1% at any radii ratio and elastocapillary number. For larger deformations in the inflation regime ($\lambda_A > 1$), the approximation error is still smaller than 1% for small capillary radii ($R_n/R_0 < 0.2$). Similar behaviour is observed in the deflation regime. However, the prediction systematically fails when approaching the critical stretch $\lambda_{A,c}$. This is because wrinkling instabilities in the skin may become relevant in this regime. This phenomenon can be captured neither within the sphere approximation, nor by our Surface Evolver simulations where the skin bending energy - crucial for wrinkling - is not taken into account. Skin bending can be implemented in Surface Evolver, but is beyond the scope of this paper. In the heatmaps we have therefore colored these zones in gray.

At small α and large R_n/R_0 an additional zone of large approximation error ($> 10\%$) appears for pressures $\Delta \hat{P} \approx 1$. This deviation arises from the increasing difference between sphere and truncated sphere geometry: As the truncated sphere shrinks, it reaches the shape of a half-sphere of radius R_n . Any further decrease in drop volume causes an actual increase in curvature radius which is not captured by the sphere theory, hence the failure of the analytical prediction beyond this point in the parameters space.

Despite those considerations for large capillary radii, the heatmaps of Fig. 4.19 provide very good news for the experimentalist aiming to quantify the elastic properties of droploon surfaces: when working with reasonable capillary sizes ($R_n/R_0 < 0.5$), reasonably small deformations (< 0.1) and reasonable elastocapillary numbers ($\alpha < 10$), experimental data can be confidently fitted by the simple sphere theory (without capillary) since experimental errors are likely to outweigh the small error introduced by the sphere assumption.

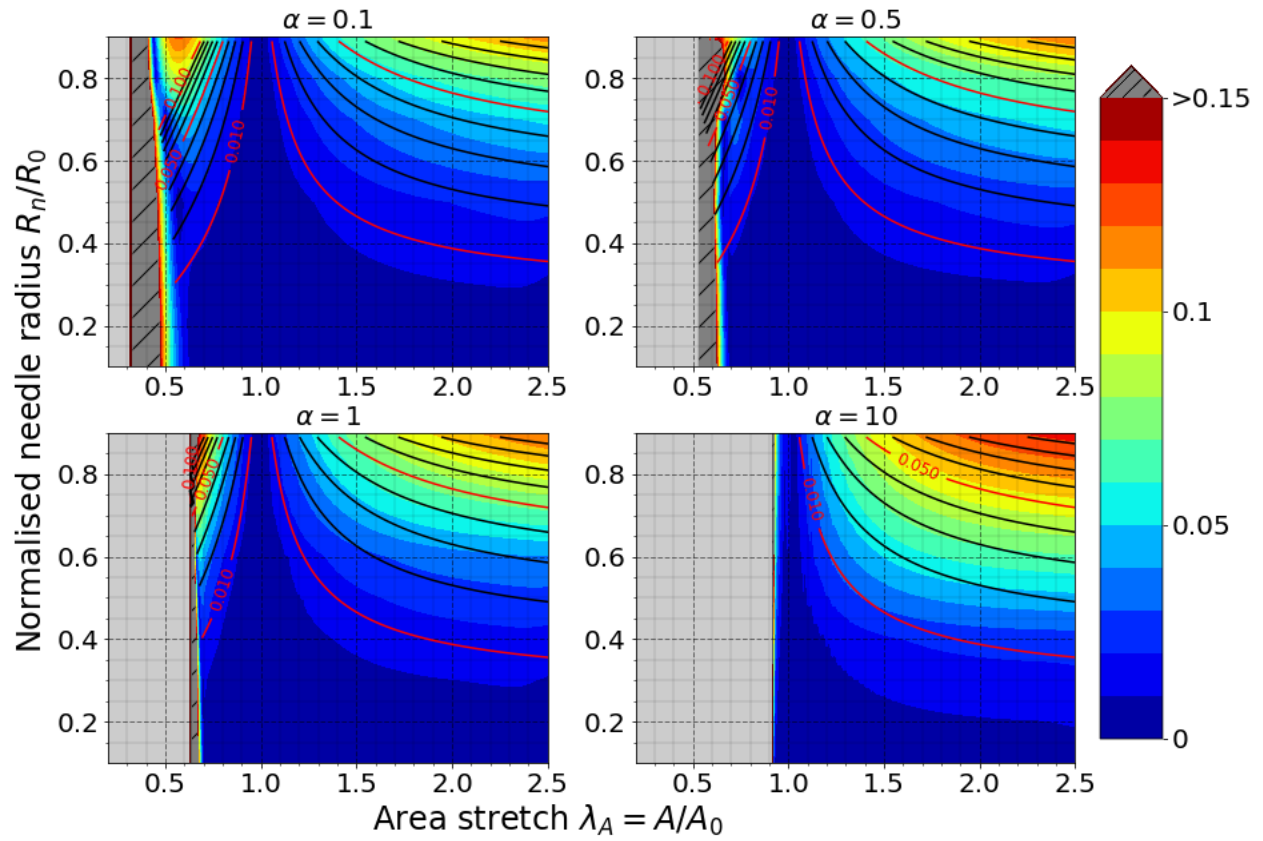


Figure 4.19: Relative error of pressure difference between Surface Evolver and Neo-Hookean perfect sphere, at the same area stretch λ_A for four elastocapillary numbers ($\alpha = 0.1, 0.5, 1, 10$). The grey boxes delimit the stretch values below critical stretch value $\lambda_{A,c}$. Full lines are lines of equal relative error between the Neo-Hookean perfect sphere and the Neo-Hookean truncated sphere, given by Eq. (4.67).

4.6 Conclusion and outlook

Treating the seemingly simple problem of a drop covered by an elastic skin attached to a circular capillary in the absence of gravity, we have been able to show that Surface Evolver simulations are a powerful tool to study systems in which surface tension and nonlinear (Neo-Hookean) elasticity co-exist within the same interface. We have chosen on purpose such a simple geometry, in order to avail of independent theoretical and numerical predictions relying on cylindrical symmetry (Section 4.3.3 and Section 4.4.2) which can be compared to the Surface Evolver solutions. In all cases, they showed excellent agreement. Surface Evolver will therefore be useful to tackle more complex geometries, such as droploons on complex capillary shapes, interacting droploons or complete emulsions composed of droploons, where theory or alternative numerical predictions requiring symmetry will not be available. In contrast to other finite element tools, the energy minimisation approach of Surface Evolver, widely used in the communities studying foams and emulsions, provides access to a wide range of problems in which interfaces of complex geometry play a key role. In the Appendix we provide a detailed description of the implementation of nonlinear elasticity in Surface Evolver simulations to facilitate future developments, and we also provide our Surface Evolver code for download in the supplementary materials of the associated publication [209]. Taking into account bending stiffness in the simulations would be an interesting perspective for future work.

For simplicity, we have been talking about drops/droploons all along. However, all presented concepts are equally valid for bubbles/bubbloons and hence for foams. Our analysis shows how complex the interplay of capillary and elastic forces at an interface is, even for the relatively simple geometry of an initially spherical droploon inflated on a circular capillary. Due to the intricate coupling of changes in interfacial curvature and area, accurate theoretical models and simulations are required to extract interfacial properties quantitatively from measured pressure-deformation relations.

The problem of the pressure deformation of a droploon covered by an elastic skin and attached to a capillary in the absence of gravity is a seemingly simple problem. From the point of view of elasticity theory it is challenging, however, because the elastic skin represents a closed curved shell and the capillary a rigid circular inclusion within this shell. Holes or rigid inclusions in elastic membranes are known to produce stress anisotropies and stress concentration upon stretching. Here, the droploon skin is stretched by inflation, contains a rigid inclusion and features the additional complication of a background curvature because the initial relaxed shape is spherical (neglecting gravity). We obtained theoretical predictions regarding the influence of the stress anisotropy induced by the capillary onto the pressure-deformation relation from Surface Evolver simulations and a careful numerical analysis of stresses and strains in the shape equation approach. A full analytical solution remains an open problem for future research.

In the parameter range investigated by our simulations, we have been able to show that for elastocapillary numbers of $\alpha < 10$ the influence of the capillary on the pressure-deformation relation is essentially of geometrical nature, i.e. the capillary modifies in the first place the relationship between the area stretch (related to interfacial stress) and the interface curvature. In this case, the droploon shapes can be represented approximately by spherical sectors and the pressure-deformation relation is given by Eq. (4.51). For interfaces with Gibbs elasticity, this expression is exact, while for (Neo-)Hookean interfaces it remains an (excellent) approximation. Deviations from this simple geometrical approximation are starting to be significant for the largest capillary sizes ($R_n/R_0 = 0.9$) and elastocapillary number ($\alpha = 10$) simulated by us, suggesting that the anisotropic contribution to the interfacial stress and deformation near the capillary is starting to

play a role.

To show that this anisotropy is indeed strongly localised at the capillary, we calculate, as a function of position on the interface, the deviation of the ratio of meridional and circumferential stretches from one. This quantity decays nearly exponentially with the distance from the capillary, over a characteristic length s^* . The extent of this anisotropically strained zone can be compared to the total droploon size by defining the non-dimensional ratio $Q = s^*/L$, where L is the total arc length of the droploon. For droploon inflation and for $\alpha > 1$, we find

$$Q = \frac{R_n}{R_0} \frac{\lambda_s^{\text{cap}} - 1}{3\pi \log(\lambda_s^{\text{cap}})} \frac{\log(\lambda_A)}{\lambda_A^{1/2}}, \quad (4.68)$$

with

$$\lambda_s^{\text{cap}} \equiv \text{const} \left(\frac{R_n}{R_0} \right)^{-1/3}, \quad (4.69)$$

being the "saturation" meridional stretch reached at the capillary for large deformations and $\text{const} = 1.47$. For large deformations, we therefore obtain

$$Q = \frac{\text{const}}{2\pi} \left(\frac{R_n}{R_0} \right)^{2/3} \frac{1}{\lambda_A^{1/2}}. \quad (4.70)$$

These relations and their analysis provided in Section 4.5.2 and Fig. 4.18 put in evidence that the extent of the anisotropic zone (and hence its influence on the pressure-deformation relation), is mainly controlled by the reference geometry of the droploon (R_n/R_0) and by the stretch λ_A . We therefore show for the first time that the extent of this zone is essentially governed by geometrical features while the influence of the elastocapillary number α remains negligible. These are very good news for experimentalists who can rely on the spherical droploon equations given in Table 4.1 combined with the geometrical correction of Eq. (4.50) to fit their data for a wide range of α as long as R_n/R_0 and λ_A remain reasonable. The heatmaps and relations provided in Section 4.5.2 will help to estimate the appropriate parameter ranges.

More importantly for the analysis of experimental data, we have also shown that when working with sufficiently small capillaries ($R_n/R_0 < 0.5$) and at small deformations ($\sim 5\%$ area), the simple analytical pressure-deformation relations of spheres *without* capillaries (Table 4.1) provide excellent approximations to the pressure-deformation relations of droploons on capillaries. The much simpler analytical relations of Table 4.1 can therefore be used to extract quantitative interfacial properties from fits to experimental data. Experimentalists are referred to Fig. 4.19 to estimate the error they make using this approximation.

In Section 4.3.2 we showed that for small deformations, the Gibbs, Neo-Hookean and Hookean models for liquid- and solid-like interfaces all predict the same kind of pressure-deformation relation. In view of the analysis presented above, this may explain why a lot of experimental data for solid-like interfaces seems to have been successfully fitted in the past by the Gibbs model. Indeed, our analysis shows that at small deformations, pendant drop experiments with nearly spherical droploons do not allow to discriminate between liquid-like and solid-like interfaces. Alternative experiments, such as interfacial shear rheology measurements or the CMD [172] are required to obtain this information.

We have chosen here a minimal model of a droploon interface where the elastic extra stress of a Neo-Hookean solid material is simply added to a constant interfacial tension. Real interfaces are not as simple [117, 192, 210, 132, 211, 28, 26, 199, 212]. Surface tension and elasticity tend to be

coupled in a complex manner [199], and the description of the response of the elastic membrane is likely to require taking into account an anisotropic, viscous and plastic response as well as non-linearities which are more complex than those of the Neo-Hookean model. Nevertheless, our simple approach already gives important insight into some fundamental properties of pressure-deformation relations of pendant droploons.

Considering that pendant drop experiments, even in the simplest configuration without gravity, overlay a geometric non-linearity with non-linearities in the material response of a solid-like interfacial material, it remains questionable if this is the appropriate experimental choice to discriminate between appropriate models to describe solid-like interfaces. Differences between models are likely to show up only at larger deformations which makes the interpretation extremely difficult. However, due to their simplicity, pendant drop experiments remain an excellent choice for a phenomenological characterisation of the dilational visco-elastic properties at small deformation.

Last but not least, all our investigations have been performed without gravity, while pendant drops (and bubbles) are prone to gravity-driven deformations rendering them non-spherical. We recall that for a nearly spherical drop the Bond number $Bo = \Delta\rho g R_0^2 / \gamma_0$ indicates the ratio of the hydrostatic pressure difference between the top and the bottom of the bubble $\Delta\rho g 2R_0$ and the Laplace pressure which is due to surface tension $2\gamma_0/R_0$. The impact of gravity on bubble shape is negligible if $Bo \ll 1$. If density-matched systems cannot be used, very small bubbles may therefore be a solution [213] to reduce the impact of gravity. This also has the advantage to increase the interface curvature, and hence the pressure and therefore experimental sensitivity.

If gravity-driven deformation cannot be completely avoided, the following two aspects need to be taken into account. The first influence of gravity is on the shape of the droploon in the reference state. Gravity may create a concave neck close to the capillary, which creates additional stress localisation. Using numerical investigations of the droplet shape bifurcation diagram (yellow line of bifurcations in Figs. 4 and 5 of Ref. [174]), we could show in previous work that only for

$$\frac{R_n}{R_0} < 2.6Bo^{1.64}, \quad (4.71)$$

the drop remains fully convex and neck formation can be neglected.

The second aspect concerns deformation with elastic skins, where the increasing droploon size upon inflation or the decreasing effective surface stresses upon deflation may make the system increasingly sensitive to gravity. In this case one may want to introduce an elastic Bond number which contains the deformation-dependent elastic contribution to the surface stress based on the Hookean expression (4.47)

$$Bo_{el} = \frac{\Delta\rho g}{\gamma_0(1 + 2\alpha(\lambda - 1))} \lambda^2 R_0^2. \quad (4.72)$$

For sufficiently small elastic Bond numbers, gravity can then be neglected. Since gravity can be implemented easily in Surface Evolver, future investigations may explore the influence of gravity more quantitatively.

Chapter 5

Rheological properties of the PEG-silicone gel

5.1 Introduction

In ordinary, static foams/emulsions, the interactions between bubbles/drops happen at their interfacial contacts. As typical bubble/drop scale is micrometric, thermal fluctuations are negligible in their motion. The large-scale organisation of foams/emulsions is thus dictated by these interactions. The relations between inter-grain interactions and collective properties of grain assemblies is an important field of investigation in granular science, as explained in Chapter 3 [44, 37, 41, 43]. The great variety of possible interactions, with sometimes competing effects, makes granular materials very sensitive to the detail of properties of their grains. For instance, adhesion between grains favours the contacts between the grains rather than between the grains and their medium, triggering flocculation well below the critical packing fraction of non-adhesive grains [214, 215]. Liquid bridges between grains creates attractive capillary forces, making the whole system more resistant to yielding [216]. Frictional surfaces, locking rotational and translational degrees of freedom of tangential forces below the Coulomb criterion [32], decrease the number of neighbours Z_c at the jamming transition and the packing fraction ϕ_l^* of the jamming transition [43]. On the other hand of the spectrum, ordinary foams and emulsions are driven only by capillary interactions, allowing for good physical insight by resorting to simple scaling arguments [45, 78, 77] : shear and bulk moduli in the static regime scale with excess packing fraction and interfacial tension $G_0 \sim \gamma_0/R_{32} \cdot (\phi_l(\phi_l - \phi_l^*))$ [79, 80]. The osmotic pressure similarly scales the interfacial tension, with $\Pi_l \sim \gamma_0/R_{32} \cdot ((\phi_l - \phi_l^*)^2/\sqrt{\phi_l})$ [45, 46]. As we show in Chapter 3, the deformation caused by the contact forces is in competition with the interfacial tension of the bubble, which tends to keep it spherical. A simple and relevant normalisation of the contact forces thus comes with the force associated with interfacial tension γ_0/R_{32} , as shown in the equations of the shear modulus and the osmotic pressure above.

Droploons, being grains with deformable, elastocapillary interfaces, are likely to have packing properties differing both from emulsions and granular systems. In fact, previous work by Giustiniani *et al.* [10] shows that drops with elastocapillary interfaces adopt geometrical configurations different from purely capillary emulsions and granular systems as shown in Fig. 5.1e. This difference also manifests at the bubble scale, with drops deforming differently than in ordinary emulsions, as shown in Fig. 5.1f. The PEG-silicone model system studied in this chapter is based on the PEG-in-silicone emulsion system described in [10]. It consists of PEG drops containing Karstedt's catalyst dispersed in vinyl-terminated PDMS, in a continuous phase of base agent Sylgard-184[®],

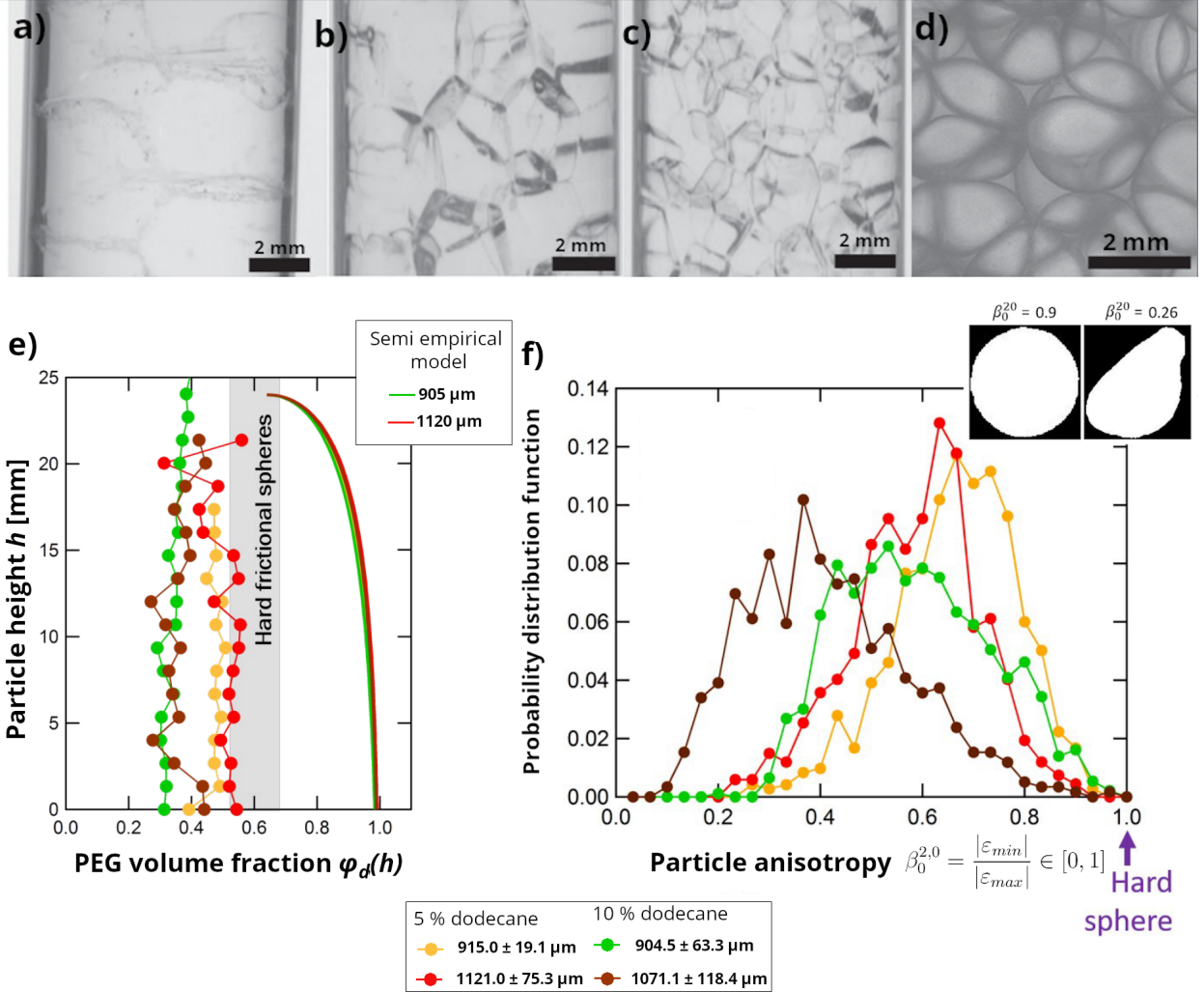


Figure 5.1: properties of PEG-in-silicone emulsions for different drop sizes and interfacial elasticity/adhesion controlled by the addition of dodecane in the silicone phase. a-c) PEG 400 in MHDS 2000-25 emulsion produced with microfluidic T-junction, confined in a tube with diameter of 2 times (a), 3 times (b) and 4.6 times (c) the drop diameter. The increasing tube diameter modified the structure of the emulsion, with an increasingly disordered geometry. d) PEG 400 emulsion in Sylgard-184[®], with mean drop radius of 850 μm . Authors link the more spherical shape to the presence of a gel in the continuous phase, formed at the interface. Four samples from Giustiniani *et al.* [10]. e) Evolution of PEG fraction with emulsion height for the PEG/Sylgard system [10], compared to a semi-empirical model for simple emulsions. [46, 71]. f) Distribution of the anisotropy of the drops, measured with the ratio of maximal and minimal eigenvalues (ε_{max} and ε_{min} , respectively) of Minkowski's tensor $\mathbf{W}_0^{2,0} = \int_K \vec{r} \otimes \vec{r} dV$ defined over a body K . Inset : XY slices of two extremal values of anisotropy. Figure from [217]. Authors suggest that the addition of dodecane increases the elastic modulus of the membrane, and that the changes in liquid profile and shape deformation is related to the change in rigidity.

a commercially available PDMS elastomer. The commercial curing agent is replaced with the unreactive octamethylcyclotetrasiloxane D_4 to get the same physical properties of the mixture. Dodecane is added to the silicone mixture to tune the viscous properties of the silicone phase, which also modifies the interactions between the drops. The platinum catalyst, diffuses from the PEG to the silicone phase. It triggers a first reaction between the C-OH groups of the PEG molecules and the Si-OH groups of the Sylgard, forming block-copolymers PDMS-b-PEG at the interface while releasing water. The Si-OH groups also react with each others, crosslinking the PDMS polymers and forming a solid PDMS skin from the interface. This reaction goes on until the whole silicone phase is crosslinked, effectively forming a gelified silicone matrix.

The volume fraction of the drops, as well as its evolution with emulsion height, depends on the interfacial properties. The individual shapes of the droplets are also affected, with shapes found to be more anisotropic when probed with the Minkowski's tensor $W_0^{2,0}$ [217], as shown in Fig. 5.1f. This tensor is defined over a body K by

$$W_0^{2,0} = \int_K \vec{r} \cdot \vec{r} dV, \quad (5.1)$$

which can be interpreted as the tensor of moments distribution. The ratio of the minimal and maximal eigenvalues $\beta_0^{2,0} = \left| \frac{\varepsilon_{min}}{\varepsilon_{max}} \right|$ serves as a measure of the anisotropy of the drops, with 1 corresponding to perfectly spherical shapes and $\beta_0^{2,0}$ becoming progressively smaller than 1 with increasing anisotropy.

The description of the transition from hard grains to packings of soft grains with elastocapillary interfaces requires a constitutive model. As we show in Chapter 3, the deformation of individual drops/bubbles is well described using only the interfacial tension and the Young-Laplace equation. In Chapter 4, we describe the elastic stresses as an additive term to the interfacial tension, leading to an effective interfacial tension γ . We present a range of experimental conditions where this approximation remains valid. This effective interfacial tension γ is a first, simple step towards the description of elastocapillary interactions where γ can be transferred directly in the scaling laws of foam and emulsion mechanics. In this chapter, we present our work to find and characterise an experimental model system to study the transition from a purely capillary interface to a purely elastic one.

The shape of droplets undergoing deformation is driven by capillary and elastic stresses, a feature whose consequences are explored in Chapter 4. The competition between these two forces is captured by the elastocapillary number α , which, for a liquid-liquid interface covered by a solid neo-Hookean layer (as is the case for polymeric skins), reads as $\alpha = 3Gh_0/\gamma_0$ (Eq. (4.45)), where G is the bulk shear modulus of the solid layer, h_0 its thickness in the reference configuration, and γ_0 the interfacial tension at the liquid-liquid interface.

In view of the elastocapillary number, the transition from a purely capillary interface ($\alpha \rightarrow 0$) to a purely elastic one ($\alpha \rightarrow +\infty$), for a fixed interfacial tension γ_0 , is controlled both by tuning the thickness of the membrane h_0 and its shear modulus G . A good experimental model system would thus allow a good control over these two parameters independently. Moreover, a system where the skin thickness grows continuously rather than by discrete steps, e.g. with layer-by-layer deposition, offers more possibilities in the fine tuning of the elastocapillary number. The formation of an interfacial gel [218, 219] satisfies these requirements, but requires a method to stop the skin formation at will, e.g. with chemical inhibition.

Among the possible model systems satisfying these conditions, emulsions covered with skins composed of polydimethylsiloxane (PDMS) attracted our attention. PDMS is known for its ver-

satility, illustrated in Fig. 5.2b [220, 221, 222, 223, 224] and its interesting mechanical properties when assembled in block copolymers, as shown in Fig. 5.2b [225, 226, 227, 228, 229, 230, 231, 232, 233, 224]. The system studied by Giustiniani in her thesis work [234] is a good illustration of how silicone-based emulsions can be used to probe the effects of interfacial elasticity on drop-drop interactions. The interfacial tension and rugosity of silicone drops change when PEG molecules are grafted at the interface, thus increasing the friction [235]. Similarly, the interactions between two drops change with the formation of the silicone skin. The PEG drops studied in Giustiniani *et al.* [217] are covered with an elastic skin of silicone gel, as shown in Fig. 5.1. Authors showed that additional forces, normal and tangential to the surface, appear as the solid skin grows, and are related to interfacial adhesion and friction. These interactions can be probed at the drop level using a double drop setup, where two drops are brought in contact and moved with respect to each other. An illustration of this setup is shown in Fig. 5.3a-b : the difference between the deformed shape of simple capillary drops (solid brown lines, obtained from Surface Evolver simulations) and drops with a solid skin after sliding are a signature of these new interactions, although their contribution to the final shape are hard to disentangle. On the emulsion level, these new interactions also modify the geometry and structure of the packing, e.g. by causing a finite angle of repose at the top of the emulsion, as shown in Fig. 5.3c. The angle of repose is a well-known phenomenon in granular matter, where its apparition and its magnitude is linked to the strength of the static friction between the grains [32, 236, 237, 238].

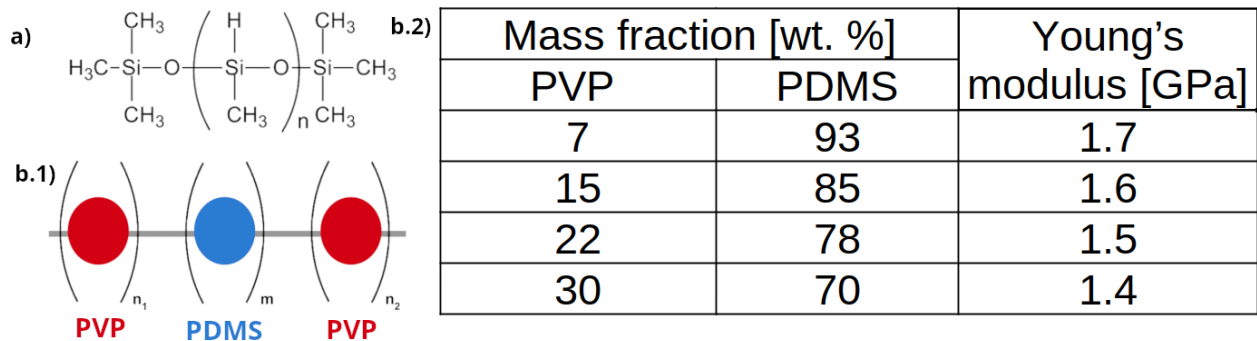


Figure 5.2: a) Plain, unfunctionalised PDMS. b) Modification of the mechanical properties of PDMS when assembled in block copolymers with polyvinylpyrrolidone. The Young's modulus of the elastomer can be decreased by increasing the weight fraction of PDMS in the polymers. Results from [231].

The production of an emulsion to structure the two-phases system, followed by the solidification of the continuous phase and the removal of the discrete inclusions, is a standard templating method to produce foam-based materials [239, 240, 241]. It gives a good control of the organisation and the structuration of the polymer blend through the size of the PEG drops [242, 243, 244]. This production route, however, aims at producing macroporous solids with controlled structural properties, where PEG drops are inclusions in the gelified silicone matrix. For that reason, the final structure of the emulsion does not only depend on the interactions between the drops, but also on the packing procedure with an increasingly solid silicone phase and the viscoelastic properties of the silicone matrix. To investigate properly the effect of interfacial interactions on the packing properties, we therefore modified this system to satisfy the conditions mentioned at the beginning of this chapter. We present here exactly how we improved Giustiniani's experimental system to produce droploons with a controlled interfacial elastocapillarity. In Section 5.2.1, we recall the basics of gel formation theory, and characterise the silicone gel kinetics and rigidity using bulk shear rheology. In Section 5.3, we characterise the rigidity and formation kinetics of the interfacial gel

through interfacial shear rheology, offering enough comprehension of the chemistry of the system to target the desired thickness and rigidity of the skin through control of the reaction time and the concentration of the reactive species. In Section 5.4, we describe how we produce droploons with a millifluidic setup, and show examples of droploons emulsions obtained with it. We further focus on the characterisation of the skin itself, its thickness being estimated through different indirect methods while its shear rigidity is measured using the experimental setup presented in Chapter 4.

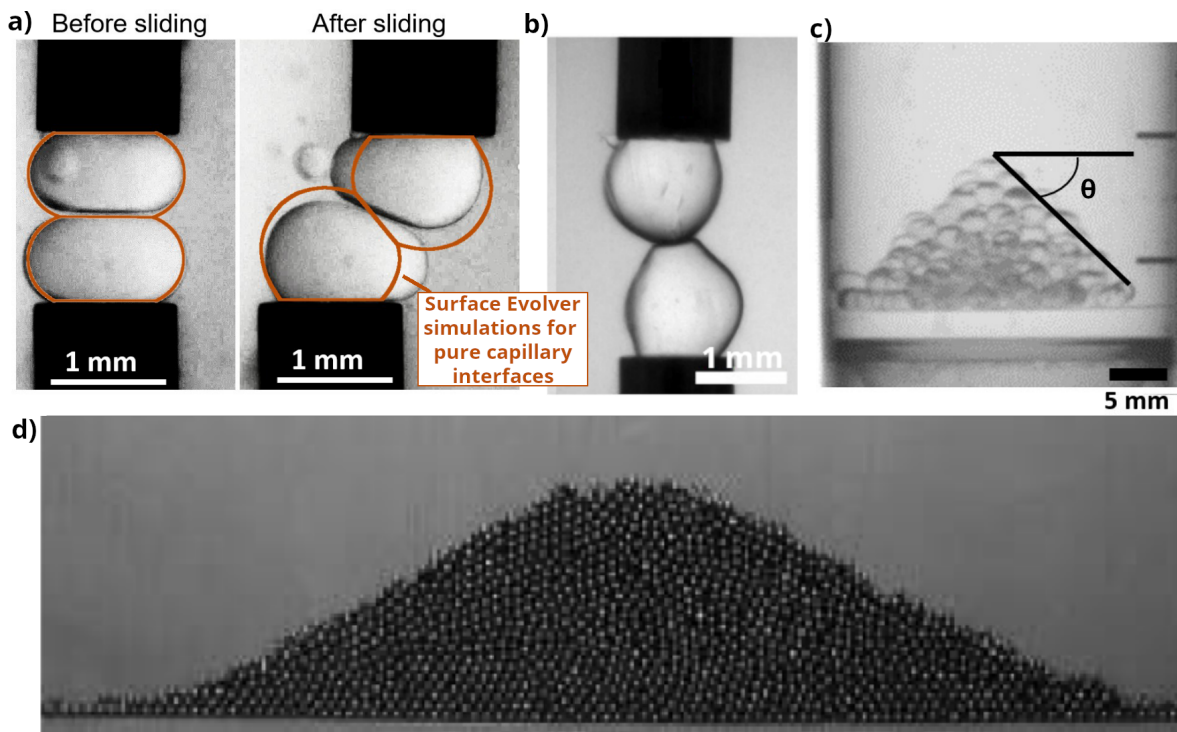


Figure 5.3: a) Sliding of two drops with a silicone skin. Brown contours represent the prediction for the shape of a pure capillary interface obtained through Surface Evolver simulations. Figure from [10]. b) Drops retracted after being put in contact. The pinch at the contact between the two drops is not possible between pure capillary interfaces, and is typical of complex interfaces. Figure from [10]. c) Skin-covered drops form piles with an angle θ with the horizontal axis, referred to as the angle of repose. Non-zero angles are a characteristic feature of sandpiles, with θ depending on grain shape and friction. Figure from [10]. d) Example of an angle of repose for a pile of lead spheres, obtained by dropping the spheres from above. Figure from [238].

5.2 Silicone gel formation

5.2.1 Background : physics of gelation

Polymers put together can under certain conditions react and form bonds with their neighbours in a process called crosslinking. Previously disconnected polymers thus end up bound within a polymeric network, as shown in Fig. 5.4a-b. As the crosslinking reaction progresses, large branched molecules appear in the mixture in a state called the sol. These molecules continue to grow until one is large enough to span the whole system : this network is called the gel, and is no longer soluble in the solvent, but can only swell in it [245]. The transition from the sol state to the gel state is also called the gelation of the system. As our PEG/silicone system gelifies through chemical crosslinking, this section will only talk about this particular type of bonds between the polymers. Interested readers are referred to the dedicated literature [245].

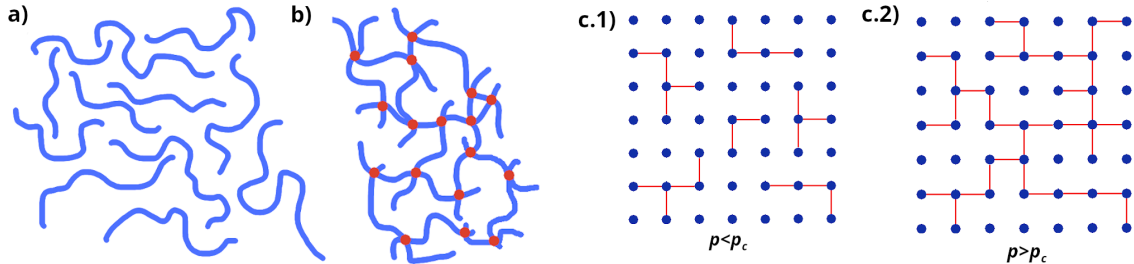


Figure 5.4: a) Unbound monomers in a polymer melt. b) Monomers (blue) bound by chemical crosslinking (red) form a larger molecule progressively spanning the whole system as the gelation progresses. c) Percolation network before ($p < p_c$) and after ($p > p_c$) gel point transition.

The sol-gel transition is sometimes described as a percolation problem [196, 246, 247]. It is best represented by a Bethe lattice, where the vertices are the molecules and the edges are the bonds. Every vertex has a number of neighbours, corresponding to the functionality degree of the molecules. At the beginning of the percolation, no edge connects the vertices. New edges form as the reaction progresses. The fraction of edges formed over the total number of possible edges is called the advancement of the reaction p . At any stage of the reaction, an arbitrary edge has the probability p of connecting two neighbouring vertices.

Because the formation of crosslinks is a random process, the first bonds are not necessarily connected to the same vertices. Rather, a few large subgraphs coexist, as represented in Fig. 5.4c.1. When p becomes large enough, a continuous path spanning the system from one side to the other appears, connecting the whole system in a *percolation transition* represented in Fig. 5.4c.2. For a polymer with a number f of functional groups, this transition happens for the critical advancement p_c

$$p_c = \frac{1}{1 - f}, \quad (5.2)$$

where the polymer melt shifts from a mixture of finite-size branched polymers ($p < p_c$) to a system containing at least one infinite polymer (the gel) coexisting with many finite-size polymers ($p > p_c$) [245]. This critical value is called the gel point, and marks the sol-gel transition. As the solution approaches the gel point, the viscosity diverges, scaling with $(p_c - p)$ (Eq. (5.3)). When this point is attained, the shear modulus becomes non-zero, and then scales as a power-law of excess advancement $(p - p_c)$ Eq. (5.3). Close to the critical advancement p_c , the zero-shear viscosity η_0 and the equilibrium shear modulus G_e scale as the following power-laws [246]

$$\begin{cases} \eta_0 & \sim (p_c - p)^{-s}, \\ G_e & \sim (p - p_c)^z \end{cases}, \quad (5.3)$$

where s and z are critical exponents. The value of these exponents depend on the universality class the material falls into, e.g. Flory-Stockmayer classical gel theory [248, 249] or random bond percolation theory [250]. Readers interested by the sol-gel transition as a critical phenomenon are referred to the dedicated literature [246].

This transition can be monitored using shear rheology, where a shear deformation is imposed on the gel while measuring its stress response. We limit the following reminder to oscillating shear rheology, where an oscillation shear field is imposed. Readers interested to other methods of shear rheology are referred to the dedicated literature [251, 252, 253, 196]. In oscillation shear rheology,

the imposed shear deformation field ε is of the form

$$\varepsilon(t) = \varepsilon_0 \sin(\omega t). \quad (5.4)$$

The stress response σ of the sheared material depends on its constitutive properties [245]. For a Hookean elastic solid (left of Fig. 5.5), its response will be linear with shear and of the form

$$\sigma(t) = G \cdot \varepsilon_0 \sin(\omega t), \quad (5.5)$$

where G is the shear modulus of the solid. For a Newtonian liquid (right of Fig. 5.5), on the other hand, the stress response depends on the temporal variation of the shear and reads as

$$\sigma(t) = \eta \frac{d\varepsilon(t)}{dt}. \quad (5.6)$$

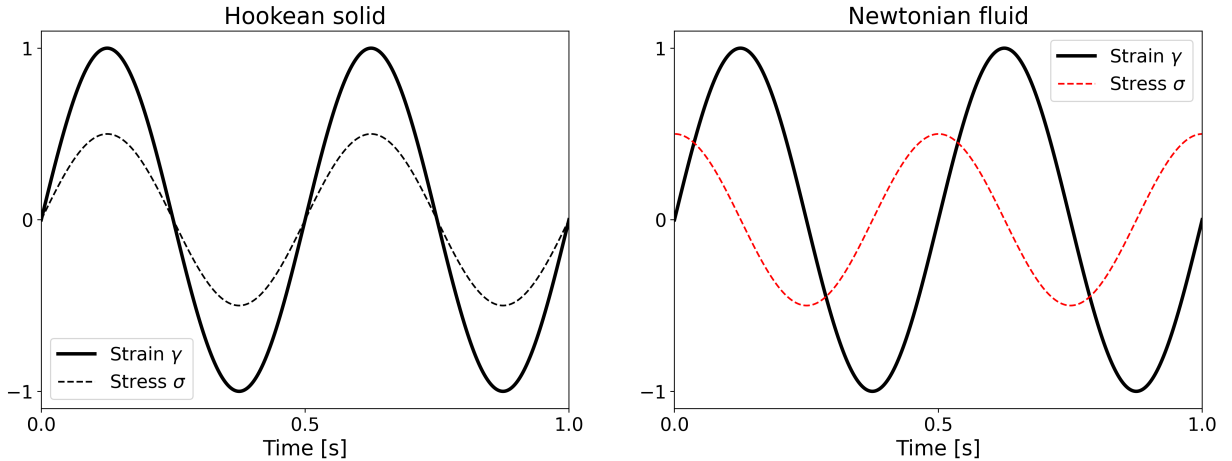


Figure 5.5: Theoretical stress responses to an oscillatory strain of a Hookean solid (left) and a Newtonian fluid (right). The coefficients are set at $G = \eta = \frac{1}{2}$.

The response of a gel is neither perfectly elastic, neither perfectly viscous : it constitutes an example of viscoelastic material, whose stress response shows both elastic and viscous components. In the limit of small amplitude of deformation, the rheology is well described within the framework of linear response theory. Linear response theory describes the response of a physical system to the perturbation of a weak, varying external field [254]. The linear stress response of a viscoelastic solid can then be considered as the sum of the viscous and elastic response, i.e.

$$\sigma(t) = G\varepsilon_0 \sin(\omega t) + \eta\omega\varepsilon_0 \cos(\omega t) \quad (5.7)$$

$$= G' \varepsilon_0 \sin(\omega t) + G'' \varepsilon_0 \cos(\omega t) \quad (5.8)$$

$$= \sigma_0 \sin(\omega t + \delta) \quad (5.9)$$

where σ_0 is amplitude of the external perturbation, and where

$$\tan(\delta) = \frac{G''}{G'}, \quad \eta = \frac{G''}{\omega} \quad \text{and} \quad G' = G \quad (5.10)$$

δ is the delay between the shear and the stress response, also called the phase angle. The phase angle is usually frequency-dependent, and is bounded between two extremal values ($0 \leq \delta \leq \frac{\pi}{2}$),

with $\delta = 0$ corresponding to a Hookean elastic solid, and $\delta = \frac{\pi}{2}$ to a Newtonian liquid. Those two limit cases are represented in Fig. 5.5. As a viscoelastic solid, the phase angle of a gel has an intermediate value, going from $\frac{\pi}{2}$ to 0 with reaction advancement p . In Eq. (5.9), we introduced the storage modulus

$$G'(\omega) = \frac{\sigma_0}{S_0} \cos(\delta) \quad (5.11)$$

and the loss modulus

$$G''(\omega) = \frac{\sigma_0}{S_0} \sin(\delta), \quad (5.12)$$

which are part of the complex shear modulus $G^* = G' + iG''$. The storage and loss moduli are used to define a complex viscosity modulus $\eta^* = \frac{G^*}{\omega}$ [255], which we use to determine the gelation time in Section 5.2.4. The complex viscosity is defined as

$$\eta^* = \eta' + i\eta'' \quad (5.13)$$

which we use in Section 5.2.4 to define the gelation time T_g , and where

$$\begin{aligned} \eta' &= \frac{G''}{\omega} \quad \text{dynamic viscosity,} \\ \eta'' &= \frac{G'}{\omega} \quad \text{storage viscosity.} \end{aligned} \quad (5.14)$$

As for any complex number, the modulus of the complex viscosity is defined as

$$|\eta^*(\omega)| = \sqrt{(\eta')^2 + (\eta'')^2}. \quad (5.15)$$

In the limit of low frequency oscillation [256], one can define the zero-shear viscosity and equilibrium shear modulus used in Eq. (5.3) from the dynamic viscosity

$$\eta_0 = \lim_{\omega \rightarrow 0} \frac{G''(\omega)}{\omega}, \quad (5.16)$$

and the equilibrium shear modulus

$$G_e = \lim_{\omega \rightarrow 0} G'(\omega), \quad (5.17)$$

Regardless of the universality class of the gel, the complex modulus goes, at gel point, through a rapid increase caused by the behaviour of the zero-shear viscosity near η_0 , followed by a steady increase as the equilibrium shear modulus G_e increases with reaction advancement p . This transitive behaviour is represented in Fig. 5.6. In Section 5.2.4, we thus define the gelation time T_g of our samples as the time at which the complex viscosity modulus $|\eta^*|$ shows its maximal variation.

5.2.2 Chemistry of the PDMS gel formation

In this section, we present how we adapt the experimental system of Giustiniani *et al.* [10] to accommodate these requirements. In particular, this section focuses on the chemistry of the silicone gel. The reaction anchoring silicone polymers to the interface is described in Section 5.3.1.

Our experimental system consists of PEG-400 drops produced in a blend of silicone polymers. The molecules involved are shown in Fig. 2.5. These silicones are of three types : (1) one plain, unreactive PDMS, (2) one PDMS where some methyl Si-CH₃ bonds along the backbone chains are

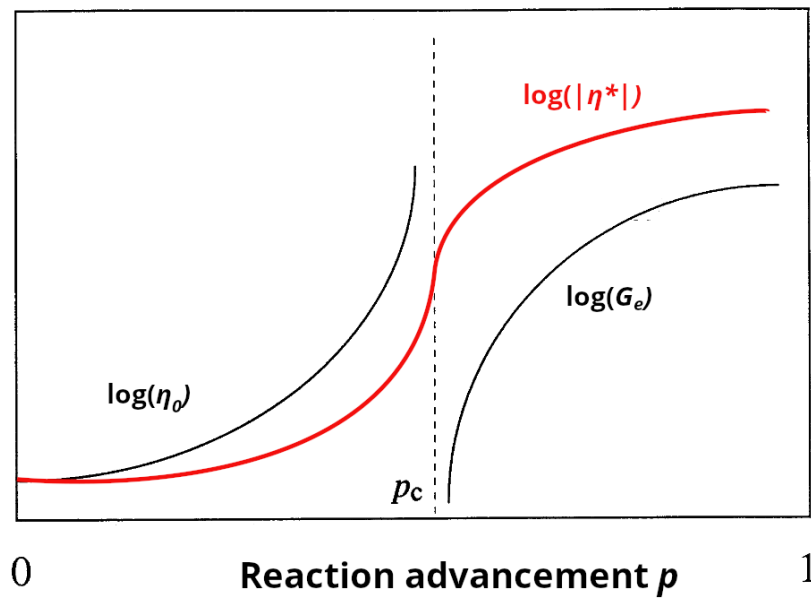


Figure 5.6: Divergence of the zero-shear viscosity η_0 and onset/increase of the static shear modulus G_e around the gel point p_c . The gel point corresponds to the maximal increase of complex viscosity modulus with advancement p . Figure adapted from [256].

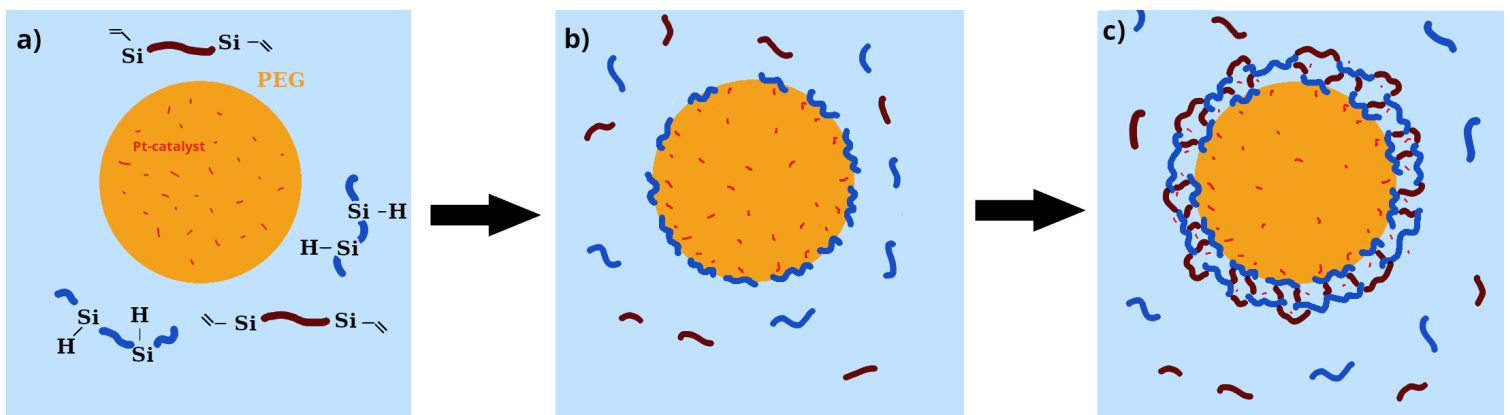


Figure 5.7: Advancement of the skin formation. a) Newly formed PEG drop in the silicone phase. b) Formation of MHDS-PEG copolymers at the interface by condensation reaction shown in Fig. 5.8A. c) Diffusion of the catalyst in the silicone phase triggers polyhydrosilylation of vinyl-terminated PDMS and MHDS to form the silicone skin, as shown in Fig. 5.8B.

replaced by Si-H bonds, and (3) one vinyl-terminated PDMS, where the two Si-CH₃ end groups are replaced by a vinyl function Si-CH=CH₂. References of the products are given in Chapter 2.

The silicone skin is formed in two steps, represented in Fig. 5.7a. The first step consists of a condensation reaction at the interface between the -OH end groups of the PEG and the Si-H groups of the MHDS (Fig. 5.7a.2 and Fig. 5.8A) catalysed by the platinum-catalyst (Pt-cat). This reaction creates amphiphilic block copolymers at the PEG-PDMS interface, lowering the interfacial tension between the two phases [10].

In a second step, the catalyst diffuses into the silicone phase creating a cross-linked silicone gel which is formed by hydrosilylation [257, 258, 259, 17, 260]. This is a platinum-catalysed addition reaction coupling silicone hydride groups (Si-H groups) to carbon-carbon double- or triple bonds. Here we make use of the most eminent example of hydrosilylation chemistry, namely the reaction between Si-H groups and Si-CH=CH₂ groups for the formation of a C-C linkage between the two differently functionalised siloxane-based oligomers and polymers [261, 262, 263, 264] represented in Fig. 5.8B. Depending on the number of functional groups f of the two types of reacting polymer chains, a linear copolymer ($f_1 = f_2 = 2$) or a crosslinked polymer matrix ($f_1 > 2$ while $f_2 \geq 2$ or $f_1 \geq 2$ while $f_2 = 2$) can be obtained through polyhydrosilylation. In our case, we have for the vinylPDMS $f_{vinylPDMS} = 2$, and for the MHDS $f_{MHDS} \approx 9$. Hence, provided that the concentration of both reactive species is high enough, a cross-linked network is created by the reaction.

The presence of water, however, may cause a cascade of side reactions, as the Si-H groups are rather sensitive to water [265, 266, 267]. For instance, the Si-H group might undergo a platinum-catalysed condensation with water, forming an Si-OH group while releasing a proton (Fig. 5.8C). This Si-OH group, in turn, may react with Si-H bonds in a platinum catalysed condensation reaction to form a siloxane bond (Fig. 5.8D). While silicone polymers are highly hydrophobic, the PEG is strongly hygroscopic, creating hence secondary reactions with water in the vicinity of the interface. To ensure reproducibility we therefore dry the PEG before use, which is detailed in Section 2.3.3.

5.2.3 Blocking the reaction : addition of a reaction inhibitor

A model system for interfacial interactions in elastocapillary drops requires to get skin of finite controlled thickness, so that the thin skin approximation remains valid and that the droplets remain separate objects. In Giustiniani's system, the gelation of the silicone phase does not stop at the interface, but extends over the whole system. The physical properties of the system relies thus more on the bulk properties of the silicone gel rather than the interactions between the drops. To transform this system in a droplet emulsion, we stop the hydrosilylation reaction, limiting the silicone gel to a finite thickness h_0 .

In the PEG-silicone system, the skin forms through polyhydrosilylation reactions, catalysed by the diffusing platinum-based compound. Its growth can thus be stopped by the addition of a chemical inhibitor to the silicone phase. Following the work of Lewis *et al.* [17], we opt for a dimethyl maleate inhibitor represented Fig. 5.9. Dimethyl maleate binds irreversibly to Karstedt's catalyst with a molar ratio 1 : 4, changing its structure and inhibiting its catalytic activity.

The efficacy of dimethyl maleate on the platinum catalyst in inhibiting the polyhydrosilylation is tested in Section 5.2.4.

5.2.4 Bulk shear rheology

The competition between capillary and elastic forces, captured by the elastocapillary number α introduced in Chapter 4, depends both on the rigidity and the thickness of the gel. The silicone gel

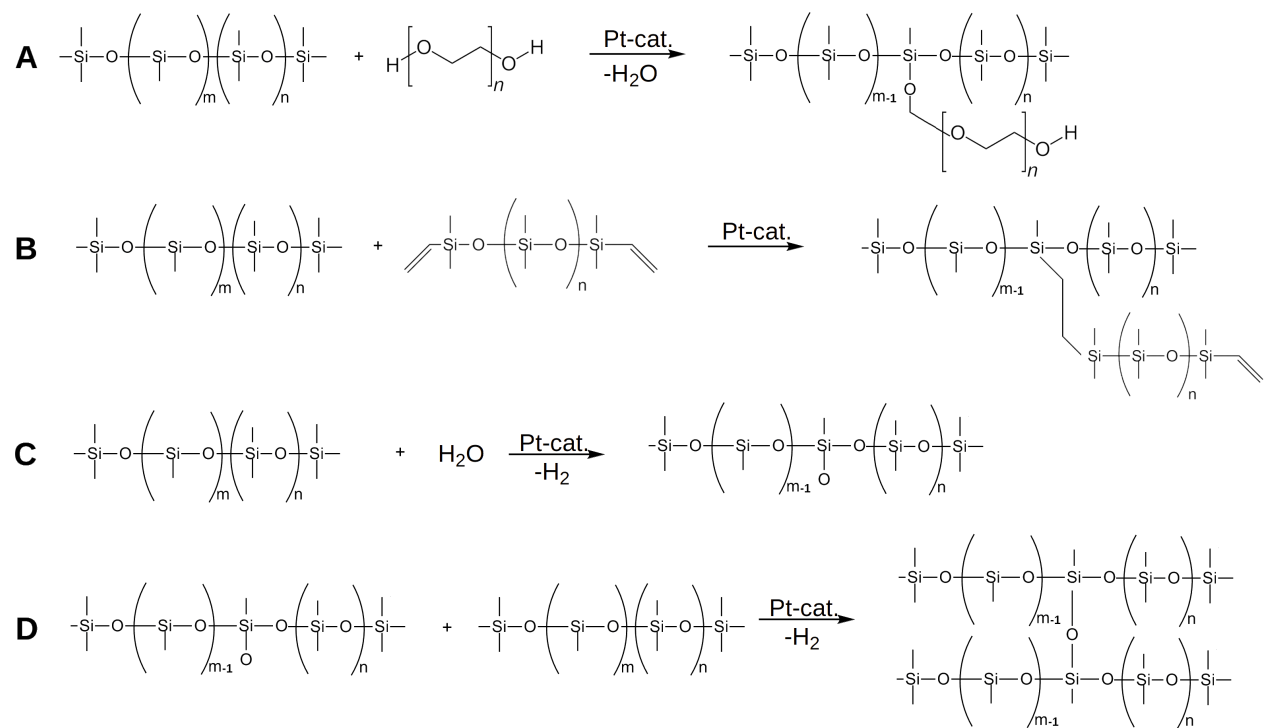


Figure 5.8: Set of chemical reactions taking place in the system.

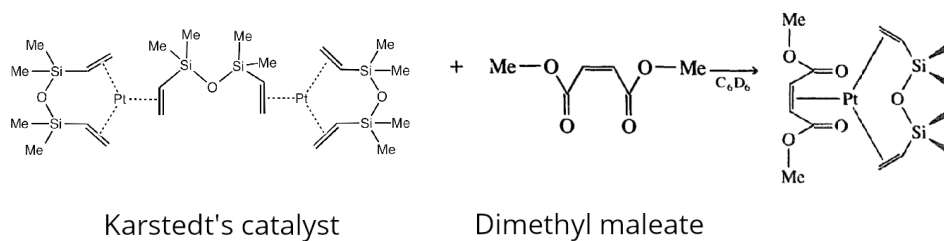


Figure 5.9: Reaction between platinum catalyst and dimethyl maleate. [17, 268]

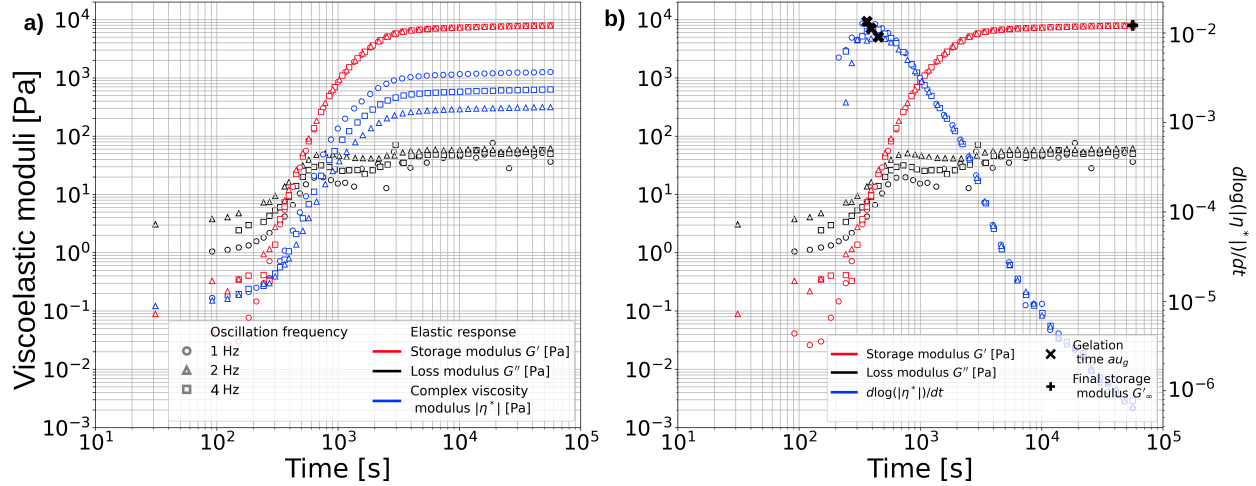


Figure 5.10: Example of the evolution of the visco-elastic response of a silicone gel at $\phi_r = 30$ wt. % and $\phi_p = 0.3$ vol. % at oscillation frequencies of 1, 2 and 4 Hz. The complex viscosity modulus is used to determine the gel time τ_g by taking the time of maximal slope, for each frequency (right). The final storage modulus G'_∞ is taken as the maximal value of the storage modulus G' over the whole experiment, for each frequency.

forms by the crosslinking of reactive silicone polymers in the continuous phase of the emulsion. Its thickness is either limited by the total amount of reactive silicone in the system, or by the time left for skin formation before the addition of maleate. The growth kinetics of the skin depends on the reaction timescale and the diffusion speed of the catalyst. A controlled elastocapillary transition requires to understand the parameters governing the rigidity and the formation kinetics of the polymeric skin, for separate control of the two-dimensional shear modulus G_{2D} and the skin thickness h_0 . In this section, we characterise the silicone gel using different experimental techniques. This section focuses on the silicone gel in bulk phase making the assumption that an understanding of the bulk behaviour can be transferred to the skin properties. We characterise both its shear modulus G and gelation time T_g as function of the concentration of reactive polymers ϕ_r and the catalyst concentration ϕ_p at stoichiometric ratio of the reactive silicone polymers (these quantities being defined in Section 2.3.2).

We studied the bulk gelation of different reactive silicone formulations in absence of PEG. Here the catalyst was directly mixed into the silicone blend just before the experiment using the blending of two non-reactive mixtures, as described in Section 2.3.2. After rapid blending of all components, we followed the temporal evolution of the visco-elastic properties of the forming gel using three different frequencies simultaneously ($\omega = 1, 2$ and 4 Hz) with the multiwave oscillation method (2.3.2). Fig. 5.10a shows the example of a typical set of curves obtained for the evolution of the storage modulus G' , the loss modulus G'' and the complex viscosity η^* for one formulation (here $\phi_r = 30$ wt. % wt% and $\phi_p = 0.3$ vol. %).

In these experiments, the silicone blend at the beginning of the experiment exhibits a liquid-like response, with a loss modulus G'' higher than its storage modulus G' . Over time, both increase, with the storage modulus increasing faster than the loss modulus. Eventually, G' becomes larger than G'' and the polymer blend becomes a gel. In the last phase of silicone crosslinking, the gelation progresses until all available reactive sites are consumed. Storage and loss moduli then converge towards final values G'_∞ and G''_∞ , respectively.

In order to determine the gelation time τ_g (time until the gel point is reached), the approach

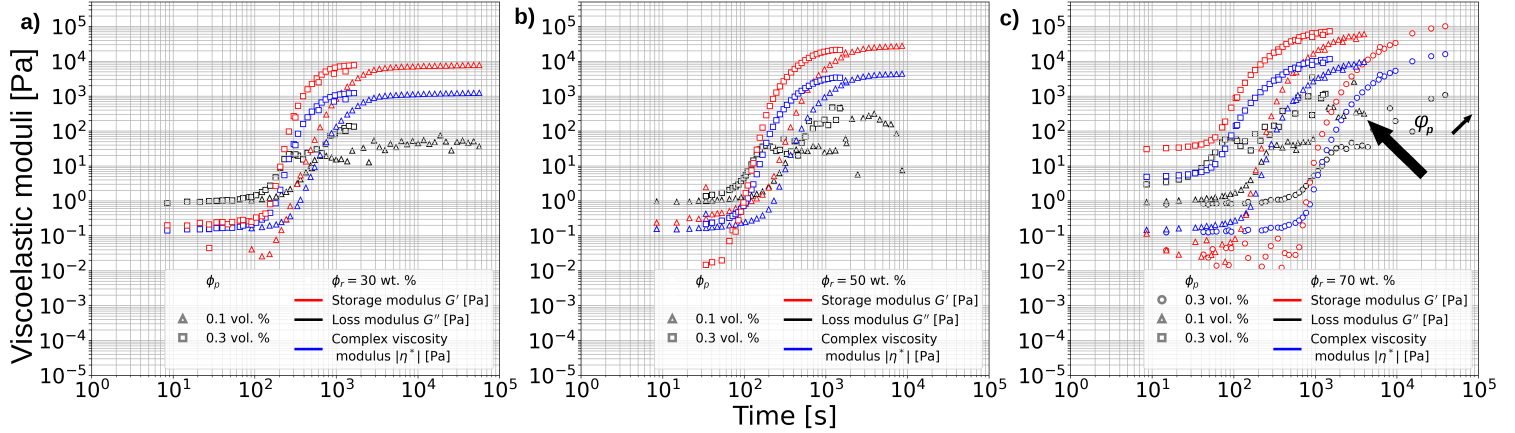


Figure 5.11: Evolution over time of the visco-elastic response of the silicone blend with a reactive mass fraction ϕ_r of (left) 30 wt. % (middle) 50 wt. % and 70 wt. %, for an oscillation frequency of 1 Hz.

of Winter is commonly used *et al.* [25, 247], which relies on the fact that the phase angle G'/G'' becomes independent of frequency at the gel point. Unfortunately, in our samples, this approach leads to very scattered results which we assign to the mechanical noise of the rheometer close to its precision threshold. We therefore analyse instead the complex viscosity modulus η^* defined as $\eta^* = G''/\omega + iG'\omega$. We define the gel time τ_g as the time of maximal variation of η^* , i.e; when $d\log(|\eta^*|)/dt$ has a maximum. This point is very well defined, as shown in Fig. 5.10. In the following we will only show the results of one frequency to simplify the graphs and the discussion. Moreover, as shown later, the rigidity and the gel time does not vary with the oscillation frequency.

In Fig. 5.11, we show how G' and G'' vary for a wide range of formulations with varying couples of ϕ_r (30, 50 and 70 wt. %) and ϕ_p (0.3, 0.1 and 0.03 vol. %). Gels with the same initial reactive fraction have close final modulus G'_∞ . The increase in catalyst concentration does not appear to change the mechanical properties of the gel ; however, it increases the gelation speed, by shifting the gelation curves to smaller times and reducing the gelation time τ_g .

We investigate how the gelation time τ_g and the final storage modulus G'_∞ depend on the formulation, i.e. on ϕ_r and ϕ_p . Fig. 5.12 summarises the results for a wide range of formulations. One observes that G'_∞ increases with ϕ_r , but vary only mildly with ϕ_p . On the other hand, the gel time τ_g varies both with ϕ_r and ϕ_p .

To understand the shape of $G'_\infty(\phi_r, \phi_p, \omega)$ and $T_g(\phi_r, \phi_p, \omega)$ we perform statistical tests in two steps : in the first step, the dependance of the tested variable y with every parameter x is tested independently, using linear regression $\log(y) = \beta_0 + \beta_1 \log(x)$. The independance hypothesis H_0 is tested by computing its P -value. The variables rejecting successfully the null hypothesis ($P < 0.05$) are then taken as variables in the second step, where we perform a non-linear regression to find the prefactors and exponents of these variables using least-square fit regression method with the Levenberg-Marquardt algorithm implemented in MATLAB [269].

Using this procedure, G'_∞ and T_g appear as independent from the oscillation frequency ($P = 0.954$ and $P = 0.386$, respectively). G'_∞ is also independent from catalyst concentration ($P = 0.066$), contrary to T_g ($P = 3.32 \cdot 10^{-14}$). T_g is independent of the reactive fraction ϕ_r ($P = 0.554$), contrary to G'_∞ ($P = 2.78 \cdot 10^{-27}$). Because the typical reaction kinetics involving catalysts often depends simultaneously on reagent and catalyst concentration, we test their dependencies with a cross-term $\phi_r \phi_p$, and found that gel time is indeed dependent on it ($P = 1.36 \cdot 10^{-19}$), contrary to G'_∞ ($P = 0.260$). Following these results, the experimental results are then fitted using non-linear

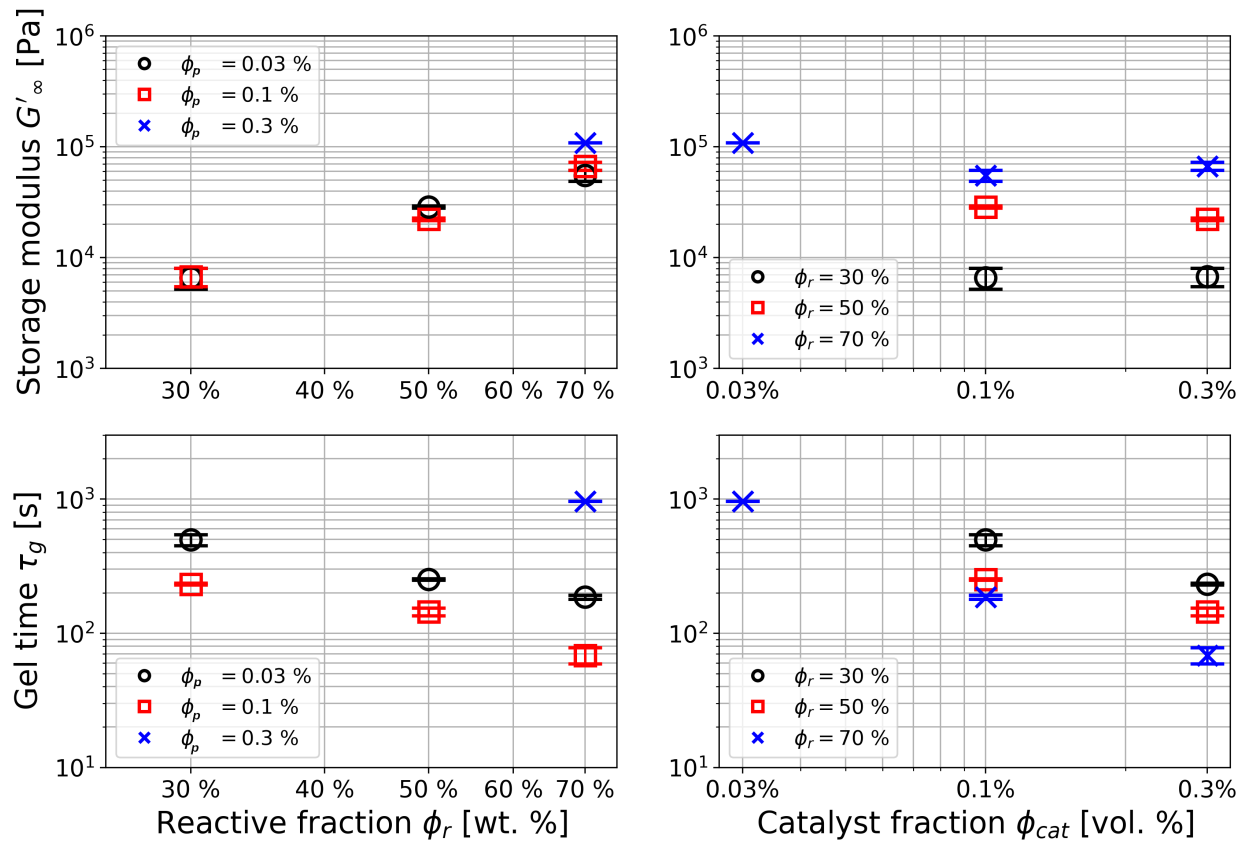


Figure 5.12: Evolution of the final storage modulus G'_∞ and the gel time τ_g with reactive fraction ϕ_r and catalyst fraction ϕ_p . The results for the three frequencies are averaged, with their standard deviation shown as errorbars.

least-square regression with the Levenberg-Marquardt algorithm, using the relations

$$G'_\infty = A_0 + A_1\phi_r^{n_1}, \quad (5.18)$$

$$T_g = B_0 + B_1\phi_p^{n_1} + B_2\phi_r^{n_2}\phi_p^{n_3}, \quad (5.19)$$

where we allow n_2 and n_3 to vary independently, as reagent and catalysts play different roles in the crosslinking reaction.

The non-linear regression of G'_∞ with Eq. (5.18) found large deviations in the estimation of the constant term A_0 , with $A_0 = 147 \pm 6750680$. Because of its undetermined sign and the lack of physical significance of an offset gel rigidity, we remove A_0 from the next non-linear regression, and fit G'_∞ with the expression

$$G'_\infty = A_1\phi_r^{n_1}. \quad (5.20)$$

The fitted coefficients are summarised in Table 5.1.

The first set of fitted parameters for T_g found a prefactor $B_1 = 168 \pm 146$ an exponent $n_1 = -0.4 \pm 0.9$: the large confidence interval and the indetermination of the sign of the exponent indicate the difficulties of the convergence algorithm to find the dependency of T_g on ϕ_p only. From a chemical point of view, the reaction kinetics cannot depend on catalyst concentration alone, hence these difficulties. Similarly, a constant term B_0 is not physically sound, and we remove it from the last fitting procedure. For the same reasons as for G'_∞ , we replace the relation of Eq.(5.19) by the more physically sound relation

$$T_g = B_2\phi_r^{n_2}\phi_p^{n_3}. \quad (5.21)$$

The coefficients found with this method are shown in Table 5.1 along with their confidence interval. Graphs in Fig. 5.13 show the experimental results along with the relations found with non-linear regression.

Within our available experimental data, we therefore show that the final storage modulus of the silicone gel depends only on the concentration of the reactive species ϕ_r when they are mixed at stoichiometric ratio. G'_∞ scales as a power-law

$$G'_\infty \sim \phi_r^{2.78 \pm 0.01}, \quad (5.22)$$

with the exponent 2.78 being slightly below the value expected from scaling the rigidity with the number of crosslinking points per unit volume. Reaction kinetics, on the other hand, depends on ϕ_r and the volume fraction of catalyst ϕ_p , with a gelation time (defined as the time of maximal variation of G''/G') scaling as

$$T_g \sim \phi_r^{-0.80 \pm 0.01}\phi_p^{-1.09 \pm 0.01}, \quad (5.23)$$

on the range of tested parameters. Using these two scaling laws, one is able to tune the rigidity of the silicone gel at constant reaction time. The scaling laws of Eqs (5.22) and (5.23) fitted from bulk shear rheology experiments are therefore used in the following to guide the formulations the PEG-in-silicone emulsions.

5.2.5 Conclusion

In this section, we investigated the formation of the silicone gel, placed at the interface of the PEG drops in our PEG-silicone system. Using bulk shear rheology, we probed the dependency of its shear modulus G'_∞ and its gelation time T_g with reactive fraction ϕ_r and catalyst fraction ϕ_p . In particular, the scaling of G'_∞ with ϕ_r gives a simple control of the rigidity of the interfacial gel. In the next section, we turn towards the characterisation of the gel formed at the interface.

	$G'_\infty = A_1 \phi_r^{n_1}$		$T_g = B_2 \phi_r^{n_2} \phi_p^{n_3}$
A_1	0.49 ± 0.06	B_2	616 ± 13
n_1	2.78 ± 0.01	n_2	-0.80 ± 0.01
		n_3	-1.09 ± 0.01

Table 5.1: Coefficients of the non-linear regression on the experimental data points obtained from bulk shear rheology.

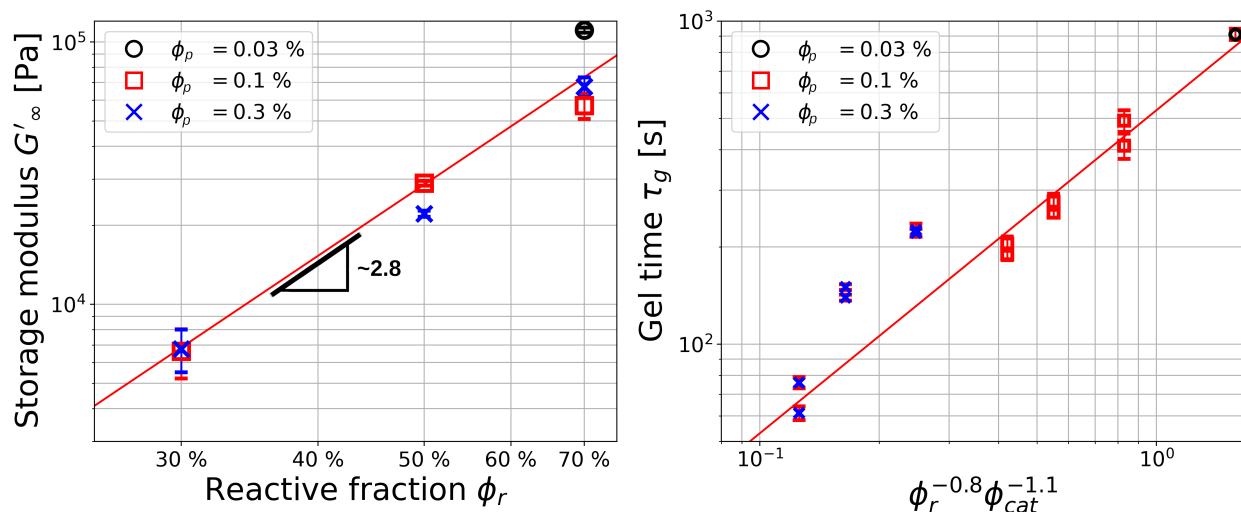


Figure 5.13: Experimental data and scaling results obtained for (a) the evolution of the final bulk shear modulus G'_∞ with reactive fraction ϕ_r and for (b) the evolution of the gel time τ_g with fraction of reactive silicones ϕ_r and catalyst ϕ_p .

5.3 PEG-PDMS interfaces

5.3.1 Chemistry of the interface

The first step of formation of the skin consists of a reaction at the interface between the PEG and the MHDS (Fig. 5.7b and Fig. 5.8A). The PEG-silicone copolymer is formed by a platinum-catalysed condensation reaction between the alcohol function of the PEG molecules and the silicone hydride groups. The amphiphilic block copolymer formed in this first reaction adsorbs at the PEG-PDMS interface, lowering the interfacial tension between the two phases [10]. Because of their large polymeric weight, these molecules can give a finite elasticity, as we will show in the next section.

The efficacy of dimethyl maleate on the platinum catalyst used in the P is tested using the dripping setup described in Section 2.3.5, with a weight fraction of reactive silicone species of $\phi_r = 100$ wt.%. The catalyst is dispersed in the PEG phase using a magnetic stirrer, with a concentration of $750 \mu\text{M}$. The inhibitor is dispersed in the PEG phase using a magnetic stirrer as well, at concentrations of $0 \mu\text{M}$, $750 \mu\text{M}$ and 7.5mM , respectively. The results are shown in Fig. 5.14. The drops dripped in silicone show a loss of stability for excess inhibitor concentration, with coalescence of the drops at the bottom of the emulsion. This distabilisation of the drops corresponds to the absence of elastic stabilising skin at the interface.

5.3.2 Interfacial shear rheology

The gel formed at the PEG/silicone interface is characterised with interfacial shear rheology, using a double-wall ring experimental setup described in Section 2.4.2. In this configuration, the interfacial gel is formed by the diffusion of the catalyst from the PEG to the reactive silicone blend. The

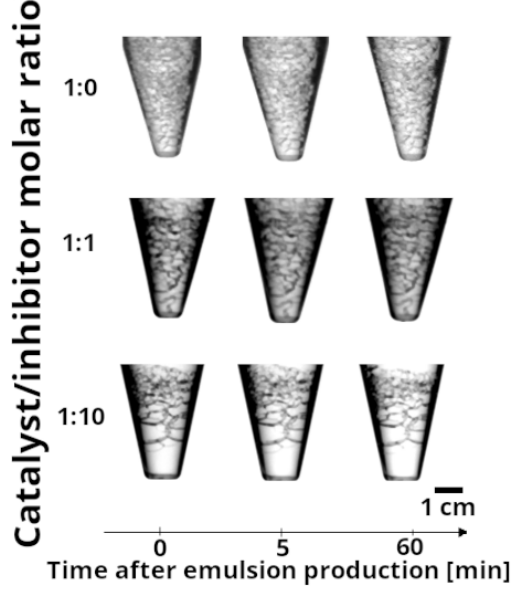


Figure 5.14: PEG drops dripped in the reactive silicone blend with dispersed dimethyl maleate. The drops are contained in centrifuge tubes, with the thin silicone films between the drops visible as dark lines. At high inhibitor concentration, the emulsion is not indefinitely stable and starts to coalesce, like ordinary emulsions.

results for two weight fractions of reactive polymers $\phi_r = 100$ wt.% and $\phi_r = 30$ wt.% at constant catalyst concentration $\phi_p = 0.3$ vol. % are shown in Fig. 5.15.

The overall evolution of the mechanical response of the skin is similar to the bulk gel described in Section 5.2.4 : an initially liquid-like system ($G'' > G'$) becomes solid-like ($G'' < G'$). The evolution of the shear modulus of the interfacial gel differs from its bulk counterpart by the existence of two distinct timescales : a first, short timescale gives the interface a non-zero 2d shear storage modulus $G'_{2D} \sim 10^{-2} - 10^{-3}$. After a time of slow evolution at low values of G'_{2D} , the storage modulus shifts to high values of shear modulus around 10^1 N.m $^{-1}$ in a timescale around $10^3 - 10^4$ s depending on ϕ_r .

We explain the coexistence of these two timescales by the two mechanisms at play in the skin formation. The first timescale corresponds to the formation of block-copolymers PEG-vinyl terminated PDMS at the interface schematised in Fig. 5.8A, triggered by the catalyst crosslinker diffusing to the interface. This step does not depend on the concentration of the silicone phase in reactive polymers ϕ_r , because the interface is quickly covered with block-copolymers in formation. Because of the importance of the catalyst diffusion kinetics towards the interface, this step is highly sensitive to the preparation of the PEG/catalyst dispersion described in Section 2.4.2. This shear modulus is due to the presence of the large block-copolymers adsorbed at the interface : the large molecular weight of the amphiphilic PDMS-PEG block copolymers gives a finite Gibbs elasticity to the interface

In a second step, the catalyst diffuses in the silicone phase and starts to crosslink the reactive silicone polymers. The kinetics of this mechanism accelerates and the final shear modulus increase with ϕ_r , as shown in Section 5.2.4. Hence, the growing difference between $\phi_r = 100$ wt.% and 30 wt.% in this second step. at this stage, it is not possible for us to relate the skin growth parameters quantitatively to the bulk gelation of Section 5.2.4. This requires to take into account the diffusion kinetics of the silicone catalyst within the silicone blend.

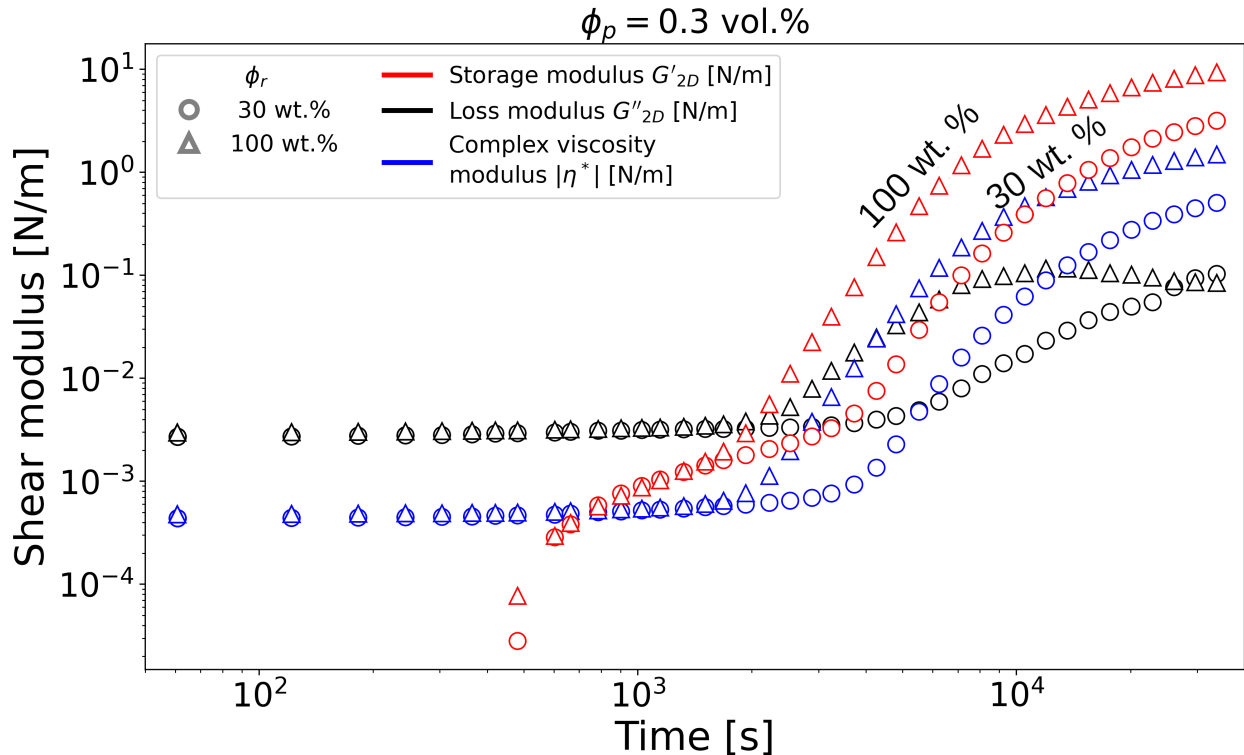


Figure 5.15: Evolution of the shear moduli of the interfacial gel probed by oscillating shear rheology with a 1 % angular deformation at 1 Hz frequency, using the experimental setup described in Section 2.4.2.

For our experimentally tested set of parameters, we found that the skin growth starts between 1000 and 4000 s, corresponding to ~ 15 -70 min depending on the reactive fraction ϕ_r . This information, along with other measurement methods of the time evolution of the skin thickness presented in Section 5.4.3, is used to determine the target reaction time in the millifluidic setup described in Section 5.4.1. In particular, at this stage, it is impossible to separate the contributions of the bulk skin modulus G'_{3D} and the skin thickness h_0 in the overall skin response. For this reason, we explore in the following section different methods to determine skin thickness.

5.4 Experimental model system : PEG-in-PDMS emulsions

Investigating the effect of interfacial elasticity on the emulsions requires to control the drop size. Furthermore, the mechanism of skin formation requires to control the reaction time. The drop production setup must allow a controlled addition of the dimethyl maleate inhibitor to the silicone phase. Addition of inhibitor after the generation of the emulsion is therefore not enough, as diffusion through the whole emulsion would rely on the slow flow of drainage and on diffusion through the complex network of the continuous phase. For that reason, we switch the drop production setup from a dripping setup to a millifluidic setup : the drop travels for a given time in the reactive silicone phase where the skin can form at the interface, before being put in a phase containing dimethyl maleate in excess concentration to quickly stop the skin formation. We designed a millifluidic production setup, which has the advantage of producing drops with a controlled diameter, and offers the possibility to introduce the inhibitor at any desired point of the setup. Our setup is

represented in Fig. 2.10. The materials, providers and dimensions of the tubes are detailed in Section 2.3.6.

5.4.1 Millifluidic droploon production

The silicone phase is placed in two syringes (60 mL Plastipak) referred to as (A) in Fig. 2.10, placed on a double syringe pump, because of the large amount of silicone required to produce the emulsion. The two syringes are connected *via* a Y-junction to make a single silicone phase flow. The PEG phase is contained in a single syringe (30 mL Plastipak) on its own syringe pump (B). The two parts are connected through a T-junction (C), where the drops are produced following the usual microfluidic drop production mechanism [270]. Changing the two flow rates is used to tune the drop size to the desired dimension. We found a stable drop size for a silicone flow rate of 20 mL/hr (corresponding to the two syringes pushed at 10 mL/hr) and a PEG flow rate of 3 mL/hr. At the beginning of the dripping, the size of the drops fluctuates until the flows stabilise after 300 s. The drops produced before the stabilisation are discarded and not collected in the sample holder, to avoid size variations.

The next part of the setup is designed to make the skin grow in conditions where it is as uniform as possible. The typical timescale of skin growth to reach thickness measurable with our available tomographic setup (around 10 μm) is of the order of 10 min, as shown in Section 5.4.3. In this time interval, the drops must be kept away from each others to avoid coalescence while the polymer skin forms. Additionally, long contacts with the walls of the tube are forbidden to avoid adhesion, which would lead to stretch and/or breaking of an inhomogeneous skin when collecting the drops. We fulfill these two requirements by putting the drops in a spiral tube held by a cross-shaped support with grooved arms to hold the tube (D). In this spiral tube, the drops flow at a speed determined by the combined flow rates of the two phases. The total reaction time T_r is thus easily tuned by changing the length of the spiral tube, before stopping the reaction by adding the inhibitor.

At the end of the spiral tube (E), a PDMS blend containing dispersed dimethyl maleate is placed in a single syringe (30 mL Plastipak) and injected through a T-junction. This solution is prepared with an inhibitor mass fraction of 5.5wt.% and a flow rate of 5 mL/hr. The exiting flow is then directed to a sample container (F) with a last plastic tube of 5 cm length. A diffusive white screen with homogeneous lighting is put behind the sample container. A camera takes pictures of the emulsion while it is created, with a framerate of 1 picture every 10 minutes. An example is shown in Fig. 5.16. This sample production recording is useful for a crude analysis of the dynamical process of emulsion packing, such as the evolution of the angle of repose described in Section 5.1.

Finally, as the silicone flow rate is large compared to the PEG one, the excess silicone in the emulsion needs to be removed. A peristaltic pump (G), with an inlet hanging at the top of the sample container, transfers the silicone in a waste container (H) when its volume reaches the top of the container.

5.4.2 Droploons emulsions

The variation of skin thickness h_0 and rigidity G_{2D} allows to probe the transition from purely capillar to purely elastic interface. The production of droploons with similar elastocapillary properties can then be used to investigate the impacts of these interfaces on the structures of the emulsions. Four examples of droploons emulsions are shown in Fig. 5.17, along with the experimental parameters used for their production.

The four samples show clear differences with each others. While sample a shows an homogeneous emulsion structure, the droploons in sample b have more silicone between them, and yet

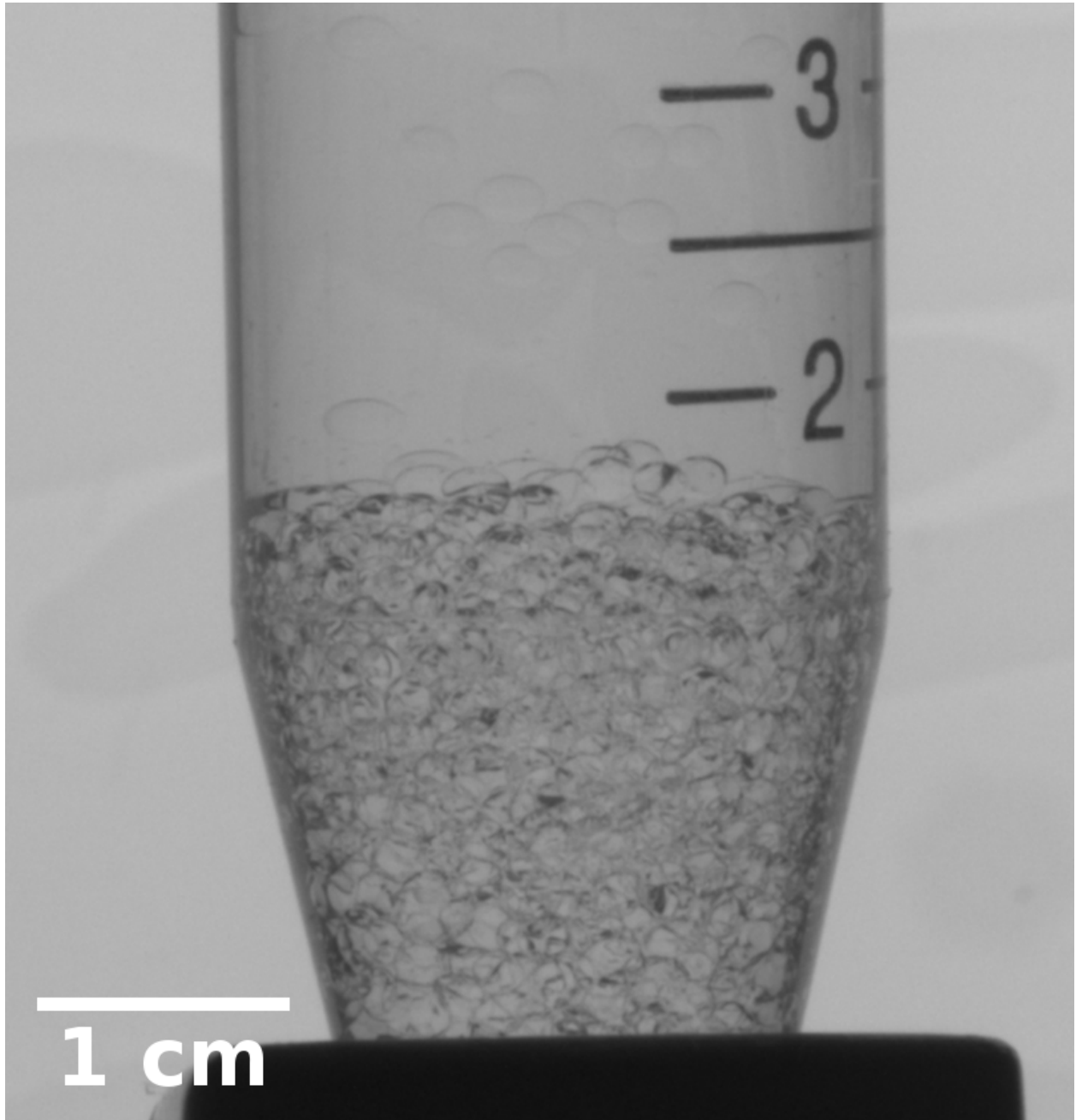


Figure 5.16: PEG in silicone emulsion produced with the millifluidic setup presented in Fig. 2.10. Experimental parameters : $\phi_r = 50\text{wt.}\%$, $\phi_p = 0.3\text{vol.}\%$, $T_r = 20$ min.

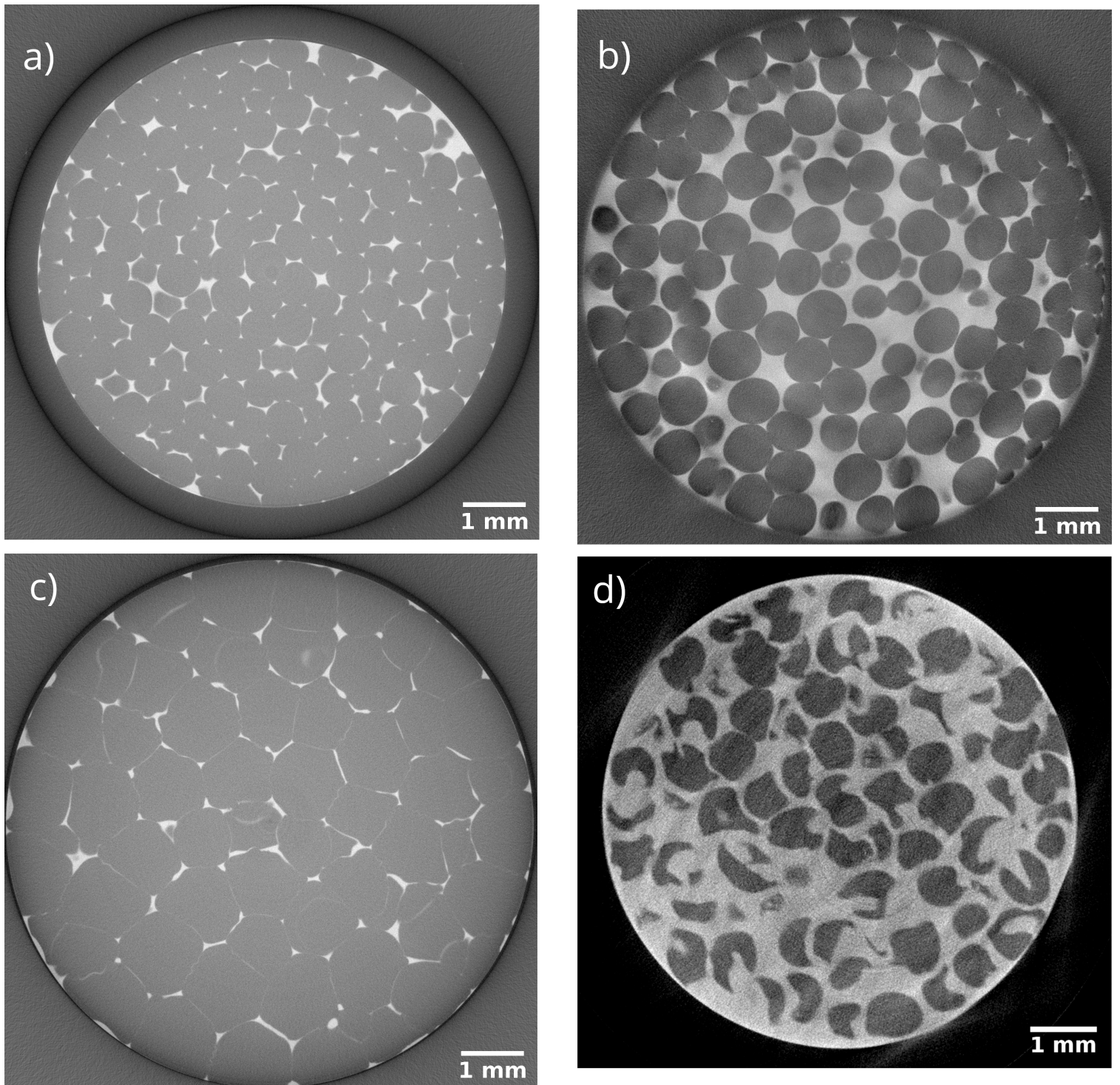


Figure 5.17: Examples of horizontal slices of droploons emulsions imaged with X-Ray tomography, obtained by varying experimental parameters. a) $\phi_r = 50$ wt.%, $\phi_p = 0.3$ vol.%, $T_r = 5$ min 45 s. b) $\phi_r = 30$ wt.%, $\phi_p = 0.3$ vol.%, $T_r = 4$ min 20 s. c) $\phi_r = 50$ wt.%, $\phi_p = 0.3$ vol.%, $T_r = 9$ min 30 s. d) $\phi_r = 100$ wt.%, $\phi_p = 1.0$ vol.%, $T_r = 22$ min.

show some buckled interfaces which are a signature of elastic interfaces. Sample c and d have very deformed droploons, with sample c having a very low silicone volume fraction. The interfaces of the droploons from sample d have the most buckled interfaces, with no droploons showing round, drop-like interfaces.

Overall, this transition from an emulsion-like structure to buckled shapes does not seem to follow what one would predict from parameters of production of the emulsions : if interfacial shear modulus G'_{2D} was increasing with ϕ_r , ϕ_p and T_r , sample b would be more emulsion-like than sample a. This discrepancy could be lifted in two ways : first, by a more controlled characterisation of the elastocapillary numbers of the samples, which could not be done because of the time limitations of this thesis. Second, by the formulation of a predictive model describing the transition of the structure from simple emulsions to droploons emulsions, and a quantitative description of these structures to be compared to experimental results. A proposition of structural description is detailed in the next chapter.

Overall, the PEG-in-silicone system shows a nice ability to modify its interface and affect the subsequent emulsion structure, in spite of its complexity. In the next section, we propose measurements of the skin thickness over time, to help designing future PEG-silicone droploons emulsions.

5.4.3 Skin growth measurement

The interfacial shear modulus G'_{2D} of the polymer skin is at first approximation a product of its bulk shear modulus G'_{3D} and its thickness h_0 , $G'_{2D} = G'_{3D}h_0$ (see Eq. (4.44)) if we assume that the bulk shear modulus is constant throughout the skin. As we show in Section 5.2.4, the bulk shear modulus depends on the weight fraction of reactive polymers ϕ_r , mixed at stoichiometric ratio. A tunable interfacial elasticity additionally requires a control of the thickness of the skin, which grows as the catalyst diffuses in the silicone phase and the crosslinking of the melt progresses (Section 5.2.2).

The skin consists of crosslinked silicone polymers in a solution of identical, unbound polymers. It is hard to measure *in situ* with ordinary imaging methods, free and crosslinked polymers having very similar optical properties. In this Section, we use three different experimental techniques to obtain an indirect measure of h_0 . Each of these methods has its own assumptions, with its associated error. The different methods give a set of results that can be used to estimate the skin thickness obtained with a given set of experimental parameters in the millifluidic drop production setup.

Finally, this estimation is compared with the results obtained from tomographic reconstruction, presented in Chapter 6 : the silicone layer between two PEG drops is taken to be two touching skins, the interdrop distance being then twice the thickness h_0 .

The interfacial shear rheology experiments of Section 5.3.2 yield the temporal evolution of the shear modulus G'_{2D} of the gel formed at the PEG-silicone interface. An indirect measure of the thickness can be obtained by inverting Eq. (4.44), giving $h_0 = G'_{2D}/G'_{\infty}$. This indirect measurement, however, assumes that the structure of the interfacial gel is equivalent to that of the bulk gel. Two physical arguments can be raised against this approach. First, the advancement of the diffusion front of the catalyst does not presume of the advancement of the gelation p . Rather, the advancement, and hence the bulk shear modulus G'_{3D} at one point depends on the history of catalyst concentration over time. As shown in Fig. 5.11a-c, the evolution of the shear modulus between

the gel point and the final state of the gel still spans up to 4 orders of magnitude. Second, the interfacial gel is obtained through a hydrosilylation triggered by a diffusing catalyst, which involves the diffusion timescales of both platinum catalyst and silicone chains with progressing reaction. The final structure of the gel may differ from its bulk counterpart, because of the structuration of the interfacial layers caused by the lateral interactions between the anchored surfactant molecules [271, 28, 1, 124]. Furthermore, the formation of patterns at the interface [272] or in the bulk [273] is also a potential source of difference between the bulk and the interfacial gel. The diffusion of the catalyst from PEG to silicone creates gradient of concentration, hence a spatially-dependent reaction timescale, with subsequent diffusion of the unbound silicone chains potentially affecting the final structure of the gel. The interfacial gel formation thus has an intrinsic spatial as much as temporal component, from which one could expect its final properties to differ from its bulk phase. Moreover, the diffusion of the catalyst from PEG to silicone is a sensitive part of the reaction : the catalyst is dispersed in a solution of vinyl-terminated PDMS, which is itself dispersed in the PEG phase using an ULTRA-TURRAX stirrer (Chapter 2). The diffusion speed of the dispersion drops to the interface depends on their size, with a typical average speed $\langle v \rangle = \sqrt{k_B T / m}$, where m is the mass of the drop : the kinetics of skin formation thus depends on the preparation of the different solutions. Finally, as the skin grows, the height of the skin exceeds the height of the double-wall ring. The results obtained beyond this point cannot be considered as reliable. Nonetheless, we use our results from interfacial shear rheology to obtain an order of magnitude of h_0 , with the obtained estimation shown as data points in Fig. 5.19.

We compare the estimation of the skin thickness with estimations obtained from other approaches. To obtain a temporal evolution of the skin with controlled experimental parameters (ϕ_r, ϕ_p) , we construct a setup represented in Fig. 5.18a. It is made of a polycarbonate plastic block drilled with circular holes with a diameter of 5 mm. On the top of the holes, we place metallic grids used in cryo-SEM, with square pores of 500 μm length, shown in Fig. 5.18b. The block is then placed in a glass container, filled with the PEG-catalyst solution up to the top of the holes. The reactive silicone mixture is then slowly poured into the container, with a height of approximately 50 mm. In this configuration, the catalyst diffuses through the grid into the upper silicone phase, like in the double-wall ring setup. After the desired reaction time, we remove the metallic grid from the silicone blend with the skin still attached to the grid, and left hanging so that the uncrosslinked silicone flows down and leaves the grid. The grid with the skin are then imaged using X-Ray tomography, with the height of the skin being taken as the height of the gel at the center of the grid, as represented in Fig. 5.18d.

By using multiple holes and grids with the same PEG and silicone solutions, this setup allows to capture the skin formation at different times with the same preparation procedure. Moreover, compared to the interfacial rheology approach, the thickness is directly measured. The results are shown by black circles in Fig. 5.19d.

The kinetics of skin growth is faster than a diffusive process ($h_0 \sim t^{1/2}$) but slower than ballistic process ($h_0 \sim t$), as shown in Fig. 5.19d. This highlights the difference between the skin formation and a simple diffusion process, as explained in the beginning of this section. This faster than diffusive process could be attributed either to transport phenomenon expelling catalyst faster, or to late stiffening of the gel after the first gelation, increasing locally the bulk shear modulus G_{3D} and hence the overall interfacial modulus of the skin G_{2D} . These contributions can not be differentiated with our current experimental knowledge of the system. Despite its advantages, the configuration of this setup does not correspond to the spherical geometry of the drop, and the impact of the grid on the skin growth must be assumed to be negligible. We therefore further confront these experimental

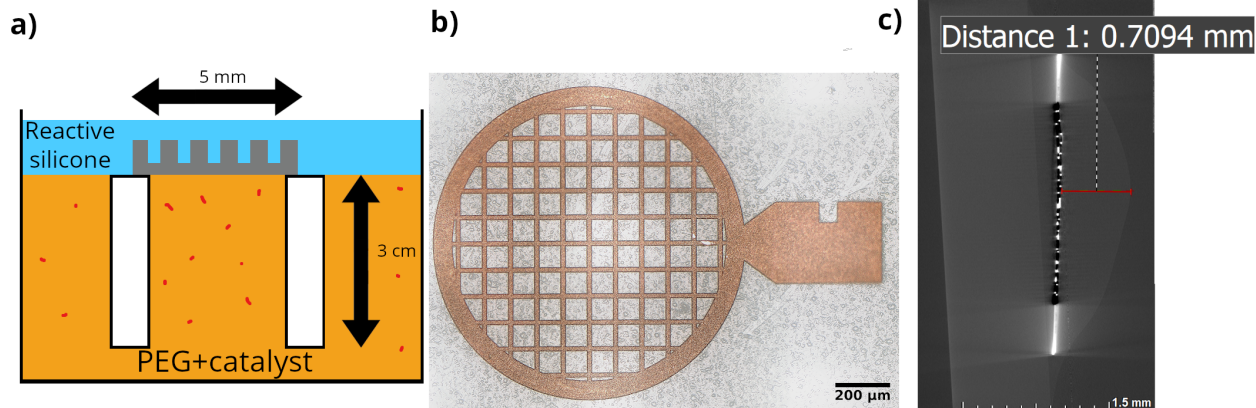


Figure 5.18: a) Scheme of the skin-on-grid setup. The metallic grid is removed after the desired reaction time and analysed using X-Ray tomography. b) The metallic grid used to grow the skin comes from SEM consumable material. c) Image of a silicone skin on a metallic grid, obtained with X-Ray tomography. The contrast between the silicone gel, the metallic grid and the air allows for an easy segmentation of the image. Bright spots close to the grid correspond to adsorption artifacts when the grid is aligned with the X-Ray beam. Experimental parameters : $\phi_r = 100$ wt.%, $\phi_p = 0.3$ vol.%, $\tau_r = 1000$ min.

results to measurements directly done on drops obtained by adding an individual PEG+Pt-catalyst drop into a vessel filled with the reactive mixture, and by rotating it continuously by hand to avoid prolonged contact with the walls of the vessel. The obtained droploons are then removed from the mixture and placed in a silicone solution filled with inhibitor to halt the skin formation. Before the observation of the skin, the droploons are placed on a grid so that unreacted silicone flows off the surface. This methods can only be applied on fully formed skins at the end of the skin formation. The data extracted from these time-consuming experiments are thus less detailed than interfacial rheology and on-grid skin growth.

The obtained droploons are then imaged using cryo-SEM (Scanning Electron Microscopy), equipped with a freeze-drying sample preparation system that freezes the droploons with liquid nitrogen [274]. The individual droploon is taken out of the silicone solution and frozen by dipping it into liquid nitrogen, before being placed in a hermetic preparation stage. The frozen skin is then broken with a thin metallic blade, before the drop is moved to the sample stage where it is imaged with a Hitachi SU-8000 SEM at 1000 V acceleration voltage and a 9000 nA emission current.

As the unreacted silicone flows away from the drop when it is removed from the solution, the silicone present in the sample can be taken as being part of the skin. We show the image obtained with cryo-SEM in Fig. 5.19b ($\phi_r = 50.2$ wt.%, $\phi_p = 1.0$ vol.%, $T_r = 20$ min). The image shows two distinct materials, with the first one forming a (broken) shell around the second. Owed to the condition of production of the droploon, we associate the shell material to the silicone skin, and the bulk material to the PEG. With the sliced images of the skin, we can estimate the thickness of the shell, which we found to be $88.3 \pm 5.5 \mu\text{m}$. This value is reported in Fig. 5.19d.

Since the cryo-SEM imaging relies on the breakage of the shell of the frozen sample, this method cannot image the full skin, but only slices of it. Moreover, the freeze-drying procedure might damage the sample and induce compression/dilation, depending on the materials and the preparation. We therefore complete these measurements with an indirect, non-destructive measurement through X-Ray tomography on emulsions obtained with the millifluidic setup described in Section 5.4.1.

Method	ϕ_r	ϕ_p	T_r	h_0
On-grid	100 wt. %	0.3 vol. %	470 s	$51.0 \pm 8.1 \mu\text{m}$
On-grid	100 wt. %	0.3 vol. %	1300 s	$99.4 \pm 4.7 \mu\text{m}$
On-grid	100 wt. %	0.3 vol. %	6000 s	$354.4 \pm 0.3 \mu\text{m}$
Cryo-SEM	50.2 wt. %	1.0 vol. %	22 min	$88.3 \pm 5.5 \mu\text{m}$
ANATOMIX	100 wt. %	0.3 vol. %	10 min	$1 \mu\text{m}$
Tomography	100 wt. %	1.0 vol. %	1320 s	$29.3 \pm 7.3 \mu\text{m}$

Table 5.2: Summary of the different skin measurement results described in Section 5.4.3. These results are shown in Fig. 5.19d, along with results from interfacial shear rheology.

The drop images obtained from tomographic reconstruction are separated by a thin silicone layer, which we assume to be their two skins in contact. An example is shown in Fig. 5.19a. Large skins ($h_0 \geq 5 \mu\text{m}$) can be imaged using the lab-owned X-Ray tomograph, described in Chapter 2. An example of results obtained with this tomograph is shown in Fig. 5.19a, with droplets produced with the set of experimental conditions ($\phi_r = 100 \text{ wt.}\%$, $\phi_p = 1.0 \text{ vol.}\%$, $T_r = 22 \text{ min}$). The skin average skin thickness was found to be $h_0 = 23.3 \pm 7.3 \mu\text{m}$.

For thinner skins ($h_0 < 5 \mu\text{m}$), one measurement at high resolution (300 nm) was performed at the ANATOMIX beamline from the SOLEIL synchrotron facility by Patrick Kékicheff, for a sample prepared with the set of experimental conditions ($\phi_r = 100 \text{ wt.}\%$, $\phi_p = 0.3 \text{ vol.}\%$, $T_r = 10 \text{ min}$). This level of resolution is obtained by switching from absorption tomography to phase-contrast imaging. The result shown in Fig. 5.19c is therefore not directly readable in terms of skin thickness, and requires complex image analysis techniques before any conclusion can be drawn from it [275]. The order of magnitude of the skin thickness can still be estimated by the gap of high gray level between the two PEG drops, which we found to be $h_0 \sim 1 \mu\text{m}$.

The results of the different methods are summarised in Table 5.2 and shown in Fig. 5.19d. From the comparison of the results, we can draw the following conclusions. First, the normalisation of the interfacial shear modulus with the bulk shear modulus yield skin thickness smaller than the other methods by one order of magnitude. This indicates that the interfacial gel is less stiff than its bulk counterpart. Second, the large difference between skin grown on a grid and on a drop's surface highlights the importance of the geometrical configuration of the system on the growth kinetics. As shown in Fig. 5.19a, we found a range of experimental parameters where the skin was thick enough for an easy segmentation of the drops in tomographic analysis of the emulsions. We used those to produce the samples described in Section 5.4.2. We further investigate the evolution of the interface in this experimental range using the capillary pressure elastometry described in Section 4.3.

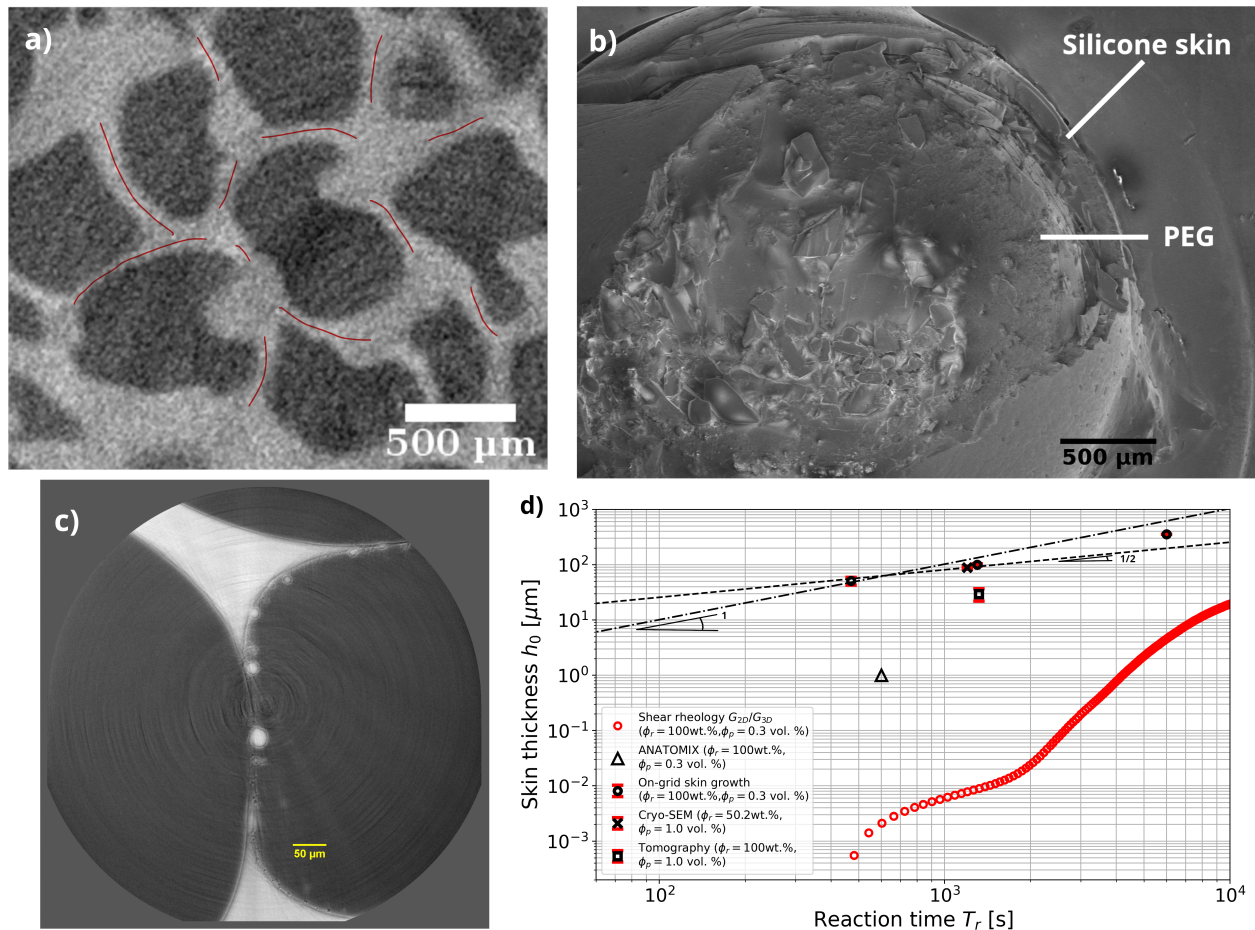


Figure 5.19: a) Slice of a PEG/silicone emulsion ($\phi_r = 100$ wt.%, $\phi_p = 1.0$ vol.%, $T_r = 22$ min) obtained by tomographic reconstruction at a resolution of $8 \mu\text{m}$ per voxel. The red lines represent the estimated position of the drops interfaces, where their skins touch. b) Image of a PEG drop with a gelified silicone skin obtained with cryo-SEM. Experimental parameters : $\phi_r = 50.2$ wt.%, $\phi_p = 1.0$ vol.%, $t = 20$ min. c) Image of PEG/silicone droplets obtained from tomographic reconstruction at ANATOMIX beamline, with a 300 nm/voxel resolution. Courtesy to Patrick Kékicheff. d) Skin growth with the different methods described in Section 5.4.3.

5.5 Conclusion

In this Chapter, we improved a PEG-PDMS system previously used by Giustiniani *et al.* [217, 234] to study the impact of interfacial interactions on the structural properties of emulsions [10]. We designed an experimental setup to replace the gelified silicone phase by an interfacial gel of controlled thickness, and characterise the rigidity and formation kinetics of the silicone skin. The origin of the later needs to be elucidated in future work. Different measurements of the skin thickness yield different results when performed with different methods. However, these results helped to select experimental parameters yielding skins thick enough for a simple tomographic segmentation of touching drops. This condition makes the packing analysis with X-Ray tomography easier and more reliable. The procedure of packing analysis will be described in Chapter 6. We also showed that the formation of the skin at the interface greatly changes the shapes of the droplets in emulsions. The PEG-silicone system is hence a good model system to investigate the interface-structure relations.

Interfacial rheological characterisation is a work-intensive task. Experimental investigation on the PEG/silicone system were therefore limited to the most simple parameter sets. The tuning of the membrane's properties could be more finely tuned by adding new parameters, such as the length and functionalisation degree f of MHDS molecules, or the stoichiometric ratio between the two reacting polymers [276]. Nonetheless, this system constitutes a promising model system for drops with interfaces of controlled elastocapillarity.

Chapter 6

Tomographic analysis of the structural properties of the droploon assemblies

6.1 Introduction

Jammed systems are ubiquitous materials [30, 31, 32], ranging from sandpiles [277, 278, 279] to powders [280, 281], up to foams and emulsions [15, 38, 49, 34]. Despite their differences, these systems share common features encouraging to capture their mechanics in an unified framework. Jammed systems are made up of unbound, distinct particles free to move with respect to each others. When these particles are brought into physical contact, they interact through contact forces, eventually supplemented by attractive or repulsive long-range forces. If the number of contacts per grain Z reaches a critical number named the isostatic contact number Z_c , grains are immobilised by their neighbours and the packing rigidifies in a jammed, static configuration [41, 37]. Furthermore, the displacements of individual grains do not vary continuously over smooth, affine displacement fields [44], discarding a description with an effective medium approach : local environment [43, 282, 283] and non-affine displacement fields (especially close to jamming [284]) are decisive components of the macroscopic behaviour of jammed materials.

The mechanical behaviour of the jammed material is then a consequence of the inter-particle interactions [41, 42, 44] and the geometrical organisation of the packing [39, 47], as described in Section 3.1.2. For instance, it has been shown that the shear response in numerical simulations of harmonic discs depended on the construction algorithm used to produce the packing [288], highlighting the necessity of a proper understanding of the packing structure to predict its mechanical properties. In particular, the description of the orientation and magnitude of the interparticle forces is a good predictor of the heat transport properties [289] and the acoustic properties of the material [110, 290, 291, 44, 292, 293]. Knowledge of the complete set of interparticle forces and the conditions of rigidity onset are an old field of investigation in granular science. The latter was already investigated by Maxwell [294] in the case of frictionless joints connected by rigid struts. By constraint counting argument, Maxwell formulated a necessary (although not sufficient) criterion for the rigidity of the structure, formulated in dimension d [295] as

$$b - dj + 2d \leq 0 \tag{6.1}$$

where b is the number of strut and j is the number of joints. Representation of stable and unstable structures in the sense of Maxwell's criterion are shown in Fig. 6.1a-b. The isostatic contact number Z_c can be deduced from a similar reasoning for granular materials : in the limit of large

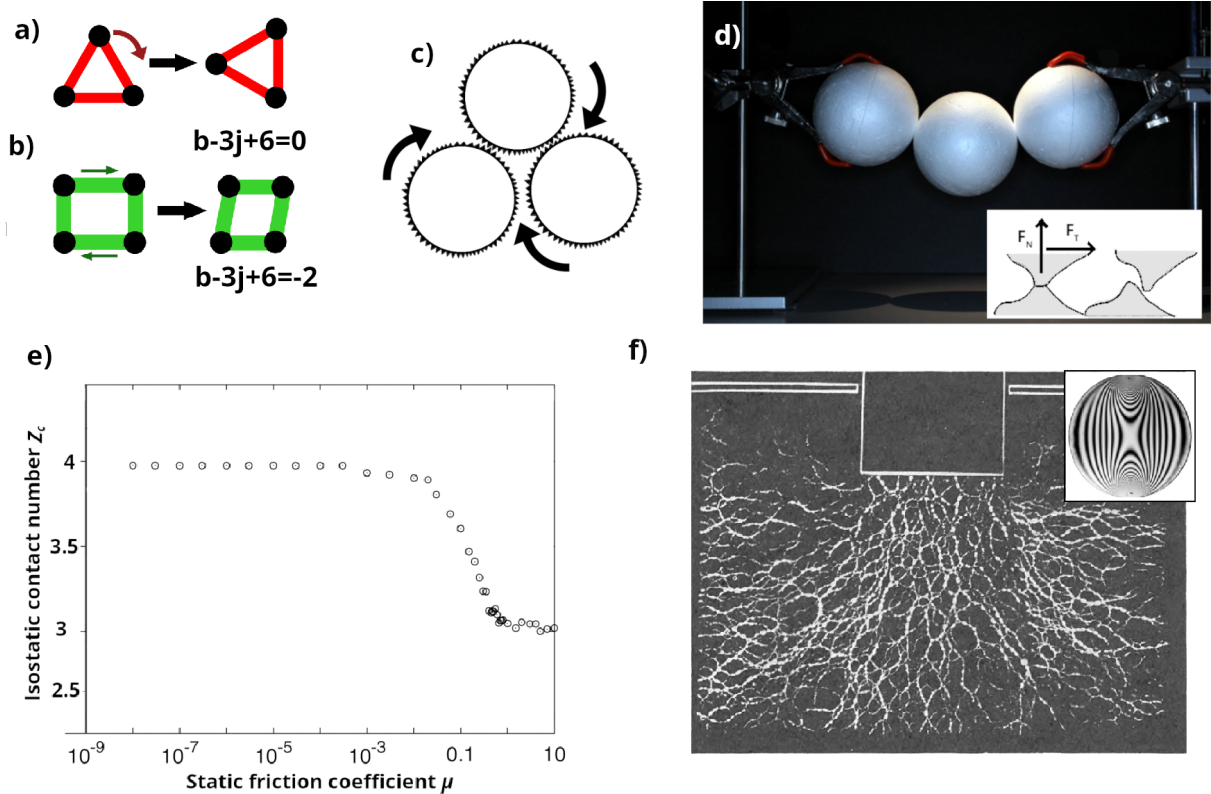


Figure 6.1: a) Three joints connected in a 3-cycle form a mechanically stable structure, with rotation and translation of the whole system being the only degrees of freedom. b) Four joints connected in a 4-cycle can deform, e.g. when subjected to shear. c) Interlocking of the indentations at the surface of the sphere hinder the rotation with static friction. d) Three Styrofoam spheres, stabilised by static friction. The normal and tangential forces respect the Amontons-Coulomb criterion, stabilising a structure that would collapse for frictionless particles. Figure from [43], inset from [32]. e) Evolution of the isostatic contact number Z_c with the static friction coefficient μ , for 2D discs. Figure adapted from [285]. f) Force chains visualised in photoelastic disks. The thickness of the filaments of transmitted light indicate the location of the strong interparticle forces, which focus in strong force chains aligned in the same direction. Figure from [286], inset from [287].

number of grains ($j \rightarrow +\infty$), the term $2d$ in Eq. (6.1) can be neglected, thus giving by inversion $b \leq dj$. Every strut is shared between two joints, and thus needs to be counted as a half strut to avoid double counting, following the handshaking lemma of graph theory [296]. In that case, the stability criterion of Eq. (6.1) becomes a condition for every joint and reads as

$$b \leq 2dj. \quad (6.2)$$

In the case of granular materials, where joints are replaced by grains and struts are replaced by interfacial contacts between them, the condition of Eq. (6.2) corresponds to the isostatic contact number $Z_c = 2d$ for frictionless grains (or $Z_c = d + 1$ for frictional grains), as shown in Fig. 6.1e. This prediction matches accurately the experimental observations for foams and emulsions, where the bubbles and the drops are frictionless. However, solid grains are not perfectly spherical objects, but rather have a geometrically rough surface. The interlocking of their asperities creates tangential friction forces at their contact [297]. In a static configuration, the friction keeps the particles static even when external forces (e.g. gravity or load stress) would cause the same packing to collapse if friction was absent, as shown in Fig. 6.1d. The stability criterion is usually well-described by the

Amontons-Coulomb law relating the tangential force F_t to the normal force F_n

$$F_t \leq \mu F_n \quad (6.3)$$

where μ is the static friction coefficient, and $\mu \geq 0$. Eq. eq6.3 gives an upper limit of the tangential force for the packing stability as a function of the normal force. First, it constrains the rotational degrees of freedom of every particle in the same manner that normal, frictionless contacts constrain the translational degrees of freedom. By imposing a condition on the tangential forces, every contact now imposes three additional constraints : in the limit of large packings, the Maxwell rigidity criterion then becomes

$$b \leq (d + 1)j, \quad (6.4)$$

which is a known result for frictional grains [37], where the isostatic number $Z_c^\mu = 4$ in 3D and 3 in 2D, as represented in Fig. 6.1e. The second consequence, closely linked to the first one, is the hyperstaticity of the packing : considering a given configuration of particle positions, the set of interparticle forces satisfying the stability of the packing is not unique [298]. Eq. (6.3) only gives an upper limit to the tangential force. A static particle configuration can thus be sustained by a whole range of normal and tangential forces [32]. This under-determination led some authors to consider the forces inside a granular material as a statistical ensemble whose configuration is a particular statistical realisation happening with a given probability [298, 299, 300, 113].

The measure of the contact forces between two grains in a packing is no simple matter : acquisition of the grain position inside of a 3D packing requires advanced imaging techniques. Commonly used techniques are confocal fuorescence microscopy for micrometric grains [114, 89, 35, 62, 301, 95, 96] or computer-assisted tomography for micro- to millimetric grains [302, 303, 304, 305, 58]. If the grains are sufficiently soft, the contact force may then be deduced from the measure of the deformation, requiring an *a priori* knowledge of the constitutive law of the material [35, 302]. As we showed in Chapter 3, this approach is fundamentally flawed by its pairwise assumptions, whilst a proper account for non-pairwise interactions has yet to be proposed in the force determination of 3D bubbles [109]. The undetermination of normal contact forces makes the makes the study of their transmission through particulate materials a difficult task for standard grains. It has thus for long been studied with photoelastic discs [287], shown in Fig. 6.1f, where the normal forces can be deduced from their optical transmission properties. The photoelastic properties of materials arise from the variation of the refractive index with the material stresses ; an anisotropic deformation thus gives rise to a birefringent material, with deformation-dependent refractive indices. The evolution of light polarisation when passing through the material thus provides a measure of its internal stress, and in particular the anisotropy of the internal stresses. By placing the photoelastic discs in a proper experimental setup, the stress can be measured as a function of the transmitted light intensity, with the number of interference fringes increasing with the applied stress. This simple experimental setup allowed, in its first iteration by Dantu [286], to establish a first measurement of the stress propagation through powdered materials , with visually striking results reproduced in Fig. 6.1d.

The interparticle forces in granular materials show complex and surprising behaviours, which further distinguish them from homogeneous, field-averaged approximated models. In Section 6.1.1, we review the descriptive approaches used to characterise granular systems, based on the organisation of their grains and the interaction forces between these grains. In Section 6.1.2, we present how these contact and force networks are described using tools from network theory, which easily

switch between lengthscales and can correlate structures at the grain scale and at the packing scale. In Section 6.1.3, we focus on the applications of these tools to the study of foams and their deformations.

6.1.1 Organisation and force transmission in granular materials

Jammed materials consist of large collections of interacting grains in a mechanically stable configuration. The typical size of these grains ranges between 1 and 1000 μm [32], where the random motion coming from thermal agitation is negligible : grains are usually taken as a-thermal particles, and the configuration of the assemblies is modified by interparticle interactions and external fields alone. For that reason, spontaneous rearrangements do not occur, trapping granular systems in metastable configurations of local energy minima that may differ significantly from the global minimum. This local entrapment can be overturned by injecting energy in the system to make it explore its configurations, i.e. by tapping the granular materials repeatedly or by allowing fluid flow through the packing, increasing the packing fraction in the process [306, 307, 308, 309, 310, 311], as represented in Fig. 6.5.

This variability in the organisation at the grain level for configurations seemingly identical at the packing level, and the large number of particles taking part in the same packing are strong incentive to describe granular systems with the tools of statistical physics. This conceptual leap was first pushed forward by Edwards *et al.* [312, 313, 117, 314], who replaced the Hamiltonian description of the microstate by a volume function $\mathcal{W}(\{\mathbf{r}_i\})$ of the particles. For the sake of simplicity, we will describe here the Edwards statistical ensemble applied to rigid, monodisperse hard spheres : it can be readily extended to soft spheres and grains of any arbitrary shape [315].

We consider an assembly of N monodisperse rigid spheres, with a configuration of particles being described by the set of positions of all the centroids $\{\vec{r}_1, \vec{r}_2, \dots, \vec{r}_N\}$. A configuration is defined as jammed if it satisfies both mechanical equilibrium (i.e. force and torque balance) and excluded volume constraints. For monodisperse spheres of radius R , this constraint is expressed as

$$\forall i \neq j, |\vec{r}_i - \vec{r}_j| \geq 2R, \quad (6.5)$$

meaning that any two sphere centers must be at a distance at least equal to twice the radius of the spheres. As sketched in Fig. 6.2a, noting \vec{d}_a^i the vector joining the particle center \vec{r}_i to the a^{th} contact point, and \vec{f}_a^i the force exerted on particle i at this contact point, the mechanical stability conditions read as

$$\sum_{a \in \partial_i} \vec{f}_a^i = 0, \quad i = 1, \dots, N \text{ (force balance)}, \quad (6.6)$$

$$\sum_{a \in \partial_i} \vec{d}_a^i \times \vec{f}_a^i = 0, \quad i = 1, \dots, N \text{ (torque balance)}, \quad (6.7)$$

where ∂_i is the set of interfacial contacts of particle i . For frictional particles, normal $f_{a,n}^i$ and tangential $f_{a,t}^i$ components of the contact force are related through the Amontons-Coulomb inequality (Eq. (6.3)), with the additional constraint

$$|f_{a,t}^i| \leq \mu f_{a,n}^i, \quad i = 1, \dots, N \quad \text{(static friction)}. \quad (6.8)$$

The contact forces are in most situations purely repulsive, and produce a counterforce of equal magnitude and opposite direction, as implied by Newton's third law. These two conditions are expressed as

$$\vec{d}_a^i \cdot \vec{f}_a^i < 0, i = 1, \dots, N \quad (\text{Repulsive forces}) \quad (6.9)$$

$$\vec{f}_a^i = -\vec{f}_a^j \quad (\text{Newton's third law}) \quad (6.10)$$

where j is the index of the particle in contact with particle i at the contact point a . The mechanical constraints expressed in Eqs.(6.6)-(6.10), along with the excluded volume constraint of Eq. (6.5), are necessary and sufficient to define a jammed state. The volume of this state is related to the configuration of its particles $\{\vec{r}^i\}$ by the volume function \mathcal{W} , with

$$\mathcal{W}(\{\vec{r}\}) = \sum_{i=1}^N \mathcal{W}_i(\vec{r}^i). \quad (6.11)$$

The microcanonical Edwards ensemble relies on the assumptions that a system of N particles, occupying a volume V , do so such that every configuration $\{\vec{r}\}$ leading to the same volume is equally probable. This assumption implies that macroscopic properties can be computed as ensemble averages over jammed configurations of equal probabilities, with the volume of the system as an external control parameter. This uniform probability distribution of the configurations allows for a simple expression of the partition function Θ_{jammed} as a sum of the possible configurations under the constraints of mechanical stability and hard-core repulsion, along with a granular entropy $S(V)$ and number of microstates $\Omega(V)$. The form of the partition function is of no interest in our case : interested readers are referred to Eq. (10) in [315].

As the system is controlled by the volume function defined in Eq. (6.11), an accurate segmentation of space is required to define a volume \mathcal{W}_i associated to every particle i . Previous work showed that the set Voronoi diagram was the most practical way to tessellate a 3D space unambiguously [316, 317]. As shown in Fig. 6.2b, this method proceeds by defining, for every body of the packing, a Voronoi cell in which every point is closer to the surface of the grain than to any other point [58, 318, 319]. Compared to other methods, such as simple Voronoi diagrams, the set Voronoi diagrams work directly with the surface of the grains, rather than their centroids. This feature is particularly useful for grains that are not isotropic spheres, e.g. deformable drops and bubbles [320, 98]. Equipped with this simple volume segmentation procedure, one can properly characterise isostatic granular packings using Edward's volume ensemble.

For isostatic systems, the ensemble of the contact forces can be determined from the positions of the particles. The configurational degrees of freedom are therefore sufficient to characterise the system, in what is called the volume ensemble [315]. On the other hand, for hyperstatic systems, the underdetermination of the contact forces decouples the forces from the positions of the grains. The force network comprises an ensemble of contact forces obeying the mechanical constraints Eqs.(6.6)-(6.10), with a fixed set of grain positions $\{\vec{r}\}$ [299, 300, 298, 284]. An experimental illustration of the ensemble of possibilities of forces distributions in hyperstatic packings was provided by Kollmer *et al.* [113] who compressed repeatedly a packings of 2D photoelastic discs, changing the distribution of contact forces without affecting the positions of the particles, as shown in Fig. 6.3. The spatial distribution of the contact forces, however, was found to be connected to the structural organisation of the packing, indicating a link between mechanics and geometry. The structural

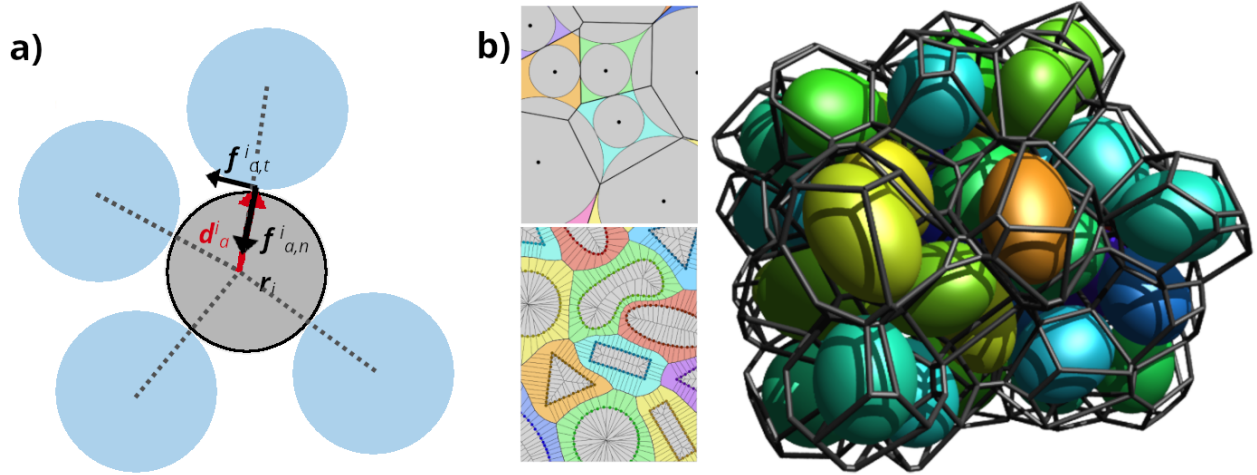


Figure 6.2: a) Schematic representation of the contact forces applied on a particle i . The vector \vec{d}_a^i joins the center of the grain to the a^{th} contact. Figure from [315]. b) Example of set Voronoi tessellation. Each colored particle is given a set Voronoi cell, corresponding to all the points closer to its surface than to that of any other particle. Figure from [318].

organisations of the packing can thus be used to infer the most probable force distributions, though finding the most accurate measure is still an unanswered question. The quantitative descriptors of forces and contact networks are detailed in Section 6.1.2.

In the cases where the contact forces can be measured, their distribution $P(f)$ can be com-

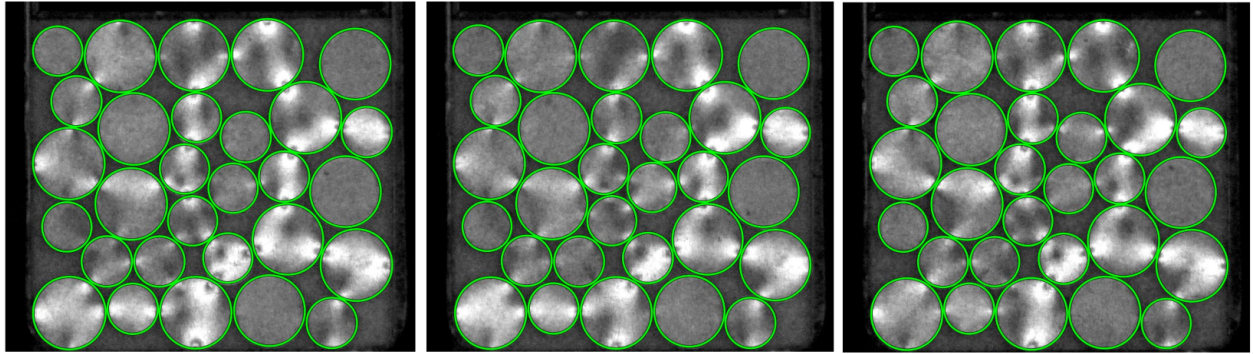


Figure 6.3: Same packing of photoelastic discs undergoing compression cycles. The distribution of the forces, visible as the white light transmitted through the discs, changes between the compression cycles without the discs changing their positions. However, this average force exerted on one disc over the ensemble of configurations is correlated to its position in the packing. Figure from [113].

puted, which gives a comparative description of the different realisation of the force networks. Experimental and numerical results showed that this force distribution exhibits a peak around the average force $\langle f \rangle$, a power law with a weak negative exponent for forces smaller than average, and an exponential decay for forces larger than average [90, 321, 35, 322, 323]. An example of force distribution is shown in Fig. 6.4d. The stress is not distributed homogeneously throughout the packing: the large stresses are concentrated along the contacts between aligned grains, forming force chains of large amplitude [324, 323, 325] correlated on length scales larger than the grain size. The existence of directions of preferred force propagation is a phenomenon first observed by Dantu

[286] when looking at the compression of photoelastic materials : the visualisation of the chains is a striking illustration of the inhomogeneities in the stress propagation, shown in Fig. 6.4c.

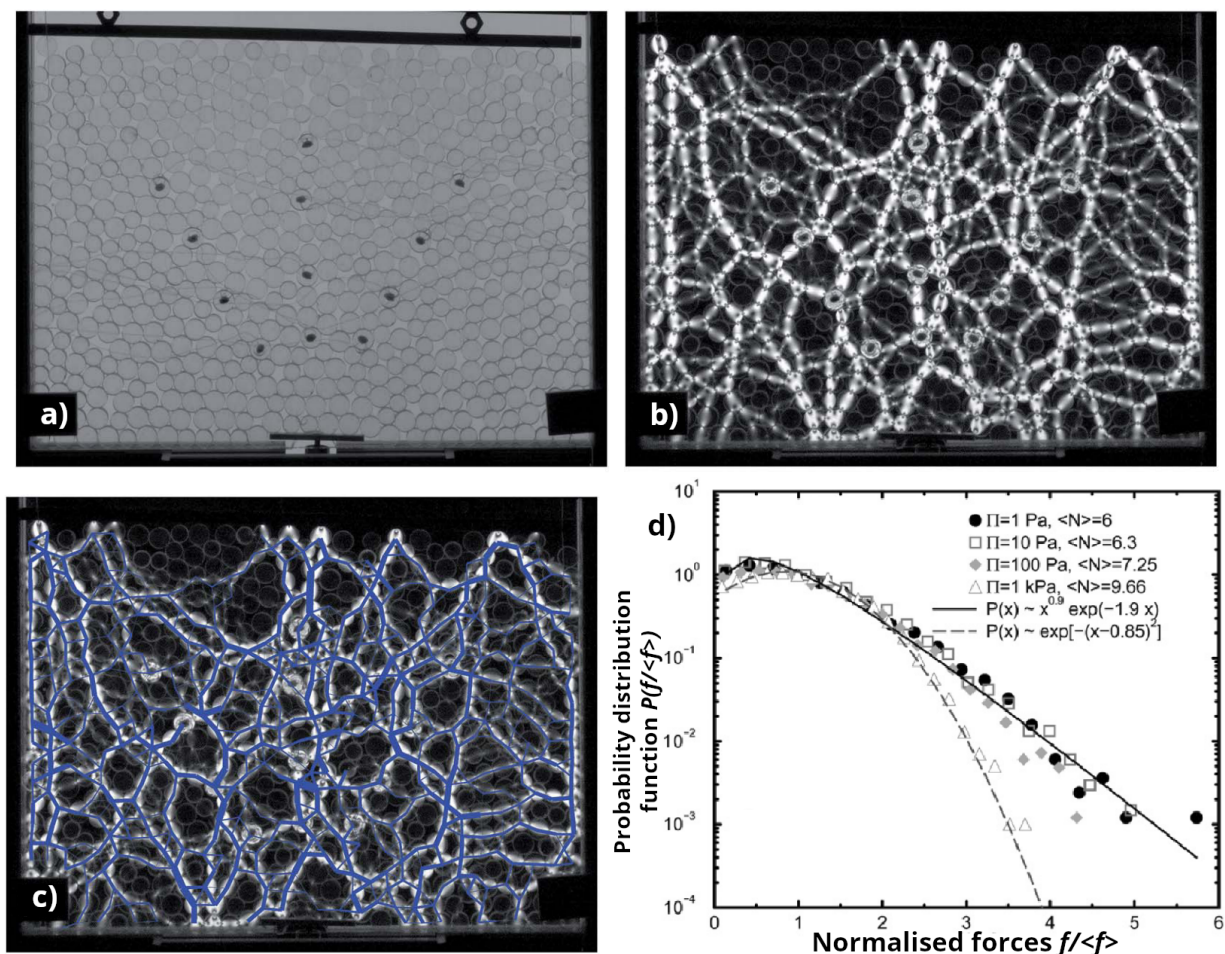


Figure 6.4: a) Packing of photoelastic discs. The plate at the top of the packing imposes the external pressure. b) Polarised light transmitted through the stressed discs. The intensity and number of fringes are used to deduce the contact forces [287]. c) Reconstructed force network. The thickness of the blue lines indicates the normal force amplitude. Images taken from [112]. d) Distribution of the contact forces in a silicone-in-water emulsion imaged with confocal microscopy. The amplitude of the forces are deduced using the Princen model [94]. Figure from [35].

Although very visual, a rigorous definition of a force chain is not straightforward. Some authors [326, 327, 328, 329, 330, 331, 332, 325] define the force chains by removing from the representation all forces below the average force $\langle f \rangle$. These force chains can be analysed in terms of force probability distribution and chain length [333]. However, contact forces smaller than average also seem to play an important role in the stabilisation of the load-bearing force chains [334] : an *a priori* threshold could miss crucial information about the packing stability. For that reason, other authors [111, 110] define a force chain as an ensemble of grains applying more forces on each other than on other grains, based on complex network tools such as community detection [335, 336] that do not exclude weak contact forces. The statistical tools of complex networks can be used to quantitatively analyse these force chain networks. The different scales involved, from the grain to the force chain to the packing, are analysed using quantitative descriptors adapted to each scale : this description thus simultaneously encompasses microscopic, mesoscopic and macroscopic scale,

and is a promising tool for inferring the relations between grain and packing properties. A detailed description is given in Section 6.1.2.

The structure of force chains stabilise the packing, bearing most of the load and maintaining the configuration of the packing until it buckles. During the mechanical loading, force chains form in the direction of major principal compressive stress [337, 338, 55, 339, 340], as shown in Fig. 6.5b : the alignment of non-sliding contacts bear most of the load, with highly anisotropic stress and deformation of the contact geometry [334]. Other contacts, with forces smaller than average, leave the grains free to slide with respect to each other, with an isotropic stress state making this secondary network more akin to a fluid. Furthermore, the arrangements of weakly stressed grains also adjust with a geometrical anisotropy of deformation orthogonal to the anisotropy of the force chains deformation, stabilising the principal force chains against buckling [334].

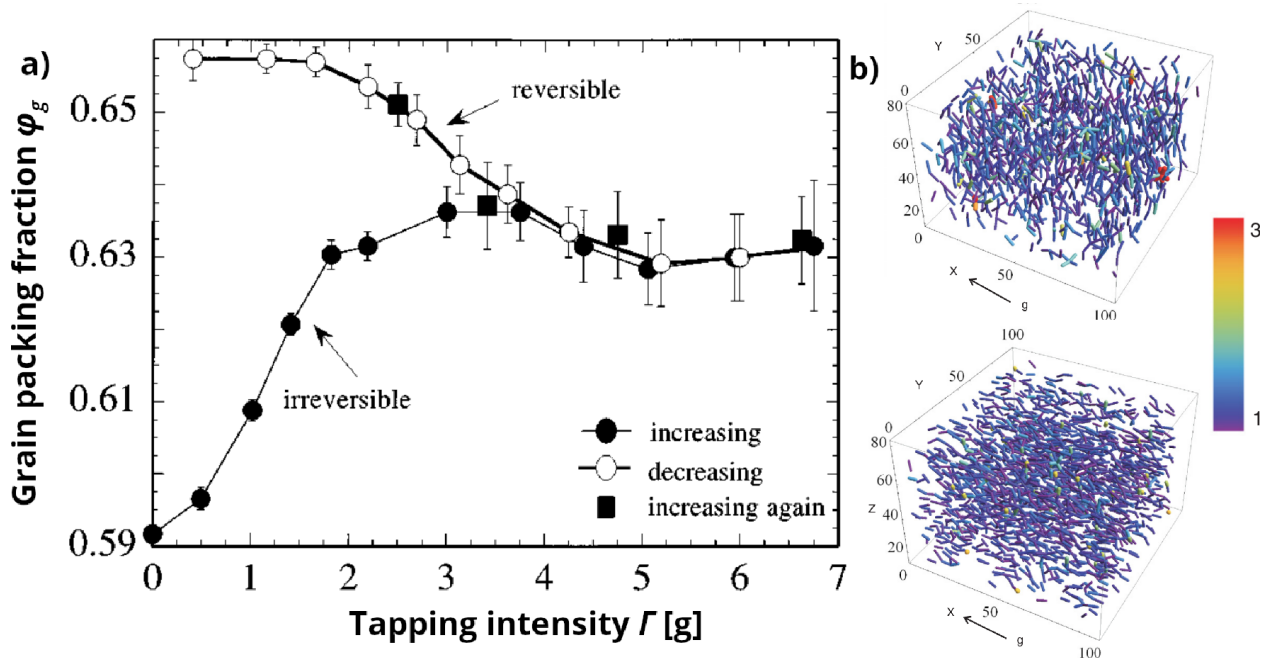


Figure 6.5: a) Evolution of the packing fraction of spherical beads with tapping intensity, with the maximal force of the tapping expressed in units of gravitational acceleration. The packing undergoes an irreversible transition from weakly packed to densely packed organisation, and remains in this densely packed state afterwards. Figure from [310]. b) Force networks between PDMS shells imaged with fluorescence confocal microscopy. The forces are deduced from the indentation depth. The packing is uniaxially compressed in the direction parallel to the gravity (x-axis) at grain volume fraction of $\phi_g = 0.699$ (top) and $\phi_g = 0.908$ (bottom)). Force magnitudes are represented with a color code as multiples of the average force. Figure from [96].

The pattern of the force chains impact the sound propagation in the packing [331, 332]. However, describing large ensembles of forces and making comparisons between different ensembles to find common features and differences is a difficult task because of the large set of data required to fully describe the packings, and the different length scales involved in their mechanical properties. Compared to other large ensembles of interacting elements (e.g. gasses or ionic solutions), the grains in granular systems only interact directly with their contact neighbours.

As we showed in Chapter 3, the interactions between bubbles/drops are intrinsically non-pairwise. Nonetheless, they remain based on contact forces, and distant bubbles/drops do not interact directly, keeping the number of independent contact forces relatively low. Comparatively,

this number grows a lot faster with the number of elements in systems where elements interact simultaneously through long-range forces. This particularity of granular materials fostered their study in the light of network theory, which we proceed to describe in Section 6.1.2. The tools developed to characterise large, complex networks have proven fruitful to yield some insight into the mechanics of large grain ensembles. Our understanding of foam and emulsion mechanics is likely to be similarly enriched by such quantitative description of their interactions at the bubble/drop scale.

6.1.2 Networks in granular science

Granular systems consist of macroscopic grains interacting through contact forces. As discussed in Section 6.1.1, the contacts can be localised and the forces can be measured, and the granular packings can be described by the number and the geometrical organisation of the contacts, as well as the distribution and spatial orientation of the contact forces. Since most grains are undeformable, the interactions remain pairwise in a good approximation. As such, a description inspired from graph theory has been successfully applied to granular systems for decades [341, 342, 343, 344, 345]. We will describe the principal tools of graph theory applied to the description of granular systems.

A mathematical graph \mathcal{G} is composed of a set \mathcal{V} of vertices, connected in pairs by a set \mathcal{E} of edges, as represented in Fig. 6.6a. In its most simple form, the graph is undirected, meaning that the edges have no preferential direction between the vertices they connect. In the case of *weighted* graphs, every edge has a given weight w_{ij} , representing for example the strength of the bond between the two vertices. The graph \mathcal{G} can be quantitatively described by the organisation of the bonds between the vertices : for example, the average number of edges $\langle k \rangle$, the frequency of clusters of three connected grains C or the number of l -paths connecting l particles in a closed loop can describe a graph without assuming the nature of the interactions between its edges.

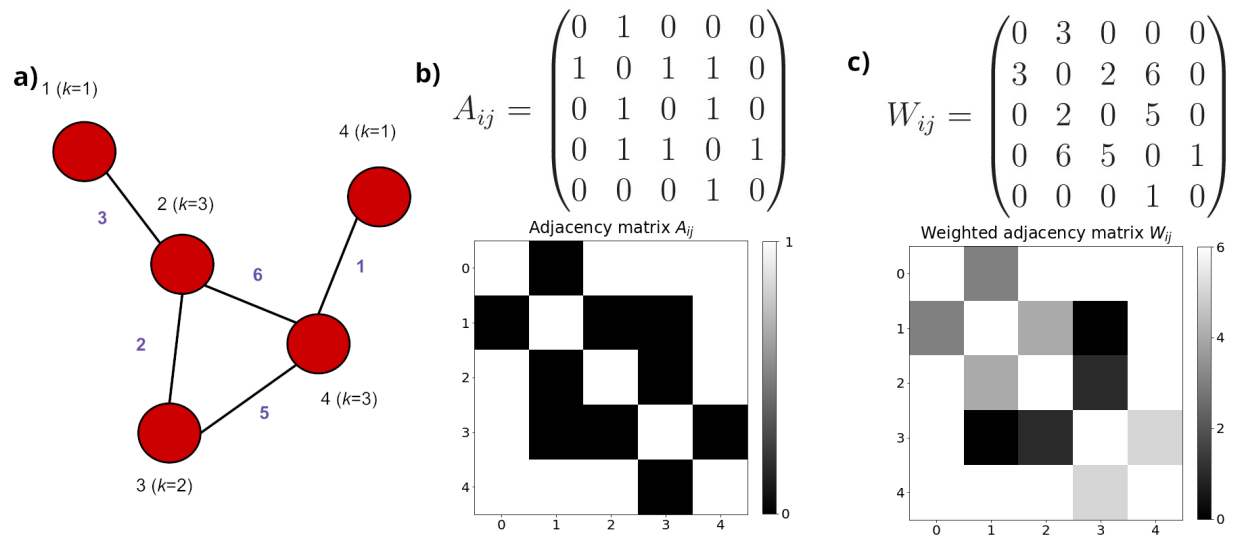


Figure 6.6: a) Example of a weighted network. Edge weights are indicated with the purple numbers along the edges. b) Adjacency matrix and its visual representation. c) Weighted adjacency matrix and its visual representation.

Granular systems can be readily translated into graphs [346], like the one represented in Figure 6.7a. The vertices are replaced by the centers of the grains, and the edges by the contacts between the grains. The list of the edges are summarised in the adjacency matrix A_{ij} , as shown in Fig.

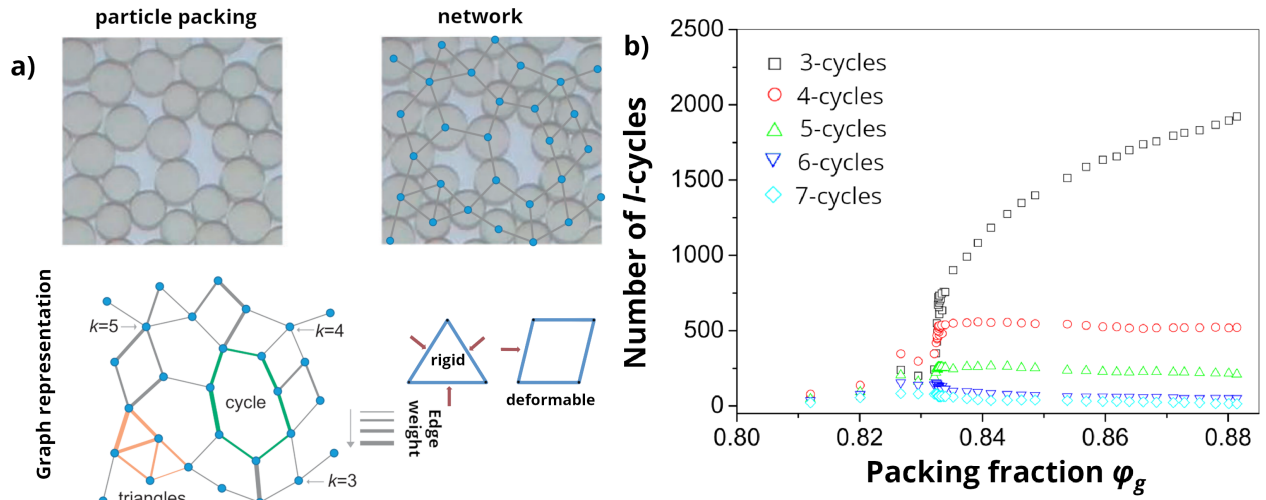


Figure 6.7: a) Example of the translation of a granular packing into a graph. The centroids of the particles take the place of the vertices, the contacts become the edges, and the contact forces give the weights of the edges. The rigidity of the structure can be estimated with the help of the edge weights and the l -cycles, with 3-cycles favoring the rigidity of the packing. Figure from [346] b) Evolution of the number of l -cycles in 2D simulations of 2048 bidisperse harmonic discs. Only the number of 3-cycles increases with the packing fraction beyond the jamming point, contributing to the increasing rigidity beyond jamming. Figure adapted from [347].

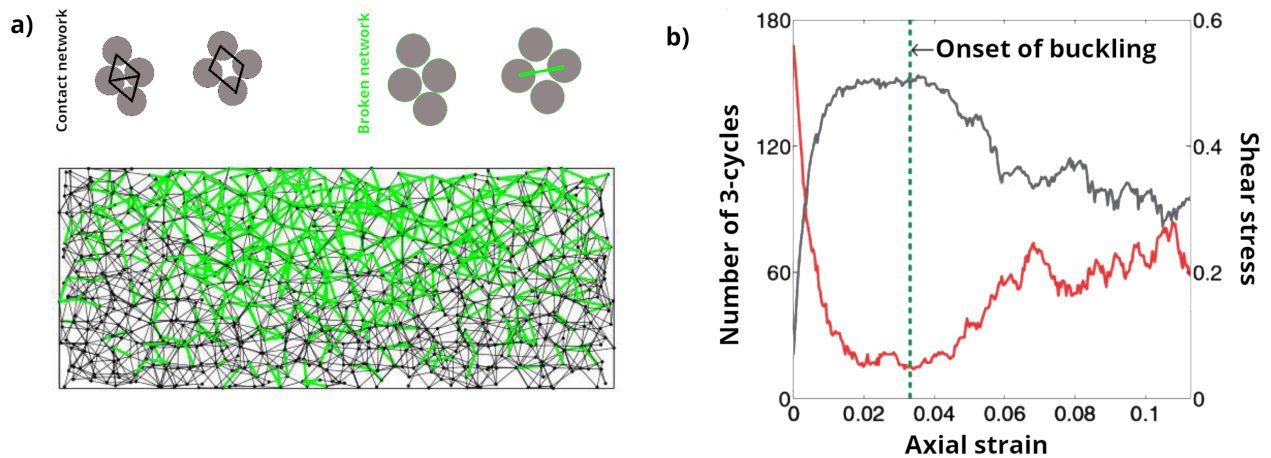


Figure 6.8: a) Example of the breakage of bonds between grains in a packing of rigid spheres subjected to shear. Four grains are touching in pairs, with the edges represented in black. During the deformation, the central edge is broken, transforming two 3-cycles in one 4-cycle. The broken edges are represented in green. The multiplication of broken edges (bottom) correspond to the yielding of the packing. Figure adapted from [348]. b) The diminution of 3-cycles number in shear experiments correspond to the diminution of the rigidity, with a buckling of the force chains when the number of 3-cycles is minimal. Reformation of 3-cycles correspond to the rigidification of the structure post-buckling. Figure from [330]

6.6b, defined as

$$A_{ij} = \begin{cases} 1, & \text{if there is an edge between } i \text{ and } j \\ 0 & \text{otherwise} \end{cases}. \quad (6.12)$$

where $i, j \in \{1, \dots, N\}$. The adjacency matrix thus encodes the contacts between the grains. The force of the interactions between the grains can be encoded in the matrix by giving to each edge a weight w_i corresponding to the contact force [290, 112] : the weight matrix W_{ij} encodes this information as shown in Fig. 6.6c, and is written as follows

$$W_{ij} = \begin{cases} w_{ij}, & \text{if there is an edge between } i \text{ and } j \\ 0 & \text{otherwise.} \end{cases} \quad (6.13)$$

Adjacency and weight matrix are invariant by permutations of rows and columns, as the information they carry is not modified by these operations. Similarly, the displacement of a vertex does not change the properties of the network, as long as its connectivity properties are preserved. With that regard, a granular system is a particular case of *spatially embedded* networks, where the positions of the vertices matter to understand the properties of the ensemble [349]. The formation of contact points between the grains at jamming and during deformation depends on the proximity of the grains.

A lot of informations about the structure of the packings can be extracted from the adjacency matrix A_{ij} : for instance, the contact number Z is expressed in graph theory as the coordination valence k_i of a vertex. For an unweighted graph, the degree of vertex i is expressed as

$$k_i = \sum_{j=1}^N A_{ij}. \quad (6.14)$$

The average degree $\langle k \rangle$, equivalent to the average contact number $\langle Z \rangle$, is computed as the mean degree of the network

$$\langle k \rangle = \frac{1}{N} \sum_{i=1}^N k_i = \frac{1}{N} \sum_{i=1}^N \sum_{j=1}^N A_{ij}. \quad (6.15)$$

The degree distribution is a straightforward feature of a graph at the grain-scale. But graph theory offers quantitative descriptions of the structure of a packing at a scale larger than the grain. For instance, an l -cycle is a path of l consecutive edges, starting and finishing at the same vertex without passing through the same vertex twice. A 7-cycle and a few 3-cycles are highlighted in Fig. 6.7a. These structures of intermediate scale contribute to the stabilisation of force chains during compressions [334]. In compression experiments, new contacts form with increasing excess packing fraction $\Delta\phi_g = \phi_g - \phi_g^*$, as explained in Section 3.1.1. The packing rigidifies with the increase of the contact number [37], making a simple connection between grain-scale organisation and macroscopic properties. Beyond the grain scale, the evolution of the local arrangement of the grains is also found to be linked to the changes in rigidity of the packing. As such, the formation of 3-cycles and the apparition of small forces they bear is linked to the jamming transition, as shown by Arevalo *et al.* [350]. Away from jamming, the reorganisation of the grains with excess packing fraction is well described by counting the evolution of the number of every cycle size [347], as shown in Fig. 6.7b. The rigidification of the packing above jamming is linked to the increase in the number of 3-cycles, the only cycle length varying with packing fraction above jamming. Similarly, the number of 3-cycles in a packing subjected to shear decreases when approaching the yield strain,

before increasing again after yield [330], as represented in Fig. 6.8b. The breakage of bonds can be used to monitor and localise yielding in the sheared packing [348]

The heterogeneities in the spatial distribution of contact forces fosters the formation of structures of intermediate scales, also called *meso*-structures. In network theory, these structures are often described in terms of *community structure*. Owing to the large scope of systems encompassed by networks, a general definition of a community can be difficult to formulate. In the case of granular systems, a community is a group of vertices strongly interconnected with each other in terms of total edge weights, but sparsely connected with other groups [346, 335]. The whole packing can then be separated in modules made of large-scale structures, which can in turn be subdivided into smaller structures all the way down to the single grain. The intrication and the hierarchies of these modules gives a comprehensive picture of the structures relevant to the properties of the packings at all scales, without requiring *a priori* assumptions about the most important scales. With the tools of community detection, the detection and characterisation of force chains can include the weak forces without setting an arbitrary threshold, important for the stabilisation of force chains [334]. Community detection is a very active field of network theory, owing to the wide variety of systems described with networks : interested readers are referred to the dedicated literature [335]. Geometrical and topological descriptors describing the force networks can be used to compare experimental packings and realisations of the force network ensemble described in Section 6.1.1 [111].

Different descriptors focus on different scales of the systems, which in turn are better suited to describe mechanisms happening at these scales. For instance, the mechanical response of a granular packing to an acoustic excitation has been found to be linked to different scales of the weighted force network [110]. The response of a packing to an external oscillating field was found to be best described at the packing scale, while its dissipative behaviour is more linked to the local environment of the grains. This separation of scale provides insight on how to tune one particular mode of propagation without affecting the other : for instance, changing the interparticle friction, which is directly linked to the local environment of the grains [43], and which directly affects the topology of the contact network [327].

The different lengthscales of analysis do not require any assumptions on their relative intrications, as long as the interparticle forces can be correctly determined. Network theory is an insightful tool to describe these different lengthscales, and how they are affected by the changes in the inter-grain interactions. In foams and emulsions however, the deformability of the particles makes the force determination in three dimensions a daunting, still unresolved task [109]. Nonetheless, the unweighted contact network is correlated with the force network. As shown by Kollmer *et al.* [113] for 2D photoelastic discs, the position of a particle in the contact network can help to predict the average force exerted on it over the sets of realisations of the force network ensemble. In particular, the betweenness centrality b , defined as

$$b_i = \sum_{j \neq k \neq i} \frac{s_{jk}(i)}{s_{jk}}, \quad (6.16)$$

was found to be a good predictor of the average pressure exerted on the particles over repeated compression cycles. This betweenness centrality of a particle i is a measure of the number of shortest paths in the contact network passing through i , where s_{jk} is the ensemble of the shortest paths between particles j and k , and $s_{jk}(i)$ is the number of these paths passing through i . The length of a path is in that case a topological measure, based on the number of vertices passed

through following the path. The correlation between betweenness centrality and average pressure of the packings of Fig. 6.3 is shown in Fig. 6.9. Even in the absence of a proper force network, the determination of the unweighted contact network and of the set of relevant descriptors, associated with a quantitative measure of the deformations of the drops/bubbles, is already a first important step towards a comprehensive description of foams and emulsions. In the next Section, we describe how the tools of network theory are applied to foams and emulsions.

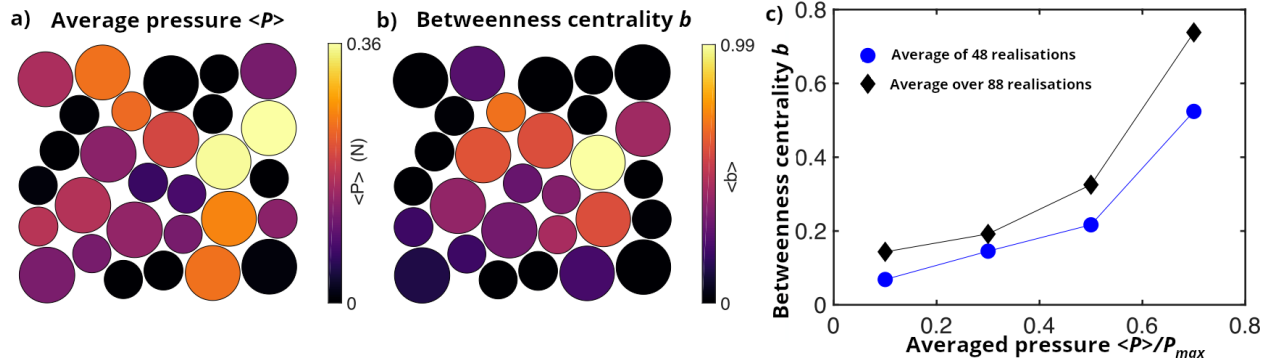


Figure 6.9: a) Average pressure exerted on the disc over compression cycles. b) Betweenness centrality of each disc, computed from the set of contacts. c) Relation between average pressure and betweenness centrality, average over 48 and 88 compression cycles. Although being obtained from statistical average, the average pressure and the position of the discs inside the packing are correlated. Figures from [113].

6.1.3 Foams as stress-transmitting particulate materials

Foams, as other granular systems, are composed of individual bubbles free to move with respect to their neighbours. Each foam state is a particular realisation of the set of accessible configurations. Because of the large number of degrees of freedom and the lack of thermal agitation, foams are usually trapped in metastable states, described by well-established geometrical rules [75, 83, 351]. The transition between different microstates can however be forced by imposing external shear. The differences in energy between states explored in that way are usually small enough to be negligible compared to the total surface energy, with a relative surface variation below $< 2\%$ [352, 353, 354], making foams good candidates for out-of-equilibrium model system described within a microcanonical ensemble. Durand [351, 33] showed that a 2D foam could be treated as a reservoir of facets and curvatures, and effectively described the variation in bubble shape and neighbour number as fluctuations in the foam microstates.

Foams, as bulk materials, are composed of a continuous phase with discrete inclusions. Unlike other materials composed of (quasi-)rigid grains, bubbles are highly deformable. An external stress applied on a foam/emulsion hence deforms its individual constituents whilst preserving their inner volume. In the limit of small applied stress, where bubbles deform without modifying their respective positions [65] as represented in Fig. 6.10a, the stress-strain relation is thus a direct consequence of their deformability and their geometrical organisation [65, 72]. The mechanical work associated to a foam deformation is thus always expressed as a function of the increase in interfacial area, provided that no structural rearrangements occur during the deformation. This is found for instance in the expression of the shear modulus $G_0 = \alpha \frac{\gamma_0}{R_{32}} \phi (\phi_l - \phi_l^*)$ [45, 77, 78] where R_{32} is the Sauter mean bubble radius $R_{32} = \langle R^3 \rangle / \langle R^2 \rangle$, and the osmotic pressure $\Pi = 7.3 \frac{\gamma_0}{R_0} \frac{(\phi_l - \phi_l^*)^2}{\sqrt{\phi_l}}$ [71, 46].

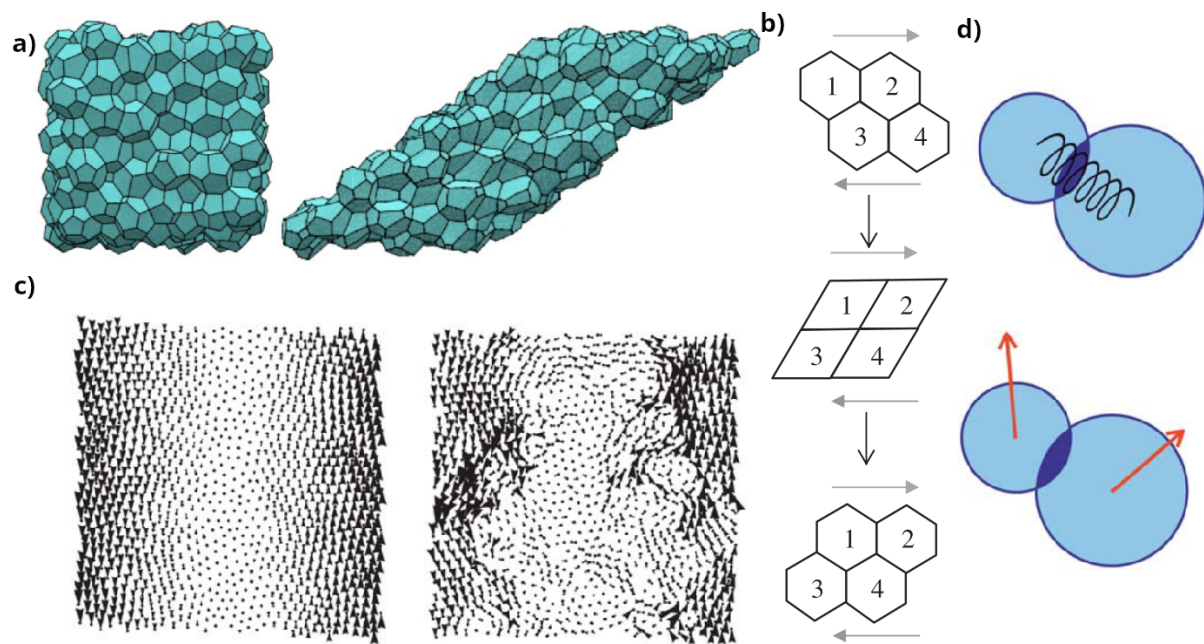


Figure 6.10: a) Example of the deformation of a foam under shear, simulated by Surface Evolver. Figure from [65]. b) The shear deformation rearranges the bubbles by switching the neighbours when a critical stress is reached. A local rearrangement locally decreases the shear stress. Figure from [65]. c) Displacement field of a 2D packing of frictionless, harmonic discs undergoing shear, in a dense packing (left) and slightly above (right), where the displacements are less homogeneous. Figure from [34]. d) Decomposition of the stress transmitted between two bubbles comes from the contact interactions (top) and the viscous friction between bubbles in relative motion (top). Figure from [34].

The stress exerted on a bubble inside a foam has two origins, shown in Fig. 6.10d : a first, direct contribution comes from the stress transmitted between the bubbles. The expression of this stress depends on the interaction law considered. As we explained in Chapter 3, in foams this interaction presents the particularity of being intrinsically non-pairwise : the deformed bubbles exert extra stresses on their neighbours, rigidifying them with increasing number of neighbours. A second contribution comes from the viscous friction between flowing bubbles, e.g. when the deformation triggers rearrangements between layers of adjacent bubbles as shown in Fig. 6.10c. This stress is linked to the relative velocity of bubbles in contact, and is thus dependent on the velocity gradient between two neighbouring bubbles/drops $|\Delta v|$ [355, 298]. When the displacement field is strongly non-affine, the velocity gradient can be locally higher because of the strong interparticle displacements, as shown in Fig. 6.10c. This combination of static and dynamic stresses gives foams their rich rheological properties, being non-linear both with shear frequency and amplitude [65, 40].

Because of the many-body interaction, the contact forces cannot be determined by considering only the local deformations. Instead, the deformations at the different contact points needs to be taken into account simultaneously. Dunne *et al.* [109] recently showed in 2D numerical foams that the contact forces could be inferred from the bubble deformations. The application to 3D foams in experiments is still an open task due to the lack of appropriate imaging techniques. In numerical 3D foams, some information can be extracted from the deformation of the bubbles. Because the deformation of a bubble increases with the applied forces, a measure of the deformation can serve as an estimator of the magnitude of the contact forces. Minkowski tensors have been shown to describe exhaustively the deformation of bubbles [356, 357, 358, 359, 360], independently of the reference frame. Evans *et al.* [361] showed in Surface Evolver simulations (Fig. 6.11a-b) that the deformation of bubbles in a compressed foam, defined as the second invariant of their interface tensor, was increasing with compression amplitude, and that the deformation of bubbles was spatially inhomogeneous, with large chunks of bubbles exhibiting stronger than average deformations. Their definition of the deformation closely resembles the $W_1^{0,2}$ Minkowski tensor, describing the isotropy of the distribution of normal vectors of the interface. A similar approach has been adopted by Giustiniani *et al.* [50] to characterise the deformations of drops covered with an elastocapillary interface in a static emulsion. The ratio of extremal eigenvalues of the moment tensor $W_0^{2,0}$ was found to discriminate efficiently between the drops shapes, drawing a relation between the physical properties of the interfaces and the behaviour of the drops in the packing.

The lack of information on the contact forces can be overcome by a proper description of the deformations they cause. This deformation-based approach is already successfully applied in granular systems to recover the interparticle forces, although by neglecting the impact of deformability on the assumption of pairwise interactions [325, 324, 55, 301, 302]. Because of the large choice in descriptors that can be used to describe deformed shapes, the identification of the most predictive ones is still an unanswered question. An extraction of the interface of the bubbles or drops is nonetheless a necessary step for the analysis of their shape. In this thesis, we therefore developed a segmentation algorithm aimed at getting the location of the border voxels of drops in 3D images of emulsions obtained by X-Ray tomography. This information is often overlooked in commercially available softwares. In Section 6.2, we present the fundamentals of the X-Ray tomography for emulsions before introducing in Section 6.2.3 a more detailed description of the algorithms developed to analyse these images. To test the algorithms, we use them first on numerical simulations of 3D foams in Section 6.3.

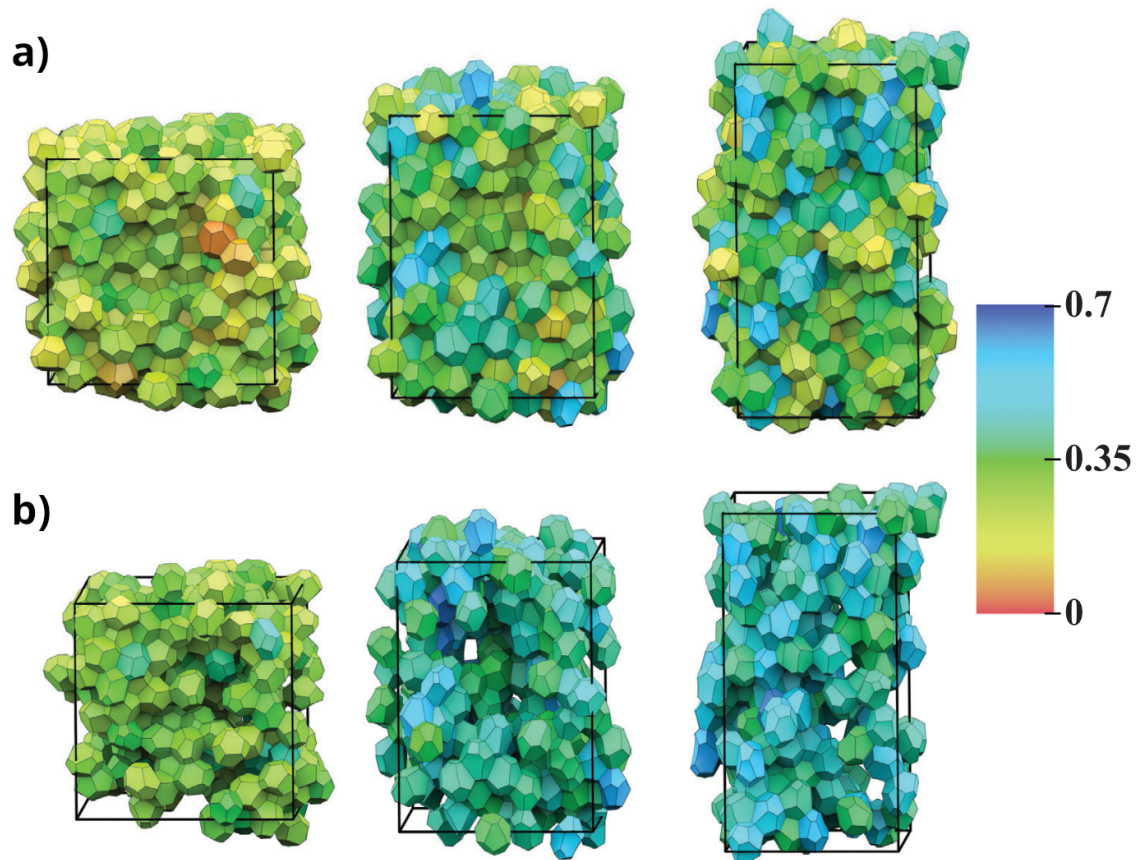


Figure 6.11: a) Stretching of a foam in a Surface Evolver simulation. Color indicates the anisotropy of the bubble, with red and blue being low and high anisotropy, respectively. b) Visualisation of the 256 most deformed bubbles in the foam. The highly deformed bubbles are localised in specific zones of the foam, rather than being homogeneously distributed. Figures from [361].

6.2 X-Ray tomography

Most available structural analysis of experimental foams is limited to 2D bubble rafts, or confined to the first layers of 3D foams as multiple light scattering renders the imaging of the inside of the foams by light impossible [303]. This limitation to the interfacial bubbles forbids the determination of their bulk structure, where most material properties stem from. Furthermore, as foam properties are intrinsically statistical because of the variations in bubbles sizes and shapes, the description of a large number of bubbles is required to understand foam properties [354, 351, 33]. Lambert *et al.* [305] proposed the first application of X-Ray tomography to the imaging of liquid foams, which proved to be a reliable tool to describe large sets of individual bubbles in bulk foams. This method has since been successfully reproduced, allowing notably to investigate the structure of bulk foams different from the structure in its interfacial layers [303] and the slow structural evolution of stabilised foams [304].

In this Section, we describe our X-Ray tomographic analysis of the droploons-composed emulsions described in Chapter 5. In Section 6.2.1, we explain the principle of X-Ray tomography imaging. In Section 6.2.2, we present its application to emulsions, the particularities encountered in these systems and how they can be taken care of experimentally. In Section 6.2.3, we respond to the need of segmentation and characterisation programs with user-defined parameters expressed in the literature [58, 305] by proposing a home-made segmentation algorithm, where every parameter can be tuned according to the needs of the experimental system considered. We also propose a physically-informed solution to the problem of neighbour definition evoked in Lambert *et al.* [305]. Due to time constraints, a robust description of experimental emulsions could not be provided : rather, we present in Section 6.3 the results of our algorithm when it is applied to numerically generated foams.

6.2.1 Principle of X-Ray tomographic imaging

X-ray tomography is an imaging technique relying on the local variation of the absorption of X-Rays in a heterogeneous sample. X-Rays penetrate the sample, with an intensity decreasing exponentially with the penetrated width l of the material and the particular absorption coefficient k_i of the material, following the Beer-Lambert law [362, 363]

$$I = I_0 e^{-k_i l}. \quad (6.17)$$

Placing a camera with a scintillator behind the sample, as shown in Fig. 6.12a, one can collect the transmitted X-rays to construct radiograms, where the differences in materials and absorption coefficients k_i appear as differences in transmitted X-Ray intensity. In computer-assisted tomography (CT), the sample is rotated 360° to make radiograms at different angles, represented in Fig. 6.12a. With the help of reconstruction algorithms, the sample can be reconstructed in three dimensions [364], with every cubic voxel of the reconstructed volume associated to an X-ray absorption coefficient, and hence, material. A slice of a 3D reconstruction of one of our emulsions is shown in Fig. 6.12b. The determination of the drop contours is performed by our home-made algorithm developed specifically for our samples, described in Section 6.2.3. The technical details and detailed experimental protocols used in this thesis are given in Section 2.5.

The application of X-Ray CT to granular materials, formed of two distinct materials, has proven successful to investigate the static and dynamic properties of granular packings [58]. Because of the low deformability of traditional granular media, the automatic segmentation is simplified by looking at shapes close to that of the isolated grain. Commercially available softwares thus already provide efficient algorithms to reconstruct horizontal slices from absorption radiograms, with an

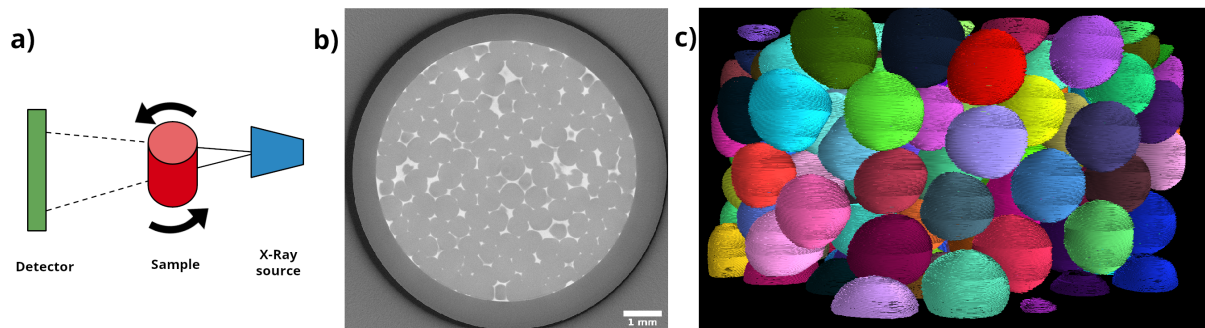


Figure 6.12: a) Principle of X-Ray tomography. The sample is rotated 360° between an X-Ray source and a detector. With the absorptin data obtained from the different projections, a 3D image can be reconstructed b) Example of slice obtained from X-Ray CT. c) Example of a reconstructed emulsion, obtained with the imaging methods described in Section 2.5 and the segmentation algorithm described in Section 6.2.3.

example of horizontal slice shown in Fig. 6.12b. For foams and emulsions, the high deformability of the grains and the small thickness of the films separating grains (of the order of the micron) make the segmentation a sensitive and difficult step of the CT reconstruction. In Section 6.2.2, we explain how X-ray CT can be applied to the study of foams and emulsions, and the specific techniques developed in this study to obtain reliable 3D informations.

6.2.2 X-Ray tomography in the analysis of emulsions

Imaging the inside of foams and emulsions with optical techniques is a long-standing problem, due to the multiple reflections and refractions at every interface [303]. Common imaging techniques focus on the bubbles close the walls containing the foams, where the bubble size and liquid fraction can be measured directly, as shown in Fig. 6.13a-b. The accessible structure of foams is therefore limited to the first layers of its surface, with no information accessible about its bulk structure. Recently, Meagher *et al.* [303] investigated the bulk structure of a foam with X-ray CT, and found an organisation closer to a random Bernal packing, whilst its first 5 interfacial layers were following a face-centered cubic lattice organisation. This structural change has direct consequences on the mechanical properties of, e.g., the mechanics of the structure obtained from the solidification of the continuous phase [12]. A good understanding of the foam structure thus requires imaging techniques able to probe the bulk foam. This has been achieved for emulsions where fluorescent dyes were grafted at the interface of the drops [114, 35, 322, 89, 62]. This method, however, is highly dependent on the chemistry of the system under consideration, and may not be applicable in every situation. X-Ray computer tomography is a more adaptable solution to the imaging of foams and emulsions.

The multiplication of the number of angles of view makes the X-ray CT a slow image acquisition technique, with characteristic acquisition time for a benchtop device ranging around 4h-8h for a $5\ \mu\text{m}$ resolution. The evolution of the foam structure with drainage, coarsening and film rupture is therefore susceptible to blur the radiograms and reduce the quality of the reconstruction. These artefacts can be minimised by introducing a stabilising gas (e.g. perfluorohexane [304]) and image the foam once the drainage is slowed down. In our PEG-in-silicone emulsions, we let the emulsions stabilise for two days before imaging, limiting the importance of fast motions.

The deformability of the drops makes the segmentation of the grains more difficult, as their shape cannot be fitted *a priori*. For too strongly compressed drops, the thickness of the thin film

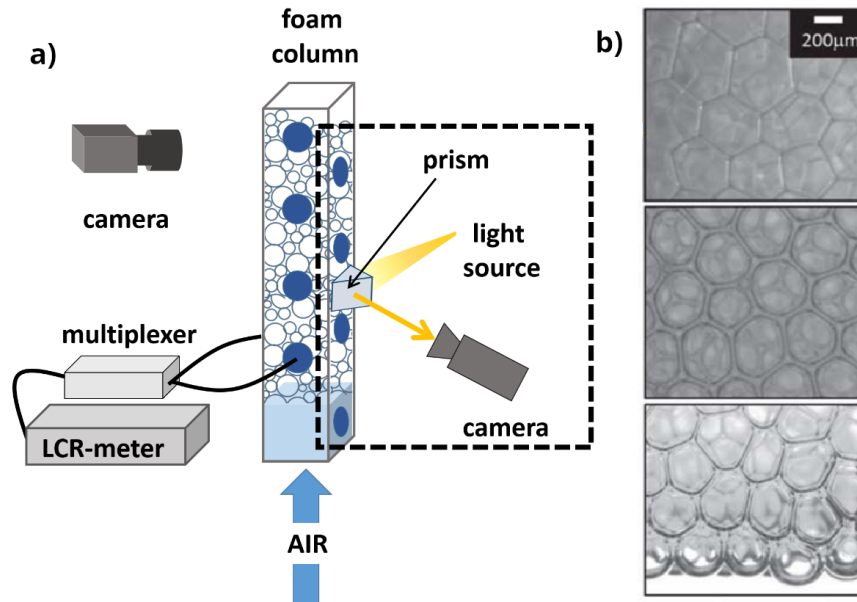


Figure 6.13: a) Example of the measure of a foam structure in a column foam setup. A foam is produced in a glass column by blowing gas at the bottom of the column. The images are taken by a camera on the side of the column. The optical deviation at the water/glass and air/glass interfaces can be minimised by placing a prism on the column wall. Figure from [365]. b) Pictures obtained by the column foam setup. The position of the bubbles in the second layer is hardly distinguishable due to the optical deformation. Image from [46].

can be below the resolution limit, and therefore indistinguishable from the drop phase. A particular care must be addressed to segment drops that are wrongly merged because of the resolution limit, as represented in Fig. 6.14a.

The strength of this segmentation procedure comes from its versatility and its ability to quickly distinguish between a large drop and two small drops close to each others : with the help of the EDM map, the peanut-shaped two drops structure is easily recognised as being composed of two small drops. However, this segmentation procedure is blind to the shape of the interface, and cannot determine its curvature. For that reason, one of the goal of the skin characterisation in Chapter 5 was to produce a skin thick enough for a simple segmentation of the drops, which would give access to the curvature of the interfaces. The definition of neighbourhood in foams is long-standing problem, appeared since the first images of foams in X-Ray tomography [305]. For (nearly) spherical particles, the shapes are usually fitted with the smallest enclosing circle (SEC) [95]. A contact is then defined with reasonable accuracy as an overlap between two SEC. Because of the high deformability of the bubbles, the determination of the contours can not rely on the assumption of a spherical shape, and another definition must be found. In Section 6.2.3, we propose a new, physically-informed way to determine the existence of contacts between bubbles, starting from the datas extracted from tomographic reconstruction.

An efficient reconstruction of the foam provides quantitative description of its structure. Meagher *et al.* [303] studied the geometrical organisation of bubbles in the bulk phase, and showed that it was closer to a Bernal random packing than a crystalline structure. Over long timescales, the same foam stabilised against coarsening with perfluorohexane was found to crystallise [304], with a coexistence of face-centered cubic (FCP) and hexagonal close packing (HCP) structure despite a

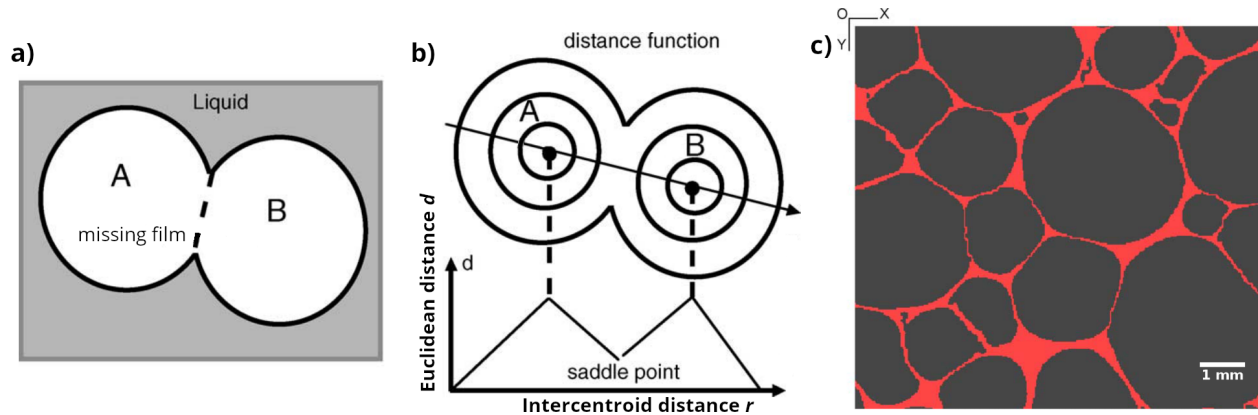


Figure 6.14: a) Example of two gas bubbles imaged with X-Ray CT. The thin liquid film is smaller than the picture resolution ($10 \mu\text{m}$). The bubbles appear as one single continuous body. b) Computation of the euclidean distance map (EDM), where every bubble voxel is attributed a value corresponding to its smallest distance to the outer phase. The two bubble centers have the highest EDM value, while the bottleneck shape of their interfacial contact remains at low value. The peaks of high EDM value are used as seeds for a watershed segmentation, with the EDM used as contour lines for the segmentation. This allows for an automatised segmentation of the merged bubbles. c) Example of bubbles segmented using EDM and watershed segmentation. Figures from [305].

preference for the FCC structure because of its better mechanical stability [366]. This spontaneous formation of a crystalline structure makes foams good candidates as model systems for the study of 3D crystalline structures, in addition to their history as model systems for 2D crystalline structures in bubble rafts [367]. Even for unstable foams, repeated fast tomographic acquisition at regular intervals can help to probe the bubble growth dynamics in the bulk phase [305].

The determination of the structure of a foam, i.e. its adjacency matrix A_{ij} , requires to define neighbourhood relations between bubbles. This relation, based on the forces exerted on each others by the bubbles, depends on the interfacial contacts between the drops. This interface is highly deformable, as we showed in Chapter 3 : a physically realist accounting of this deformable interface is therefore crucial to understand correctly the neighbourhood relations between the bubbles. Most commercially available softwares develop their own black box segmentation algorithms, based on the most widely studied undeformable granular materials. These numerical tools are not well adapted for deformable particles, where the distances between the centroids cannot suffice to conclude on the presence of contacts between the bubbles. Contacts between bubbles are usually defined when the distance between the centroids is smaller than the sum of their radii, and the interparticle force defined as a function of this reduced intercentroid distance [114, 35, 322, 89, 368, 61]. However, the compression of a drop in one direction leads to its expansion in the orthogonal directions, potentially creating contact areas between bubbles further from each others than the sum of their radii, especially for very deformed drops. For that reason, a physically relevant determination of the neighbourhood relations must rely on the distances between the interfaces rather than the centroids. In Section 6.2.3, we describe a home-made reconstruction algorithm developed to describe the structures of foams and emulsions from the horizontal slices obtained from X-ray CT.

6.2.3 Development of an adapted algorithm for interface detection

Because of the deformability of the bubbles, the existence of contacts and forces between them cannot be accurately inferred from the distances between their centroids. Rather, the distance

between two interfaces must be looked after. This requires to know the location of the voxels delimiting every drop, an information not provided by currently commercially available softwares. Furthermore, as explained in Section 6.1.3, the measure of drop deformation is a promising route to understand foam mechanics when contact forces cannot be measured accurately. In this section, we describe a home-made algorithm we developed specifically to access this interface position. Section 6.2.3 focuses on the treatment of images acquired in X-ray CT. In Section 6.2.3, we propose our own neighbourhood definition, based on the physical details of a drop/drop contact. In Section 6.2.3, we propose quantitative descriptors that can be computed from the knowledge of the contact relations between drops (or bubbles).

Workflow/output

With the tomographic setup and the reconstruction algorithms described in Section 2.5, the radiograms are reconstructed in slices in the horizontal plane, as shown in Fig. 6.12. The PEG drops appear darker than the silicone phase, because of the lower absorption coefficient of PEG, the grey level being inverted in the reconstruction. Before segmenting the emulsion, the slices are filtered to enhance the contrast between the inner phase and the outer phase. Because the films separating two drops can be very thin, the usual gaussian filter is replaced with a bilateral filter, known for its edge-preserving properties [369, 370, 371, 58]. The kernel of the bilateral filter reads as

$$I(\vec{r}) = \frac{1}{W} \sum_{\vec{r}_i \in \text{Image}} G_{\sigma_s}(\vec{r} - \vec{r}_i) \cdot G_{\sigma_i}(I_0(\vec{r}) - I_0(\vec{r}_i)) \cdot I_0(\vec{r}_i) \quad (6.18)$$

where the usual Gaussian spatial kernel

$$G_{\sigma_s}(\vec{r} - \vec{r}_i) = \frac{1}{\sigma_s \sqrt{2\pi}} e^{-\frac{|\vec{r} - \vec{r}_i|^2}{2\sigma_s^2}}$$

comes with a Gaussian kernel on the photometric distance (i.e. grey level difference)

$$G_{\sigma_i}(I_0(\vec{r}) - I_0(\vec{r}_i)) = \frac{1}{\sigma_i \sqrt{2\pi}} e^{-\frac{\|I_0(\vec{r}) - I_0(\vec{r}_i)\|^2}{2\sigma_i^2}},$$

with W being a normalisation coefficient $W = \sum_{\vec{r}_i \in \text{Image}} G_{\sigma_s}(\vec{r} - \vec{r}_i) \cdot G_{\sigma_i}(I_0(\vec{r}) - I_0(\vec{r}_i))$. The two standard deviations of the Gaussian filters σ_s and σ_i are two tunable, user-defined parameters that can be modified depending on the input pictures to get the best resolution out of it. An example of the impact of the variation of σ_s and σ_i is shown in Fig. 6.15a. The bilateral filter is applied on every slice separately, as no standard library can perform a 3D bilateral filter in a reasonable amount of time. To make every direction equivalent with respect to segmentation, the data block containing the grey value of every voxel is rotated twice, as shown in Fig. 6.15b. The bilateral filter is applied again between each rotation. The data block is then rotated back in place to its original shape. The filtered images are saved for further analysis.

The grey values of the filtered images, shown in Fig. 6.16a, are normalised between 0 and 1. The image is then binarised, giving to every voxel a binary label of 1 if its grey level is in a user-defined intensity range $[i_{min}, i_{max}]$, and 0 otherwise, as shown in Fig. 6.16b. At this stage, lonely voxels can be wrongly segmented in one phase or the other, resulting in holes in identified drops or tiny spots of the silicone phase identified as PEG, as shown in Fig. 6.16b. These wrongly labeled voxels are corrected using two morphological operations on the binarised images using the

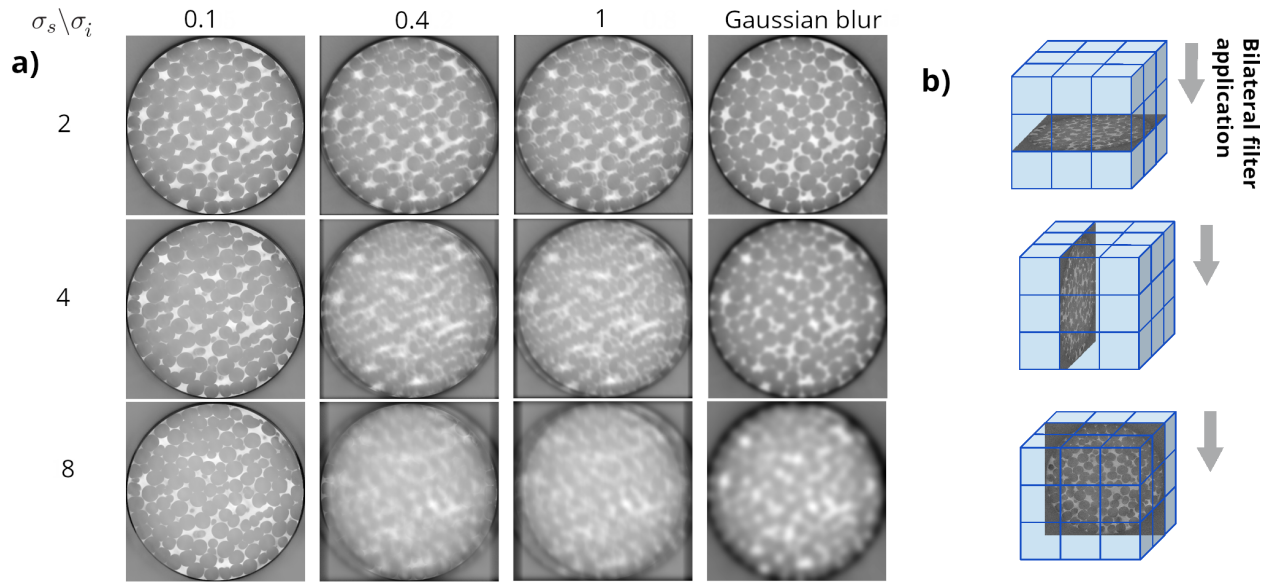


Figure 6.15: a) Bilateral filter applied to the same image with different filter parameters (σ_i, σ_s) . The Gaussian blur filter is shown for comparison. b) The two-dimensional bilateral filter is applied once in every direction to obtain a quasi-3D bilateral filter.

Skimage library [372]. The erosion, performed with the `morphology.erosion` function removes the outer voxels of the shapes with a binary label of 1, by attributing to every voxel the minimal label found in its neighbourhood in a cube of 5 voxels length. The dilation on the other hand, performed with the `morphology.dilation`, includes the voxels directly close to the shapes with a binary label of 1, by switching to the maximal label found the same cube. In the first step, the binarised images undergo an erosion followed by a dilation. The tiny islands of voxels wrongly labeled as being part of a drop disappear in the erosion, and do not grow back in the dilation phase. In the second step, the images are transformed by a dilation followed by an erosion. This time, the small voxels included in the drops that have been labeled as being part of the silicone phase disappear in the first phase, and do not appear again at the end of the erosion. Wrongly labelled voxels are hence suppressed from the final images. The shapes of the drops are however deformed by the successive morphological operations. A careful choice in the filter parameters is up to the user, such as the size and the shape of the filter box in the erosion and dilation operations.

After the binarisation step, the binary shapes are segmented and given a label. In our experiments, the segmentation is performed following the procedure described by Lambert *et al.* [305], described in detail in Section 6.2.3. The labeled picture is transformed in an euclidean distance map (EDM), where every pixel identified as a bubble is encoded with the smallest distance separating it from the continuous phase. For every shape identified with a label, the local maxima of its associated EDM are identified with a minimal distance between their localisation, as shown in Fig. 6.14b. The value of this minimal distance depends on the resolution and the grain size, and typically lies around one drop radius. Peaks closer than this minimal distance are merged together. At the end of this step, the shapes with more than one maximum are segmented using a watershed segmentation algorithm [373] with the peak location as the seed (shown in red in Fig. 6.16b), and the EDM as the basin. The shapes obtained from this segmentation step, shown in Fig. 6.14d are taken as the final grain shapes. At this stage, every drop is labeled with an integer number. This label can be visualised on the slices, where the grey value is 0 for the outer phase, and an integer $n > 0$ for voxels that are part of a drop, as shown in Fig. 6.16c. The labeled images are

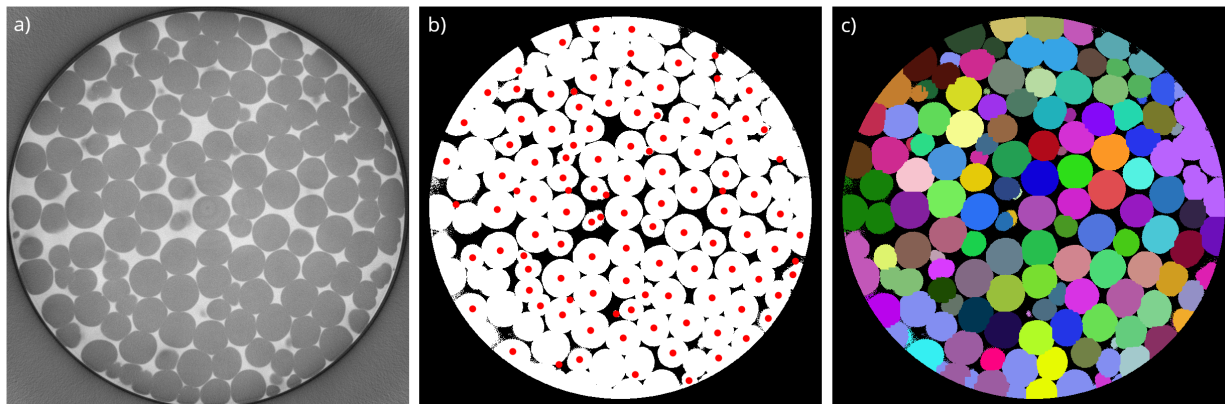


Figure 6.16: Example of a segmentation procedure. a) Original horizontal slice. b) The same slice, binarised and with the peaks obtained from the euclidean distance map procedure described in Section 6.2.2 inspired from Lambert *et al.* [305]. c) Final segmented image obtained from the watershed flooding algorithm, using the seeds obtained from the euclidean distance map computation.

then stored for further analysis. The voxels that form the contours of the drops are identified using the `measure.label` function of the `Skimage` library. The extracted information is stored in three different files in `csv` format : a first file containing the position of every centroid and its associated label; a second file containing all the positions and labels of every voxel being part of a contour; and a third file containing the number of voxels carrying the same label, which can be translated as a list of the volumes of the drops. The workflow of the algorithm is represented in Fig. 6.17.

Surface-to-surface distance

The determination of a contact between two drops must rely on the proximity of their contours, which can move due to the deformations, rather than on the positions of their centroids. The surface-to-surface distance (S2S) between two drops is not uniquely defined, as a distance can be computed between every pair of voxels belonging to different drops. For perfectly delimited spheres, the smallest distance of all the sets of pairs would be a good definition of the S2S distance. But due to the segmentation procedure, wrongly labelled voxels can mess up with this minimal distance. We therefore choose a more robust approach to the S2S definition.

The potential pairs of touching drops are detected with a Delaunay triangulation of the space, using the centroids of the drops as seeds. Every pair is further tested using the surface voxels to compute the S2S distance. For every test pair, the voxels used to compute the pair distances are selected as being inside a cylinder (with a radius of 40 voxels) joining the two centroids, as represented in Fig. 6.18a. We compute all the distances between pairs of voxels from different drops, shown in Fig. 6.18b. This part is computationally expansive, and thus performed using a `C` algorithm. All the pair distances are then stored in a file associated to the pair of drops. In the last step, we summarise this file by associating every drops pair to the 5th centile of its pair distance distribution represented in Fig. 6.18c, taken as the S2S distance between the two drops. The final list of pairs associate every test pair with a S2S distance. A selection by the user of a threshold distance can further discriminate between touching and non-touching drop, depending on the physical properties of the emulsion considered.

Equipped with the computation of the S2S distance and a criterion of mechanical contact for neighbour definition, we can thus construct the contact network of the emulsion. An example of

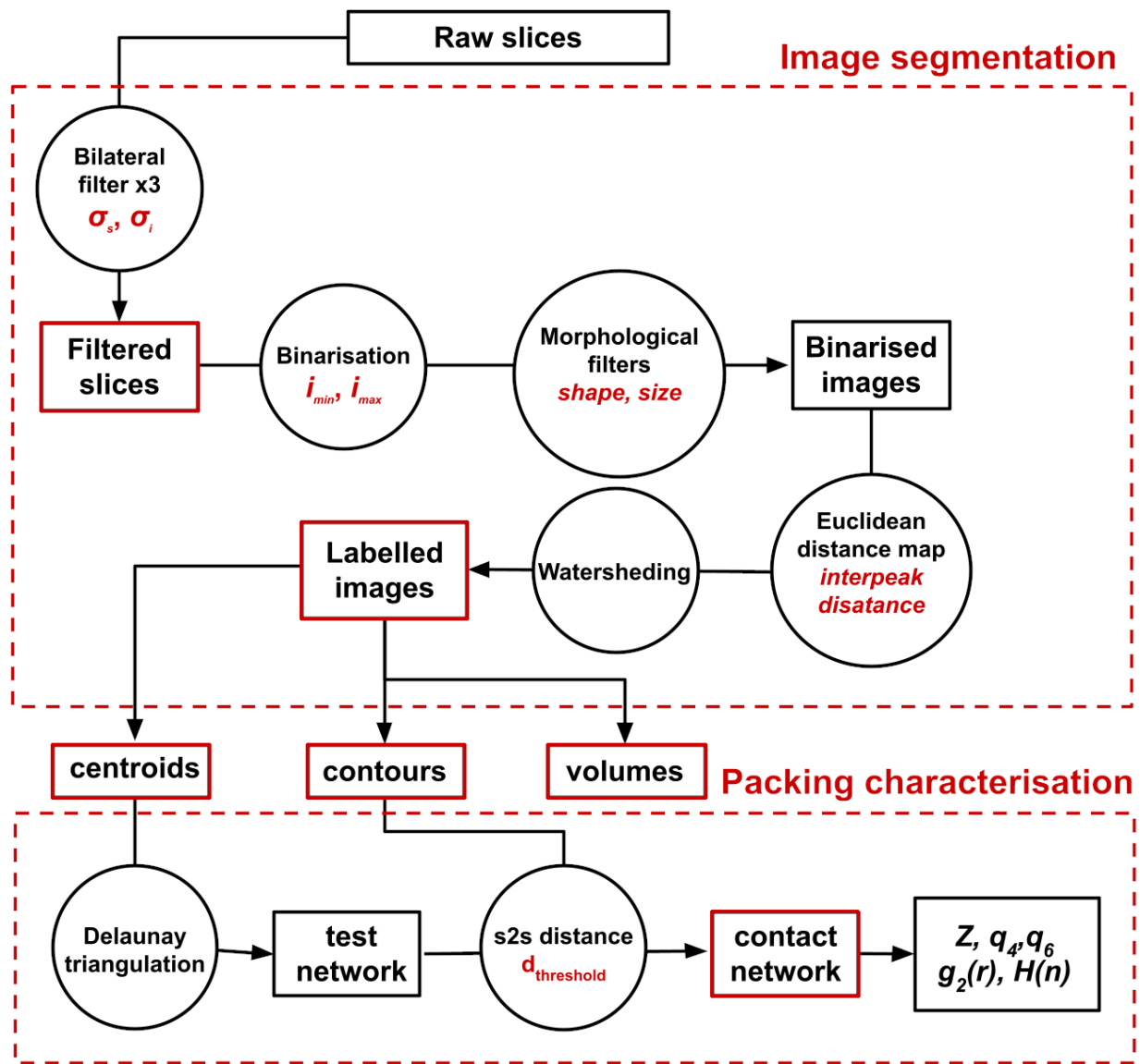


Figure 6.17: Workflow of the segmentation/characterisation algorithm. The red boxes indicate the steps where the intermediate data is saved.

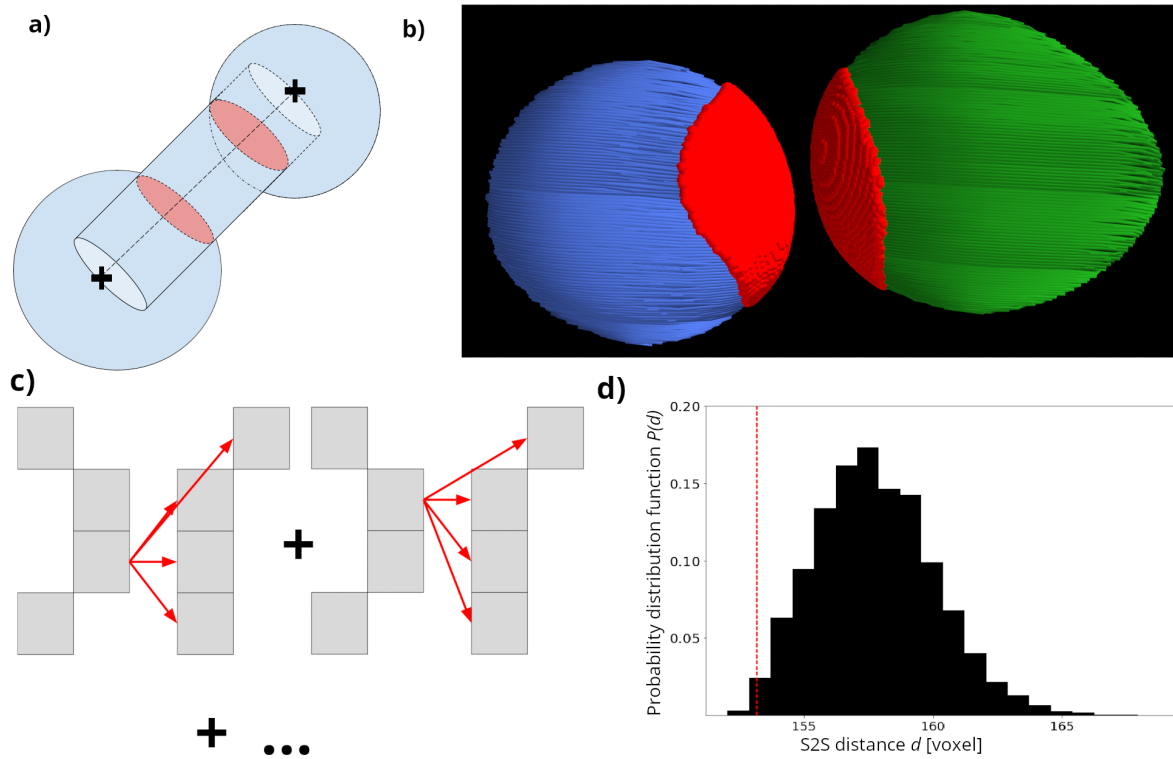


Figure 6.18: a) Schematic representation of the choice of interface voxels for the S2S distance computation. The interface voxels are taken into account if they fit inside a cylinder joining the two centroids. They are represented by the red surface sections. b) Illustration of the selection of the interface voxels for the S2S computation. The voxels used to compute the distances are represented with the red points. c) The S2S method proceeds by computing all the distances between pairs of voxels belonging to different drops in the set of pre-selected ones. d) Example of final distribution of S2S distances.

a reconstructed emulsion, obtained from the slices of the sample shown in Fig. 5.17c, is shown in Figs. 6.19 and 6.20. In Section 6.2.3, we detail the quantitative descriptions used to characterise the emulsion once the contact relations are known.

Structural description of emulsion systems

The simplest and most straightforward quantity obtained from the contact network is the coordination number Z , obtained for each particle as the number of time its label appears in the list of pairs of drops closer than the defined distance threshold.

The location of the centroids of the drops gives more information about the geometrical organisation of the emulsion. This organisation can be measured using the bond orientational order parameter, initially defined to discriminate between different lattices [374, 375]. Starting from a centroid i and the vectors $\{\vec{r}_{ij}\}$ joining it to the centroids of its N_b neighbours, the bond orientational parameter of order l is computed as

$$q_l(i) = \sqrt{\frac{4\pi}{2l+1} \sum_{m=-l}^l |q_{lm}(i)|^2}, \quad (6.19)$$

where $q_{lm}(i)$ is the complex vector of particle i , defined as

$$q_{lm}(i) = \frac{1}{N_b(i)} \sum_{j=1}^{N_b(i)} Y_{lm}(\vec{r}_{ij}), \quad (6.20)$$

with \vec{r}_{ij} being the distance vector between drops i and j in the Euclidean space and the Y_{lm} functions being the spherical harmonics [376]. Different orders of l are sensitive to different symmetries of the lattices, with q_6 values being higher for fcc structures [377, 378], as shown in Fig. 6.21. Bond orientational parameters are a powerful tool to probe locally the geometrical structure. An approach more resistant to noise can be adopted by taking the averaged form of the parameter as

$$\bar{q}_l(i) = \sqrt{\frac{4\pi}{2l+1} \sum_{m=-l}^l |\bar{q}_{lm}(i)|^2} \quad (6.21)$$

with

$$\bar{q}_{lm}(i) = \frac{1}{\tilde{N}_b(i)} \sum_{k=0}^{\tilde{N}_b(i)} q_{lm}(k) \quad (6.22)$$

where \tilde{N}_b is the set of neighbours of the particle i , including i itself. As shown in Fig. 6.21, this averaged form discriminates better between different lattice geometries, as the overlap between the different lattices is less important in the averaged version of the bond orientational parameters. We perform the computation of the bond order parameter with the PyBoo library [379]. In particular, the parameters q_4 and q_6 have been shown to discriminate efficiently between standard lattices such as body-centered cubic (BCC), face-centered cubic (FCC) and hexagonal close packing (HCP) in granular materials, as shown in Fig. 6.21.

The knowledge of the contact network of the system also gives access to its Shannon entropy, which Brujić *et al.* [89] links to the configurational entropy in the sense of the Edward ensemble [314], as explained in Section 6.1.1. The density of state of a jammed system still being an open

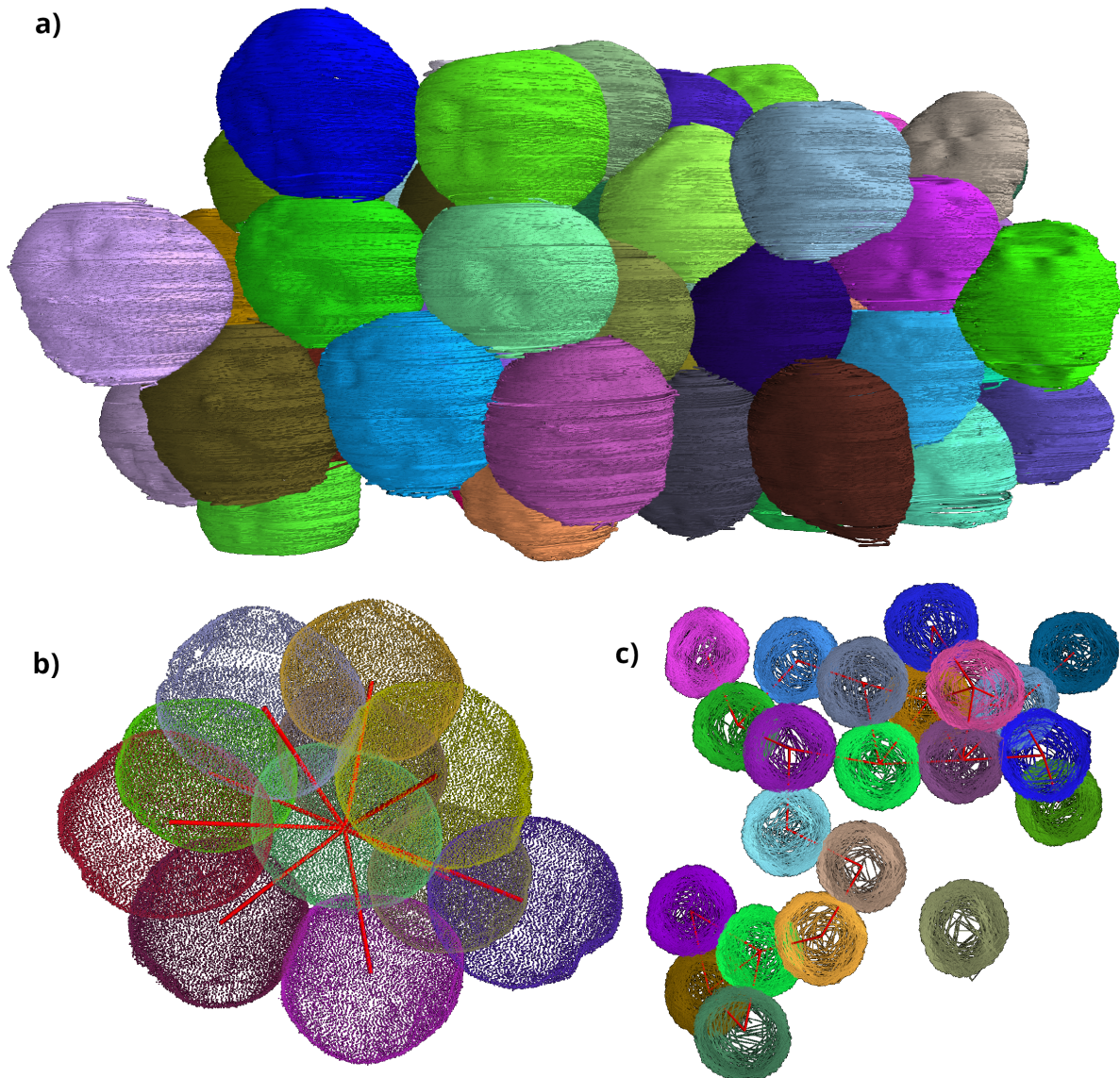


Figure 6.19: Example of the reconstruction of an emulsion, using the tomographic slices obtained from the sample from Fig. 5.17c. a) Reconstruction of the drop contours, obtained by excluding the drops close to the sample boundary. b) Reconstruction of the contacts between the drops, obtained using the surface to surface distance method described in Section 6.2.3. The contacts between the central drop (in green) and its neighbours are visualised by the red lines joining their centroids. c) Top view of the upper layer of the emulsion. The contacts are represented by the red lines. Close, but not in contact surfaces are recognised and not counted in the list of contacts.

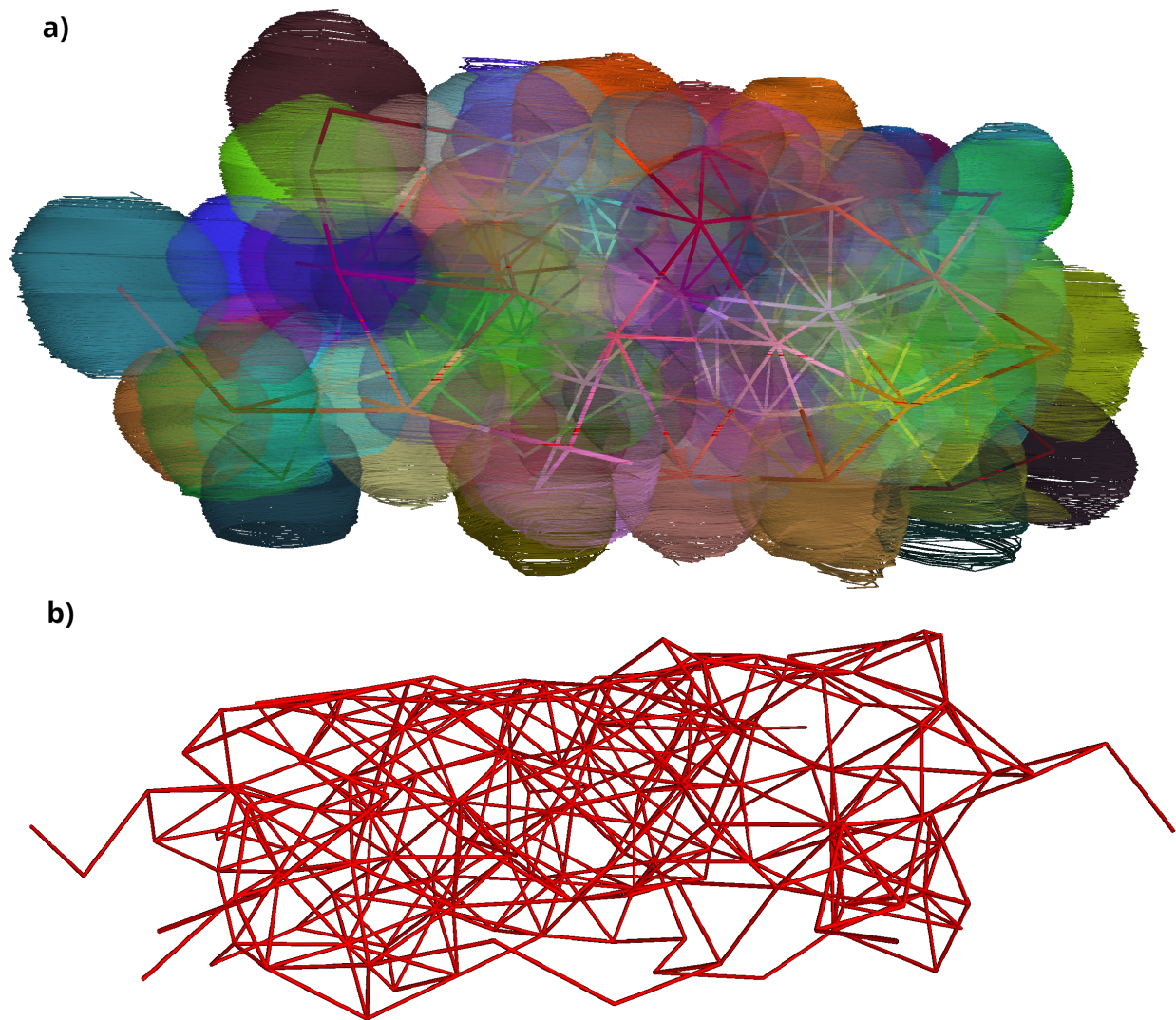


Figure 6.20: Visualisation of the contact network for the reconstructed emulsion showed in Fig. 6.19. a) The red lines join the centroids of touching drops, shown in transparency. b) The same contact network, shown without the droplets. This contact network can be analysed using the tools of network theory described in Section 6.1.2, as it is done in granular materials.

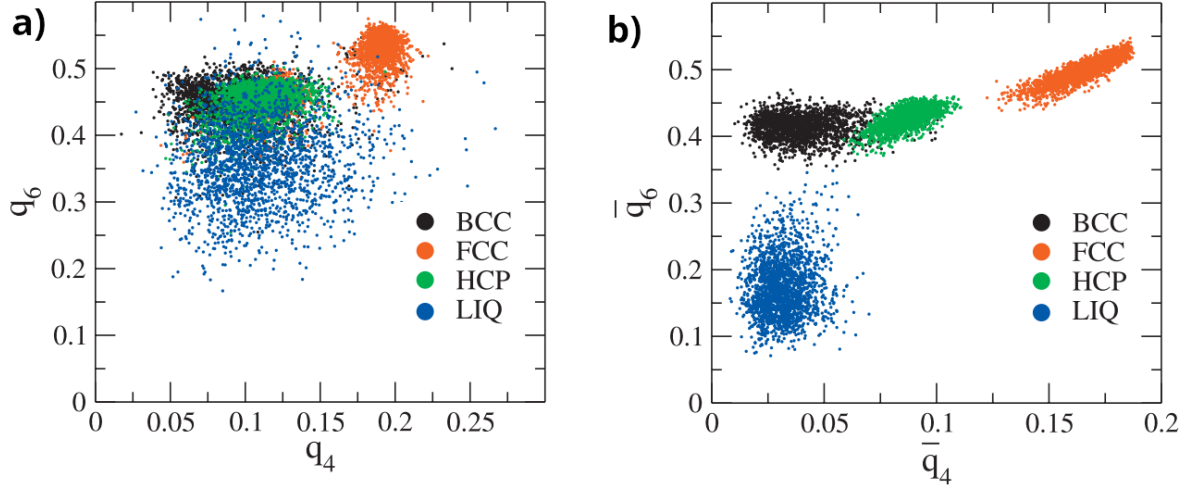


Figure 6.21: a) Bond orientation parameter and b) averaged bond orientational parameters for particles interacting through Lennard-Jones in molecular dynamics simulations. The four phases shown are body centered cubic (BCC), face centered cubic (FCC), hexagonal close packing (HCP) and liquid phase (LIQ) corresponding to the random-close packing of granular materials. Figures from [374].

question, we compute the configurational entropy following the procedure described by Brujić *et al.* [89, 380]. A position is taken at random in the contact network, from which a sphere is grown until a number n of vertices are included in it. The graph formed by the vertices is reduced to its standard form (or "class"), which is the same for topologically equivalent graphs. By doing so, one can sort the graphs in classes, and count the number of graphs of each class. The class determination is obtained by reducing it to its set of automorphisms generators S_f using Nauty [381] as represented in Fig. 6.22a. The repetition of this operation by taking new random positions at n constant gives a probability distribution of the graph classes and their probability of occurrence $p(S_f)$. The Shannon entropy H of a cluster of size n is then defined by

$$H(n) = - \sum_i p(i) \ln(p(i)), \quad (6.23)$$

with i running over all the clusters of size n , assuming a Boltzmann constant $k_B = 1$. The entropy per bubble s is calculated as the limit

$$s = \lim_{n \rightarrow \infty} [H(n+1) - H(n)]. \quad (6.24)$$

Clusters of infinite size are impossible to obtain due to the finite size of the emulsions, but a good approximation of Eq. (6.24) can be obtained by taking the slope of $H(n)$ when it increases linearly with the graph size n , as shown in Fig. 6.22b.

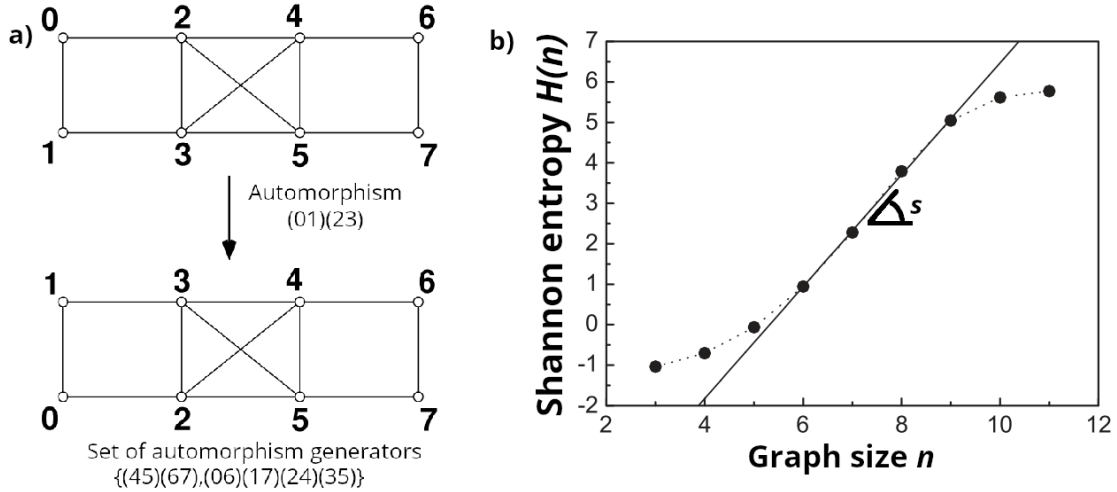


Figure 6.22: a) A graph transformation leaving its connectivity relations unchanged is called an automorphism. The ensemble of automorphisms of a graph can be reduced to its set of automorphisms generators, constituting its class. Graph and set from [381]. b) The slope of the Shannon entropy $H(n)$ in its linear zone can be extrapolated to determine the average entropy per grain s (expressed in units of k_B). The decrease of the entropy at large graph size corresponds to size limitation effects. Figure from [89].

6.3 Image analysis test case : numerically generated foams

Critically analysing the results obtained from the numerical procedures described in Section 6.2.3 is difficult, as it is a result of graph analysis after segmentation of deformed drops with no insight on their impact on the packing organisation. To disentangle the different levels of complexity, we first test our analysis tool on the packing properties of numerically generated foams (Section 6.3). These foams avoid all segmentation issues, voxels already carrying a binary label obtained from the foam generation simulation. The generation procedure of these numerical foams is described in Section 6.3.1. The quantitative descriptors listed in Section 6.2.3 are shown in Section 6.3.2 for three different foams, with structure randomisation factors of 0, 0.2 ad 0.3, respectively.

6.3.1 Generation procedure

The numerical foams are simulated using an *ad hoc* modeling method developed by Dabo *et al.* [382], based on the physical description of the foaming process in a polymer melt with a chemical blowing agent (CBA). In this process, a thermoplastic polymer melt is mixed with the CBA homogeneously. The melt is then heated to decompose the CBA and produce gas bubbles inside the melt through nucleation events, which further grow through coarsening and coalescence. The foam is then solidified by decreasing its temperature, fixing its final morphology.

The foam formation is simulated through the growth of bubbles from nucleation sites, whose position is determined following the procedure shown in Fig. 6.23. The sites of the FCC lattices are displaced following an unit vector with a random orientation. The randomness of the foam structure is tuned by multiplying the randomly oriented vector by a scalar called the randomness parameter α . Once the bubbles are nucleated, their growth is simulated by solving the Navier-Stokes equations for the interface position. The stress in the Navier-Stokes equations is composed of an elastic and a viscous components, with coefficients varying with temperature. During the

growth, bubbles exert a stress on the outer medium. When two interfaces come close to each others, these stresses hinder further growth, keeping bubbles disjoint. The thickness of the wall between two bubbles is hence not fixed *ab initio*, but rather defined by the parameters of the simulated material. In 3D, we opted for the face centered cubic (FCC) structure, more representative of the structure of a high density foam than the BCC structure (adapted for low density foam [85]) or the simple cubic structure [383]. All the cells are nucleated at the same time to adapt this cell distribution algorithm in the microstructure generator. Different microstructure morphologies can be generated by varying the spatial distribution of the cells, the process parameters and the polymer melt characteristic properties. Variation in the spatial distribution is explored with the parameter α , a structure randomisation factor moving all the nucleation sites by the displacement vector $\alpha l_0 \vec{U}_i$, where l_0 is the mesh parameter of the initial regular distribution and \vec{U}_i is a unitary vector randomly oriented from the point i . α ranges between 0 and 0.3, $\alpha = 0$ corresponding to the regular FCC structure. Increasing α means increasing the disorder in the positions of the points, giving more irregular structures as we show in Section 6.3.2

As shown in Fig.6.23b, at the beginning of the foam formation, each bubble nucleates with identical radii and internal pressures. A numerical resolution of the Navier-Stokes equations allows to simulate the bubble growth, adding the interfacial tension and the gas pressure to the stress of the interface. These are solved using a Eulerian approach, described in [382]. A cubic grid of nodes represents the geometrical domain on which the numerical simulation is carried out and a meshing technique is used to describe the evolution of the gas-mixture interface. Each cell at nucleation is represented by a polyhedron with a set of equidistant vertices. A regular mesh of these vertices with equilateral triangular elements is adopted to form the spherical polyhedron delimiting the contour of each cell. As cells grow, a re-meshing technique is adopted to improve the description of interface location and keep a good accuracy in the output. An equilibrium state is assumed to be reached once the foam porosity does not change by more than 0.01% between two time steps.

Fig. 6.23c shows examples of generated 3D microstructures by varying the α parameter only. To run the simulation, the physico-chemical properties of the materials were the same as the one used in Dabo *et al.* [382]. Each sample foam includes 1024 cells, with examples of final structures for the three randomisation factors shown in Fig. 6.23c.

6.3.2 Results

The distances between the bubbles are determined from the slices of the foam, shown in Fig. 6.23c, using the surface-to-surface distance as defined in Section 6.2.3. The average contact number $\langle Z \rangle$ increases with the distance threshold d at which two bubbles are taken as neighbours, and reaches a plateau value. The beginning of this plateau for ordered foams ($\alpha = 0^+$), represented with a dotted line in Fig. 6.24a, is defined as the distance threshold for the other foams. The evolution of $\langle Z \rangle$ with the distance threshold d is represented in Fig. 6.24. To limit the border effects, the average of the contact number is calculated by taking into account only the bubbles inside a subvolume obtained by shrinking the box volume of 15% in every direction, as shown in Fig. 6.24b. For the foam with a minimal disorder in the initial structure ($\alpha = 0^+$), $\langle Z \rangle$ quickly reaches a plateau at $\langle Z \rangle = 13.4 \pm 0.7$. This value is close to the values expected for dry ordered foams (14 for BCC, 13.5 for Weaire-Phelan) and dry disordered foams (13.7) [75]. This value is, however, higher than expected for a FCC structure. We hence compute the average contact number for a regular FCC lattice of perfect spheres for comparison. As shown in Fig. 6.24a, the number

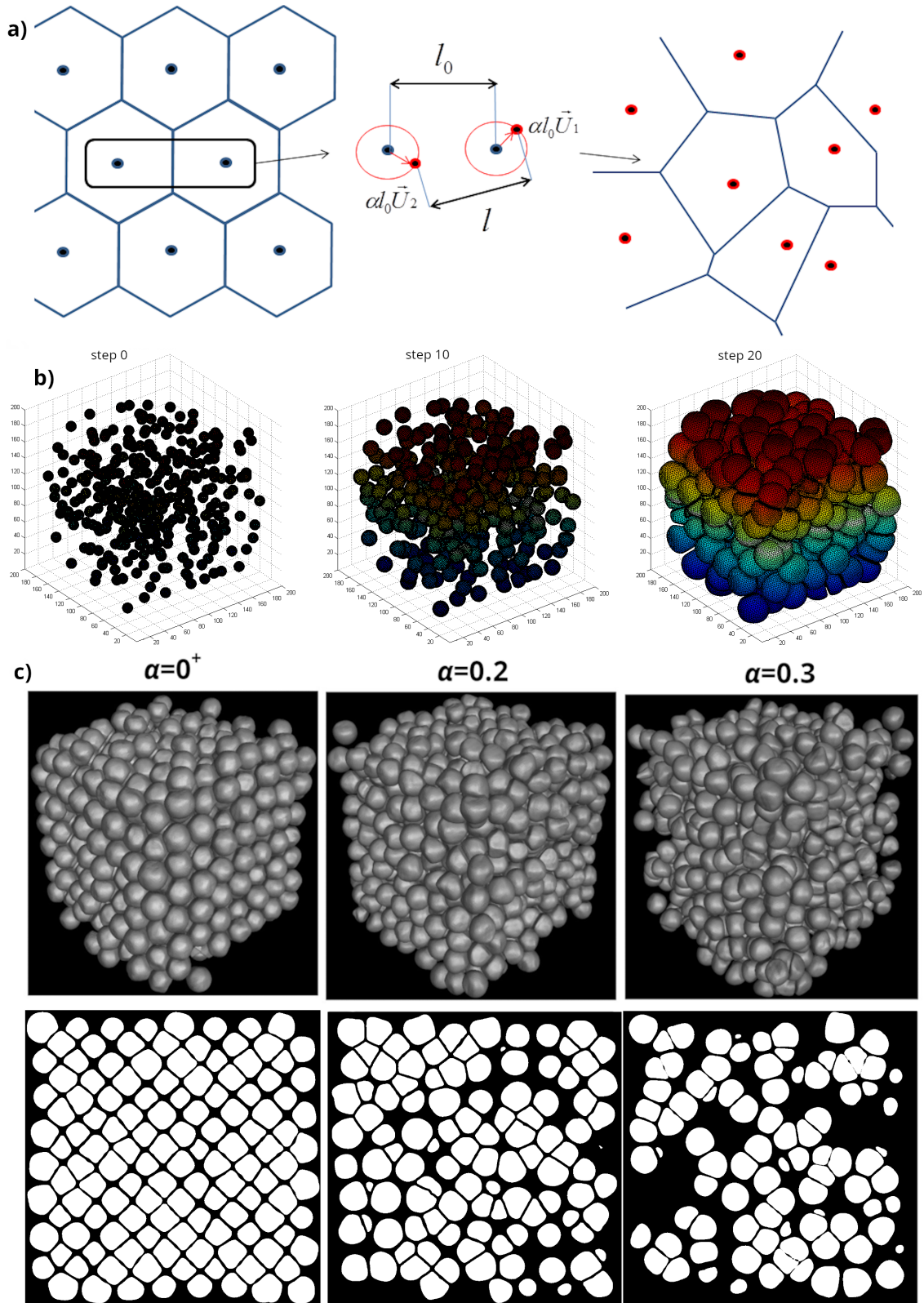


Figure 6.23: a) Initiation of the spatial distribution of cell seeds. The positions of the seeds is perturbed by a displacement in a random direction by a distance proportional to the interseed distance l_0 and the structure randomisation factor α . b) Example of cell growth over time. The cells nucleate from initial sites and grow over iterations, following the growth algorithm described by Dabo *et al.* [382]. c) Top : 3D foam-like microstructures generated with the procedure described in Section 6.3.1, using $\alpha = 0^+$ (left), $\alpha = 0.2$ (middle) and $\alpha = 0.3$ (right). Bottom : 2D slice of a foam generated numerically following the procedure described in Section 6.3.1. The positions of the nucleation sites were randomised with a parameter $\alpha = 0.2$.

of neighbours first increases to 4, corresponding to the neighbours distant from one basis vector, before reaching a plateau around 12. The variations in the number of neighbours come from the discrete representation of the interface on a square grid. Hence, the number of neighbours for the numerically generated foams is higher than that of a FCC foam : this difference may come from the generation procedure, and in particular the elastic and viscous stresses in the continuous phase during the bubble growth (see Dabo *et al.* [382] for a detailed description of the implementation of the foam generation).

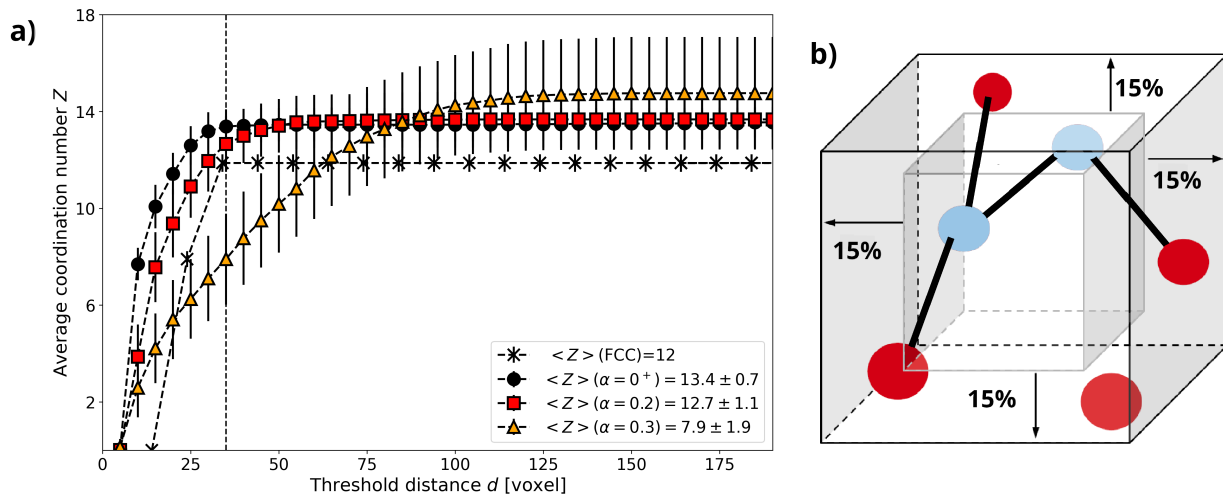


Figure 6.24: a) Evolution of the average contact number $\langle Z \rangle$ with the threshold distance d for contact definition. d is chosen as the position of the plateau in $\langle Z \rangle$ for the foam with minimal disorder in initial structure ($\alpha = 0^+$). The result for a regular FCC lattice of perfect spheres is shown for comparison. b) The number of contacts of a particle is taken in account in the average only if its centroid is inside a subvolume, delimited by shrinking the foam volume of 15 % in every direction. The contacts with bubbles outside of the subvolume are preserved and counted to obtain $\langle Z \rangle$.

The local geometrical organisation is probed with the bond orientational parameters, described in Section 6.2.3. The distance threshold d for neighbour determination is taken from the contact number determination, shown in Fig. 6.24a. The (q_4, q_6) coordinates of every bubble is represented in Fig. 6.25a, as well as their averaged coordinates (\bar{q}_4, \bar{q}_6) in Fig. 6.25b. The q_6 parameter decreases with the structure randomisation factor α , while the q_4 increased, indicating a change in the structural order from the initially FCC structure to a disordered state, different from the usual lattices studied with bond orientational parameters shown in Fig. 6.21.

The large-scale structure of the foams is also investigated using the radial distribution function $g_2(r)$ and the configurational entropy $H(n)$. The radial distribution function is computed using the centroid positions as interparticle distance r . The results are shown in Fig. 6.26. The most organised foam structure shows strong peaks corresponding to a FCC structure. For an increasing α , the peaks shorten in height and broaden in height, indicating a less localised distribution of neighbours in the first shells. For instance, the second peak splitting disappears for $\alpha \leq 0.2$, and the correlation disappears beyond the first peak for strongly randomised foam structure $\alpha = 0.3$. With the bond orientational parameters of Fig. 6.25, this loss of correlation indicates the vanishing of long-range order in the foam with increasing randomness in the positions of the nucleation sites.

The configurational entropies of the three foams are computed following the procedure described in [380]. The contacts between the bubbles used for the determination of the contact network

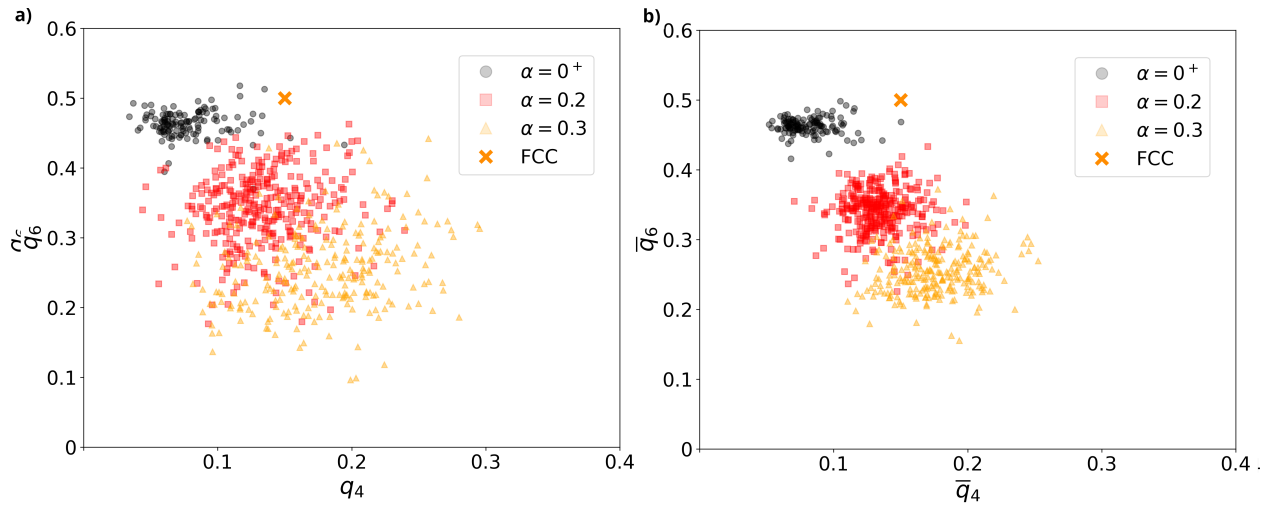


Figure 6.25: Bond orientational parameters (q_4, q_6) and averaged bond orientational parameters (\bar{q}_4, \bar{q}_6) for the three different foams of Fig. 6.23c. The contacts are determined using S2S distances and the plateau distance of $\langle Z \rangle$ as a threshold. The parameters for every drop are computed using the PyBoo library [379]. Values for FCC are taken from [374].

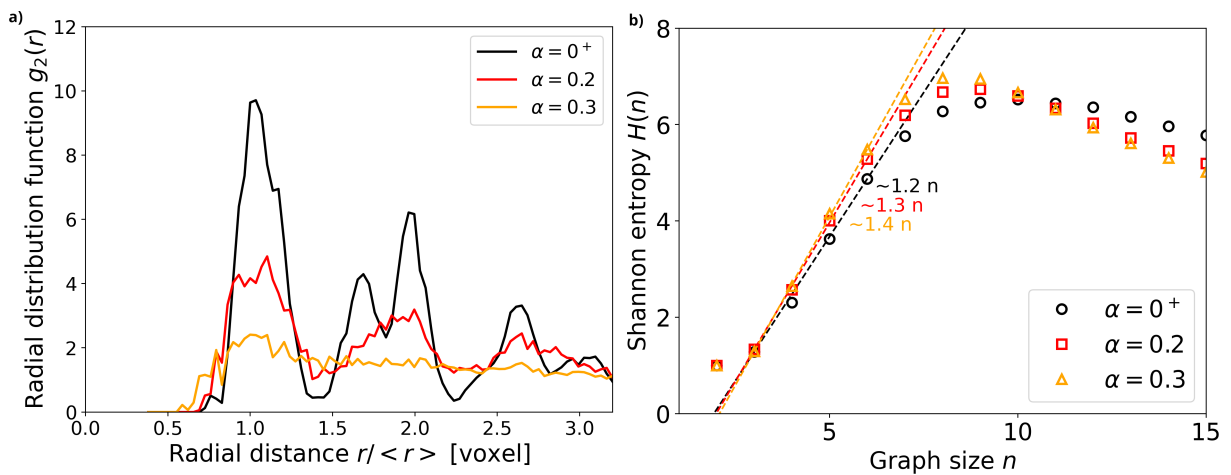


Figure 6.26: a) Radial distribution function for the three numerical foams, computed using the positions of the centroids as distance between bubbles. b) Configurational entropy for the three numerical foams. The slope of the linear fit between $n = 2$ and $n = 5$ gives the average entropy per bubble s , expressed in unit of the Boltzmann constant k_B .

are defined in the same manner as for the average contact number and the bond orientational parameters. The resulting Shannon entropy H as a function of the graph size n is shown in Fig. 6.26. The average entropy density s increases with the structure randomisation factor, going from $\sim 1.2 k_B$ for the most regular lattice ($\alpha = 0^+$) to $\sim 1.4 k_B$ for the most disorganised one ($\alpha = 0.3$). The precision of the linear fit is limited by the maximal number of drops n in a graph due to the boundary effects. More precise quantification of the impact of structure randomness on the Shannon entropy would require larger samples. Nonetheless, the results shown in Fig. 6.26b show an increase in the Shannon entropy $H(n)$ at its maximal value, encouraging its usage in foam characterisation at the packing scale.

6.3.3 Discussion

Our characterisation of the numerical foams found structural features that evolved with the degree of randomness in the nucleation structure. The most ordered structure was found to be close to a body-centered cubic structure, as intended. Interestingly, the average contact number $\langle Z \rangle$ was found to be closer to the one expected for dry foams than the one for FCC structures ($\langle Z \rangle = 12$). This could indicate the variation of the structure with the growth of the bubbles, as the FCC structure is present in wet foams only : ordered dry foams structure is closer to BCC packings ($\langle Z \rangle = 14$). Similarly, the bond orientational parameters (q_4, q_6) evolved with the structure randomness, with broader distributions and values differing from the FCC results. These observations correlate with the disparition of long-range correlation observed in the pair correlation function $g_2(r)$. Finally, the increase of configurational entropy per grain seems to correlate with the structure randomness, and thus looks like a good candidate to evaluate the randomness of a bulk structure based on the physical contacts between the particles. Its implications with respect to Edwards volume ensemble remains to be investigated.

Future extensions of this analysis would have to focus on the measure of $g_2(r)$ based on the S2S distance rather than the centroids, which was not done in this study because of the multiplication of long computation times involved. A description of the anisotropy of the bubbles using the *Karambola* software [384] could help to correlate the variation in bubble shapes with the variation in contact number. This part requires the triangulation of the surfaces, which can be performed using the information obtained from image segmentation, but are outside the scope of the present thesis. Furthermore, the deformation of the structure with compression in the case of liquid foams could be measured with the same algorithm, with a closer look given to the emergence of meso- and macrostructures during the compression, as described in Section 6.1.2. In particular, the correlation between the position of a bubble in the contact network and the average force exerted on it in compression cycles is a promising investigation approach to uncover the relations between structure and properties [113].

6.4 Conclusion and outlooks

Granular systems constitute athermal, rigid systems, where the mechanical stability of the ensemble is ensured by the contacts between the grains. Because the number of contacts Z per grain are usually larger than the minimal, isostatic number Z_c , the set of contact forces in a rigid packing is not uniquely determined, and constitutes an additional degree of freedom of the packing for a given grain configuration. This gives rise to a rich and complex behaviour in the distribution of the contact forces, with aligned chains of forces larger than the grain scale bearing most of the load during compression and smaller structures of weakly interacting grains serving as fortifications of the force chains. The description of these complex and filamentous structures is one application

where network theory has been proven useful, in particular because of its ability to probe simultaneously different length scales using different descriptors. With tomographic analysis of granular packings, analysis of contact and force networks have been shown to be good predictors of the static and dynamic properties of granular packings. In foams however, because of the many-body interactions between bubbles, the force cannot be determined by standard methods. Forces could be extracted using Morse-Witten law in 2D foams, but the extension of this method to 3D foams is still an open question [109].

In this Chapter, we proposed a conceptual leap between the network analysis of granular materials and the analysis of foams and emulsions. This leap is achieved following two paths : first, by implementing a home-made segmentation and reconstruction algorithm of foams based on horizontal slices obtained from standard tomographic acquisition. This program offers the long sought after possibility for future users to define their own segmentation parameters [305, 58], giving it a great versatility in its applications, and avoiding black-box numerical procedures. Furthermore, it allows for an extraction of the voxel positions of the interfaces, an information that is inaccessible with commercially available softwares at time of writing. This additional information paves the way to our second conceptual path, defining neighbourhood relations in a physically relevant way. Because of the deformations of bubbles, a contact between two bubbles cannot be determined solely by the distance between their centroids anymore, but rather by the distance between their interfaces, let it be thin liquid films for ordinary foams or thick skins when the interface is covered by polymers. We propose a numerical procedure to determine the surface to surface (S2S) distance between two drops, and propose an efficient implementation to speed up the computationally expensive procedure to reasonable timescales. In the second part of this chapter, we applied our segmentation algorithm to numerically generated foams, which have the advantage of not being impaired with experimental noise. Starting from horizontal slices similar to that produced by standard tomographic imaging techniques, we defined the neighbourhood relations between bubbles formed by nucleation at sites corresponding to the particle positions in a regular FCC lattice, with a random displacement factor slightly shifting their positions. The average contact number $\langle Z \rangle$ obtained from our S2S method was closer to a dry foam than to a wet FCC structure. Other quantitative descriptors further corroborate the introduction of randomness in the structure of the foam, encouraging its widened usage in future foam characterisation.

The application of our segmentation characterisation algorithm to emulsion of droplets beyond the simple proof of concept was halted by the limited amount of time associated to the realisation of this thesis. As we showed in Chapter 4, the thickness of the skin in our emulsions made the segmentation of the drops easier than in ordinary emulsions. A first and direct application would thus be the characterisation of these emulsions with our algorithm, which is made freely available for the interested users¹. As the positions of contour voxels are determined by the algorithm, the quantification of shape anisotropy and its distribution throughout the packing is also a promising route for foam characterisation. Preliminary tests showed that Karambola software [384] could already been used to get Minkowski tensors of individual drops, but with results sensitive to the surface triangulation. A robust triangulation method still needs to be chosen for a proper shape characterisation. Similarly, the measure of local liquid fraction $\phi_l(\vec{r})$ and its correlation with other structural properties is a promising outlook, which could easily be performed with Pomelo software [318, 50].

The current limitation to the determination of the set of contact forces limit the information that can be extracted. For purely capillary interfaces, this would require a reliable segmentation of

¹<https://github.com/SimianLibrarian/vritra>

drops. Drops from the PEG-PDMS emulsions are actually good candidates as a model system, in the limit of very soft skin (e.g. reactive fraction $\phi_r < 50$ wt.%) with low elastocapillary numbers, thick enough to visually segregate droplets. Our algorithm, along with the emulsion system, could thus help to test experimentally the validity of Morse-Witten law in 3D foams and emulsions in the limit of low elastocapillary numbers ($\alpha \ll 1$).

The deformation of drops is a good indicator of the applied forces. A possible investigation is the deformation of individual drops during compression, and how the amount of this deformation correlates with the position of the drop within the contact network. Finding the structural descriptors predicting the deformation with most precision is a promising way to link structure and properties, as was done in previous work on photoelastic discs [113].

Finally, we hope that our example of the importance of the localisation of the interface boundaries will foster interest in the granular community, and encourage developers of commercial tomographic suites to propose the voxel positions of the interfaces in future implementations of their softwares.

Chapter 7

General conclusion

As stated in the introduction, this thesis is part of the METAFOAM ERC project, aimed at the production of foam- and emulsion-based metamaterials with mechanical and acoustic properties akin to those of metamaterials (e.g. negative Poisson ratio). These properties arise from the structure of the metamaterials, which in the case of foams is a result of the contact interactions between the bubbles/drops. A physically sound production route is thus the alteration of the interfaces and the associated interactions, targeting to produce self-assembled structures of interest. We decided to conduct this investigation following two axis. The first axis concerns the interactions between bubbles/drops, and how they are affected by interfacial changes. The second axis focuses on the production of a descriptive framework adapted to foam/emulsion structures.

In Chapter 3, we proposed the first experimental verification of an interaction law first proposed by Morse and Witten in 1993 [4], which accounts for the deformation of bubbles/drops when subjected to compression. Using a simple experimental setup investigating bubble trains in capillaries and numerical simulations with the Surface Evolver software [9], we showed that the experimental deformation of a bubble subjected to forces exerted by its neighbours corroborates the Morse-Witten interaction law in the limit of small contact forces, hence strongly deviating from the soft-sphere approximation previously used to describe bubble-bubble interactions. We further confirmed experimentally that this deformability makes the bubble-bubble interaction intrinsically many-body, with a stiffening of the bubble with increasing number of neighbours. This finding has important consequences, as it links the mechanical response to the contact number Z and the geometry of the foam. The extension of this experimental verification in 2D and 3D foams would be a cornerstone in the reconstruction of force networks in foams/emulsions.

In Chapter 4, we investigate the impact of interfacial elasticity on an otherwise purely capillary interface of a bubble/drop attached to a needle. Our approach is distinguished by its approximation of the elastic stresses as an isotropic additive stress to the simple interfacial tension. By comparing the predictions of our model to the state equations of a thin shell, we showed that it could be used to characterise with reasonable accuracy the elastic shear modulus of the interface in a pendant drop geometry. We further provide experimental parameters where our approximation remains valid, to help future experimentalists to design and dimension their experimental setups. We finally use this problem to propose the first usage, to our knowledge, of the Surface Evolver software to simulate elastocapillary interfaces. The benchmarking of these results comfort the usage of Surface Evolver for these new systems, paving the way for numerical assemblies of elastocapillary bubbles/drops, or bubbloons/droploons.

In Chapter 5, we designed an experimental system to investigate the effect of an increasingly elastic interface on drops and emulsions. This system is composed of PEG drops in a silicone phase, with the crosslinking of an interfacial silicone gel triggered by the diffusion of a catalyst from the PEG phase into the silicone phase. We studied separately the gel, the interface and the drops to disentangle the complex contributions at play in the droploons. The characterisation of the silicone gel in its bulk phase gives an understanding of the parameters governing its rigidity and formation kinetics. This characterisation was subsequently used to produce silicone foams of controlled morphology (Appendix 8.3). We studied the PEG-silicone interface using interfacial shear rheology, identifying the skin formation, mechanics and kinetics to guide the production of drops with thick polymeric skins. At last, we produced emulsions of droploons using a home-made millifluidic setups, with skins of different thicknesses and rigidities. The variations in emulsion structures obtained with this approach is a first encouraging result on the way of understanding the interface-structure relations. The PEG-silicone system is now sufficiently characterised to be a model system for future investigations on this topic.

In Chapter 6, we developed a software aimed at the reconstruction and the characterisation of 3D images of foams/emulsions based on slices obtained from tomographic reconstruction. This software fulfills the long-sought requirements of a segmentation with all parameters controlled by the user, and the necessity of defining a contact between bubbles/drops in a physically relevant way. Tomographic analysis is usually focused on granular materials with rigid, undeformable grains. Because of the deformation of bubbles/drops, the distance between two bubbles/drops cannot be assumed from the distance between their centroids, as it is currently the case. We implement a new definition of this distance based on the distance between the bubble/drop interfaces, and further provide access to the positions of the voxels of the interfaces. We benchmark our software on numerically generated foams and show that the randomness in the initial structure of nucleating sites is reflected in the final foam structure. These results strongly encourage the use of our software in future analysis of foam/emulsion structures of various natures. We thus make it freely available online. Furthermore, the description of the shapes of the interfaces through the positions of their interface voxels is a new information, not provided by currently commercially available softwares. This information could be used in future studies to access to shape descriptors, e.g. with Minkowski's tensors, and local liquid fraction, further refining the foam/emulsion structural description at the bubble/drop scale.

Outlook

The broader topic of the rules underlying the packing of foams/emulsions of elastocapillary bubbles/droploons is far from being exhausted with the work presented in this manuscript. We propose three different axes where the findings of this thesis could be used to investigate this field further, which we represent in Fig. 7.1.

First, improvements on the PEG-PDMS model system could lead to control precisely the thickness and the rigidity of the silicone skin. This control could help to produce droploon emulsions with precisely controlled elastocapillary number α . Its solid interface also makes it a sought-after system in the field of granular science to understand the impact of grain deformability on packing properties [95] and the impact of the transition from a soft to a hard elastic shell [385]. Further-

more, a quantification of the frictional and viscous properties of the skin are required to understand the interactions between these droploons.

Second, access to the forces between bubbles/drops in ordinary foams/emulsions would help to understand their mechanical properties, similarly to the approach used in granular science. The determination of these forces in 3D is still an unsolved problem, even though 2D systems could be resolved experimentally [60]. In addition to this interaction when only the capillary stress is considered, the consequence of the tangential elastic stress described in Chapter 4 on the Morse-Witten interaction law still needs to be considered. The rewriting of the classical Young-Laplace equation with the additional elastic stress would have to be plugged into the Morse-Witten derivation based on it. The interactions between droploons/bubbloons would have to be investigated as we did for ordinary bubbles/drops, with the goal of deriving a "Morse-Witten-Hooke" interaction law for elastocapillary bubbles/drops.

Third, our analysis software is a powerful and versatile tool, applicable to any foam/emulsion where the absorption contrast is high enough to segment the two phases. It could thus be used to analyse bubbloons/droploons packing regardless of the physicochemical details of the interface. Our current description could be substantiated with other useful descriptors inspired from granular science and network theory, such as the distribution of l -cycles. Furthermore, our extraction of the positions of interfacial voxels opens up the possibility to tessellate the foam/emulsion and give access to the local liquid fraction $\phi_l(r)$ defined at the bubble/drop scale, e.g. with the *Pomelo* software [318]. This fine gain analysis could be complemented by the bubble/drop deformation e.g. using Minkowski's tensors as computed by the *Karambola* software [384]. Determining the most predictive shape descriptors would be a first step in the good direction, as different descriptors have been used successfully in the literature but without comparing their results [217, 361]. The tomographic imaging of foams/emulsions during deformation (e.g. shear or compression) could also be performed with our software, hopefully indicating correlations between shape and structural changes, combined in an exhaustive morphostructural analysis of foams/emulsions.

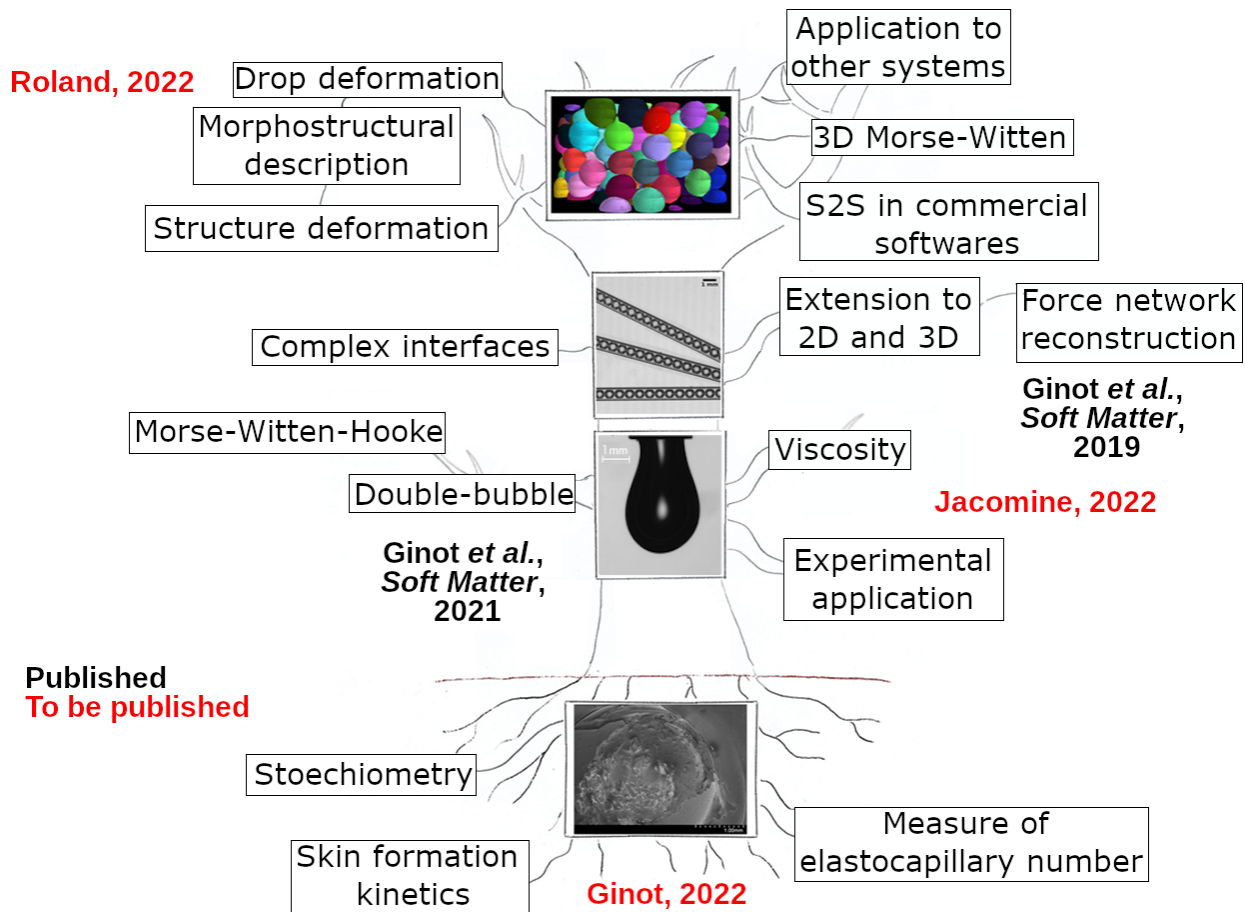


Figure 7.1: The mechanical properties of foams/emulsions depend on the length scales considered. These length scales interact through mechanisms, some of which being annotated along the black arrows. A proper mechanical description thus requires to consider the different length scales simultaneously. In this thesis, the relations between the different scales are investigated using adapted experimental methods, represented between the black arrows.

One-year progression plan

The work presented in this thesis gathered broadly different topics, from polymer chemistry to tomographic reconstruction. Furthermore, it is intended to serve as future foundations for the design of new foam-templated and emulsion-templated materials. In our current point of view, this goal can be achieved by the improvement of the understanding and the control of the PEG-silicone system to make it a model system for physical investigation of interfacial elasticity. We thus propose here a one-year work plan for readers interested in the characterisation of the PEG-silicone system in order to study the elastocapillary transition in foams and emulsions. The different steps are summarised in Fig. 7.2.

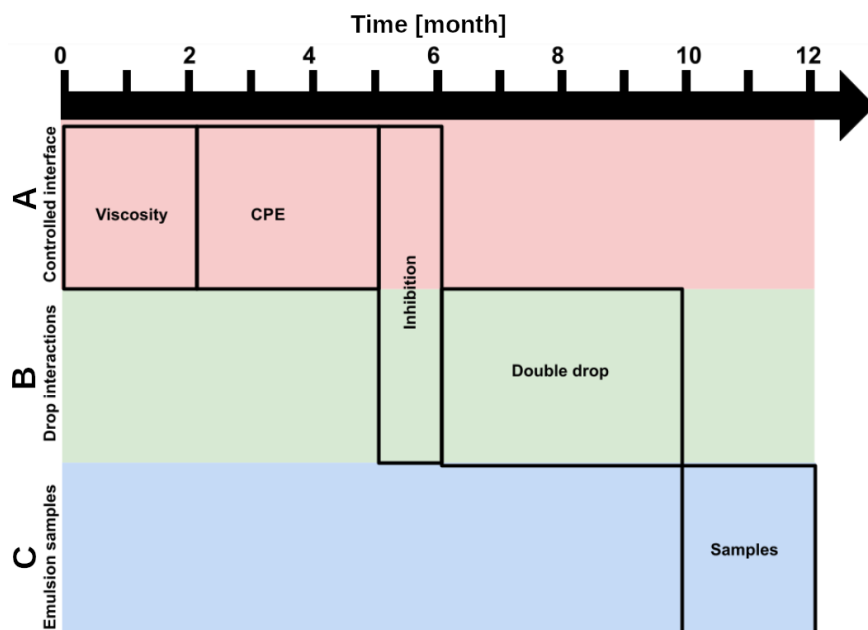


Figure 7.2: Planning proposition for a one-year project aimed at the improvement of the PEG-silicone system towards a model system for the physical investigation of the onset of interfacial elasticity in foams and emulsions.

This one-year plan is structured around three tasks, represented by color blocks in Fig. 7.2. The first task is the characterisation and control of the interface of the PEG-silicone system. As preliminary experiments on other experimental systems showed, the pressure-deformation experiments presented in Chapter 4 actually showed signs of viscosity, as the pressure depended both on the stretch ratio and on the history of the deformation, such as the deformation speed. Thanks to the theoretical work of Kierfeld and collaborators, the interfacial viscosity can now be deduced from this dependency, giving more information about the physical properties of the studied interfaces within the current experimental setup. Careful theoretical study and experimental considerations are further required to deduce the experimental parameters best suited for a precise measurement of elastic and viscous moduli.

After the incorporation of the interfacial viscosity, the reaction kinetics of the PEG-silicone interface will have to be characterised using the capillary pressure elastometry described in Chapter 4. Currently, the elastocapillary number is quite high because of the decrease of interfacial tension caused by the formation of copolymers. This could be improved by a better control of the chemistry of the system, limiting the side reactions and the formation of these polymers. In addition, the temporal evolution of the interfacial elasticity will be of interest to design drops with controlled

elastocapillary number with the millifluidic device described in Chapter 5. The variation of the kinetics with reactive fraction and catalyst fraction also have to be investigated using this setup. Finally, a quantitative analysis of the action of the inhibitor needs to be performed, e.g. by measuring the variation of the kinetics of skin growth caused by the addition of the inhibitor : so far, its action was hypothesised to be instantaneous, while the kinetics of inhibitor-catalyst reaction may impact the skin formation. Again, the capillary pressure elastometry setup is well adapted to study the variation of the kinetics.

The second task is the characterisation of the interactions between droploons, as represented in Fig. 7.2B. The fine grain control of the elastocapillary number gained by the study of the inhibitor action would allow to produce multiple droploons of equivalent elastocapillary numbers, whose interactions can be characterised using the double-bubble experiment used by Giustiniani *et al.* [10]. A good understanding of the interactions between the droploons are required to understand the mechanical properties of droploons assemblies. A particular care should be adressed to the possible entanglement of polymers from different skins, potentially altering the interaction forces between drops depending on the duration of their contacts.

Finally, once the fine-grain control of the elastocapillary number is achieved through these first steps, controlled and large-scale samples of controlled elastocapillarity will be produced, allowing to relate the structure and the morphology of the droploon emulsions to their interfacial properties and their contact interactions. This characterisation could be performed using X-Ray tomography and the lab-made reconstruction algorithm designed to this intent ¹.

¹<https://github.com/SimianLibrarian/vritra>

Conclusion générale

Tel qu’annoncé dans l’introduction, cette thèse fait partie du projet ERC METAFOAM pour la production de matériaux basés sur des mousses et des émulsions, et aux propriétés mécaniques et acoustiques similaires à celles de métamatériaux. Ces propriétés proviennent de la structure des métamatériaux, qui, dans le cas des mousses et des émulsions, proviennent des interactions entre les bulles et les gouttes. L’altération des interfaces et de leurs interactions est donc une voie physique possible pour la production de nouvelles structures. Nous avons mené ces travaux suivant deux axes : un premier axe focalisé sur les interactions entre bulles et entre gouttes, et sur l’impact des changements interfaciaux sur ces interactions ; et un second axe focalisé sur la production d’un cadre descriptif adapté à la structure des mousses et des émulsions.

Dans le chapitre 3, nous avons proposé la première vérification expérimentale d’une loi d’interaction à N -corps proposé par Morse et Witten en 1993 [4], prenant en compte la déformation des bulles et des gouttes lorsque celles-ci sont sujettes à la compression. Au moyen d’un système expérimental simple de trains de bulles dans des capillaires carrés et de simulations avec le logiciel Surface Evolver [9], nous avons montré que la déformation expérimentale d’une bulle soumise à des forces exercées par ses voisines corrobore la loi d’interaction de Morse et Witten dans la limite des faibles forces de contact, avec une forte déviation de l’approximation des sphères molles utilisée précédemment pour décrire ces interactions. Nous avons ainsi montré expérimentalement que la déformabilité fait des interactions bulle-bulle une interaction à N -corps, avec une rigidification des bulles et gouttes lorsque le nombre de voisins augmente. Ce résultat a d’importantes conséquences, reliant la réponse mécanique au nombre de contact Z et à la géométrie de la mousse. L’extension de cette vérification expérimentale aux mousses 2D et 3D sera à l’avenir une pierre angulaire de la reconstruction des réseaux de forces de contact dans les mousses et les émulsions.

Dans le chapitre 4, nous étudions l’impact de l’ajout d’une élasticité interfaciale sur l’interface capillaire d’une bulle produite à l’extrémité d’une aiguille. Notre approche se distingue par l’approximation des contraintes élastiques comme des contraintes isotropes s’additionnant à la tension interfaciale d’origine. La comparaison de notre modèle avec les prédictions de l’équation d’état de la membrane mince montre qu’il peut être utilisé pour mesurer le module élastique de cisaillement d’une interface dans une configuration de goutte pendante avec une bonne précision. Nous fournissons les paramètres expérimentaux pour lesquels notre approximation reste valide, afin d’aider de futurs expérimentateurs et futures expérimentatrices lors de la conception et du dimensionnement de leurs montages expérimentaux. Nous proposons enfin la première utilisation, à notre connaissance, de Surface Evolver pour simuler des interfaces élastocapillaires. La comparaison de ces résultats à des modèles éprouvés conforte l’utilisation de Surface Evolver pour nos systèmes et l’ouvre à la possibilité de simulations numériques d’assemblées de droplons et de bubbloons.

Dans le chapitre 5, nous avons conçu un système expérimental permettant d’étudier l’effet

d'une élasticité interfaciale de module croissant sur des gouttes et des émulsions. Ce système est composé de gouttes de PEG dans une phase de silicone. Un gel de silicone réticulé est formé à l'interface par la diffusion d'un catalyseur de la phase PEG dans la phase silicone. Nous avons étudié séparément le gel, l'interface et les gouttes pour séparer les différentes contributions en jeu dans les droploons. La caractérisation du gel de silicone en volume nous permet de comprendre les paramètres contrôlant la rigidité et la cinétique de formation du gel. Cette caractérisation a par la suite été utilisée pour produire des mousses silicone de morphologie contrôlée (Annexe B). Nous avons étudié l'interface PEG-silicone par rhéologie interfaciale de cisaillement en identifiant la formation de la peau, sa cinétique et sa rigidité pour guider la production de gouttes avec une peau de polymères suffisamment épaisse pour segmenter facilement des gouttes très déformées dans une reconstruction tomographique. Enfin, nous avons produit des émulsions de droploons au moyen d'un montage millifluidique, avec des peaux de différentes épaisseurs et rigidités. La variation dans la structure des émulsions obtenues avec cette approche est un premier résultat encourageant pour la compréhension des relations interface-structure. Le système PEG-silicone est désormais suffisamment compris pour constituer un bon système modèle pour de futures investigations sur ce sujet.

Dans le chapitre 6, nous avons développé un algorithme visant à reconstruire et caractériser des mousses et émulsions à partir d'images obtenues par imagerie tomographique par absorption. Cet algorithme répond également au besoin exprimé dans la littérature de donner aux utilisateurs et utilisatrices le contrôle sur le processus de reconstruction, ainsi qu'à la nécessité de définir les contacts entre bulles et gouttes de façon physiquement pertinente. L'analyse tomographique est habituellement focalisée sur des matériaux granulaires dont les grains sont indéformables. À cause de leur déformabilité, la distance entre deux gouttes ou deux bulles ne peut pas être déduite directement de la distance entre leurs centroïdes, comme c'est le cas pour des sphères rigides. Nous avons donc implémenté une nouvelle mesure de la distance entre deux bulles ou gouttes, basée sur la distance entre les interfaces, et produit une description explicite de la position des voxels des interfaces. Nous avons testé les résultats de notre logiciel sur des mousses générées numériquement et montré que l'introduction de désordre dans la structure initiale de nucléation des bulles se reflétait dans la structure finale de la mousse. Ces résultats encouragent l'utilisation de notre algorithme pour de futures analyses de mousses et d'émulsions de compositions variées. Nous mettons donc ce code en accès libre en ligne. De plus, la description de la forme des interfaces grâce à la position des voxels qui les composent est une nouvelle information qui n'était jusque là pas fournie par les logiciels commerciaux actuels. Cette information pourra être utilisée à l'avenir pour accéder à des descripteurs de forme, tels que les tenseurs de Minkowski, et la fraction liquide locale, ce qui raffinera encore la description structurelle des mousses et émulsions à l'échelle de la bulle et de la goutte.

Perspectives

La détermination de règles sous-jacentes aux ensembles de mousses et émulsions de bubbloons/droploons est un sujet loin d'être épuisé par le travail présenté dans ce manuscrit. Nous proposons trois axes différents se dégageant des travaux qui y sont décrits, et que nous espérons pouvoir porter la suite des investigations, que nous schématisons dans la Fig. 7.1.

Premièrement, l'amélioration du système modèle PEG-PDMS pourra mener au contrôle précis de l'épaisseur et de la rigidité de la peau de silicone. Ce contrôle pourra aider à la production d'émulsions de droploons au nombre élastocapillaire α précisément ajusté. Son interface solide en fait également un système très recherché dans le domaine des matériaux granulaires pour l'étude

de l'impact de la déformabilité des grains sur les propriétés d'ensembles [95] ainsi que l'impact de la transition d'une membrane molle à une membrane rigide [385].

Deuxièmement, l'accès aux forces entre bulles/gouttes dans les mousses/émulsions ordinaires pourra aider à la compréhension des propriétés mécaniques, suivant l'approche utilisée dans les matériaux granulaires. La détermination des forces en 3D est problème irrésolu à ce jour, bien que des systèmes bidimensionnels aient déjà pu être analysés expérimentalement [60]. En plus de cette interaction purement capillaire, les conséquences du stress tangentiel décrit dans le Chapitre 4 sur la loi d'interaction Morse-Witten reste à considérer. La réécriture de la relation classique de Young-Laplace avec un stress élastique additionnel devra être introduit dans la dérivation de la loi de Morse-Witten sur laquelle elle est basée. Les interactions entre *bubbloons* et *droploons* devront ainsi être étudiées tel que nous l'avons fait pour des bulles purement capillaires, avec pour but de dériver une loi d'interaction "Morse-Witten-Hooke" pour les bulles et gouttes élastocapillaires.

Troisièmement, notre algorithme d'analyse est un outil d'analyse puissant et adaptable, applicable à tout système mousse/émulsion dont le contraste d'indice d'absorption est suffisamment élevé pour segmenter les deux phases. Il pourra être utilisé pour analyser les ensembles de *bubbloons*/*droploons* indépendamment des détails physico-chimiques des interfaces. Notre niveau actuel de description pourra être enrichi avec d'autres descripteurs inspirés des matériaux granulaires et de la théorie des réseaux, tel que la distribution des *l*-cycles. De plus, notre extraction de la position des voxels de l'interface ouvre la possibilité de tesseler les mousses et les émulsions et de donner accès à la fraction liquide locale $\phi_l(r)$ définie à l'échelle de la bulle et de la goutte, par exemple au moyen du logiciel *Pomelo* [318]. Cette analyse à petite échelle pourra être complétée par celle de la déformation des bulles et des gouttes, par exemple en utilisant les tenseurs de Minkowski calculés par le logiciel *Karambola* [384]. La détermination des descripteurs de forme permettant la prédiction la plus fiable des forces exercées serait une première direction possible, puisque différents descripteurs ont été utilisés avec succès dans la littérature mais sans comparaison de leurs résultats [217, 361]. L'imagerie tomographique des mousses et des émulsions pendant la déformation (cisaillement ou compression) pourra également être réalisé grâce à notre algorithme, indiquant de potentielles corrélations entre changements de formes et changements de structures combinés dans une analyse morphostructurelle exhaustive des mousses et des émulsions.

Plan de travail à un an

Le travail présenté dans cette thèse rassemble une variété très vaste de sujets, de la chimie des polymères à la reconstruction tomographique de mousses et d'émulsions. De plus, il est conçu pour servir de base de travail pour la conception de nouveaux matériaux modelés à partir de mousses et d'émulsions. Au vu de l'état actuel des connaissances, il nous semble que ce but peut être atteint par l'amélioration de la compréhension et du contrôle du système PEG-PDMS, dans le but d'en faire un système modèle pour l'étude des propriétés physiques des mousses et émulsions élastocapillaires. Nous proposons ici un plan de travail sur un an pour les lecteurs et lectrices intéressés par cette problématique. Les différentes étapes ainsi que leurs temporalités sont résumées dans Fig. 7.2.

Ce plan de travail est structuré autour de trois tâches, représentées par les blocs colorés Fig. 7.2. La première tâche est la caractérisation et le contrôle de l'interface du système PEG-silicone. Des expériences préliminaires sur d'autres systèmes expérimentaux (non décrits dans ce manuscrit) ont montré que la relation pression-déformation présentée au chapitre 4 montrait en réalité des signes de l'impact de la viscosité, la pression dépendant à la fois du ratio de déformation et de l'historique

de la déformation, tel que la fréquence d'oscillation du cycle de déformation. Grâce au travail théorique de Kierfeld et ses collaborateurs, la viscosité interfaciale peut être mesurée grâce à cette variation, donnant plus d'informations sur les propriétés physiques de l'interface tout en conservant la même configuration expérimentale. Une étude théorique et expérimentale précautionneuse sera nécessaire pour déduire les paramètres expérimentaux les plus à même de produire une mesure simultanée des modules d'élasticité et de viscosité.

Après l'incorporation de la viscosité, l'interface PEG-silicone devra être caractérisée selon la méthode de l'élastométrie par pression capillaire décrite dans le chapitre 4. L'évolution temporelle de l'élasticité interfaciale sera d'un intérêt tout particulier pour fabriquer des gouttes de nombre élastocapillaire contrôlé à l'aide du dispositif millifluidique décrit au chapitre 5. Les variations de la cinétique avec la fraction réactive et la fraction de catalyseur pourra également être étudiée grâce à ce dispositif. Finalement, une analyse quantitative de l'action de l'inhibiteur devra être menée, par exemple en mesurant les variations de la cinétique de croissance de peau lors de l'ajout de l'inhibiteur : jusqu'ici, l'action de l'inhibiteur était supposée immédiate. Mais la cinétique de réaction inhibiteur-catalyseur pourrait avoir un impact sur la formation de la peau. Le montage expérimental de la goutte pendante sera ici aussi utilisable en l'état pour mener cette étude.

La deuxième tâche de ce plan de travail est la caractérisation des interactions entre les droploons, comme montré sur le bloc B de Fig. 7.2. Le contrôle fin du nombre élastocapillaire par l'étude de l'action de l'inhibiteur permettra la production de plusieurs droploons de nombres élastocapillaires similaires, dont les interactions pourront être caractérisées grâce au montage expérimental de double bulle utilisé par Giustiniani *et al.* [10]. Une compréhension quantitative de ces interactions sera requise pour comprendre les propriétés mécaniques d'émulsions de droploons. Une attention particulière devra être portée à l'entremêlement possible de polymères appartenant à des peaux différentes, provoquant une altération possible des forces d'interactions entre gouttes dépendamment de la durée des contacts.

La dernière tâche de ce plan de travail, représentée Fig. 7.2C, consistera en la production à grande échelle d'échantillons à nombre élastocapillaire contrôlé, permettant de relier la structure et la morphologie des émulsions aux propriétés interfaciales des droploons et à leurs interactions de contact. Cette caractérisation pourra être menée au moyen de tomographie à rayons X et grâce l'algorithme de reconstruction conçu en laboratoire spécifiquement à cet effet ².

²<https://github.com/SimianLibrarian/vritra>

Chapter 8

Appendices

8.1 Numerical determination of the interfacial deformation

We use the Surface Evolver software to determine the bubble or droplet shapes for which interfacial energy is minimal, respecting volume constraints and boundary conditions. The case where an elastic skin is attached to the interface raises the question how local strain should be deduced from the representation of the interface as an assembly of triangular facets. Section 8.1.1 explains how *convected* coordinates are used for this. Section 8.1.2 provides details about the calculation of the elastic energy density, based on the Neo Hooke constitutive model.

8.1.1 Strain represented using convected coordinates

The shape of the triangular facets used in the Surface Evolver as finite elements is fully defined if two edge vectors are given. Upon deformation of the investigated bubble, the facet is generally displaced and the edge vectors are changed, spanning a facet of modified shape. In the spirit of a linear discretization, an affine displacement field is assumed within each facet. One could describe the facet deformation using a coordinate system whose origin is attached to a given vertex of the facet, and express how the Cartesian coordinates of each point on the facet evolve. Alternatively, one may interpret the edge vectors as basis vectors which evolve upon a deformation and which are therefore in general non orthogonal. In this latter approach, the coordinates of each point of the interface are fixed and the deformation is represented in terms of a change of the basis vectors. This "convected coordinate" method goes back to pioneering work by Hencky [386]. In the Surface Evolver this method is convenient because the relevant edge vectors can easily be derived from the three facet vertex positions in the current configuration, denoted $\vec{x}_1, \vec{x}_2, \vec{x}_3$ and in the reference configuration $\vec{X}_1, \vec{X}_2, \vec{X}_3$,

$$\begin{aligned}\vec{S}_1 &= \vec{X}_3 - \vec{X}_1, & \vec{s}_1 &= \vec{x}_3 - \vec{x}_1, \\ \vec{S}_2 &= \vec{X}_2 - \vec{X}_1, & \vec{s}_2 &= \vec{x}_2 - \vec{x}_1.\end{aligned}\tag{8.1}$$

The edge vectors are represented using a cartesian orthonormal basis (\vec{e}_x, \vec{e}_y) such that $\vec{S}_i = S_{ix}\vec{e}_x + S_{iy}\vec{e}_y$ and $\vec{s}_i = s_{ix}\vec{e}_x + s_{iy}\vec{e}_y$.

As mentioned, convected coordinates remain constant upon a deformation; this introduces simplicity. But this choice also introduces complexity since the expression of the scalar product is no longer given by contraction $\vec{a} \cdot \vec{b} = a_i b_i$, additional terms appear since the basis vectors are generally not orthogonal. To avoid such complexity, one represents vectors and tensors that one wishes to associate in products using two different bases: a "covariant" and contravariant one.

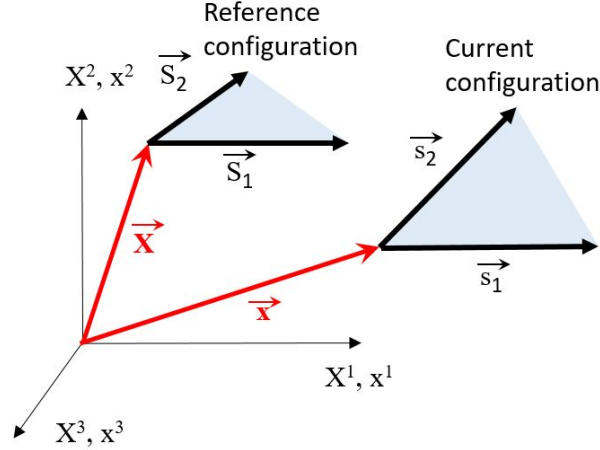


Figure 8.1: A triangular finite element of an interface is represented in the reference configuration and in the current, deformed configuration. The figure illustrates the notations used in the text: \vec{x} for vectors pointing to vertices and \vec{s} for finite element edge vectors. Capital letters are used for the reference configuration and small letters for the current configuration. For the sake of simplicity, only one of the three vectors pointing to vertices is shown in each configuration. The contravariant components of both \vec{X} and \vec{x} are indicated on the same set of Cartesian axes.

Covariant basis vectors follow the deformation of the edge facets. They are denoted \vec{G}_1, \vec{G}_2 in the reference state and \vec{g}_1, \vec{g}_2 in the current state. Covariant quantities are identified by lower indices,

$$\begin{aligned}\vec{G}_1 &= \vec{S}_1, & \vec{g}_1 &= \vec{s}_1, \\ \vec{G}_2 &= \vec{S}_2, & \vec{g}_2 &= \vec{s}_2.\end{aligned}\tag{8.2}$$

Contravariant basis vectors (\vec{G}^1, \vec{G}^2) or (\vec{g}^1, \vec{g}^2), are identified by upper indices, and they are defined through the following orthogonality relations:

$$\vec{G}^i \cdot \vec{G}_j = \delta_j^i, \quad \vec{g}^i \cdot \vec{g}_j = \delta_j^i,\tag{8.3}$$

where $\delta_j^i = 1$ if $i = j$ and $\delta_j^i = 0$ otherwise. The Cartesian coordinate system is a special case within this general framework where covariant and contravariant bases coincide. Using co- and contravariant bases simplifies the expressions of the scalar products of vectors and tensors in the case of non-orthogonal basis vectors.

An arbitrary vector $d\vec{X}$ representing a small line element on the surface reads in terms of the covariant basis

$$d\vec{X} = d\Theta^j \vec{G}_j.\tag{8.4}$$

$d\Theta^j$ are the convected contravariant coordinates. We use the Einstein summation convention and sum over repeated indices.

Descriptions of strain in large deformation continuum mechanics are commonly based on the deformation gradient tensor \mathbf{F} , represented by a matrix that transforms a line element $d\vec{X}$ in the reference state into $d\vec{x}$ in the current state,

$$d\vec{x} = \mathbf{F}d\vec{X}.\tag{8.5}$$

In terms of convected coordinates, \mathbf{F} may be written

$$\mathbf{F} = g_j \otimes G^j.\tag{8.6}$$

The symbol \otimes indicates an operation assembling two vectors into a tensor, called tensor product. Indeed, in view of Eq. 8.3 we have

$$\mathbf{F}d\vec{X} = (\vec{g}_i \otimes \vec{G}^i) d\Theta^i G_j = d\Theta^i \vec{g}_i = d\vec{x}. \quad (8.7)$$

The deformation gradient tensor contains information about rotations that is irrelevant for interfacial energy. The interfacial energy in the Surface Evolver is computed using the 2D right Cauchy-Green strain tensor \mathbf{C} which is invariant to rotations [198], contrary to \mathbf{F} :

$$\mathbf{C} = \mathbf{F}^T \mathbf{F} = (\vec{G}^i \otimes \vec{g}_i)(\vec{g}_j \otimes \vec{G}^j) = g_{ij} \vec{G}^i \otimes \vec{G}^j. \quad (8.8)$$

g_{ij} is the metric tensor in the current configuration, defined as follows:

$$g_{ij} = \vec{g}_i \cdot \vec{g}_j. \quad (8.9)$$

To determine the elastic energy of a facet in a simulation, \mathbf{C} needs to be determined numerically. The components of the contravariant basis vectors in the reference state G^i are deduced from the covariant ones using the orthogonality properties (8.3):

$$\begin{aligned} \vec{G}^1 \cdot \vec{G}_1 = 1 &= S^{1x} S_{1x} + S^{1y} S_{1y} \rightarrow S^{1x} = \frac{1 - S^{1y} S_{1y}}{S_{1x}} \\ \vec{G}^2 \cdot \vec{G}_1 = 0 &= S^{2x} S_{1x} + S^{2y} S_{1y} \rightarrow S^{2x} = -S^{2y} \frac{S_{1y}}{S_{1x}} \\ \vec{G}^2 \cdot \vec{G}_2 = 1 &= S^{2x} S_{2x} + S^{2y} S_{2y} \rightarrow S^{2x} = \frac{1 - S^{2y} S_{2y}}{S_{2x}} \\ \vec{G}^1 \cdot \vec{G}_2 = 0 &= S^{1x} S_{2x} + S^{1y} S_{2y} \rightarrow S^{1x} = -S^{1y} \frac{S_{2y}}{S_{2x}}. \end{aligned} \quad (8.10)$$

Solving the system (8.10) yields the components of the vectors \vec{G}^i :

$$\begin{aligned} \vec{G}^1 = \vec{S}^1 &= \left(\frac{S_{2y}}{S_{1x}S_{2y} - S_{1y}S_{2x}}, -\frac{S_{2x}}{S_{1x}S_{2y} - S_{1y}S_{2x}} \right) \\ \vec{G}^2 = \vec{S}^2 &= \left(-\frac{S_{1y}}{S_{1x}S_{2y} - S_{1y}S_{2x}}, \frac{S_{1x}}{S_{1x}S_{2y} - S_{1y}S_{2x}} \right). \end{aligned} \quad (8.11)$$

To express the Cauchy Green strain tensor directly as a function of the edge vectors, it is convenient to introduce Gram matrices. The Gram matrix of two arbitrary vectors \vec{v}_1 and \vec{v}_2 is a 2x2 matrix whose element ij is by definition given by the scalar product $\vec{v}_i \cdot \vec{v}_j$. The covariant metric tensor defined in Eq. (8.9) is thus the Gram matrix of the edge vectors in the current configuration. Following the notation used in the Surface Evolver manual, we will call this quantity \mathbf{s} :

$$\mathbf{s} = \begin{pmatrix} \vec{s}_1 \cdot \vec{s}_1 & \vec{s}_1 \cdot \vec{s}_2 \\ \vec{s}_2 \cdot \vec{s}_1 & \vec{s}_2 \cdot \vec{s}_2 \end{pmatrix} = g_{ij}. \quad (8.12)$$

The Gram matrix of the edge vectors in the reference state is denoted \mathbf{S} :

$$\mathbf{S} = \begin{pmatrix} \vec{S}_1 \cdot \vec{S}_1 & \vec{S}_1 \cdot \vec{S}_2 \\ \vec{S}_2 \cdot \vec{S}_1 & \vec{S}_2 \cdot \vec{S}_2 \end{pmatrix}. \quad (8.13)$$

We note that the denominators in Eqs. (8.11) are the determinant of \mathbf{S} :

$$\det \mathbf{S} = \left(\vec{S}_1 \cdot \vec{S}_1 \right) \cdot \left(\vec{S}_2 \cdot \vec{S}_2 \right) - \left(\vec{S}_1 \cdot \vec{S}_2 \right)^2 = (S_{1x}S_{2y} - S_{1y}S_{2x})^2. \quad (8.14)$$

Since the components of the tensor $G^i \otimes G^j$ are the scalar products of G^i and G^j [387] we can now write Eq. (8.8) in terms of the cartesian components of \mathbf{S} , using Eqs. (8.11) and (8.14),

$$\begin{aligned}\vec{G}^1 \cdot \vec{G}^1 &= \frac{S_{2x}S_{2x} + S_{2y}S_{2y}}{\det(\mathbf{S})} = \frac{\vec{S}_2 \cdot \vec{S}_2}{\det(\mathbf{S})} \\ \vec{G}^2 \cdot \vec{G}^2 &= \frac{S_{1x}S_{1x} + S_{1y}S_{1y}}{\det(\mathbf{S})} = \frac{\vec{S}_1 \cdot \vec{S}_1}{\det(\mathbf{S})} \\ \vec{G}^1 \cdot \vec{G}^2 &= -\frac{S_{1x}S_{2x} + S_{1y}S_{2y}}{\det(\mathbf{S})} = -\frac{\vec{S}_1 \cdot \vec{S}_2}{\det(\mathbf{S})}.\end{aligned}\tag{8.15}$$

This result shows that $G^i \otimes G^j$ is the inverse of the Gram matrix \mathbf{S} ,

$$G^i \otimes G^j = \frac{1}{\det|\mathbf{S}|} \begin{pmatrix} \vec{S}_2 \cdot \vec{S}_2 & -\vec{S}_1 \cdot \vec{S}_2 \\ -\vec{S}_1 \cdot \vec{S}_2 & \vec{S}_1 \cdot \vec{S}_1 \end{pmatrix} = \mathbf{S}^{-1}.\tag{8.16}$$

We can finally express the 2D right Cauchy-Green tensor (Eq. 8.6), needed in section 8.1.2 to calculate the elastic energy, in terms of the Gram matrices \mathbf{s} and \mathbf{S} :

$$\mathbf{C} = \mathbf{F}^T \mathbf{F} = \mathbf{s} \mathbf{S}^{-1}.\tag{8.17}$$

We note that Eq. (8.17) can also be used to compute the Green-Lagrange strain tensor $\mathbf{E} = \mathbf{F}^T \mathbf{F} - \mathbf{I}$ from the vertex coordinates. \mathbf{E} converges to the infinitesimal strain tensor ε in the limit of small deformations. Eq. (8.17) is thus the key result for evaluating strain in Surface Evolver calculations. We note that Eq.(8.17) also gives the correct strain for displacements of vertices normal to the surface.

8.1.2 Elastic energy

In this section we explain how the elastic contribution to the interfacial energy is determined in our simulations. According to the compressible 3D Neo Hookean model implemented in the Surface Evolver [16], and commonly used in the literature [388] the elastic energy per volume is

$$W_{3D} = \frac{G}{2}(Tr \mathcal{C} - 3) - G \ln J + \frac{\Lambda}{2}(\ln J)^2.\tag{8.18}$$

G and Λ are the Lamé parameters. $J^2 = \det(\mathcal{C})$ is an invariant of \mathcal{C} , a scalar quantity independent of the reference frame. It is given by the ratio of the volumes of a material element in the current deformed and initial states. In the limit of small deformations, the energy density Eq.8.18 reduces as expected to the one deduced from Hooke's law for linear elastic isotropic materials [128], using the infinitesimal strain tensor ε defined by Eq. 4.19.

$$W_{3D} = \frac{\Lambda}{2}Tr(\varepsilon)^2 + GTr(\varepsilon^2).\tag{8.19}$$

The elastic skins considered in our work are so thin that their bending stiffness is negligible. Their resistance to shear deformations where the two opposite faces are displaced relative to each other is very strong, we neglect this mode of deformation and assume a state of *plane stress*, consistently with the Kirchhoff hypotheses of thin shell theory [389]. Using Cartesian coordinates with an x_3 axis perpendicular to an element of the skin, this is expressed as $\mathcal{C}_{31} = \mathcal{C}_{32} = \mathcal{C}_{13} = \mathcal{C}_{23} = 0$. In the same spirit, we consider the case where the stress normal to the skin has a negligible

effect on its shape, so that we can assume $\sigma_{33} = 0$ without loss of generality. For plane stress, the changes of volume and changes of skin thickness are directly related. To analyse this feature, we recall a general relation between the energy density and the Cauchy stress of hyperelastic materials [198]

$$J\mathbf{F}^{-1}\boldsymbol{\sigma}\mathbf{F}^{-T} = 2\frac{\partial W_{3D}}{\partial \mathcal{C}}. \quad (8.20)$$

The plane stress condition can thus be expressed as

$$\frac{\partial W_{3D}}{\partial \mathcal{C}_{33}} = 0. \quad (8.21)$$

Using Eq.(8.18) this yields.

$$\Lambda \ln J = G(1 - \mathcal{C}_{33}). \quad (8.22)$$

Physically speaking, this equation previously derived for a similar constitutive equation [390] relates the squared ratio of the current and initial skin thicknesses given by \mathcal{C}_{33} to the ratio of the current and initial skin volumes, expressed by J . In the aim to derive a 2D energy density, we write Eq. (8.22) as a function of the components of \mathcal{C} , taking into account that many of them are zero in the case of plane stress, as pointed out above:

$$\mathcal{C}_{33}(\mathcal{C}_{11}\mathcal{C}_{22} - \mathcal{C}_{12}^2) = \exp\left[\frac{2G}{\Lambda}(1 - \mathcal{C}_{33})\right] \quad (8.23)$$

To represent the skin as a 2D material whose deformation is fully specified by $\mathcal{C}_{11}, \mathcal{C}_{22}$ and \mathcal{C}_{12} , we need to express \mathcal{C}_{33} in terms of these other variables. This can be done by solving Eq. (8.23) either numerically [390], or analytically, using Lambert's W function [391]:

$$\mathcal{C}_{33} = \frac{\Lambda}{2G} W\left[\frac{2G \exp(2G/\Lambda)}{\Lambda \det(\mathbf{C})}\right] = \frac{\Lambda}{2G} W\left[\frac{2G \exp(2G/\Lambda)}{\Lambda(\mathcal{C}_{11}\mathcal{C}_{22} - \mathcal{C}_{12}^2)}\right] \quad (8.24)$$

The latter option has been implemented by R. Bouzidi in the Surface Evolver software. Inserting the expression of \mathcal{C}_{33} in Eq. (8.22) and the resulting expression for $\ln J$ into the 3D energy density Eq. (8.18), we obtain the following 2D energy density for a Neo-Hookean skin, where h_0 is the skin thickness in the reference state,

$$W_{2D} = Gh_0 \left(\frac{1}{2}(\text{Tr} \mathbf{C} - 3) - \frac{G}{\Lambda}(1 - \mathcal{C}_{33}) + \frac{G}{2\Lambda}(1 - \mathcal{C}_{33})^2 \right). \quad (8.25)$$

Gh_0 may be interpreted as a 2D shear modulus. Neglecting constant terms which are irrelevant for a potential energy and expressing the result in terms of the 2D right Cauchy Green tensor using $\text{Tr} \mathbf{C} = \text{Tr} \mathbf{C} + \mathcal{C}_{33}$, we obtain

$$W_{2D} = \frac{Gh_0}{2} \left(\text{Tr} \mathbf{C} + \mathcal{C}_{33} + \frac{G}{\Lambda} \mathcal{C}_{33}^2 \right). \quad (8.26)$$

The skin materials considered in the present paper are much easier to shear than to compress such that $G \ll \Lambda$. In this case, the last term in Eq. (8.26) can be neglected.

Besides the Neo-Hookean model discussed so far, the Surface Evolver software provides an alternative energy density expression called "linear elastic model" which yields behavior consistent with Eq. (8.19) in the limit of small deformations. However, one should be aware that for large deformations this numerical model based on the right Cauchy Green tensor is not consistent with Eq. (8.19).

8.2 Pressure-deformation relations of droploons on capillaries expressed via radial stretch

In the main body of the article we expressed all relations in terms of area stretch λ_A . The same approach can be done for the radial stretch λ leading, however, to expressions which are less intuitive and less directly accessible by experiments and simulations. For completeness, we shall provide the resulting equations here.

We can rewrite the interfacial A for a droploon on a capillary larger than a hemisphere as

$$\begin{aligned} A &= 2\pi R^2 \left(1 - \sqrt{1 - \left(\frac{R_n}{R}\right)^2} \right) \\ &= 2\pi R^2 f(R_n/R). \end{aligned} \quad (8.27)$$

The function $F(R_n/R)$ defined by Eq.(8.27) helps to express the result in a more concise way.

The term $\ln(A/A_0)$ in the Gibbs relation (4.33) can then be rewritten using Eq. (8.27) to give the normalised surface stress of the droploon on the capillary

$$\hat{\sigma} = 1 + 2\alpha \ln \lambda + \alpha \ln \xi. \quad (8.28)$$

The last term, depending on the geometric factor

$$\xi = \frac{f(R_n/R)}{f(R_n/R_0)}, \quad (8.29)$$

expresses the impact of a capillary on the elastic stress at the surface of a sphere, assuming a spherical sector shape.

In the first two terms one recognises the result previously obtained for the perfect sphere (Eq. (4.33)). One can therefore rewrite

$$\hat{\sigma} = \hat{\sigma}_{sphere} + \alpha \ln \xi. \quad (8.30)$$

Compared to a sphere with the same radius, the presence of the capillary introduces a corrective term in the surface stress which depends on α , R , R_n and R_0 .

For Neo-Hookean droploons, the droploon shapes on capillaries are no longer perfect spherical sectors, making analytical descriptions much harder - which is why numerical simulations are required. Nevertheless, we shall make here the seemingly crude approximation that the shapes can be approximated as spherical sectors.

Using exactly the same approach as for the Gibbs interface but with the Neo-Hookean relation (see Table 4.1), one finds for a Neo-Hookean droploon on a capillary

$$\hat{\sigma} = 1 + \frac{\alpha}{3} (1 - \lambda^{-6} \xi^{-3}). \quad (8.31)$$

After some algebra, this can be rewritten as the expression for the perfect sphere with a corrective term taking account of the capillary

$$\hat{\sigma} = \hat{\sigma}_{sphere} + \frac{\alpha}{3} (1 - \xi^{-3}) \lambda^{-6}. \quad (8.32)$$

In the limit of small deformations, our results for both Gibbs and Neo-Hooke elasticity yield the same relation

$$\hat{\sigma} = \hat{\sigma}_{sphere} + \alpha (\xi - 1) \lambda, \quad (8.33)$$

Model on capillary	Normalised surface stress $\hat{\sigma}$	Critical stretch λ_c
Gibbs	$\hat{\sigma}_{sphere} + \alpha \ln \xi$	$\frac{R_0 \left(1 + \sqrt{1 - \left(\frac{R_n}{R_0}\right)^2}\right) e^{-\frac{1}{\alpha}}}{\sqrt{2R_0^2 \left(1 + \sqrt{1 - \left(\frac{R_n}{R_0}\right)^2}\right) e^{-\frac{1}{\alpha}} - R_n^2}}$
Neo-Hooke	$\hat{\sigma}_{sphere} + \frac{\alpha}{3} \left(1 - \xi^{-3}\right) \lambda^{-6}$	$\frac{R_0 \left(1 + \sqrt{1 - \left(\frac{R_n}{R_0}\right)^2}\right) \left(1 - \frac{1}{2\alpha}\right)^2}{\sqrt{2R_0^2 \left(1 + \sqrt{1 - \left(\frac{R_n}{R_0}\right)^2}\right) \left(1 - \frac{1}{2\alpha}\right)^2 - R_n^2}}$
Hooke	$\hat{\sigma}_{sphere} + \alpha (\xi - 1) \lambda$	$\frac{R_0 \left(1 + \sqrt{1 - \left(\frac{R_n}{R_0}\right)^2}\right) \left(\frac{\alpha}{\alpha+3}\right)^{\frac{1}{3}}}{\sqrt{2R_0^2 \left(1 + \sqrt{1 - \left(\frac{R_n}{R_0}\right)^2}\right) \left(\frac{\alpha}{\alpha+3}\right)^{\frac{1}{3}} - R_n^2}}$

Table 8.1: Summary of the normalised expressions for the surface stress of drops on capillaries using the approximation that the drop can be described by a spherical sector. While for Gibbs droploons these are correct, they are only approximations for Hookean and Neo-Hookean droploons. The expressions for $\hat{\sigma}_{sphere}$ are given in Table 4.1. The geometric factor ξ is given in Eq. (8.29).

consistently with what one would obtain for a perfectly spherical sector droploon with Hookean skin on a capillary. In all cases, the corrective term is zero in the reference state where $R = R_0$. Once the interfacial stresses are known, the pressure-deformation relation can be calculated using the Young-Laplace law given in Eq. (4.40).

Table 8.1 summarises normalised expressions derived from this simple geometrical approximation model, together with expressions for the critical stretch.

8.3 C- PDMS foam generation

Our characterisation of the PDMS gel in Section 5.2.4 shows that the rigidity and the gelation kinetics can be controlled separately : the final shear modulus G'_∞ scales as a power-law of the mass fraction of reactive silicone polymers ϕ_r (MHDS and vinyl-terminated PDMS, see Section 2.3.1) at stoichiometric ratio $G'_\infty \sim \phi_r^{2.78 \pm 0.01}$, while the gelation time T_g scales as a power-law of ϕ_r and the volume fraction of the platinum catalyst ϕ_p , defined here as the ratio of the volume of catalyst and the volume of the whole mixture $T_g \sim \phi_r^{-0.80 \pm 0.01} \phi_p^{-1.09 \pm 0.01}$.

These scaling laws help us to prepare silicone blends with varying shear moduli G'_∞ and similar gelation time T_g . We prepare three different silicone mixtures, with $\phi_r = 100$ wt. %, 81.4 wt. % and 47.6 wt. %, with the last solution having an expected modulus 8 times smaller than the first one. We aim at a gelation time of 40 s, and scale ϕ_p accordingly (0.335 vol. %, 0.389 vol. % and 0.57 vol. %, respectively). The foams are generated following the procedure described in Section 2.3.7. The solidified foams are then imaged using X-Ray tomography, as shown in Fig. 8.2, using the tomographic setup described in Section 2.5. The pore sizes and the thicknesses of the struts between the pore are measured using the Vgstudio software provided by the constructor. Their distribution is shown in Fig. 8.3.

The average pore size decreases when the mixing time is increased. Similarly, the struts become thinner, indicating a foam composed of a larger number of smaller bubbles. The lateral slices of the foams shown in Fig. 8.2 also show that the smaller bubbles are less spherical, indicating a deformation of the bubbles during the foam generation. This could be due to the deformation of the foam after gelation, during the depression step. A more detailed description of the bubble shape could help to describe more precisely the foam morphology. During the foam generations, we also noticed that the foam gelation was faster when repeating the mixing procedure with the same

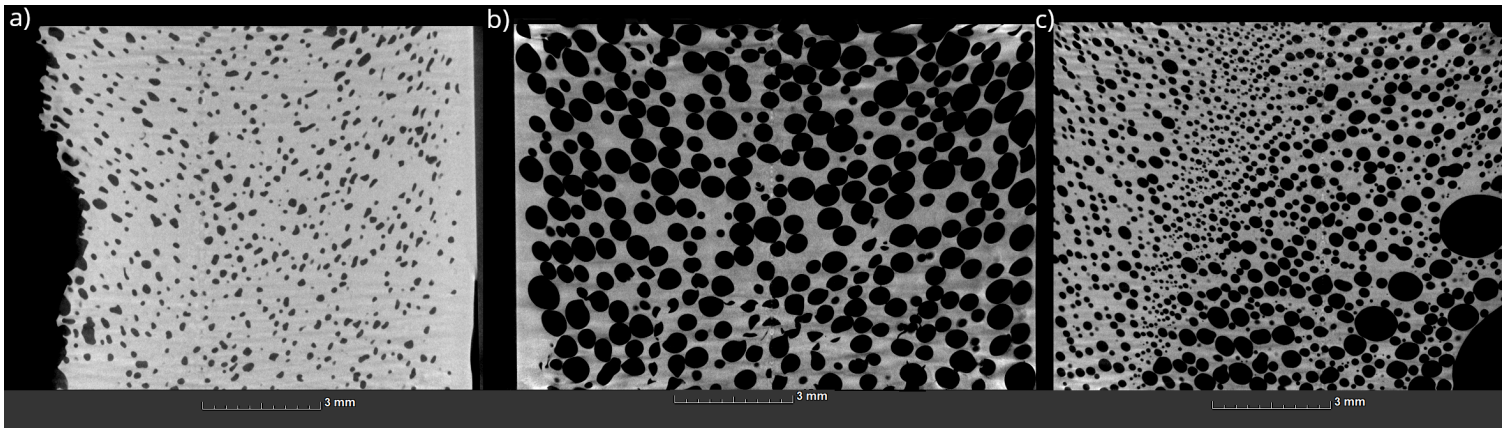


Figure 8.2: Three examples of PDMS foams prepared with different experimental parameters. a) $\phi_r = 47.6$ wt.%, $\phi_p = 0.57$ vol.%, $T = 40$ s, $V_{depression} = 50$ %. b) $\phi_r = 81.4$ wt.%, $\phi_p = 0.389$ vol.%, $T = 43$ s, $V_{depression} = 100$ %. c) $\phi_r = 100$ wt.%, $\phi_p = 0.335$ vol.%, $T = 40$ s, $V_{depression} = 25$ %.

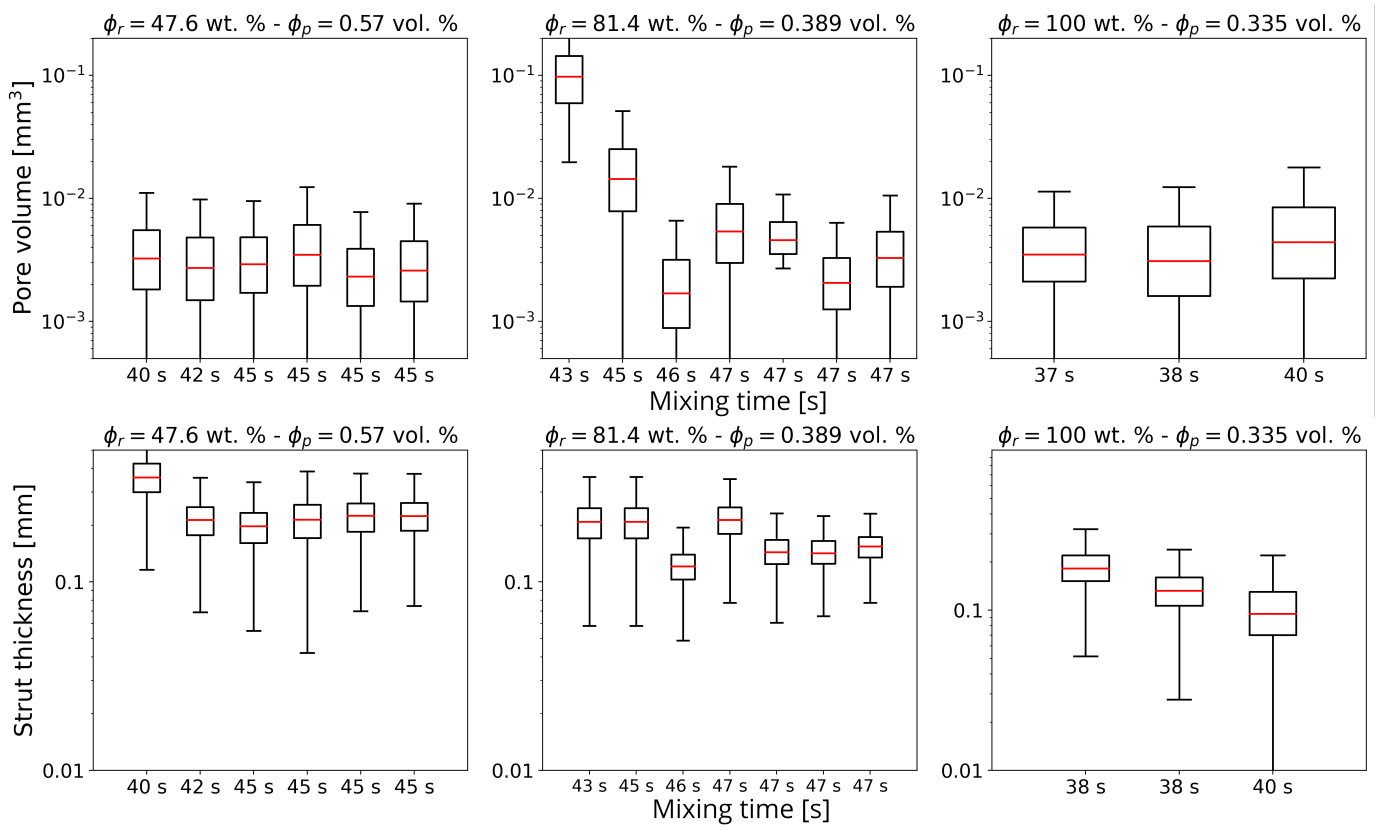


Figure 8.3: Characterisation of the foam morphology through the pore size distribution and the thickness of the struts between the pores. Identical solutions are mixed for different times to investigate the effect of mixing time on the morphology.

Luer lock connector. This could be due to the presence of gelified silicone enriched in catalyst in the connector, hastening the crosslinking of the gel.

Overall, our foam generation procedure produces foams with different morphologies, which can be controlled with the solution parameters ϕ_r and ϕ_p and the mixing time.

Bibliography

- [1] M. Nagel, T. A. Tervoort, and J. Vermant, “From drop-shape analysis to stress-fitting elastometry,” *Advances in Colloid and Interface Science*, vol. 247, pp. 33–51, 2017.
- [2] D. J. Durian, “Foam Mechanics on the Bubble Scale,” *Phys. Rev. Lett.*, vol. 75, no. 26, pp. 4780–4783, 1995.
- [3] M. D. Lacasse, G. S. Grest, and D. Levine, “Deformation of small compressed droplets,” *Physical Review E - Statistical Physics, Plasmas, Fluids, and Related Interdisciplinary Topics*, vol. 54, no. 5, pp. 5436–5446, 1996.
- [4] D. C. Morse and T. A. Witten, “Droplet elasticity in weakly compressed emulsions,” *EPL*, vol. 22, no. 7, pp. 505–510, 1993.
- [5] A. Testouri, *Highly structured polymer foams from liquid foam templates using microfluidic lab-on-a-chip techniques*. PhD thesis, Université Paris Sud-Paris XI, 2012.
- [6] S. Andrieux, W. Drenckhan, and C. Stubenrauch, “Highly ordered biobased scaffolds: From liquid to solid foams,” *Polymer*, vol. 126, pp. 425–431, 2017.
- [7] M. F. Ashby, “The properties of foams and lattices,” *Philosophical Transactions of the Royal Society A: Mathematical, Physical and Engineering Sciences*, vol. 364, no. 1838, pp. 15–30, 2006.
- [8] B. Xu, F. Arias, S. T. Brittain, X.-M. Zhao, B. Grzybowski, S. Torquato, and G. M. Whitesides, “Making negative poisson’s ratio microstructures by soft lithography,” *Advanced Materials*, vol. 11, no. 14, pp. 1186–1189, 1999.
- [9] K. Brakke, “The surface evolver,” *Exp. Math.*, vol. 1, p. 141, 1992.
- [10] A. Giustiniani, P. Guégan, W. Drenckhan, C. Poulard, and M. Marchand, “Generation of Silicone Poly-HIPES with Controlled Pore Sizes via Reactive Emulsion Stabilization,” *Macromolecular Rapid Communications*, vol. 37, no. 18, pp. 1527–1532, 2016.
- [11] P. A. Kralchevsky, K. D. Danov, and S. E. Anachkov, “Depletion forces in thin liquid films due to nonionic and ionic surfactant micelles,” *Current Opinion in Colloid and Interface Science*, vol. 20, no. 1, pp. 11–18, 2015.
- [12] A. van der Net, L. Blondel, A. Saugey, and W. Drenckhan, “Simulating and interpreting images of foams with computational ray-tracing techniques,” *Colloids and Surfaces A: Physicochemical and Engineering Aspects*, vol. 309, pp. 159–176, nov 2007.

- [13] G. Ginot, R. Höhler, S. Mariot, A. Kraynik, and W. Drenckhan, “Juggling bubbles in square capillaries : an experimental proof of non-pairwise bubble interactions,” *Soft Matter*, vol. 15, pp. 4570–4582, 2019.
- [14] K. Brakke, “The surface evolver.” <http://facstaff.susqu.edu/brakke/evolver/evolver.html>, 2013. [Online; accessed 13-october-2021].
- [15] J. Winkelmann, F. F. Dunne, V. J. Langlois, M. E. Möbius, D. Weaire, and S. Hutzler, “2D foams above the jamming transition: Deformation matters,” *Colloids and Surfaces A: Physicochemical and Engineering Aspects*, vol. 534, pp. 52–57, 2017.
- [16] R. Bouzidi and A. L. Van, “Numerical solution of hyperelastic membranes by energy minimization,” *Computers & Structures*, vol. 82, no. 23, pp. 1961–1969, 2004.
- [17] L. N. Lewis, J. Stein, R. E. Colborn, Y. Gao, and J. Dong, “The chemistry of fumarate and maleate inhibitors with platinum hydrosilylation catalysts,” *Journal of Organometallic Chemistry*, vol. 521, no. 1-2, pp. 221–227, 1996.
- [18] S. Cohen, Y. Marcus, Y. Migron, S. Dikstein, and A. Shafran, “Water sorption, binding and solubility of polyols,” *J. Chem. Soc., Faraday Trans.*, vol. 89, pp. 3271–3275, 1993.
- [19] J. A. Baird, R. Olayo-Valles, C. Rinaldi, and L. S. Taylor, “Effect of molecular weight, temperature, and additives on the moisture sorption properties of polyethylene glycol,” *Journal of Pharmaceutical Sciences*, vol. 99, no. 1, pp. 154–168, 2010.
- [20] T. Padfield, J. Winslow, W. B. Pedersen, and J. Gastrup, “Decomposition of polyethylene glycol (peg) on heating,” in *ICOM Committee for Conservation, 9th triennial meeting, Dresden, German Democratic Republic, 26-31 August 1990: preprints*, pp. 243–245, 1990.
- [21] S. Han, C. Kim, and D. Kwon, “Thermal degradation of poly(ethyleneglycol),” *Polymer Degradation and Stability*, vol. 47, no. 2, pp. 203–208, 1995.
- [22] S. Han, C. Kim, and D. Kwon, “Thermal/oxidative degradation and stabilization of polyethylene glycol,” *Polymer*, vol. 38, no. 2, pp. 317–323, 1997.
- [23] T. T. Esq., “On the magnitude of a drop of liquid formed under different circumstances,” *The London, Edinburgh, and Dublin Philosophical Magazine and Journal of Science*, vol. 27, no. 181, pp. 176–180, 1864.
- [24] A. W. Adamson and A. P. Gast, *Physical chemistry of surfaces*, vol. 150. Interscience publishers New York, 1967.
- [25] H. R. Winter, “Can the gel point of a cross-linking polymer be detected by the g' - g'' crossover?,” *Polymer Engineering and Science*, 1987.
- [26] L. M. C. Sagis and P. Fischer, “Nonlinear rheology of complex fluid–fluid interfaces,” *Current Opinion in Colloid & Interface Science*, vol. 19, no. 6, pp. 520–529, 2014.
- [27] N. Jaensson and J. Vermant, “Tensiometry and rheology of complex interfaces,” *Current Opinion in Colloid & Interface Science*, vol. 37, pp. 136–150, 2018.
- [28] G. G. Fuller and J. Vermant, “Complex Fluid-Fluid Interfaces: Rheology and Structure,” *Annual Review of Chemical and Biomolecular Engineering*, vol. 3, pp. 519–543, jun 2012.

- [29] T. Instruments, “Interfacial rheology : accessories,” 2021.
- [30] J. L. Andrea and R. N. Sindey, “Jamming is not just cool any more,” *Nature*, vol. 81, no. 2, pp. 226–231, 1998.
- [31] R. L. Brown and J. C. . Richards, “Principles of Powder Mechanics,” *Powder Technology*, vol. 4, no. 2, p. 114, 1971.
- [32] J. Duran, *Sands, Powders, and Grains : an introduction to the physics of granular materials*. 1997.
- [33] M. Durand, “Statistical mechanics of two-dimensional foams: Physical foundations of the model,” *European Physical Journal E*, vol. 38, no. 12, pp. 1–16, 2015.
- [34] G. Katgert, B. P. Tighe, and M. Van Hecke, “The jamming perspective on wet foams,” *Soft Matter*, vol. 9, no. 41, pp. 9739–9746, 2013.
- [35] J. Brujić, S. F. Edwards, I. Hopkinson, and H. A. Makse, “Measuring the distribution of interdroplet forces in a compressed emulsion system,” *Physica A: Statistical Mechanics and its Applications*, vol. 327, no. 3-4, pp. 201–212, 2003.
- [36] T. Gaillard, “Ecoulements confinés à haut et bas Reynolds : génération millifluidique de mousse et drainage de films minces de copolymères To cite this version : HAL Id : tel-01402333 Ecoulements confinés à haut et bas Reynolds : génération millifluidique de mousse et ,” 2016.
- [37] M. Van Hecke, “Jamming of soft particles: Geometry, mechanics, scaling and isostaticity,” *Journal of Physics Condensed Matter*, vol. 22, no. 3, 2010.
- [38] G. Katgert and M. Van Hecke, “Jamming and geometry of two-dimensional foams,” *EPL*, vol. 92, no. 3, 2010.
- [39] W. G. Ellenbroek, E. Somfai, M. Van Hecke, and W. Van Saarloos, “Critical scaling in linear response of frictionless granular packings near jamming,” *Physical Review Letters*, vol. 97, no. 25, pp. 1–4, 2006.
- [40] M. B. Sexton, M. E. Möbius, and S. Hutzler, “Bubble dynamics and rheology in sheared two-dimensional foams,” *Soft Matter*, vol. 7, no. 23, pp. 11252–11258, 2011.
- [41] A. O. Siemens and M. Van Hecke, “Jamming: A simple introduction,” *Physica A: Statistical Mechanics and its Applications*, vol. 389, no. 20, pp. 4255–4264, 2010.
- [42] C. S. O’Hern, L. E. Silbert, A. J. Liu, and S. R. Nagel, “Jamming at zero temperature and zero applied stress: The epitome of disorder,” *Physical Review E - Statistical Physics, Plasmas, Fluids, and Related Interdisciplinary Topics*, vol. 68, no. 1, p. 19, 2003.
- [43] M. Schröter, “A local view on the role of friction and shape,” *EPJ Web of Conferences*, vol. 140, p. 01008, 2017.
- [44] H. A. Makse, N. Gland, D. L. Johnson, and L. M. Schwartz, “Why effective medium theory fails in granular materials,” *Physical Review Letters*, vol. 83, no. 24, pp. 5070–5073, 1999.
- [45] H. Princen, “Osmotic pressure of foams and highly concentrated emulsions. i. theoretical considerations,” *Langmuir*, 1986.

- [46] A. Maestro, W. Drenckhan, E. Rio, and R. Höhler, “Liquid dispersions under gravity: Volume fraction profile and osmotic pressure,” *Soft Matter*, vol. 9, no. 8, pp. 2531–2540, 2013.
- [47] W. G. Ellenbroek, Z. Zeravcic, W. Van Saarloos, and M. Van Hecke, “Non-affine response: Jammed packings vs. spring networks,” *Epl*, vol. 87, no. 3, 2009.
- [48] N. Myshkin, M. Petrokovets, and A. Kovalev, “Tribology of polymers: Adhesion, friction, wear, and mass-transfer,” *Tribology International*, vol. 38, no. 11, pp. 910–921, 2005. Tribology International A Celebration Issue.
- [49] H. P. Zhang and H. A. Makse, “Jamming transition in emulsions and granular materials,” *Physical Review E - Statistical, Nonlinear, and Soft Matter Physics*, vol. 72, no. 1, pp. 1–12, 2005.
- [50] A. Giustinani, W. S. Garcia-Moreno, P. Christophe, and K. Paul, “Skinny emulsions take on granular matter,” *Soft Matter*, vol. 49, no. 49, pp. 1–9, 2013.
- [51] S. Lower, “Cubic lattices and close packing,” 2021.
- [52] L. E. Silbert, A. J. Liu, and S. R. Nagel, “Structural signatures of the unjamming transition at zero temperature,” *Physical Review E - Statistical, Nonlinear, and Soft Matter Physics*, vol. 73, no. 4, 2006.
- [53] A. Donev, S. Torquato, and F. H. Stillinger, “Pair correlation function characteristics of nearly jammed disordered and ordered hard-sphere packings,” *Physical Review E - Statistical, Nonlinear, and Soft Matter Physics*, vol. 71, no. 1, pp. 1–14, 2005.
- [54] M. Wyart, L. E. Silbert, S. R. Nagel, and T. A. Witten, “Effects of compression on the vibrational modes of marginally jammed solids,” *Physical Review E - Statistical, Nonlinear, and Soft Matter Physics*, vol. 72, no. 5, 2005.
- [55] T. S. Majmudar and R. P. Behringer, “Contact force measurements and stress-induced anisotropy in granular materials,” *Nature*, vol. 435, no. 7045, pp. 1079–1082, 2005.
- [56] F. M. Schaller, M. Neudecker, M. Saadatfar, G. W. Delaney, G. E. Schröder-Turk, and M. Schröter, “Local origin of global contact numbers in frictional ellipsoid packings,” *Phys. Rev. Lett.*, vol. 114, p. 158001, Apr 2015.
- [57] F. M. Schaller, S. C. Kapfer, M. E. Evans, M. J. Hoffmann, T. Aste, M. Saadatfar, K. Mecke, G. W. Delaney, and G. E. Schröder-Turk, “Set voronoi diagrams of 3d assemblies of aspherical particles,” *Philosophical Magazine*, vol. 93, no. 31-33, pp. 3993–4017, 2013.
- [58] S. Weis, P. W. A. Schönhofer, F. M. Schaller, M. Schröter, and G. E. Schröder-Turk, “Pomelo, a tool for computing Generic Set Voronoi Diagrams of Aspherical Particles of Arbitrary Shape,” pp. 5–8, 2017.
- [59] S. Weis, “Pomelo,” 2021.
- [60] F. F. Dunne, F. Bolton, D. Weaire, and S. Hutzler, “Statistics and topological changes in 2D foam from the dry to the wet limit,” *Philosophical Magazine*, vol. 97, pp. 1768–1781, jul 2017.

- [61] K. W. Desmond, P. J. Young, D. Chen, and E. R. Weeks, “Experimental study of forces between quasi-two-dimensional emulsion droplets near jamming,” *Soft Matter*, vol. 9, pp. 3424–3436, mar 2013.
- [62] I. Jorjadze, L. L. Pontani, and J. Brujic, “Microscopic approach to the nonlinear elasticity of compressed emulsions,” *Physical Review Letters*, vol. 110, no. 4, p. 48302, 2013.
- [63] T. L. Vu and J. Barés, “Soft-grain compression: Beyond the jamming point,” *Physical Review E*, vol. 100, no. 4, 2019.
- [64] S. Weis and M. Schröter, “Analyzing X-ray tomographies of granular packings,” *Review of Scientific Instruments*, vol. 88, no. 5, 2017.
- [65] R. Höhler and S. Cohen-Addad, “Rheology of liquid foam,” *Journal of Physics Condensed Matter*, vol. 17, no. 41, p. R1041, 2005.
- [66] A. Boromand, A. Signoriello, J. Lowensohn, C. S. Orellana, E. R. Weeks, F. Ye, M. D. Shattuck, and C. S. O’Hern, “The role of deformability in determining the structural and mechanical properties of bubbles and emulsions,” *Soft Matter*, vol. 15, no. 29, pp. 5854–5865, 2019.
- [67] D. Weaire, *The Kelvin Problem : Foam Structures of Minimal Surface Area*. CRC Press, 1997.
- [68] D. Weaire and R. Phelan, “A counter-example to kelvin’s conjecture on minimal surfaces,” *Philosophical Magazine Letters*, vol. 69, no. 2, pp. 107–110, 1994.
- [69] J. Brennan-Craddock, G. A. Bingham, R. J. M. Hague, and R. Wildman, “Impact Absorbent Rapid Manufactured Structures (IARMS),” 2008.
- [70] V. M. Ievlev, V. I. Putlyaev, T. V. Safronova, and P. V. Evdokimov, “Additive technologies for making highly permeable inorganic materials with tailored morphological architectonics for medicine,” dec 2015.
- [71] R. Höhler, Y. Cheun Sang, and S. Lorenceau, E.and Cohen-Addad, “Osmotic pressure and structures of monodisperse ordered foam,” *Langmuir*, vol. 71, no. 2, pp. 418–425, 2008.
- [72] R. Höhler and S. Cohen-Addad, “Many-body interactions in soft jammed materials,” *Soft Matter*, vol. 13, no. 7, pp. 1371–1383, 2017.
- [73] T. G. Mason, M.-D. Lacasse, G. S. Grest, D. Levine, J. Bibette, and D. A. Weitz, “Osmotic pressure and viscoelastic shear moduli of concentrated emulsions,” *Phys. Rev. E*, vol. 56, pp. 3150–3166, sep 1997.
- [74] N. Kern and D. Weaire, “Approaching the dry limit in foam,” *Philosophical Magazine*, vol. 83, pp. 2973–2987, sep 2003.
- [75] D. Weaire and S. Hutzler, *Physics of foams*. Oxford University Press, 1999.
- [76] C. Macosko, *Rheology, Principles, Measurements and Applications*. Wiley, 1994.
- [77] A. M. Kraynik and D. Reinelt, “International congress on rheology (seoul, south korea),” 2004.

- [78] A. M. Kraynik, D. Reinelt, and F. van Swol, “3rd euro cong on foams, emulsions and applications,” 2000.
- [79] A. Saint-Jalmes and D. J. Durian, “Vanishing elasticity for wet foams: Equivalence with emulsions and role of polydispersity,” *Journal of Rheology*, vol. 43, pp. 1411–1422, nov 1999.
- [80] T. G. Mason, J. Bibette, and D. A. Weitz, “Elasticity of compressed emulsions,” *Phys. Rev. Lett.*, vol. 75, pp. 2051–2054, Sep 1995.
- [81] D. A. Reinelt and A. M. Kraynik, “Simple shearing flow of dry soap foams with tetrahedrally close-packed structure,” *Journal of Rheology*, vol. 44, pp. 453–471, may 2000.
- [82] S. Cohen-Addad, H. Hoballah, and R. Höhler, “Viscoelastic response of a coarsening foam,” *Phys. Rev. E*, vol. 57, pp. 6897–6901, Jun 1998.
- [83] I. Cantat, S. Cohen-Addad, F. Elias, F. Graner, R. Höhler, and O. Pitois, *Foams: Structure and Dynamics*. OUP Oxford, 2013.
- [84] J. Plateau, *Experimental and theoretical statics of liquids subject to molecular forces only*. 1873.
- [85] W. Drenckhan and S. Hutzler, “Structure and energy of liquid foams,” *Advances in colloid and interface science*, vol. 224, pp. 1–16, 2015.
- [86] S. Arditty, C. P. Whitby, B. P. Binks, V. Schmitt, and F. Leal-Calderon, “Some general features of limited coalescence in solid-stabilized emulsions,” *European Physical Journal E*, vol. 11, no. 3, pp. 273–281, 2003.
- [87] J. Ding, E. Ma, M. Asta, and R. O. Richie, “Second-nearest-neighbor correlations from connection of atomic packing motifs in metallic glasses and liquids,” *Scientific reports*, 2015.
- [88] X. Fang, C. Wang, S. Hao, M. Kramer, Y. Yao, M. Mendeleev, Z. Ding, R. Napolitano, and M. HO, “Spatially resolved distribution function and the medium-range order in metallic liquid and glass,” *Scientific reports*, vol. 1, no. 194, 2011.
- [89] J. Brujić, C. Song, P. Wang, C. Briscoe, G. Marty, and H. A. Makse, “Measuring the coordination number and entropy of a 3D jammed emulsion packing by confocal microscopy,” *Physical Review Letters*, vol. 98, no. 24, p. 248001, 2007.
- [90] H. A. Makse, D. L. Johnson, and L. M. Schwartz, “Packing of compressible granular materials,” *Physical Review Letters*, vol. 84, no. 18, pp. 4160–4163, 2000.
- [91] F. Bolton, “Software plat : a computer code for simulating two-dimensional liquid foams.” <https://github.com/fbolton/plat>, 1996.
- [92] F. Bolton and D. Weaire, “The effects of plateau borders in the two-dimensional soap froth. II. General simulation and analysis of rigidity loss transition,” *Philosophical Magazine B: Physics of Condensed Matter; Statistical Mechanics, Electronic, Optical and Magnetic Properties*, vol. 65, no. 3, pp. 473–487, 1992.
- [93] S. Hutzler, R. P. Murtagh, D. Whyte, S. T. Tobin, and D. Weaire, “Z-cone model for the energy of an ordered foam,” *Soft Matter*, vol. 10, pp. 7103–7108, jul 2014.

- [94] H. Princen, “Rheology of foams and highly concentrated emulsions: I. elastic properties and yield stress of a cylindrical model system,” *Journal of Colloid and Interface Science*, vol. 91, no. 1, pp. 160–175, 1983.
- [95] J. Jose, G. A. Blab, A. Van Blaaderen, and A. Imhof, “Jammed elastic shells—a 3D experimental soft frictionless granular system,” *Soft Matter*, vol. 11, no. 9, pp. 1800–1813, 2015.
- [96] J. Jose, A. Van Blaaderen, and A. Imhof *Physical Review E*, vol. 93, no. 6, 2016.
- [97] A. Šiber and P. Zihlerl, “Many-body contact repulsion of deformable disks,” *Physical Review Letters*, vol. 110, no. 21, p. 214301, 2013.
- [98] A. Boromand, A. Signoriello, F. Ye, C. S. O’Hern, and M. D. Shattuck, “Jamming of Deformable Polygons,” *Physical Review Letters*, vol. 121, no. 24, p. 248003, 2018.
- [99] Q. Sun and S. Hutzler, “Lattice gas simulations of two-dimensional liquid foams,” *Rheologica Acta*, vol. 43, no. 5, pp. 567–574, 2004.
- [100] R. Benzi, M. Bernaschi, M. Sbragaglia, and S. Succi, “Rheological properties of soft-glassy flows from hydro-kinetic simulations,” *Epl*, vol. 104, no. 4, pp. 1–6, 2013.
- [101] T. Kähärä, T. Tallinen, and J. Timonen, “Numerical model for the shear rheology of two-dimensional wet foams with deformable bubbles,” *Physical Review E - Statistical, Nonlinear, and Soft Matter Physics*, vol. 90, p. 032307, sep 2014.
- [102] N. Kern, D. Weaire, A. Martin, S. Hutzler, and S. J. Cox, “Two-dimensional viscous froth model for foam dynamics,” *Physical Review E - Statistical Physics, Plasmas, Fluids, and Related Interdisciplinary Topics*, vol. 70, p. 13, oct 2004.
- [103] P. Rognon and C. Gay, “Soft Dynamics simulation. 1. Normal approach of two deformable particles in a viscous fluid and optimal-approach strategy,” *European Physical Journal E*, vol. 27, pp. 253–260, nov 2008.
- [104] A. P. Subnikov, Y. A. Brychkov, and O. Marichev, *Integrals and Series*, vol. formulae (5.10), (5.11). Gordon and Breach, New York, N. Y., 1986.
- [105] D. Weaire, R. Höhler, and S. Hutzler, “Bubble-bubble interactions in a 2d foam, close to the wet limit,” *Advances in Colloid and Interface Science*, vol. 247, pp. 491–495, sep 2017.
- [106] P. Aussillous and D. Quere, “Properties of liquid marbles,” *Proceedings of the Royal Society A*, vol. 462, pp. 973–999, mar 2006.
- [107] F. Chevy, A. Chepelianskii, D. Quere, and E. Raphael, “Liquid Hertz contact: Softness of weakly deformed drops on non-wetting substrates,” *EPL*, vol. 100, no. 5, 2012.
- [108] S. Hutzler, J. C. F. Ryan-Purcell, F. Dunne, and D. Weaire, “A simple formula for the estimation of surface tension from two length measurements for a sessile or pendant drop,” *Philosophical Magazine Letters*, 2018.
- [109] F. F. Dunne, J. Winkelmann, D. Weaire, and S. Hutzler, “Implementation of Morse–Witten theory for a polydisperse wet 2D foam simulation,” *Philosophical Magazine*, vol. 99, no. 18, pp. 2303–2320, 2019.

- [110] D. S. Bassett, E. T. Owens, K. E. Daniels, and M. A. Porter, “Influence of network topology on sound propagation in granular materials,” *Physical Review E - Statistical, Nonlinear, and Soft Matter Physics*, vol. 86, no. 4, pp. 1–17, 2012.
- [111] C. Giusti, L. Papadopoulos, E. T. Owens, K. E. Daniels, and D. S. Bassett, “Topological and geometric measurements of force-chain structure,” *Physical Review E*, vol. 94, no. 3, pp. 1–12, 2016.
- [112] D. S. Bassett, E. T. Owens, M. A. Porter, M. L. Manning, and K. E. Daniels, “Extraction of force-chain network architecture in granular materials using community detection,” *Soft Matter*, vol. 11, no. 14, pp. 2731–2744, 2015.
- [113] J. E. Kollmer and K. E. Daniels, “Betweenness centrality as predictor for forces in granular packings,” *Soft Matter*, vol. 15, no. 8, pp. 1793–1798, 2019.
- [114] J. Brujić, *Experimental Study of Stress Transmission Through Particulate Matter*. PhD thesis, University of Cambridge, 2004.
- [115] A. Giustiniani, “Linking Adhesive Properties and Pore Organisation of Silicone Emulsions Obtained by Reactive Blending,” 2018.
- [116] J. W. M. Bush, “Surface tension module,” tech. rep. ”Available from <http://web.mit.edu/1.63/www/Lec-notes/Surfacetension/Lecture1.pdf>”.
- [117] D. A. Edwards, H. Brenner, and D. T. Wasan, *Interfacial Transport Processes and Rheology*. Butterworth-Heinemann,Stonham,USA, 1991.
- [118] A. N. Frumkin and V. Levich, “The effect of surface active substances on the motion at liquid interfaces,” *Zh. Fiz. Khim.*, vol. 21, p. 1183–1204, 1947.
- [119] I. B. Ivanov and P. A. Kralchevsky, “Stability of emulsions under equilibrium and dynamic conditions,” *Colloids and Surfaces A: Physicochemical and engineering aspects*, vol. 128, no. 1-3, pp. 155–175, 1997.
- [120] I. Cantat, S. Cohen-Addad, F. Elias, F. Graner, R. Höhler, O. Pitois, F. Rouyer, and A. Saint-Jalmes, *Foams: structure and dynamics*. OUP Oxford, 2013.
- [121] N. Ayawei, N. Ebelegi, and D. Wankasi, “Modelling and Interpretation of Adsorption Isotherms,” *Journal of Chemistry*, 2017.
- [122] C. Johans and P. Suomalainen, “Exercise in physical chemistry: Surface tension and adsorption,” 2004.
- [123] R. Miller and D. Moebius, *Drops and Bubbles in Interfacial Research*. Elsevier Science B.V., 1998.
- [124] N. O. Jaensson, P. D. Anderson, and J. Vermant, “Computational interfacial rheology,” *Journal of Non-Newtonian Fluid Mechanics*, vol. 290, no. February, p. 104507, 2021.
- [125] E. Aumaitre, S. Knoche, P. Cicuta, and D. Vella, “Wrinkling in the deflation of elastic bubbles,” *European Physical Journal E*, vol. 36, p. 22, mar 2013.

- [126] S. Knoche, D. Vella, E. Aumaitre, P. Degen, H. Rehage, P. Cicuta, and J. Kierfeld, “Elastometry of Deflated Capsules: Elastic Moduli from Shape and Wrinkle Analysis,” *Langmuir*, vol. 29, no. 40, pp. 12463–12471, 2013.
- [127] C. Gu and L. Botto, “Direct calculation of anisotropic surface stresses during deformation of a particle-covered drop,” *Soft Matter*, vol. 12, pp. 705–716, jan 2016.
- [128] L. Landau and E. Lifshitz, *Theory of Elasticity, 2nd edition*. Pergamon Press, 1970.
- [129] R. Shuttleworth, “The Surface Tension of Solids,” *Proceedings of the Physical Society. Section A*, vol. 63, no. 5, p. 444, 1950.
- [130] L. R. S. R.S., “Xxxiv. on the theory of surface forces,” *The London, Edinburgh, and Dublin Philosophical Magazine and Journal of Science*, vol. 30, no. 185, pp. 285–298, 1890.
- [131] M. van den Tempel and E. Lucassen-Reynders, “Relaxation processes at fluid interfaces,” *Advances in Colloid and Interface Science*, vol. 18, no. 3, pp. 281–301, 1983.
- [132] P. Erni, “Deformation modes of complex fluid interfaces,” *Soft Matter*, vol. 7, no. 17, pp. 7586–7600, 2011.
- [133] D. Carvajal, E. J. Laprade, K. J. Henderson, and K. R. Shull, “Mechanics of pendant drops and axisymmetric membranes,” *Soft Matter*, vol. 7, no. 22, pp. 10508–10519, 2011.
- [134] G. L. Gaines, “Insoluble monolayers at liquid-gas interfaces,” 1966.
- [135] C. Lautz, T. M. Fischer, M. Weygand, M. Lösche, P. B. Howes, and K. Kjaer, “Determination of alkyl chain tilt angles in langmuir monolayers: A comparison of brewster angle autocorrelation spectroscopy and x-ray diffraction,” *The Journal of Chemical Physics*, vol. 108, no. 11, pp. 4640–4646, 1998.
- [136] N. Denkov, S. Tcholakova, and D. Cholakova, “Surface phase transitions in foams and emulsions,” *Current Opinion in Colloid and Interface Science*, vol. 44, pp. 32–47, 2019.
- [137] D. Zang, D. Langevin, B. P. Binks, and B. Wei, “Shearing particle monolayers: Strain-rate frequency superposition,” *Phys. Rev. E*, vol. 81, p. 011604, Jan 2010.
- [138] B. Brugger, J. Vermant, and W. Richtering, “Interfacial layers of stimuli-responsive poly-(n-isopropylacrylamide-co-methacrylicacid) (pnipam-co-maa) microgels characterized by interfacial rheology and compression isotherms,” *Phys. Chem. Chem. Phys.*, vol. 12, pp. 14573–14578, 2010.
- [139] A. Torcello-Gómez, J. Maldonado-Valderrama, M. J. Gálvez-Ruiz, A. Martín-Rodríguez, M. A. Cabrerizo-Vílchez, and J. de Vicente, “Surface rheology of sorbitan tristearate and beta-lactoglobulin: Shear and dilatational behavior,” *Journal of Non-Newtonian Fluid Mechanics*, vol. 166, no. 12, pp. 713–722, 2011.
- [140] S. Cohen-Addad, R. Höhler, and O. Pitois, “Flow in Foams and Flowing Foams,” *Annual Review of Fluid Mechanics*, vol. 45, no. 1, pp. 241–267, 2013.
- [141] D. Weaire, N. Pittet, S. Hutzler, and D. Pardal, “Steady-state drainage of an aqueous foam,” *Physical Review Letters*, vol. 71, pp. 2670–2673, oct 1993.

- [142] D. Weaire, S. Hutzler, G. Verbist, and E. Peters, “A Review of Foam Drainage,” in *Advances in Chemical Physics*, vol. 102, pp. 315–374, Wiley, mar 2007.
- [143] M. Safouane, A. Saint-Jalmes, V. Bergeron, and D. Langevin, “Viscosity effects in foam drainage: Newtonian and non-newtonian foaming fluids,” *European Physical Journal E*, vol. 19, no. 2, pp. 195–202, 2006.
- [144] S. A. Koehler, S. Hilgenfeldt, and H. A. Stone, “Liquid flow through aqueous foams: The node-dominated foam drainage equation,” *Physical Review Letters*, vol. 82, pp. 4232–4235, may 1999.
- [145] S. A. Koehler, S. Hilgenfeldt, and H. A. Stone, “Generalized view of foam drainage: Experiment and theory,” *Langmuir*, vol. 16, pp. 6327–6341, jul 2000.
- [146] S. A. Koehler, S. Hilgenfeldt, E. R. Weeks, and H. A. Stone, “Drainage of single plateau borders: Direct observation of rigid and mobile interfaces,” *Physical Review E - Statistical Physics, Plasmas, Fluids, and Related Interdisciplinary Topics*, vol. 66, no. 4, p. 4, 2002.
- [147] J. Duplat, B. Bossa, and E. Villermaux, “On two-dimensional foam ageing,” *Journal of Fluid Mechanics*, vol. 673, pp. 147–179, 2011.
- [148] D. Weaire and V. Pagonis, “Frustrated froth: Evolution of foam inhibited by an insoluble gaseous component,” *Philosophical Magazine Letters*, vol. 62, no. 6, pp. 417–421, 1990.
- [149] J. Banhart, “Metal foams: Production and stability,” *Advanced Engineering Materials*, vol. 8, no. 9, pp. 781–794, 2006.
- [150] C.G.K., “The scientific papers of j. willard gibbs,” *Nature*, vol. 75, pp. 361–362.
- [151] W. Kloek, T. Van Vliet, and M. Meinders, “Effect of bulk and interfacial rheological properties on bubble dissolution,” *Journal of Colloid and Interface Science*, vol. 237, pp. 158–166, may 2001.
- [152] K. Malysa, R. Miller, and K. Lunkenheimer, “Relationship between foam stability and surface elasticity forces: Fatty acid solutions,” *Colloids and Surfaces*, vol. 53, no. 1, pp. 47–62, 1991.
- [153] K. Wantke, K. Malysa, and K. Lunkenheimer, “A relation between dynamic foam stability and surface elasticity,” *Colloids and Surfaces A: Physicochemical and Engineering Aspects*, vol. 82, no. 2, pp. 183–191, 1994.
- [154] L. Wang and R.-H. Yoon, “Effects of surface forces and film elasticity on foam stability,” *International Journal of Mineral Processing*, vol. 85, no. 4, pp. 101–110, 2008.
- [155] D. Georgieva, A. Cagna, and D. Langevin, “Link between surface elasticity and foam stability,” *Soft Matter*, vol. 5, pp. 2063–2071, 2009.
- [156] M. B. Meinders and T. van Vliet, “The role of interfacial rheological properties on ostwald ripening in emulsions,” *Advances in Colloid and Interface Science*, vol. 108-109, pp. 119–126, 2004. *Emulsions, From Fundamentals to Practical Applications*.
- [157] T. B. Blijdenstein, P. W. De Groot, and S. D. Stoyanov, “On the link between foam coarsening and surface rheology: Why hydrophobins are so different,” *Soft Matter*, vol. 6, pp. 1799–1808, apr 2010.

- [158] A. Cervantes Martinez, E. Rio, G. Delon, A. Saint-Jalmes, D. Langevin, and B. P. Binks, “On the origin of the remarkable stability of aqueous foams stabilised by nanoparticles: link with microscopic surface properties,” *Soft Matter*, vol. 4, pp. 1531–1535, 2008.
- [159] A. Stocco, W. Drenckhan, E. Rio, D. Langevin, and B. P. Binks, “Particle-stabilised foams: an interfacial study,” *Soft Matter*, vol. 5, pp. 2215–2222, 2009.
- [160] A. R. Cox, D. L. Aldred, and A. B. Russell, “Exceptional stability of food foams using class II hydrophobin HFBII,” *Food Hydrocolloids*, 2008.
- [161] A. G. Salonen Cyprien, M. A. D. W, and R. Emmanuelle, “Gas pressure in bubble attached to tube circular outlet,” *ArXiv*, 2016.
- [162] S. Heitkam, “Bubbles, foam and froth,” 2020. <https://bildungsportal.sachsen.de/opal/auth/RepositoryEntry>
- [163] R. Miller and L. Liggieri, *Interfacial Rheology*. Boca Raton: CRC Press, 2009.
- [164] J. Krägel and S. R. Derkatch, “Interfacial shear rheology,” *Current Opinion in Colloid & Interface Science*, vol. 15, no. 4, pp. 246–255, 2010.
- [165] G. Fuller, “Interfacial rheology : Fundamental overview and applications,” 2013. <https://www.tainstruments.com/interfacial-rheology-fundamental-overview-and-applications/>.
- [166] S. Vandebril, A. Franck, G. G. Fuller, P. Moldenaers, and J. Vermant, “A double wall-ring geometry for interfacial shear rheometry,” *Rheologica acta*, vol. 49, no. 2, pp. 131–144, 2010.
- [167] C. F. Brooks, G. Fuller, C. Frank, and C. Robertson, “An interfacial stress rheometer to study rheological transitions in monolayers at the air-water interface,” *Langmuir*, vol. 15, pp. 2450–2459, 1999.
- [168] C. Gao, E. Donath, S. Moya, V. Dudnik, and H. Möhwald, “Elasticity of hollow polyelectrolyte capsules prepared by the layer-by-layer technique,” *The European Physical Journal E*, vol. 5, no. 1, pp. 21–27, 2001.
- [169] B. Dollet, P. Marmottant, and V. Garbin, “Bubble Dynamics in Soft and Biological Matter,” *Annual Review of Fluid Mechanics*, vol. 51, pp. 331–355, jan 2019.
- [170] J. Hegemann, S. Knoche, S. Egger, M. Kott, S. Demand, A. Unverfehrt, H. Rehage, and J. Kierfeld, “Pendant capsule elastometry,” *Journal of Colloid and Interface Science*, vol. 513, no. Supplement C, pp. 549–565, 2018.
- [171] S. C. Russev, N. Alexandrov, K. G. Marinova, K. D. Danov, N. D. Denkov, L. Lyutov, V. Vulchev, and C. Bilke-Krause, “Instrument and methods for surface dilatational rheology measurements,” *Review of Scientific Instruments*, vol. 79, p. 104102, oct 2008.
- [172] K. D. Danov, R. D. Stanimirova, P. A. Kralchevsky, K. G. Marinova, N. A. Alexandrov, S. D. Stoyanov, T. B. J. Blijdenstein, and E. G. Pelan, “Capillary meniscus dynamometry – Method for determining the surface tension of drops and bubbles with isotropic and anisotropic surface stress distributions,” *Journal of Colloid and Interface Science*, vol. 440, no. 0, pp. 168–178, 2015.

- [173] Y. Rotenberg, L. Boruvka, and A. W. Neumann, “Determination of surface tension and contact angle from the shapes of axisymmetric fluid interfaces,” *Journal of Colloid And Interface Science*, vol. 93, no. 1, pp. 169–183, 1983.
- [174] F. S. Kratz and J. Kierfeld, “Pendant drop tensiometry: A machine learning approach,” *The Journal of Chemical Physics*, vol. 153, no. 9, p. 094102, 2020.
- [175] J. K. Ferri, S. Y. Lin, and K. J. Stebe, “Curvature effects in the analysis of pendant bubble data: Comparison of numerical solutions, asymptotic arguments, and data,” *Journal of Colloid and Interface Science*, vol. 241, no. 1, pp. 154–168, 2001.
- [176] S. Zholob, A. Makievski, R. Miller, and V. Fainerman, “Optimisation of calculation methods for determination of surface tensions by drop profile analysis tensiometry,” *Advances in Colloid and Interface Science*, vol. 134-135, pp. 322–329, 2007. Surface forces: wetting phenomena, membrane separation, rheology. Topical issue in honour of Victor Starov.
- [177] F. Ravera, G. Loglio, and V. I. Kovalchuk, “Interfacial dilational rheology by oscillating bubble/drop methods,” *Current Opinion in Colloid & Interface Science*, vol. 15, no. 4, pp. 217–228, 2010.
- [178] J. Lucassen and M. Van Den Tempel, “Dynamic measurements of dilational properties of a liquid interface,” *Chemical Engineering Science*, vol. 27, no. 6, pp. 1283–1291, 1972.
- [179] E. Ventsel and T. Krauthammer, *Thin Plates and Shells : Theory, Analysis, and Applications*. Marcel Dekker, 2001.
- [180] V. Kovalchuk, F. Ravera, L. Liggieri, G. Loglio, P. Pandolfini, A. Makievski, S. Vincent-Bonnieu, J. Krägel, A. Javadi, and R. Miller, “Capillary pressure studies under low gravity conditions,” *Advances in Colloid and Interface Science*, vol. 161, no. 1, pp. 102–114, 2010. Physico-chemical and flow behaviour of droplet based systems.
- [181] P. Kralchevsky, J. Eriksson, and S. Ljunggren, “Theory of curved interfaces and membranes: Mechanical and thermodynamical approaches,” *Advances in Colloid and Interface Science*, vol. 48, pp. 19–59, 1994.
- [182] P. Kralchevsky and K. Nagayama, *Particles at fluid interfaces and membranes: attachment of colloid particles and proteins to interfaces and formation of two-dimensional arrays*. Elsevier, 2001.
- [183] A. Libai and J. G. Simmonds, *Nonlinear Elastic Shell Theory*, vol. 23. 1983.
- [184] C. Quilliet, A. Farutin, and P. Marmottant, “Effect of gaussian curvature modulus on the shape of deformed hollow spherical objects,” *The European Physical Journal E*, vol. 39, no. 6, p. 58, 2016.
- [185] M. Rachik, D. Barthes-Biesel, M. Carin, and F. Edwards-Levy, “Identification of the elastic properties of an artificial capsule membrane with the compression test: Effect of thickness,” *Journal of Colloid and Interface Science*, vol. 301, no. 1, pp. 217–226, 2006.
- [186] L. M. C. Sagis, “Chapter 10 - Determination of Mechanical Properties of Microcapsules,” pp. 195–205, San Diego: Academic Press, 2015.
- [187] P. Graf, R. Finken, and U. Seifert, “Adhesion of microcapsules,” Tech. Rep. 16, 2006.

- [188] C. I. Zoldesi, I. L. Ivanovska, C. Quilliet, G. J. Wuite, A. Imhof, L. Pauchard, and S. Rica, “Elastic properties of hollow colloidal particles,” *Physical Review E - Statistical, Nonlinear, and Soft Matter Physics*, vol. 78, no. 5, pp. 1–8, 1998.
- [189] L. Pauchard and S. Rica, “Contact and compression of elastic spherical shells: The physics of a ‘ping-pong’ ball,” *Philosophical Magazine B: Physics of Condensed Matter; Statistical Mechanics, Electronic, Optical and Magnetic Properties*, vol. 78, no. 2, pp. 225–233, 1998.
- [190] E. Reissner, “Stresses and Small Displacements of Shallow Spherical Shells. I,” *Journal of Mathematics and Physics*, vol. 25, no. 1-4, pp. 80–85, 1912.
- [191] E. Reissner, “Stresses and Small Displacements of Shallow Spherical Shells. II,” *Journal of Mathematics and Physics*, vol. 25, no. 1-4, pp. 80–85, 1946.
- [192] H. Rehage, M. Husmann, and A. Walter, “From two-dimensional model networks to microcapsules,” *Rheologica Acta*, vol. 41, no. 4, pp. 292–306, 2002.
- [193] N. A. Alexandrov, K. G. Marinova, T. D. Gurkov, K. D. Danov, P. A. Kralchevsky, S. D. Stoyanov, T. B. Blijdenstein, L. N. Arnaudov, E. G. Pelan, and A. Lips, “Interfacial layers from the protein HFBII hydrophobin: Dynamic surface tension, dilatational elasticity and relaxation times,” *Journal of Colloid and Interface Science*, vol. 376, pp. 296–306, jun 2012.
- [194] P. Erni, H. A. Jerri, K. Wong, and A. Parker, “Interfacial viscoelasticity controls buckling, wrinkling and arrest in emulsion drops undergoing mass transfer,” *Soft Matter*, vol. 8, pp. 6958–6967, jul 2012.
- [195] M. F. Beatty, “Topics in Finite Elasticity: Hyperelasticity of Rubber, Elastomers, and Biological Tissues—With Examples,” *Applied Mechanics Reviews*, vol. 40, pp. 1699–1734, dec 1987.
- [196] C. W. Macosko, *Rheology: Principles, Measurements and Applications*. Wiley-VCH, 1994.
- [197] B. Audoly and Y. Pomeau, *Elasticity and geometry: from hair curls to the non-linear response of shells*. Oxford: Oxford University Press, 2010.
- [198] A. Mal and S. Singh, *Deformation of Elastic Solids*. Prentice Hall, 1991.
- [199] “Separating viscoelastic and compressibility contributions in pressure-area isotherm measurements,” *Advances in Colloid and Interface Science*, vol. 206, pp. 428–436, 2014.
- [200] K. J. Mysels, M. C. Cox, and J. D. Skewis, “The measurement of film elasticity,” *Journal of Physical Chemistry*, vol. 65, no. 7, pp. 1107–1111, 1961.
- [201] J. Kitchener, “Confirmation of the Gibbs Theory of Elasticity of Soap Films,” *Nature*, vol. 196, pp. 1048–1050, 1962.
- [202] I. Müller and P. Strehlow, *Rubber and Rubber Balloons: Paradigms of Thermodynamics*. Springer, 2004.
- [203] R. G. Larson, *Structure and rheology of complex fluids*. Oxford University Press, 1998.
- [204] C. O. Horgan, “The remarkable Gent constitutive model for hyperelastic materials,” *International Journal of Non-Linear Mechanics*, vol. 68, pp. 9–16, 2015.

- [205] G. Puglisi and G. Saccomandi, “The Gent model for rubber-like materials: An appraisal for an ingenious and simple idea,” *International Journal of Non-Linear Mechanics*, vol. 68, pp. 17–24, 2015.
- [206] B. Buffel, F. Desplentere, K. Brakke, and I. Verpoest, “Modelling open-cell foams based on the weaire-phelan unit cell with a minimal surface energy approach,” *International Journal of Solids and Structures*, vol. 51, pp. 3461–3470, 2014.
- [207] S. Sacanna, W. T. M. Irvine, L. Rossi, and D. J. Pine, “Lock and key colloids through polymerization-induced buckling of monodisperse silicon oil droplets,” *Soft Matter*, vol. 7, no. 5, p. 1631, 2011.
- [208] F. S. Wong and R. T. Shield, “Large plane deformations of thin elastic sheets of neo-Hookean material,” *Zeitschrift für Angew. Math. und Phys. ZAMP*, vol. 20, pp. 176–199, mar 1969.
- [209] G. Ginot, F. S. Kratz, F. Walzel, J. Farago, J. Kierfeld, R. Höhler, and W. Drenckhan, “Pressure–deformation relations of elasto-capillary drops (droploons) on capillaries,” *Soft Matter*, pp. –, 2021.
- [210] L. M. C. Sagis, “Dynamic properties of interfaces in soft matter: Experiments and theory,” *Reviews of Modern Physics*, vol. 83, no. 4, pp. 1367–1403, 2011.
- [211] G. G. Fuller and J. Vermant, “Editorial: dynamics and rheology of complex fluid-fluid interfaces,” *Soft Matter*, vol. 7, no. 17, pp. 7583–7585, 2011.
- [212] M. Pepicelli, N. Jaensson, C. Tregouet, B. Schroyen, A. Alicke, T. Tervoort, C. Monteux, and J. Vermant, “Surface viscoelasticity in model polymer multilayers: From planar interfaces to rising bubbles,” *Journal of Rheology*, vol. 63, pp. 815–828, aug 2019.
- [213] A. P. Kotula and S. L. Anna, “Regular perturbation analysis of small amplitude oscillatory dilatation of an interface in a capillary pressure tensiometer,” *Journal of Rheology*, vol. 59, pp. 85–117, dec 2014.
- [214] D. J. Koeze and B. P. Tighe, “Sticky matters: Jamming and rigid cluster statistics with attractive particle interactions,” *Phys. Rev. Lett.*, vol. 121, p. 188002, Nov 2018.
- [215] D. J. Koeze, L. Hong, A. Kumar, and B. P. Tighe, “Elasticity of jammed packings of sticky disks,” *Phys. Rev. Research*, vol. 2, p. 032047, Aug 2020.
- [216] E. Koos and N. Willenbacher *Science*, vol. 311, pp. 897–900.
- [217] A. Giustiniani, , W. S. Garcia-Moreno, P. Christophe, and K. Paul, “Skinny emulsions take on granular matter,” *Soft Matter*, vol. 49, no. 49, pp. 1–9, 2018.
- [218] S. Thutupalli, S. Herminghaus, and R. Seemann, “Bilayer membranes in micro-fluidics: From gel emulsions to soft functional devices,” *Soft Matter*, vol. 7, no. 4, pp. 1312–1320, 2011.
- [219] A. Blandino, M. Macias, and D. Cantero, “Formation of calcium alginate gel capsules: Influence of sodium alginate and cacl2 concentration on gelation kinetics,” *Journal of Bioscience and Bioengineering*, vol. 88, no. 6, pp. 686–689, 1999.
- [220] İ. Yilgör and J. E. McGrath, *Polysiloxane containing copolymers: A survey of recent developments*. Berlin, Heidelberg: Springer Berlin Heidelberg, 1988.

- [221] G. Belorgey and G. Sauvet, *Organosiloxane Block and Graft Copolymers*. Dordrecht: Springer Netherlands, 2000.
- [222] J. Chojnowski, M. Cypriak, W. Fortuniak, M. Scibiorek, and K. Rozga-Wijas, “Synthesis of branched polysiloxanes with controlled branching and functionalization by anionic ring-opening polymerization,” *Macromolecules*, vol. 36, no. 11, pp. 3890–3897, 2003.
- [223] A. Yoshimoto and G. Takahiro, “Oligo- and polysiloxanes,” *Progress in Polymer Science*, vol. 29, no. 3, pp. 149–182, 2004.
- [224] E. Pouget, J. Tonnar, P. Lucas, P. Lacroix-Desmazes, F. Ganachaud, and B. Boutevin, “Well-architected poly(dimethylsiloxane)-containing copolymers obtained by radical chemistry,” *Chemical Reviews*, vol. 110, no. 3, pp. 1233–1277, 2010.
- [225] J. Saam and J. Falender, “De 2717192,” tech. rep., Dow Corning Corp., USA, 1977.
- [226] J. Falender, J. Saam, and C. Mettler, “De 2717227,” tech. rep., Dow Corning Corp., USA, 1977.
- [227] B. M. Baysal, N. Uyanik, E. E. Hamurcu, and M. Cvetkovska, “Styrene polymerization with a macroinitiator having siloxane units,” *Journal of Applied Polymer Science*, vol. 60, no. 9, pp. 1369–1378, 1996.
- [228] E. E. Hamurcu, B. Hazer, Z. Misirli, and B. M. Baysal, “Preparation and characterization of block and graft copolymers using macroazoinitiators having siloxane units,” *Journal of Applied Polymer Science*, vol. 62, no. 9, pp. 1415–1426, 1996.
- [229] E. Elif Hamurcu, B. Hazer, and B. Baysal, “Polystyrene-b-polydimethyl siloxane (pdms) multicomponent polymer networks: Styrene polymerization with macromonomeric initiators (macroinimers) having pdms units,” *Polymer*, vol. 38, no. 12, pp. 2981–2987, 1997.
- [230] N. Uyanik, “Synthesis and characterization of five-block copolymers prepared by vinyl pyrrolidinone and a macro initiator with poly(dimethylsiloxane) and polycaprolactone,” *Journal of Applied Polymer Science*, vol. 64, no. 10, pp. 1961–1969, 1997.
- [231] N. Uyanik, B. Köker, and Y. Yildiz, “Synthesis and characterization of poly(dimethyl siloxane) containing poly(vinyl pyrrolidinone) block copolymers,” *Journal of Applied Polymer Science*, vol. 71, no. 11, pp. 1915–1922, 1999.
- [232] H. Shinoda, K. Matyjaszewski, L. Okrasa, M. Mierzwa, and T. Pakula, “Structural control of poly(methyl methacrylate)-g-poly(dimethylsiloxane) copolymers using controlled radical polymerization : effect of the molecular structure on morphology and mechanical properties,” *Macromolecules*, vol. 36, no. 13, pp. 4772–4778, 2003.
- [233] D. Neugebauer, Y. Zhang, T. Pakula, and K. Matyjaszewski, “Pdms-peo densely grafter copolymers,” *Macromolecules*, vol. 38, no. 21, pp. 8687–8693, 2005.
- [234] A. Giustiniani, “Linking Adhesive Properties and Pore Organisation of Silicone Emulsions Obtained by Reactive Blending,” tech. rep., 2018.
- [235] M. Dirany, L. Dies, F. Restagno, L. Léger, C. Poulard, and G. Miquelard-Garnier, “Chemical modification of pdms surface without impacting the viscoelasticity: Model systems for a better understanding of elastomer/elastomer adhesion and friction,” *Colloids and Surfaces A: Physicochemical and Engineering Aspects*, vol. 468, pp. 174–183, 2015.

- [236] D. J. Hornbaker, R. Albert, I. Albert, A. L. Barabasi, and P. Schiffer, “What keeps sandcastles standing ?,” *Nature*, vol. 387, Jan. 1997.
- [237] T. C. Halsey and A. J. Levine, “How sandcastles fall,” *Phys. Rev. Lett.*, vol. 80, pp. 3141–3144, Apr 1998.
- [238] H. Herrmann, “Granular matter,” *Physica A: Statistical Mechanics and its Applications*, vol. 313, no. 1, pp. 188–210, 2002. Fundamental Problems in Statistical Physics.
- [239] S. Andrieux, A. Quell, C. Stubenrauch, and W. Drenckhan, “Liquid foam templating – a route to tailor-made polymer foams,” *Advances in Colloid and Interface Science*, vol. 256, pp. 276–290, 2018.
- [240] S. Andrieux, *Monodisperse highly ordered and polydisperse biobased solid foams*. Springer Nature, 2019.
- [241] G. Lutzweiler, *Matériaux poreux à base de polyuréthane pour l’ingénierie tissulaire*. Theses, Université de Strasbourg, Sept. 2019.
- [242] A. van der Net, A. Gryson, M. Ranft, F. Elias, C. Stubenrauch, and W. Drenckhan, “Highly structured porous solids from liquid foam templates,” *Colloids and Surfaces A: Physicochemical and Engineering Aspects*, vol. 346, no. 1, pp. 5–10, 2009.
- [243] I. Pulko and P. Krajnc, “High internal phase emulsion templating – a path to hierarchically porous functional polymers,” *Macromolecular Rapid Communications*, vol. 33, no. 20, pp. 1731–1746, 2012.
- [244] A. Quell, J. Elsing, W. Drenckhan, and C. Stubenrauch, “Monodisperse polystyrene foams via microfluidics – a novel templating route,” *Advanced Engineering Materials*, vol. 17, no. 5, pp. 604–609, 2015.
- [245] M. Rubinstein and R. Colby, *Polymer Physics*. Oxford University Press, 2003.
- [246] D. Stauffer, A. Coniglio, and M. Adam, “Gelation and critical phenomena,” pp. 103–158, 1982.
- [247] “On the universality of the scaling relations during sol-gel transition,” *Journal of Rheology*, vol. 64, no. 4, pp. 863–877, 2020.
- [248] P. J. Flory, *Principles of polymer chemistry*. Cornell University Press, 1953.
- [249] W. Stockmayer, “J. chem. phys., 11, 45; stockmayer, wh, 1944,” *J. chem. Phys.*, vol. 12, p. 125, 1943.
- [250] J. W. Essam, “Percolation theory,” *Reports on progress in physics*, vol. 43, no. 7, p. 833, 1980.
- [251] A. Y. Malkin and A. I. Isayev, *Rheology : Concepts, Methods, and Applications*. Chemtec Publishing, 2012.
- [252] T. G. Mezger. Vincentz Network, 2006.
- [253] M. T. Shaw, *Introduction to polymer rheology*. Wiley, 2012.

- [254] N. Pottier, *Physique statistique hors d'équilibre : processus irréversibles linéaires*. CNRS Éditions, 2004.
- [255] M. I. Limited, “A basic introduction to rheology,” tech. rep., 2016.
- [256] H. Winter and M. Mours, *Rheology of Polymers Near Liquid-Solid Transitions*, vol. 134, pp. 165–234. 09 1997.
- [257] A. J. Chalk and J. F. Harrod, “Homogeneous Catalysis. II. The Mechanism of the Hydrosilylation of Olefins Catalyzed by Group VIII Metal Complexes,” *Journal of the American Chemical Society*, vol. 87, no. 1, pp. 16–21, 1965.
- [258] B. Karstedt, “Platinum complexes of unsaturated siloxanes and platinum containing organopolysiloxanes,” apr 1971.
- [259] B. Marciniac, *Comprehensive Handbook on Hydrosilylation*. Pergamon, 1st editio ed., 1992.
- [260] Y. Nakajima and S. Shimada, “Hydrosilylation reaction of olefins: Recent advances and perspectives,” *RSC Advances*, vol. 5, no. 26, pp. 20603–20616, 2015.
- [261] M. A. Llorente and J. E. Mark, “Model Networks of End-Linked Poly(dimethylsiloxane) Chains. 8. Networks Having Cross-Links of Very High Functionality,” *Macromolecules*, vol. 13, no. 3, pp. 681–685, 1980.
- [262] F. Chambon and H. H. Winter, “Linear viscoelasticity at the gel point of a crosslinking pdms with imbalanced stoichiometry,” *Journal of Rheology*, vol. 31, no. 8, pp. 683–697, 1987.
- [263] J. Stein, L. N. Lewis, K. A. Smith, and K. X. Lettko, “Mechanistic Studies of Platinum-Catalyzed Hydrosilylation,” *Journal of Inorganic and Organic Polymers*, vol. 1, no. 3, 1991.
- [264] J. L. Braun, J. E. Mark, and B. E. Eichinger, “Formation of poly(dimethylsiloxane) gels,” *Macromolecules*, vol. 35, no. 13, pp. 5273–5282, 2002.
- [265] L. Lestel, H. Cheradame, and S. Boileau, “Crosslinking of polyether networks by hydrosilylation and related side reactions,” *Polymer*, vol. 31, no. 6, pp. 1154–1158, 1990.
- [266] N. A. Alcantar, E. S. Aydil, and J. N. Israelachvili, “Polyethylene glycol-coated biocompatible surfaces,” *Journal of Biomedical Materials Research: An Official Journal of The Society for Biomaterials, The Japanese Society for Biomaterials, and The Australian Society for Biomaterials and the Korean Society for Biomaterials*, vol. 51, no. 3, pp. 343–351, 2000.
- [267] A. C. Esteves, J. Brokken-Zijp, J. Laven, H. P. Huinink, N. J. Reuvers, M. P. Van, and G. de With, “Influence of cross-linker concentration on the cross-linking of PDMS and the network structures formed,” *Polymer*, vol. 50, no. 16, pp. 3955–3966, 2009.
- [268] Smokefoot, 2013. <https://commons.wikimedia.org/wiki/File:KartstedtCatalyst.png>.
- [269] D. Alexander, “Levenberg-marquardt toolbox,” 2021. <https://www.mathworks.com/matlabcentral/fileexchange/levenberg-marquardt-toolbox>.
- [270] M. De menech, P. Garstecki, F. Jousse, and H. A. Stone, “Transition from squeezing to dripping in a microfluidic T-shaped junction,” *Journal of Fluid Mechanics*, vol. 595, pp. 141–161, 2008.

- [271] M. Pepicelli, T. Verwijlen, T. A. Tervoort, and J. Vermant, “Characterization and modelling of Langmuir interfaces with finite elasticity,” *Soft Matter*, vol. 3, pp. 10715 – 10722, 2010.
- [272] *Spatial structures formed by chemical reactions at liquid interfaces : phenomenology, model simulations, and pattern analysis*, Springer, 1984.
- [273] *Pattern formation in chemical systems : the effect of convection*, Springer, 1984.
- [274] C. Défarge, O. M. Issa, and J. Trichet, “Apports du cryo-microscope électronique à balayage à émission de champ à l’étude des matières organiques et des relations organo-minérales naturelles. application aux croûtes microbiotiques des sols,” *Comptes Rendus de l’Académie des Sciences - Series IIA - Earth and Planetary Science*, vol. 328, no. 9, pp. 591–597, 1999.
- [275] T. Weitkamp, D. Haas, D. Wegrzynek, and A. Rack, “ANKAphase: Software for single-distance phase retrieval from inline X-ray phase-contrast radiographs,” *Journal of Synchrotron Radiation*, vol. 18, no. 4, pp. 617–629, 2011.
- [276] H. H. Henning Winter, P. Morganelli, and F. Chambon, “Stoichiometry Effects on Rheology of Model Polyurethanes at the Gel Point,” *Macromolecules*, vol. 21, no. 2, pp. 532–535, 1988.
- [277] A. Mehta, G. Barker, and J. Luck, “Cooperativity in sandpiles: statistics of bridge geometries,” *Journal of Statistical Mechanics: Theory and Experiment*, vol. 2004, no. 10, p. P10014, 2004.
- [278] A. Mehta, J. Luck, J. Berg, and G. Barker, “Competition and cooperation: aspects of dynamics in sandpiles,” *Journal of Physics: Condensed Matter*, vol. 17, no. 24, p. S2657, 2005.
- [279] I. Zuriguel and T. Mullin, “The role of particle shape on the stress distribution in a sandpile,” *Proceedings of the Royal Society A: Mathematical, physical and engineering sciences*, vol. 464, no. 2089, pp. 99–116, 2008.
- [280] J. Valverde, M. Quintanilla, and A. Castellanos, “Jamming threshold of dry fine powders,” *Physical review letters*, vol. 92, no. 25, p. 258303, 2004.
- [281] W. Nan, M. Pasha, T. Bonakdar, A. Lopez, U. Zafar, S. Nadimi, and M. Ghadiri, “Jamming during particle spreading in additive manufacturing,” *Powder Technology*, vol. 338, pp. 253–262, 2018.
- [282] J. G. Puckett, F. Lechenault, and K. E. Daniels, “Local origins of volume fraction fluctuations in dense granular materials,” *Phys. Rev. E*, vol. 83, p. 041301, Apr 2011.
- [283] R. Blumenfeld and S. F. Edwards, “Granular entropy: Explicit calculations for planar assemblies,” *Phys. Rev. Lett.*, vol. 90, p. 114303, Mar 2003.
- [284] B. P. Tighe, “Relaxations and Rheology near Jamming,” *Phys. Rev. Lett.*, vol. 107, no. 15, p. 158303, 2011.
- [285] T. Unger, J. Kertész, and D. E. Wolf, “Force indeterminacy in the jammed state of hard disks,” *Phys. Rev. Lett.*, vol. 94, p. 178001, May 2005.
- [286] P. Dantu, “International Society for soil mechanics and geotechnical engineering : contribution à l’ Étude Mécanique et Géométrique des Milieux Pulvérulents,”

- [287] A. Abed Zadeh, J. Barés, T. A. Brzinski, K. E. Daniels, J. Dijksman, N. Docquier, H. O. Everitt, J. E. Kollmer, O. Lantsoght, D. Wang, M. Workamp, Y. Zhao, and H. Zheng, “Enlightening force chains: a review of photoelasticity in granular matter,” *Granular Matter*, vol. 21, no. 4, 2019.
- [288] S. Dagois-Bohy, B. P. Tighe, J. Simon, S. Henkes, and M. Van Hecke, “Soft-sphere packings at finite pressure but unstable to shear,” *Physical Review Letters*, vol. 109, no. 9, 2012.
- [289] V. Vitelli, N. Xu, M. Wyart, A. J. Liu, and S. R. Nagel, “Heat transport in model jammed solids,” *Phys. Rev. E*, vol. 81, p. 021301, Feb 2010.
- [290] E. T. Owens and K. E. Daniels, “Sound propagation and force chains in granular materials,” *EPL (Europhysics Letters)*, vol. 94, no. 5, p. 54005, 2011.
- [291] P. Digby, “The effective elastic moduli of porous granular rocks,” *Journal of Applied Mechanics*, 1981.
- [292] R. C. Hidalgo, C. U. Grosse, F. Kun, H. W. Reinhardt, and H. J. Herrmann, “Evolution of percolating force chains in compressed granular media,” *Physical review letters*, vol. 89, no. 20, p. 205501, 2002.
- [293] E. Somfai, J.-N. Roux, J. H. Snoeijer, M. Van Hecke, and W. Van Saarloos, “Elastic wave propagation in confined granular systems,” *Physical Review E*, vol. 72, no. 2, p. 021301, 2005.
- [294] J. C. M. F.R.S., “L. on the calculation of the equilibrium and stiffness of frames,” *The London, Edinburgh, and Dublin Philosophical Magazine and Journal of Science*, vol. 27, no. 182, pp. 294–299, 1864.
- [295] C. R. Calladine, “Buckminster fuller’s “tensegrity” structures and clerk maxwell’s rules for the construction of stiff frames,” *International journal of solids and structures*, vol. 14, no. 2, pp. 161–172, 1978.
- [296] R. J. Wilson, *Introduction to graph theory*. Addison Wesley, 4 ed., 1996.
- [297] F. P. Bowden and D. Tabor, *Friction: an introduction to tribology*. Anchor, 1973.
- [298] B. P. Tighe, J. H. Snoeijer, T. J. Vlugt, and M. van Hecke, “The force network ensemble for granular packings,” *Soft Matter*, vol. 6, no. 13, pp. 2908–2917, 2010.
- [299] J. H. Snoeijer, T. J. Vlugt, M. van Hecke, and W. van Saarloos, “Force network ensemble: a new approach to static granular matter,” *Physical review letters*, vol. 92, no. 5, p. 054302, 2004.
- [300] J. H. Snoeijer, T. J. Vlugt, W. G. Ellenbroek, M. van Hecke, and J. Van Leeuwen, “Ensemble theory for force networks in hyperstatic granular matter,” *Physical Review E*, vol. 70, no. 6, p. 061306, 2004.
- [301] S. Mukhopadhyay and J. Peixinho, “Packings of deformable spheres,” *Physical Review E - Statistical, Nonlinear, and Soft Matter Physics*, vol. 84, no. 1, pp. 2–6, 2011.
- [302] M. Saadatfar, A. P. Sheppard, T. J. Senden, and A. J. Kabla, “Mapping forces in a 3D elastic assembly of grains,” *Journal of the Mechanics and Physics of Solids*, vol. 60, no. 1, pp. 55–66, 2012.

- [303] A. J. Meagher, M. Mukherjee, D. Weaire, S. Hutzler, J. Banhart, and F. Garcia-Moreno, “Analysis of the internal structure of monodisperse liquid foams by X-ray tomography,” *Soft Matter*, vol. 7, no. 21, pp. 9881–9885, 2011.
- [304] A. J. Meagher, D. Whyte, J. Banhart, S. Hutzler, D. Weaire, and F. García-Moreno, “Slow crystallisation of a monodisperse foam stabilised against coarsening,” *Soft matter*, vol. 11, no. 23, pp. 4710–4716, 2015.
- [305] J. Lambert, I. Cantat, R. Delannay, A. Renault, F. Graner, J. A. Glazier, I. Veretennikov, and P. Cloetens, “Extraction of relevant physical parameters from 3D images of foams obtained by X-ray tomography,” *Colloids and Surfaces A: Physicochemical and Engineering Aspects*, vol. 263, no. 1-3 SPEC. ISS., pp. 295–302, 2005.
- [306] J. Bernal, “Geometry of the structure of monatomic liquids,” *Nature*, vol. 185, 1960.
- [307] J. D. Bernal, “The bakerian lecture, 1962. the structure of liquids,” *Proceedings of the Royal Society of London. Series A, Mathematical and Physical Sciences*, vol. 280, no. 1382, pp. 299–322, 1964.
- [308] J. B. Knight, C. G. Fandrich, C. N. Lau, H. M. Jaeger, and S. R. Nagel, “Density relaxation in a vibrated granular material,” *Physical review E*, vol. 51, no. 5, p. 3957, 1995.
- [309] E. Nowak, J. Knight, M. Povinelli, H. Jaeger, and S. Nagel, “Reversibility and irreversibility in the packing of vibrated granular material,” *Powder technology*, vol. 94, no. 1, pp. 79–83, 1997.
- [310] E. R. Nowak, J. B. Knight, E. Ben-Naim, H. M. Jaeger, and S. R. Nagel, “Density fluctuations in vibrated granular materials,” *Physical Review E*, vol. 57, no. 2, p. 1971, 1998.
- [311] P. Philippe and D. Bideau, “Compaction dynamics of a granular medium under vertical tapping,” *EPL (Europhysics Letters)*, vol. 60, no. 5, p. 677, 2002.
- [312] S. F. Edwards and R. Oakeshott, “Theory of powders,” *Physica A: Statistical Mechanics and its Applications*, vol. 157, no. 3, pp. 1080–1090, 1989.
- [313] A. Mehta and S. Edwards, “A phenomenological approach to relaxation in powders,” *Physica A: Statistical Mechanics and its Applications*, vol. 168, no. 2, pp. 714–722, 1990.
- [314] S. F. Edwards, “The role of entropy in the specification of a powder,” in *Granular Matter*, pp. 121–140, Springer, 1994.
- [315] A. Baule, F. Morone, H. J. Herrmann, and H. A. Makse, “Edwards statistical mechanics for jammed granular matter,” *Reviews of Modern Physics*, vol. 90, no. 1, p. 15006, 2018.
- [316] C. Song, P. Wang, and H. A. Makse, “A phase diagram for jammed matter,” *Nature*, vol. 453, no. 7195, pp. 629–632, 2008.
- [317] L. Portal, M. Danisch, A. Baule, R. Mari, and H. A. Makse, “Calculation of the voronoi boundary for lens-shaped particles and spherocylinders,” *Journal of Statistical Mechanics: Theory and Experiment*, vol. 2013, no. 11, p. P11009, 2013.
- [318] S. Weis, P. W. A. Schönhofer, F. M. Schaller, M. Schröter, and G. E. Schröder-Turk, “Pomelo, a tool for computing Generic Set Voronoi Diagrams of Aspherical Particles of Arbitrary Shape,” pp. 5–8, 2017.

- [319] V. A. Luchnikov, N. N. Medvedev, L. Oger, and J.-P. Troadec, “Voronoi-Delaunay analysis of voids in systems of nonspherical particles,” tech. rep., 1999.
- [320] I. Jorjadze, L. L. Pontani, K. A. Newhall, and J. Brujić, “Attractive emulsion droplets probe the phase diagram of jammed granular matter,” *Proceedings of the National Academy of Sciences of the United States of America*, vol. 108, no. 11, pp. 4286–4291, 2011.
- [321] C. S. O’Hern, S. A. Langer, A. J. Liu, and S. R. Nagel, “Force distributions near jamming and glass transitions,” *Physical review letters*, vol. 86, no. 1, p. 111, 2001.
- [322] J. Brujić, S. F. Edwards, D. V. Grinev, I. Hopkinson, D. Brujić, and H. A. Makse, “3d bulk measurements of the force distribution in a compressed emulsion system,” *Faraday discussions*, vol. 123, pp. 207–220, 2003.
- [323] F. Radjai, M. Jean, J.-J. Moreau, and S. Roux, “Force distributions in dense two-dimensional granular systems,” *Phys. Rev. Lett.*, vol. 77, pp. 274–277, Jul 1996.
- [324] M. Cates, J. Wittmer, J.-P. Bouchaud, and P. Claudin, “Jamming, force chains, and fragile matter,” *Physical review letters*, vol. 81, no. 9, p. 1841, 1998.
- [325] C.-H. Liu, S. R. Nagel, D. A. Schecter, S. N. Coppersmith, S. Majumdar, O. Narayan, and T. A. Witten, “Force fluctuations in bead packs,” *Science*, vol. 269, no. 5223, pp. 513–515, 1995.
- [326] R. Arévalo, L. A. Pugnaloni, I. Zuriguel, and D. Maza, “Contact network topology in tapped granular media,” *Physical Review E*, vol. 87, no. 2, p. 022203, 2013.
- [327] L. Kondic, A. Goulet, C. O’Hern, M. Kramar, K. Mischaikow, and R. Behringer, “Topology of force networks in compressed granular media,” *EPL (Europhysics Letters)*, vol. 97, no. 5, p. 54001, 2012.
- [328] M. Kramár, A. Goulet, L. Kondic, and K. Mischaikow, “Persistence of force networks in compressed granular media,” *Physical Review E*, vol. 87, no. 4, p. 042207, 2013.
- [329] M. Kramár, A. Goulet, L. Kondic, and K. Mischaikow, “Evolution of force networks in dense particulate media,” *Physical Review E*, vol. 90, no. 5, p. 052203, 2014.
- [330] A. Tordesillas, D. M. Walker, and Q. Lin, “Force cycles and force chains,” *Physical Review E*, vol. 81, no. 1, p. 011302, 2010.
- [331] C.-h. Liu and S. R. Nagel, “Sound in sand,” *Physical review letters*, vol. 68, no. 15, p. 2301, 1992.
- [332] C.-h. Liu and S. R. Nagel, “Sound in a granular material: disorder and nonlinearity,” *Physical Review B*, vol. 48, no. 21, p. 15646, 1993.
- [333] A. J. Liu and S. R. Nagel, “The Jamming Transition and the Marginally Jammed Solid,” in *Annual Review of Condensed Matter Physics, Vol 1* (J. S. Langer, ed.), vol. 1, pp. 347–369, Annual Reviews, 2010.
- [334] F. Radjai, D. E. Wolf, M. Jean, and J. J. Moreau, “Bimodal character of stress transmission in granular packings,” *Physical Review Letters*, vol. 80, no. 1, pp. 61–64, 1998.

- [335] M. A. Porter, J.-P. Onnela, and P. J. Mucha, “Communities in Networks,” *Notice of the AMS*, 2009.
- [336] S. Fortunato, “Community detection in graphs,” *Physics reports*, vol. 486, no. 3-5, pp. 75–174, 2010.
- [337] M. Oda, J. Konishi, and S. Nemat-Nasser, “Experimental micromechanical evaluation of strength of granular materials: effects of particle rolling,” *Mechanics of materials*, vol. 1, no. 4, pp. 269–283, 1982.
- [338] M. Oda and H. Kazama, “Microstructure of shear bands and its relation to the mechanisms of dilatancy and failure of dense granular soils,” *Geotechnique*, vol. 48, no. 4, pp. 465–481, 1998.
- [339] A. Tordesillas, “Force chain buckling, unjamming transitions and shear banding in dense granular assemblies,” *Philosophical Magazine*, vol. 87, no. 32, pp. 4987–5016, 2007.
- [340] M. Muthuswamy and A. Tordesillas, “How do interparticle contact friction, packing density and degree of polydispersity affect force propagation in particulate assemblies?,” *Journal of Statistical Mechanics: Theory and Experiment*, vol. 2006, no. 09, p. P09003, 2006.
- [341] S. Coppersmith, C.-h. Liu, S. Majumdar, O. Narayan, and T. Witten, “Model for force fluctuations in bead packs,” *Physical Review E*, vol. 53, no. 5, p. 4673, 1996.
- [342] P. Claudin, J.-P. Bouchaud, M. Cates, and J. Wittmer, “Models of stress fluctuations in granular media,” *Physical Review E*, vol. 57, no. 4, p. 4441, 1998.
- [343] M. G. Sexton, J. E. Socolar, and D. G. Schaeffer, “Force distribution in a scalar model for noncohesive granular material,” *Physical Review E*, vol. 60, no. 2, 1999.
- [344] J. E. Socolar, D. G. Schaeffer, and P. Claudin, “Directed force chain networks and stress response in static granular materials,” *The European Physical Journal E*, vol. 7, no. 4, pp. 353–370, 2002.
- [345] J. Peters, M. Muthuswamy, J. Wibowo, and A. Tordesillas, “Characterization of force chains in granular material,” *Physical review E*, vol. 72, no. 4, p. 041307, 2005.
- [346] L. Papadopoulos, M. A. Porter, K. E. Daniels, and D. S. Bassett, “Network analysis of particles and grains,” *Journal of Complex Networks*, vol. 6, no. 4, pp. 485–565, 2018.
- [347] R. Arevalo, I. Zuriguel, and D. Maza, “Topology of the force network in the jamming transition of an isotropically compressed granular packing,” *Physical Review E*, vol. 81, no. 4, p. 041302, 2010.
- [348] M. Herrera, S. McCarthy, S. Slotterback, E. Cephas, W. Losert, and M. Girvan, “Path to fracture in granular flows: Dynamics of contact networks,” *Physical Review E*, vol. 83, no. 6, p. 061303, 2011.
- [349] M. Barthélemy, “Spatial networks,” *Physics Reports*, vol. 499, no. 1, pp. 1–101, 2011.
- [350] R. Arevalo, I. Zuriguel, S. A. Trevijano, and D. Maza, “Third order loops of contacts in a granular force network,” *International Journal of Bifurcation and Chaos*, vol. 20, no. 03, pp. 897–903, 2010.

- [351] M. Durand, “Statistical mechanics of two-dimensional foams Recent citations Statistical mechanics of two-dimensional foams,” 2010.
- [352] Y. Jiang, P. J. Swart, A. Saxena, M. Asipauskas, and J. A. Glazier, “Hysteresis and avalanches in two-dimensional foam rheology simulations,” *Physical Review E*, vol. 59, no. 5, p. 5819, 1999.
- [353] F. Graner, Y. Jiang, E. Janiaud, and C. Flament, “Equilibrium states and ground state of two-dimensional fluid foams,” *Physical Review E*, vol. 63, no. 1, p. 011402, 2000.
- [354] A. M. Kraynik, D. A. Reinelt, and F. van Swol, “Structure of random foam,” *Physical Review Letters*, vol. 93, no. 20, p. 208301, 2004.
- [355] Y. Wang, K. Krishan, and M. Dennin, “Impact of boundaries on velocity profiles in bubble rafts,” *Phys. Rev. E*, vol. 73, p. 031401, Mar 2006.
- [356] K. R. Mecke, “Integral geometry in statistical physics,” *International Journal of Modern Physics B*, vol. 12, no. 09, pp. 861–899, 1998.
- [357] C. H. Arns, M. A. Knackstedt, W. V. Pinczewski, and K. R. Mecke, “Euler-poincaré characteristics of classes of disordered media,” *Phys. Rev. E*, vol. 63, p. 031112, Feb 2001.
- [358] G. E. Schröder-Turk, W. Mickel, S. C. Kapfer, M. A. Klatt, F. M. Schaller, M. J. F. Hoffmann, N. Kleppmann, P. Armstrong, A. Inayat, D. Hug, M. Reichelsdorfer, W. Peukert, W. Schwieger, and K. Mecke, “Minkowski tensor shape analysis of cellular, granular and porous structures,” *Advanced Materials*, vol. 23, no. 22-23, pp. 2535–2553, 2011.
- [359] M. E. Evans, J. Zirkelbach, G. E. Schröder-Turk, A. M. Kraynik, and K. Mecke, “Deformation of platonic foam cells: Effect on growth rate,” *Phys. Rev. E*, vol. 85, p. 061401, Jun 2012.
- [360] G. E. Schröder-Turk, W. Mickel, S. C. Kapfer, F. M. Schaller, B. Breidenbach, D. Hug, and K. Mecke, “Minkowski tensors of anisotropic spatial structure,” *New Journal of Physics*, vol. 15, p. 083028, aug 2013.
- [361] M. E. Evans, G. E. Schröder-Turk, and A. M. Kraynik, “A geometric exploration of stress in deformed liquid foams,” *Journal of Physics Condensed Matter*, vol. 29, feb 2017.
- [362] J. H. Lambert, *Photometria, Sive de Mensura et Gradibus Luminis, Colorum et Umbrae*. Eberhard Klett, 1760.
- [363] Beer, “Bestimmung der absorption des rothen lichts in farbigen flüssigkeiten,” *Annalen der Physik*, vol. 162, no. 5, pp. 78–88, 1852.
- [364] T. M. Buzug, “Computed tomography: from photon statistics to modern cone-beam ct,” 2009.
- [365] A. Mikhailovskaya and C. Monteux, “Drainage-induced control of avalanches in foam coalescence,” 2020.
- [366] “Packing spheres tightly: Influence of mechanical stability on close-packed sphere structures,” *Physical Review Letters*, vol. 108, no. 14, 2012.

- [367] W. L. Bragg and J. F. Nye, “A dynamical model of a crystal structure,” *Proceedings of the Royal Society of London. Series A. Mathematical and Physical Sciences*, vol. 190, no. 1023, pp. 474–481, 1947.
- [368] K. W. Desmond and E. R. Weeks, “Random close packing of disks and spheres in confined geometries,” *Physical Review E - Statistical, Nonlinear, and Soft Matter Physics*, vol. 80, no. 5, 2009.
- [369] C. Tomasi and R. Manduchi, “Bilateral filtering for gray and color images,” in *Sixth international conference on computer vision (IEEE Cat. No. 98CH36271)*, pp. 839–846, IEEE, 1998.
- [370] S. Bae, S. Paris, and F. Durand, “Two-scale tone management for photographic look,” *ACM SIGGRAPH 2006 Papers, SIGGRAPH '06*, vol. 1, no. 212, pp. 637–645, 2006.
- [371] S. Paris, P. Kornprobst, J. Tumblin, and F. Durand, “A gentle introduction to bilateral filtering and its applications,” *ACM SIGGRAPH 2008 Classes*, no. c, p. 1, 2008.
- [372] S. van der Walt, J. L. Schönberger, J. Nunez-Iglesias, F. Boulogne, J. D. Warner, N. Yager, E. Gouillart, T. Yu, and the scikit-image contributors, “scikit-image: image processing in Python,” *PeerJ*, vol. 2, p. e453, 2014.
- [373] A. S. Kornilov and I. V. Safonov, “An overview of watershed algorithm implementations in open source libraries,” *Journal of Imaging*, vol. 4, no. 10, 2018.
- [374] W. Lechner and C. Dellago, “Accurate determination of crystal structures based on averaged local bond order parameters,” *Journal of Chemical Physics*, vol. 129, no. 11, 2008.
- [375] P. J. Steinhardt, D. R. Nelson, and M. Ronchetti, “Bond-orientational order in liquids and glasses,” *Physical Review B*, vol. 28, no. 2, p. 784, 1983.
- [376] G. Arfken, *Mathematical Methods for Physicists*. Academic Press, 1985.
- [377] D. Moroni, P. R. ten Wolde, and P. G. Bolhuis, “Interplay between structure and size in a critical crystal nucleus,” *Phys. Rev. Lett.*, vol. 94, p. 235703, Jun 2005.
- [378] S. Ogata, “Monte carlo simulation study of crystallization in rapidly supercooled one-component plasmas,” *Phys. Rev. A*, vol. 45, pp. 1122–1134, Jan 1992.
- [379] M. Leocmach, “Pyboo: A python package to compute bond orientational order parameters,” 2017.
- [380] R. L. Vink and G. T. Barkema, “Configurational Entropy of Network-Forming Materials,” *Physical Review Letters*, vol. 89, no. 7, pp. 1–4, 2002.
- [381] B. D. McKay, “nauty and Traces User ’ s Guide (Version 2 . 5) How to use this Guide,” pp. 1–94, 2013.
- [382] M. Dabo, T. Roland, G. Dalongeville, C. Gauthier, and P. Kékicheff, “Ad-hoc modeling of closed-cell foam microstructures for structure-properties relationships,” *European Journal of Mechanics-A/Solids*, vol. 75, pp. 128–141, 2019.
- [383] M. Dabo, *Analyse du comportement mécanique des mousses polymères : apport de la tomographie X et de la simulation numérique*. Theses, Université de Strasbourg, 2015.

- [384] F. Schaller and S. Kapfer, “User manual for the minkowski tensor package karambola,” 2013.
- [385] A. V. Pogorelov, *Bendings of surfaces and stability of shells*, vol. 72. American Mathematical Soc., 1988.
- [386] H. Hencky, “11. die bewegungsgleichungen beim nichtstationären fließen plastischer massen,” *Zeitschrift für Angewandte Mathematik und Mechanik*, vol. 5, no. 2, pp. 144–146, 1925.
- [387] P. Kelly, “Mechanics lecture notes: An introduction to solid mechanics,” 2015.
- [388] T. J. Pence and K. Gou, “On compressible versions of the incompressible neo-hookean material,” *Mathematics and Mechanics of Solids*, vol. 20, no. 2, pp. 157–182, 2015.
- [389] “Chapter 1 - foundations of thin-shell theory,” in *Theory of Flexible Shells* (E. Axelrad, ed.), vol. 28 of *North-Holland Series in Applied Mathematics and Mechanics*, pp. 1–68, North-Holland, 1987.
- [390] J. Pascon, “Large deformation analysis of plane-stress hyperelastic problems via triangluar membrane finite elements,” *International Journal of Advanced Structural Engineering*, no. 11, pp. 331–350, 2019.
- [391] R. M. Corless, G. H. Gonnet, D. E. G. Hare, D. J. Jeffrey, and D. E. Knuth, “On the lambertw function,” *Advances in Computational Mathematics*, vol. 5, pp. 329–359, 1996.

Interfacially-controlled soft granular matter : from non-pairwise to elastocapillary interactions in foams and emulsions stabilised by polymeric skins

Résumé

Les mousses et émulsions sont des systèmes omniprésents dont la structure est déterminée par les interactions interfaciales entre les bulles/gouttes. Dans cette thèse, nous visons la production de matériaux basés sur des mousses/émulsions avec de nouvelles structures et propriétés mécaniques, contrôlés par la modification des interfaces par une peau solide de polymères. En mêlant expériences, modèles théoriques et simulations par éléments finis, cette thèse étudie l'effet de la déformabilité des bulles/gouttes sur leurs interactions, l'apparition d'une élasticité interfaciale et son impact sur la relation pression-déformation des bulles/gouttes. Nous développons un modèle d'élasticité interfaciale simplifiant la mesure du module de cisaillement d'une interface, et donnons les intervalles de paramètres expérimentaux dans lesquels notre approximation est valide. Nous développons également un système expérimental modèle à rigidité et épaisseur de peau contrôlées pour étudier la transition d'une interface purement capillaire à une interface purement élastique. Nous développons enfin un algorithme de segmentation pour la reconstruction et l'analyse des mousses et émulsions, produisant des informations inaccessibles avec les logiciels commerciaux actuels. En parallèle, nous confirmons la précision des résultats du logiciel d'éléments finis Surface Evolver, pour de futures simulations d'interfaces elastocapillaires.

mots-clés : mousses, émulsions, élasticité interfaciale, tomographie rayons X, Surface Evolver, gel de silicone

Résumé en anglais

Foams and emulsions are ubiquitous materials whose structure is dictated by interfacial interactions between the bubbles/drops. In this thesis, we aim at the production of foam- and emulsion-based materials with new structures and mechanical properties, controlled by the modification of the interfaces by solid polymeric skin. Using experiments, finite element simulations and theory, we investigate the effect of the deformability of the bubbles/drops on their interactions and the onset of interfacial elasticity and its impact on their pressure-deformation relation. We develop a model for interfacial elastocapillarity simplifying the measure of interfacial shear modulus, and provide the range of parameters where our approximation remains valid. We develop an experimental model system with controlled skin thickness and rigidity to investigate the transition from purely capillary interfaces to purely elastic ones. We also develop a home-made algorithm for the reconstruction and analysis of foams and emulsions, with information unavailable with current commercial softwares. We also benchmark the finite element software Surface Evolver for future simulations of elastocapillary interfaces.

keywords : foams, emulsions, interfacial elasticity, X-Ray tomography, Surface Evolver, silicone gel